2017-10-01

Characterization of Military Aircraft Jet Noise Using Wavepacket Analysis and Other Array Processing Methods

Blaine M. Harker
Brigham Young University

Characterization of Military Aircraft Jet Noise Using Wavepacket Analysis and Other Array Processing Methods

Blaine M. Harker

A dissertation submitted to the faculty of
Brigham Young University
in partial fulfillment of the requirements for the degree of

Doctor of Philosophy

Kent L. Gee, Chair
Timothy W. Leishman
Tracianne B. Neilsen
Scott D. Sommerfeldt
Alan T. Wall
Karl F. Warnick

Department of Physics and Astronomy

Brigham Young University

ABSTRACT

Characterization of Military Aircraft Jet Noise
Using Wavepacket Analysis and Other
Array Processing Methods

Blaine M. Harker
Department of Physics and Astronomy, BYU
Doctor of Philosophy

Sound generation and radiation properties are studied of full-scale tactical jet engine noise. This is motivated by the high sound exposure levels from jet noise, particularly for tactical engines. Acoustic source reconstruction methods are implemented computationally on existing jet noise data. A comparative study is performed using numerical simulations to understand the capabilities of more advanced beamforming methods to successfully estimate the source properties of a distributed, partially correlated source distribution. The properties and limitations of each beamforming method are described. Having validated the methods, beamforming with regularization—via the Hybrid Method—is implemented on linear array measurements near an installed tactical engine. A detailed analysis of the correlation and coherence properties associated with the phased array measurements guides the implementation of the beamforming. When the measurements are used as inputs to the beamforming, they produce partially correlated, distributed sources in a full-order model representation. A processing technique is also implemented that increases the usable bandwidth of the array measurements to almost an order of magnitude above the array design frequency. To more appropriately study the equivalent sources, a decomposition technique is designed and implemented to create a reduced-order wavepacket model of the jet noise. The wavepacket model is modular and scalable to allow for the efficient characterization of similar jet noise measurements. It is also appropriate for its physical significance, as wavepackets are attributed to the turbulent flow as well as the hydrodynamic and acoustic properties of the radiation. The reduced order model can estimate the levels and coherence properties of the acoustic radiation and represents a significant step towards a complete jet noise prediction model.

Keywords: jet, aeroacoustics, wavepacket, phased array, beamforming

ACKNOWLEDGMENTS

I would like to thank the support of my mentors. They have been such an inspiration of hard work, persistence, and of striving for excellence in their conduct and work. To my mentor and running buddy, thank you for pushing me to go the extra mile (literally), and to set a high achievement bar. I have learned to enjoy the journey, to laugh and to joke even when deadlines are looming. To my more compassionate mentor, thank you for your example of diligence for difficult tasks, coupled with your patience and kindness. To my friend and PhD forerunner, thank you for your help with my myriad questions, for your inquisitive thinking that inspired me to dig deeper, and for your example of persistence. These are all traits I wish to emulate.

I would also like to acknowledge the Acoustics Research Group. I found what I was looking for when I joined this team as a sophomore because of its comradery, abundant faculty support and many opportunities for group collaboration and wonderful research experiences. I have had the privilege to attend and present at over a dozen national conferences, to publish multiple times as an undergraduate and graduate researcher, to take part in and organize various acoustic field experiments and to gain many new friends. None of this would have been possible without this group and the support of its housing institutions of the Department of Physics and Astronomy and Brigham Young University.

Lastly, I would like to thank those who have been a personal support to me. To my parents who have always loved and supported me. To my paternal grandfather for inspiring me to get involved in physics, and my maternal grandfather for always reminding me how proud he is of his grandkids. To my high school calculus teacher who inspired me to aim high and be passionate about life. And finally, to my wonderful and supportive wife for the never-ending pep talks, for

the patience and for riding this crazy roller coaster of a year with me (I can see the light at the end of the tunnel)!

This research was supported in part by the appointment of Blaine Harker to the Student Research Participation Program at USAFRL, 711th Human Performance Wing, Human Effectiveness Directorate, Warfighter Interface Branch, Battlespace Acoustics Branch administered by the Oak Ridge Institute for Science and Education through an interagency agreement between the U.S. Department of Energy and USAFRL.

The author gratefully acknowledges the funding for this analysis from the Office of Naval Research. The measurements were funded by the U.S. Air Force Research Laboratory (USAFRL) through the Small Business Innovation Research program, and supported through a cooperative research and development agreement between Blue Ridge Research and Consulting, Brigham Young University, and the U.S. Air Force.

Contents

List of Tables

List of Figures

Chapter 1

Introduction

> *"I am an old man now, and when I die and go to heaven there are two matters on which I hope for enlightenment. One is quantum electrodynamics, and the other is the turbulent motion of fluids. And about the former I am rather optimistic."* – Horace Lamb

Sound generation and radiation properties related to turbulent structures have been a topic of active study for over six decades.[1] In this time, significant progress has been made to better understand the various noise components, and efforts to characterize the noise from a first-principles basis are actively being pursued.[2, 3] However, a complete model describing source and field behavior does not exist. Understanding the jet noise sources and radiation properties has significant application to aerospace research, where next-generation fighter jet aircraft demand improved power and performance that consequently increases the radiated sound levels. The increasing sound levels affect military personnel who are frequently exposed to high sound levels, that induce hearing loss. The most prevalent service-connected disabilities continue to be tinnitus and hearing loss among both new recipients and total recipients receiving veteran compensations.[4] In addition to the military personnel concerns, communities near military bases are adversely

affected. As researchers gain a better understanding of the mechanisms of jet noise, future designs and mitigation technologies are expected to provide solutions to these challenges.

1.1 The Sources of Jet Noise

The first attempts to characterize the aerodynamic jet noise sources were published by Lighthill, who pioneered the study of jet noise when he developed an acoustic analogy that modeled the noise source as an equivalent set of acoustic quadrupoles.[5, 6] These quadrupole sources characterized the turbulent mixing noise, which is the dominant source of the overall radiation. A detailed description of the classical theories of jet noise as well as recent developments can be found in review papers by Lilley[7] as well as Tam[1] and Visanathan.[8] One such theory, the two-source model of jet noise, was introduced in the 1970s, postulating that turbulent mixing noise consists of large-scale turbulent structures (LSS) that radiate primarily downstream and more incoherent fine-scale structures (FSS) which radiate omnidirectionally. A visualization of a jet noise sources model is shown in Fig. 1.1. The FSS radiation consists of multiple independently radiating events that propagate omnidirectionally. This radiation is primarily manifest in the direction perpendicular to the jet centerline. In contrast, LSS radiation is directed primarily to the aft of the aircraft and at an angle that is related to the LSS convective speed. This radiation is much more highly correlated than the FSS radiation, both in time and space, and these structures create a “wavy wall” at the shear layer of the flow. Its generation has been attributed to the “Mach wave” radiation of a supersonically convecting structure,[9] although other theories have been presented suggesting that LSS and Mach wave radiation are distinct.[10] The contributions of each component depend on the jet temperature and velocity effects, and the LSS radiation was found to be a dominant component of supersonic jet noise while playing a lesser role for subsonic jets.[1, 9]

Additional source characterizations followed for supersonic jets, including broadband shock-associated noise (BBSAN) and screech tones.[11, 12] The BBSAN and screech tones result from the interaction of turbulent vortices with the shock-cell structures and these are believed to play a lesser role towards the overall radiation, although a recent study of a full-scale engine postulates a connection between shock-cells and multiple-lobe radiation features.[13] In this study, an increased understanding of LSS and FSS is of primary interest to both the source characterization studies as well as for noise prediction models.

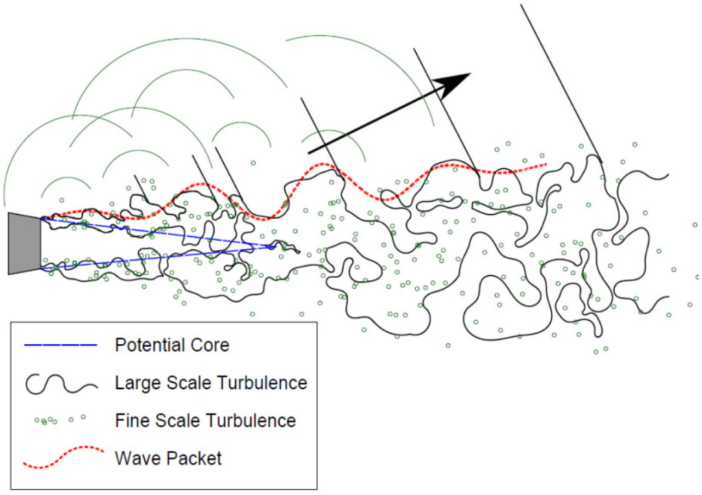

Fig. 1.1. Two-source model of turbulent mixing noise. From Gee et al.[14]

Efforts to better understand and model the radiation of jet noise using wavepacket-like distributions have seen increased interest over the past decade.[2, 15-18] Wavepacket models have been used in the description of acoustic, hydrodynamic, and turbulent features of jet noise.[2] The growth and decay of the oscillating shear layer can be modeled as a wavepacket, which is particularly useful to model the LSS (and related[10]) structures. However, while studies have attempted to relate the various turbulent, hydrodynamic and acoustic components using wavepackets,[3] one such model that describes the three environments has yet to be determined.[2]

1.2 Methods to Understand Jet Noise Sources and Radiation

The methods used to characterize the jet noise sources and understand the radiation take several forms. For instance, flow visualization technology using Schlieren and shadowgraph techniques are widely used that show both the turbulent vortices as well as the corresponding acoustic radiation[19] and have shown success in relating flow parameters to acoustic radiation of laboratory-scale jets.[20] Computational fluid dynamics models, including large eddy simulation (LES), design turbulence models with corresponding acoustic radiation properties using parameters taken from experimental data,[10] although the fields are highly sensitive to the input modeling parameters.[21] Acoustic measurements, both for model- and full-scale jets, are also prevalent.[22, 23] These are taken either in the near field of the jet, [15] the mid field,[24] or the far field.[16] These studies have been used to correlate the turbulence flow properties to the acoustic parameters,[25, 26] and to identify the levels and origins of the sources within the flow and along the shear layer.[16]

While direct measurement of the flow is feasible for study in many laboratory-scale jet setups, full-scale measurements in many cases prohibit direct measurement. Instead, indirect methods that are used to estimate the source parameters are employed, and each uses different assumptions and approaches. Intensity-based methods utilize the propagation vector to bound the source location.[27] Polar arrays allow for correlation methods to estimate the source distribution.[28] Inverse methods such as acoustical holography and beamforming provide an even more complete estimate of the jet noise source properties and have the capabilities to both characterize and model the radiation.[11, 29, 30] For example, near-field acoustical holography has been demonstrated to reconstruct measurement planes closer to the jet using acoustic field measurements.[11, 31-33] In previous studies by Wall[32] and Wall *et al.*[29] near-field acoustical holography was applied to

measurements of a supersonic, heated, full-scale jet. They characterized the acoustic radiation using cylindrical wave functions to predict the radiative properties at multiple engine conditions and for frequencies up to limitations imposed on the measurement geometry. These results provide a benchmark for further source and radiation modeling efforts on similar full-scale measurements.

1.3 Phased Array Methods for Jet Noise Analysis

Phased-array methods are commonly used as a means of estimating the distributions of the jet noise sources from indirect measurements.[34, 35] Elliptic mirrors[36] and the polar correlation technique[28] are used to spatially focus acoustic measurements such that acoustic pressure measurements from a desired focal location arrive in phase at the measurement point while acoustic sources from other positions arrive out of phase. Beamforming methods also rely on time delays or phase shifts to obtain equivalent source properties from limited array apertures. These algorithms function by artificially altering the arrival time of incoming waveforms such that sources from a desired location arrive in phase, thus allowing for arbitrary array geometries.[37, 38] However, there are method-specific assumptions for each particular beamforming algorithm that influence the calculated source characteristics.

Various jet noise phased-array analyses have been conducted using conventional methods,[16, 39] but because jet noise sources are generally noncompact and partially correlated in nature,[9] more advanced beamforming methods have been proposed to address potential discrepancies arising from the traditional beamforming assumptions.[40] For instance, Venkatesh *et al.*[35] as well as Schlinker *et al.*[41] utilized beamforming methods that weighted the measurements to account for the distributed nature of the source, but without explicitly considering source correlation. Several methods have since been developed that account for source correlation, many

of which involve cross beamforming. Brooks and Humphreys[42] developed the deconvolution approach for the mapping of acoustic sources (DAMAS), and then extended the DAMAS algorithm to allow for correlated and partially correlated sources (DAMAS-C), although at a relatively high computational cost.[43] These deconvolution techniques allow for the removal of the array point-spread function, thus improving spatial resolution and source level estimates. Some methods have circumvented the beamforming map to solve a cost function for source distributions that match the measured microphone array levels.[44, 45] Michel and Funke[44] developed the source directivity modeling of a cross-spectral matrix (SODIX) to model jet engine noise as a linear source distribution along the jet centerline where each source distribution element had an associated directivity. Their source models were able to correctly predict the far-field radiation benchmarks and to spatially separate the inlet, cowling and jet noise contributions in the radiation predictions. Regularized inverse techniques have also been introduced in conjunction with cross-beamforming algorithms that allow for source correlation, including the hybrid method (HM)[46] and generalized inverse beamforming (GINV).[40, 47] These methods provide a more simplistic and computationally efficient means to solve for the source distributions, and while they can be used in conjunction with the deconvolution approaches, the advanced beamforming methods need not necessarily utilize deconvolution to improve results. The results from these methods generate a full-order source cross-spectral matrix that can be used as an equivalent source model of the jet noise.

1.4 Objectives and Scope of Work

The purpose of this study is to apply phased-array methods to full-scale military jet noise and to enhance those methods to better understand source mechanisms and radiation properties.

First, a spatiotemporal analysis of the measurements is performed to better understand the characteristics of the radiated field. Next, various beamforming methods are applied in a numerical case study to determine a method that can adequately capture both source level and coherence properties of a jet-noise-like source distribution. Measurements in the mid field of a tactical aircraft are then used as inputs for the selected beamforming method to characterize the source. From the beamforming results an equivalent source model that can estimate the radiation characteristics. Additionally, this source model is decomposed using an analytical wavepacket basis that can more effectively characterize the noise in terms of a physically significant basis set. The computationally efficient wavepacket source model provides a framework to model the jet noise and provides insight to the component radiation properties. Each chapter is briefly described here.

In Chapter 2, various beamforming methods are compared and validated in a numerical study using measurements of a distributed, partially correlated source distribution. The coherence properties and sound level predictions from five beamforming methods are compared, i.e., cross beamforming (CBF),[43] the hybrid method (HM),[46] improved generalized inverse beamforming (GINV),[40] functional beamforming (FBF),[48] and the mapping of acoustic correlated sources (MACS),[49] to quantify the performance of each method in obtaining the correct source cross spectral matrix. The validity of each beamforming-based source is evaluated in terms of its ability to estimate the source distribution levels and coherence properties. In addition, the unwrapped phase array interpolation (UPAINT) method is applied to the cross-spectral matrix for results above the array spatial Nyquist frequency.[50] This unwrapping technique provides the ability to remove grating lobes and other aliasing features at frequencies multiple times higher than the spatial Nyquist frequency, and it has shown promise in application to lab-scale rocket measurements.[51] The resultant equivalent sources are also used to predict the near and far-field

levels and coherence properties. An understanding of the efficacy of each method to generate an equivalent source distribution that accurately predicts the radiation levels and coherence characteristics in benchmark cases leads to improved understanding of the behavior of these methods when applied to unknown sources, such as full-scale jet noise.[52] The purpose of this chapter is to select an appropriate beamforming method that will be used to input the full-scale measurements in Chapter 4.

Prior to applying a given beamforming algorithm to full-scale jet noise measurements, a spatiotemporal characterization of the field is performed in Chapter 3 to provide an improved understanding of the noise radiation and to provide a benchmark case for comparing against modeling and laboratory-scale experiments. Auto- and cross-correlation functions of the pressure field from an array of ground-based microphones near a tactical aircraft at intermediate and afterburner condition are presented to investigate the broadband features of the sound field. Some of the correlation features of the full-scale jet are not exhibited in previous laboratory-scale jet studies. To investigate these features further, a complementary study of the coherence of the noise at select frequencies is presented, and findings yield a more complete picture of tactical jet noise characteristics and highlight features of noise from high-performance military aircraft that have not yet been replicated in laboratory-scale jets.

Having characterized the sound field, a beamforming method is implemented in Chapter 4 to the array measurements of a high-performance tactical aircraft. The levels and source coherence properties of the beamforming-based one-dimensional source distribution are evaluated for multiple engine conditions as a function of frequency. This represents the first such detailed source coherence characterization of a full-scale engine to the author's knowledge. The source coherence highlights the potential necessity of using a source coherence method that can include multiple

independent sources to adequately describe the radiation. In addition, the coherence analysis from Chapter 3 will be used to guide an acoustic source investigation using subarrays to better discriminate between the various radiators as a function of the radiation directivity. The beamforming results will be used to identify the source level and coherence properties, particularly between the beamforming results corresponding to the sideline radiation and the Mach-wave radiation farther downstream.

The capstone of this work is the decomposition of the full-order beamforming results into a multiple-wavepacket source model in Chapter 5. The resultant reduced-order frequency-dependent equivalent source distribution is useful to predict both the levels and spatiotemporal properties of the corresponding radiation. The wavepacket model predicts the radiated level and coherence properties, and the method is applied to the jet noise data at three engine powers to produce a complex, extended-source reconstruction. A validation of the beamforming results and the multiple-wavepacket models are performed using benchmark jet noise measurements in the mid field. The reduced-order models provide a simplified analytical framework with which to capture the salient radiation features as well as the more intricate properties observed in full-scale jet noise measurements. The models also provide physical insight into the source characteristics as they vary with frequency and engine condition.

These results represent a significant step to further understand jet noise sources, particularly for full-scale jet engines. However, certain bounds have been applied to limit the scope of the present work and represent additional opportunities to complete the jet noise source puzzle. While numerous phased-array algorithms exist, an effort has been made to consider algorithms that provide the most promise towards effectively estimating the more complex characteristics of jet noise. In consideration of all the available beamforming algorithms, five have been selected

and implemented in the present work. In the beamforming implementations, flow models, including computational fluid-dynamics simulations, are neglected such that an equivalent noise source representation is obtained. In addition, while much is done to incorporate a wavepacket ansatz into the beamforming methods, the results primarily focus on the acoustic radiation and wavepacket properties. While similarities exist in some characteristics of the turbulent, hydrodynamic and acoustic wavepackets, Towne *et al.* [3] suggest that there is little or no correlation between the wavepackets of the three regimes and, thus, additional insight into the flow mechanisms is necessary to relate them. Furthermore, linear propagation is assumed, a reasonable assumption for the geometry and frequencies of interest.

1.5 On Nonlinearity

Inverse techniques, including beamforming, assume that the radiation propagation is a linear process. However, full-scale jet noise measurements include nonlinear source and propagation phenomena that can potentially violate the linear assumptions of the source-to-array propagation model.[53, 54] For example, significant nonlinear steepening of the acoustic radiation violates the linear assumptions assumed in beamforming. However, while nonlinear effects in the near and mid field of a jet are difficult to characterize, they are cumulatively significant only at distances beyond the shock formation distance, which is a measure of the distance required for shock formations to occur. Gee *et al.*[55] used linear and nonlinear propagation prediction models to show that the effects of nonlinear propagation for full-scale tactical measurements are significant over large distances (>100 m) and for high frequencies (>1000 Hz). In addition, Wall[32] previously justified the use of near-field acoustical holography to measurements of a full-scale tactical aircraft at arrays in the mid-field of the jet. Future work to characterize the nonlinear effects of a

distributed, high-amplitude source that emits broadband noise and to quantify the appropriate shock-formation distances could provide a more quantitative assessment of the nonlinear effects. However, for small propagation distances and for frequencies below about 2 kHz, linear propagation models and linear inverse methods should adequately characterize the acoustic source phenomena.

Chapter 2

Beamforming Methods for Extended, Partially Correlated Sources

2.1 Introduction

2.1.1 Background

Advancements in beamforming methods have increased significantly over the past decade, particularly when applied to aeroacoustic studies. A number of aeroacoustic sources have been investigated using beamforming, including flap edge noise,[42] jet-flap interaction,[47], inlet noise,[56] combustion noise[57] and jet noise.[37] In traditional beamforming, it is assumed that the sources are comprised of incoherent monopole radiators. While some aeroacoustic sources have been successfully modeled as monopoles or distributions of incoherent monopoles,[39, 42] more complicated applications—e.g., jet noise—consist of distributed and partially correlated sources that violate the traditional beamforming assumptions. The amount which the source correlation (a frequency-independent correspondent to the source coherence) and extent affect the beamforming results depends on the array geometry and sources in question. However, some recent

beamforming methods have addressed these cases.[40, 58] Improvements to beamforming techniques over the past decade have allowed for the characterization of extended, partially correlated sources that span multiple wavelengths.[52]

Beyond source characterization, beamforming results using near-field input array measurements have been used as an equivalent source model (ESM) for limited far-field sound level predictions.[40] A beamforming-based ESM is useful to understand the propagation effects of the sound sources and, when successfully implemented, provides a more complete picture of the sound field than the original input measurements. However, while sound field levels have been estimated using a beamforming-based ESM,[40, 45] the ability of the ESM to produce the correct sound field coherence properties has not been examined in prior work. Assuming a sufficiently low measurement noise floor and insignificant nonlinear radiation effects (see Section 1.5 for comments on nonlinearity), the sound field coherence properties provide insight to the relative radiation contributions from multiple independent sources.[59]

When choosing a beamforming method, its ability to produce an effective ESM for field level and coherence estimates is an important consideration. In this study, coherence properties and sound level predictions from five beamforming methods are compared, i.e., cross beamforming (CBF),[43] the hybrid method (HM),[60] improved generalized inverse beamforming (GINV),[40] functional beamforming (FBF),[48] and the mapping of acoustic correlated sources (MACS).[49] The goal is to quantify the performance of each method in obtaining an equivalent source distribution specific to jet noise and in modeling the corresponding radiation as an ESM.

2.1.2 Prior Work

There have been many beamforming methods implemented in the past decade for aeroacoustic sources. Traditional beamforming has been used for measuring lab-scale edge-noise

and jet noise[34, 39] as well as for LES data.[61] More advanced algorithms began to appear, including integration approaches to beamforming for jet noise[35] and deconvolution algorithms such as DAMAS[42] that remove artifacts of the point-spread function from the beamforming results to obtain discrete source representations. Because DAMAS was computationally expensive, DAMAS-2 and DAMAS-3 which assumed an invariant point-spread function to speed up calculations.[62, 63] CLEAN-SC was developed to allow for source deconvolution without assuming a particular point-spread function.[58] Other methods were introduced that assumed signal sparsity, including covariance matrix fitting (CMF) and SC-DAMAS.[64] In addition, FBF was developed that uses a nonlinear method to reduce sidelobes present in the beamforming results.[48] A comparison of the performance of many of these methods has been conducted recently.[65, 66] However, these methods carry an incoherent monopoles assumption, thus limiting their use for correlated source distributions.

In addition to algorithms that assume distributions of incoherent monopoles, some methods were also developed that allowed for potentially correlated source distributions. Cross beamforming (CBF)—a way to measure source coherence between sources—was developed along with an extension of DAMAS, called DAMAS-C,[43] where CBF results are deconvolved to reduce array effects. This method has been applied to full-scale tactical jet noise sources to estimate correlated jet noise source distributions,[67] however the method development is from an uncorrelated source model. Michel and Funke[44] developed a method, source directivity modeling in cross spectral matrix (SODIX), that treats monopole phase-components separately and propagates them individually into the radiation field to identify location-based source contributions, although the process is an involved one. Papamoschou also visits the idea of source coherence.[68] He develops an extension to standard beamforming that incorporates source

coherence and then deconvolving the results, and he uses complex coherence as opposed to a standard cross-spectral matrix as inputs to the beamforming method. Ravetta *et al.*[69] modified the LORE algorithm (noise source localization and optimization of phased-array results) to incorporate coherent source information, although the deconvolution discretizes the sources. Padois *et al.*[60] developed HM, which is an inverse method that incorporates a type of Tikhonov regularization customized to more accurately converge on physically meaningful distributed source estimates, and showed the regularization led to improvements over other methods when applied to full-scale jet noise. Li *et al.*[70] combined HM with FBF to further improve the resolution of HM. Dougherty[40] improved upon the L_1 Generalized Inverse method introduced by Suzuki[47], called generalized inverse beamforming, which uses a pseudo inverse and regularization to estimate a coherent, distributed source region. He used beamforming source estimates of noise from model-scale jets to predict far-field radiation levels and compared them with theoretical expectations. Although some of these methods have been successfully applied to jet noise sources, many have not been directly compared, particularly for jet noise applications.

2.1.3 Array Geometry for Jet Noise Source Modeling

In addition to the beamforming methods, many approaches have been considered in array design to the source characteristics estimates.[71] Small- and large-aperture logarithmic-spiral arrays measure particular angles of jet noise at a given time. These have been primarily implemented in lab-scale tests,[37, 72] although they have also been used in full-scale tests including for rocket measurements.[73] In many circumstances, azimuthal arrays have been utilized which are generally placed in either the near field or the mid field of the jet noise.[15, 23, 74] These arrays, however, are difficult to implement in full-scale measurements as the temperature and flow of the jet provides additional challenges. Polar arrays have also seen wide usage, both in lab-scale[75] and full-scale[56,76]

settings for noise source identification. They are particularly useful when studying source coherence, as an extended aperture is required to sufficiently span the large coherence lengths present in the radiation field. When considering a detailed source environment characterization, however, the distance at which polar arcs are typically placed from the source necessitate a large number of microphones to adequately capture source information, and it is common to employ subarrays that span a small portion of the polar arc for high-resolution processing.[56]

In many circumstances, linear arrays are used in lab-scale[39] and full-scale environments,[24] both to span the jet noise source and to feasibly capture the salient features of the jet noise. Schlinker *et al.*[41] used 30 microphones to form two uniform collinear arrays that were of differing interelement spacing to capture the maximum radiation levels. Michel and Funke[44]used 128 microphones in a variable-spacing design according to the angle of incidence from the jet (1.25° spacing). They measured primarily fan, core and combustion noise as well as some jet noise (although the array was not centered on the jet noise), and this was measured in the geometric near field (although not the acoustic near field) of the jet. A similar experiment was also conducted by Tester and Holland[57] in a similar free-space setting using a linear array as well as a commercial engine measurement in a semi-reverberant chamber to measure combustion noise sound power. Brusniak *et al.*[77] employed three parallel uniform linear arrays of differing in the commercial engine test measurement to study jet noise, in addition to a spiral array for fan and core noise and polar array for standard noise measurements. In practical considerations, the relatively low element count and ability to span large jet noise sources makes the use of linear arrays ideal for jet noise experiments.

2.1.4 Overview

The work of the past decade to improve beamforming methods for extended, partially correlated sources has been significant, yet, there is a need to carefully compare their performance, particularly when using the beamforming results as an ESM to generate the corresponding acoustic field properties. In this study, CBF, HM, GINV, FBF, and MACS are compared in a numerical study to determine the capabilities and limitations of each. The algorithms for each method are described and the differences are compared in Section 2.2. In Section 2.3, the multiple-wavepacket (MWP) source distribution is used to create a simulated sound field and is designed to reproduce features of a jet noise field.[78] In Section 2.4, a linear array that spans the source region is used as input to the beamforming methods, and the performance of each method is compared in the numerical case study to obtain estimates of the source levels and coherence properties. In addition, the resultant ESMs are also used to predict the near- and far-field levels and coherence properties. To further efforts to characterize unknown sources, such as full-scale jet noise, an understanding of each method's efficacy is essential when estimating the source characteristics and the ESM to predict the sound field characteristics.[52]

2.2 Beamforming Methods

The beamforming algorithms to be applied to characterize a distributed and partially correlated source are described here. First, cross beamforming is described, which is a foundational method that extends naturally from traditional beamforming. Whereas traditional beamforming only provides output levels and assumes that sources are uncorrelated, CBF preserves the phase information across the source estimate region. FB builds on CBF by using a nonlinear process to improve the source estimate resolution while lowering beamforming artifacts (sidelobes). GINV

and HM both attempt to find an inverse of the assumed source-to-array propagation equation, and they incorporate different regularization schemes to reject noise that is amplified under the inversion process. Finally, MACS is described, which casts the problem into a second-order cone problem that can be solved using a commercial optimization solver for the source information. A comparison and summary of each method is provided in Section 2.2.4. Finally, as the success of these methods is highly dependent on the chosen regularization parameters, a regularization study of GINV and HM is given in Section 2.2.5. Each method is applied in Section 2.4 to measurements of a one-dimensional numerical source model that simulates important characteristics of jet noise.

2.2.1 Beamforming Overview

Beamforming is a method to ascertain source characteristics using pressure measurements at certain observation locations and by making assumptions about the source propagation. Consider an array consisting of m microphones in the vicinity of a source distribution (i.e., multiple sources) as shown in Fig. 2.1(a). Each array element is used to measure the pressure field, $p(t)$, at each array element location, $\vec{r}_j$, where $j = 1 \dots m$. The complex pressure, $\tilde{p}_j(f)$, is obtained for each measurement via a Fourier transform for a given frequency, f, which is not explicitly referenced for convenience. Considering potential sources located at positions $\vec{r}_i$, each with a complex source strength of $\hat{\tilde{q}}_i$, where $i = 1 \dots s$, the acoustic pressure measured at $\vec{r}_j$ can be described as

$$\tilde{p}_j = \sum_{i=1}^{s} g(\vec{r}_j, \vec{r}_i)\hat{\tilde{q}}_i. \tag{2.1}$$

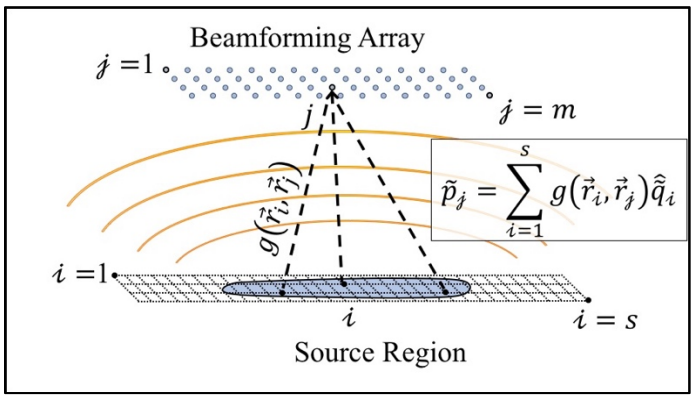

Fig. 2.1 (a) Source radiation example near a beamforming array. (b) Conventional beamforming example for a complex source estimate.

Here, the free-field Green function for a monopole,

$$g(\vec{r}_j, \vec{r}_i) = \frac{\tilde{A}}{\|\vec{r}_j - \vec{r}_i\|} \exp(-jk\|\vec{r}_j - \vec{r}_i\|) \tag{2.2}$$

incorporates the propagation from the sources to the measurement location, where

$$\tilde{A} = \frac{j\rho_o ck}{4\pi}, \tag{2.3}$$

which is the monopole amplitude when combined with the volume velocity, $\hat{\tilde{q}}$.[79] In addition, $\|\vec{r}_j - \vec{r}_i\|$ represents the Euclidean distance between $\vec{r}_i$ and $\vec{r}_j$, k is the acoustic wavenumber, ρ_0 is the ambient density, c is the speed of sound and j is the imaginary unit.

Using the array measurements, we seek to estimate the source strength at $\vec{r}_i$. Multiple methods have been put forth to solve for the sources, $\hat{\tilde{q}}_i$, in Eq. (2.1).[80, 81] By assuming that the sources are mutually incoherent, we can treat them independently and solve for each source position separately. This approach is presented by Dougherty in Ref. [34] and by Suzuki in Ref. [81]. Conversely, we can form a more general problem where sources are considered simultaneously and solve a system of equations. The prior approach is presented first, followed by

the more general formulation. Each produces different beamforming approaches with benefits and limitations, which are discussed in Section 2.2.2.[80]

2.2.1.2 Beamforming Assuming Incoherent Monopoles

Assuming a single source located at $\vec{r}_i$, the complex pressures measured at the array are

$$\mathbf{p} = \tilde{q}_i \mathbf{g}_i, \tag{2.4}$$

where $\mathbf{p}$ is the $[m, 1]$ vector of pressures, $\tilde{p}_j$, and $\mathbf{g}_i$ is the vector of steering elements from the source to each array element location. To solve for the complex source strength, the norm of the error is minimized,

$$\begin{aligned} \|\mathrm{e}_i\|^2 &= \|\tilde{q}_i \mathbf{g}_i - \mathbf{p}\|^2 \\ &= (\tilde{q}_i \mathbf{g}_i - \mathbf{p})^{\mathrm{H}} (\tilde{q}_i \mathbf{g}_i - \mathbf{p}) \\ &= \tilde{q}_i^* \mathbf{g}_i^{\mathrm{H}} \tilde{q}_i \mathbf{g}_i - \mathbf{p}^{\mathrm{H}} \tilde{q}_i \mathbf{g}_i - \tilde{q}_i^* \mathbf{g}_i^{\mathrm{H}} \mathbf{p} - \mathbf{p}^{\mathrm{H}} \mathbf{p}, \end{aligned} \tag{2.5}$$

where * signifies conjugation and $^{\mathrm{H}}$ the conjugate transpose. By taking the derivative of Eq. (2.5) with respect to $\tilde{q}_i$ we obtain

$$\frac{\partial \|\mathrm{e}_i\|^2}{\partial \tilde{q}_i} = \tilde{q}_i^* \mathbf{g}_i^{\mathrm{H}} \mathbf{g}_i - \mathbf{p}^{\mathrm{H}} \mathbf{g}_i, \tag{2.6}$$

which, by setting the result equal to zero and solving for $\tilde{q}_i$ produces the source strength that minimizes the error:

$$\tilde{q}_{i,\min} = \frac{\mathbf{g}_i^{\mathrm{H}} \mathbf{p}}{\mathbf{g}_i^{\mathrm{H}} \mathbf{g}_i}. \tag{2.7}$$

Inserting Eq. (2.7) into Eq. (2.5) produces

$$\begin{aligned}\left\|\mathrm{e}_{i,\min}\right\|^2 &= \left\|\left(\frac{\mathbf{g}_i^{\mathrm{H}}\mathbf{p}}{\mathbf{g}_i^{\mathrm{H}}\mathbf{g}_i}\right)\mathbf{g}_i - \mathbf{p}\right\|^2 \\ &= \left\|\frac{\mathbf{g}_i^{\mathrm{H}}\mathbf{p}}{\mathbf{g}_i^{\mathrm{H}}\mathbf{g}_i}\right\|^2 \mathbf{g}_i^{\mathrm{H}}\mathbf{g}_i - \left(\frac{\mathbf{g}_i^{\mathrm{H}}\mathbf{p}}{\mathbf{g}_i^{\mathrm{H}}\mathbf{g}_i}\right)\mathbf{p}^{\mathrm{H}}\mathbf{g}_i - \left(\frac{\mathbf{g}_i^{\mathrm{H}}\mathbf{p}}{\mathbf{g}_i^{\mathrm{H}}\mathbf{g}_i}\right)^* \mathbf{g}_i^{\mathrm{H}}\mathbf{p} - \mathbf{p}^{\mathrm{H}}\mathbf{p} \\ &= -\frac{\mathbf{g}_i^{\mathrm{H}}\mathbf{p}}{\mathbf{g}_i^{\mathrm{H}}\mathbf{g}_i}\mathbf{p}^{\mathrm{H}}\mathbf{g}_i + \mathbf{p}^{\mathrm{H}}\mathbf{p}.\end{aligned} \tag{2.8}$$

Note that, because the inserted solution is a scalar term, it commutes and the first and third terms cancel. Finally, the beamforming solution is defined in such a way to discard the squared array pressures term in Eq. (2.8), producing

$$\mathrm{Q}_{ii} \equiv \mathbf{p}^{\mathrm{H}}\mathbf{p} - \left\|\mathrm{e}_{i,\min}\right\|^2 = \frac{\mathbf{g}_i^{\mathrm{H}}}{\|\mathbf{g}_i\|}\mathbf{p}\mathbf{p}^{\mathrm{H}}\frac{\mathbf{g}_i}{\|\mathbf{g}_i\|}. \tag{2.9}$$

Equation (2.9) is commonly referred to as the conventional beamforming result or beamforming output, corresponding to a source at $\vec{r}_i$. The term $\mathbf{C} \equiv \mathbf{p}\mathbf{p}^{\mathrm{H}}$ is known as the cross-spectral matrix. The terms surrounding the cross spectral matrix are known as the beamforming steering vectors, with $\|\mathbf{g}_i\| = \sqrt{(\mathbf{g}_i^{\mathrm{H}}\mathbf{g}_i)}$. Additional choices for steering vectors are available and these are discussed in Section 2.2.2. Depending on the steering vector selection, the beamforming results will be at a maximum at the location of a source. The response of the beamforming algorithm to a single monopole is known as the *point spread function*.[42] Depending on the array setup and the proximity of the array to a given source, the point spread function will peak at the source location, and quickly decay in level as a function of distance from the source. *Sidelobes* also arise, which are mathematical artifacts of the beamforming process that create additional local maxima in the beamforming results that are not at the source location. The *dynamic range* (or sidelobe level) of beamforming results is a measure of the highest sidelobe level relative to the level of the main lobe (i.e., the source location). The *resolution* of beamforming results is a characterization of the

distinguishability of individual sources that are separated by a given distance and is usually given in terms of wavelengths.

In some cases it is desirable to remove the effects of the beamforming response and increase the source map resolution using deconvolution algorithms. Deconvolution algorithms such as DAMAS are employed to remove the array effects in conventional beamforming from the original source properties. The problem is cast into a linear system of equations,

$$\mathbf{A}\vec{\mathrm{Q}}_{\mathrm{DC}} = \vec{\mathrm{Q}}\,. \tag{2.10}$$

where the DAMAS algorithm assumes that incoherent monopoles, each with a different complex amplitude, comprise the original source region. In Eq. (2.10), $\vec{\mathrm{Q}}_{\mathrm{DC}}$ is a vector of monopole source strengths located at each scanning grid point $\vec{r}_i$. The vector $\vec{\mathrm{Q}}_{\mathrm{DC}}$, when convoluted by $\mathbf{A}$, produces the beamforming response at each scanning grid location, grouped into a vector as $\vec{\mathrm{Q}} = [Q_{11}, \ldots, Q_{ii=ss}]$. The matrix $\mathbf{A}$ is formed by combining anticipated convolution data, with each matrix column representing the beamforming output of a single monopole at position $\vec{r}_i$, vectorized into a column format. Because Eq. (2.10) is typically an underdetermined problem, DAMAS solves for the discrete monopoles using a Gauss-Seidel solver with a non-negativity constraint. [42]

2.2.1.3 Beamforming Assuming Potentially Correlated Sources

Implicit in the formulation for Eq. (2.9) was that each potential source location can be treated independently. A more generalized approach can also be taken to simultaneously solve the system of all potential sources, and doing so allows for possible correlation to exist between the sources.

Equation (2.4) can conveniently be rewritten in a more generalized matrix format, such that

$$\mathbf{p} = \mathbf{G}\,\mathbf{q}, \tag{2.11}$$

where the vector of acoustic pressures, $\mathbf{p}$, is $[m, 1]$ in size, the vector of complex source strengths, $\mathbf{q}$, is $[s, 1]$. The Green function matrix, $\mathbf{G}$, is comprised of steering vectors along the columns such that

$$\mathbf{G} = [\mathbf{g}_{i=1} \quad \cdots \quad \mathbf{g}_{i=s}], \tag{2.12}$$

and accounts for the free-field propagation from each source to each array element. A least-squares solution to Eq. (2.11) starts by defining an error function, $\mathrm{e_{all}}$, similar to Eq. (2.5). By minimizing the norm of the error, we obtain

$$\begin{aligned} \|\mathrm{e_{all}}\|^2 &= \|\mathbf{p} - \mathbf{G}\,\mathbf{q}\|^2 \\ &= \mathbf{p}^{\mathrm{H}}\mathbf{p} - \mathbf{p}^{\mathbf{H}}\,\mathbf{G}\,\mathbf{q} - \mathbf{q}^{\mathbf{H}}\mathbf{G}^{\mathbf{H}}\mathbf{p} + \mathbf{p}^{\mathbf{H}}\mathbf{G}^{\mathbf{H}}\mathbf{G}\,\mathbf{p}. \end{aligned} \tag{2.13}$$

We then differentiate with respect to $\mathbf{q}$ (see Appendix E of Ref. [82] for matrix operations with complex vectors) and set the result to zero to solve for the minimum solution of Eq. (2.13). Differentiating yields

$$\frac{\boldsymbol{\partial}}{\boldsymbol{\partial}\mathbf{q}}\|\mathrm{e_{all}}\|^2 = -\mathbf{G}^{\mathbf{T}}\mathbf{p}^{*} + (\mathbf{G}^{\mathbf{H}}\mathbf{G})^{\mathbf{T}}\mathbf{q}^{*}. \tag{2.14}$$

By setting the left side to zero and performing both transpose and Hermitian conjugate operations on the equation, the equation becomes

$$\mathbf{0} = -\mathbf{G}^{\mathrm{H}}\mathbf{p} + (\mathbf{G}^{\mathbf{H}}\mathbf{G})\mathbf{q}, \tag{2.15}$$

that when rearranged results in the source strength vector that minimizes the error:

$$\mathbf{q}_{\mathrm{min}} = (\mathbf{G}^{\mathrm{H}}\mathbf{G})^{-1}\mathbf{G}^{\mathrm{H}}\mathbf{p}. \tag{2.16}$$

This is the Moore-Penrose pseudo-inverse solution and represents the least-squares solution to Eq. (2.11).[82] The solution assumes that $\mathbf{G}^{\mathrm{H}}\mathbf{G}$ is invertible, which holds when the columns of $\mathbf{G}$ (i.e.,

the steering vectors) are linearly independent. The linear independence of the columns of $\mathbf{G}$ is dependent on both the array geometry and the assumed source locations, and can be verified by taking a singular value decomposition of $\mathbf{G}^{\mathrm{H}}\mathbf{G}$. This is discussed in more detail in Section 2.3.3.

Finally, the beamforming result is obtained by taking the outer product of $\mathbf{q}_{\mathrm{min}}$ with itself from Eq. (2.16) to obtain the general beamforming result,

$$\mathbf{Q_{MP}} = (\mathbf{G}^{\mathrm{H}}\mathbf{G})^{-1}\mathbf{G}^{\mathrm{H}}\mathbf{p}\mathbf{p}^{\mathbf{H}}\mathbf{G}(\mathbf{G}^{\mathrm{H}}\mathbf{G})^{-1}. \tag{2.17}$$

This result is similar in form to Eq. (2.9), although there are important differences as well. The cross spectral matrix, $\mathbf{C} \equiv \mathbf{p}\mathbf{p}^{\mathrm{H}}$, is present, as well as the steering vector operators. However, whereas each steering vector in Eq. (2.9) is adjusted by $\|\mathbf{g}_i\|$, independent of other steering vector arguments, the steering vector matrix in Eq. (2.17) is modified by the inverse of $\mathbf{G}^{\mathrm{H}}\mathbf{G}$, which incorporates all possible source-to-steering vector arrangements. Because this is a squared quantity, Eq. (2.17) will have different units than Eq. (2.9). In addition, the result of Eq. (2.17) is a square matrix of dimension $[s, s]$, with diagonal terms representing the squared results of Eq. (2.16). In practice, Eq. (2.17) is seldom used because regularization is often required to prevent the amplification of noise under the inversion, and algorithms that incorporate regularization are discussed in Section 2.2.3.

2.2.2 Steering Vector Selection

Section 2.2.1 described two methods for deriving beamforming solutions, dependent on the approach used. Equations (2.9) and (2.17) each had steering vector operators that, by multiplication of the cross spectral matrix produced the beamforming output. In addition, many steering vector formulations exist. Sarradj[80] compared four steering vector formulations using the incoherent monopole assumption and a modified propagation term of Eq. (2.2),

$$\mathrm{g}(\vec{r}_j, \vec{r}_i) = \frac{\left\|\vec{r}_{j_0} - \vec{r}_i\right\|}{\left\|\vec{r}_j - \vec{r}_i\right\|} \exp\left(-jk\left\|\vec{r}_j - \vec{r}_i\right\|\right), \tag{2.18}$$

where $\vec{r}_{j_0}$ is the array center location. The inclusion of the $\left\|\vec{r}_{j_0} - \vec{r}_i\right\|$ term produces beamforming output levels on par with levels measured at the array. and using Eq. (2.18). Sarradj included the term $\vec{r}_{j_0}$ in the exponential of the steering vector elements such that the exponential argument of Eq. (2.18) is $-jk\left\|\vec{r}_j - \vec{r}_i - \vec{r}_{j_0}\right\|$, outputting a phase for each steering vector element relative to the array center. While this is convenient notation for a single monopole source problem, it is desirable to maintain the phase relationship that may exist between multiple sources and therefore the $\vec{r}_{j_0}$ term is neglected here. Using Eq. (2.18), the four steering vectors compared by Sarradj are:

$$\begin{aligned} \mathrm{g}^{\mathrm{I}}(\vec{r}_j, \vec{r}_i) &= \frac{1}{m} \frac{\mathrm{g}(\vec{r}_j, \vec{r}_i)}{\left|\mathrm{g}(\vec{r}_j, \vec{r}_i)\right|} \\ &= \frac{1}{m} \exp\left(-jk\left\|\vec{r}_j - \vec{r}_i\right\|\right), \end{aligned} \tag{2.19}$$

$$\begin{aligned} \mathrm{g}^{\mathrm{II}}(\vec{r}_j, \vec{r}_i) &= \frac{1}{m} \frac{\mathrm{g}(\vec{r}_j, \vec{r}_i)}{\mathrm{g}(\vec{r}_j, \vec{r}_i)^* \mathrm{g}(\vec{r}_j, \vec{r}_i)} \\ &= \frac{1}{m} \frac{\left\|\vec{r}_j - \vec{r}_i\right\|}{\left\|\vec{r}_{j_0} - \vec{r}_i\right\|} \exp\left(-jk\left\|\vec{r}_j - \vec{r}_i\right\|\right), \end{aligned} \tag{2.20}$$

$$\begin{aligned} \mathrm{g}^{\mathrm{III}}(\vec{r}_j, \vec{r}_i) &= \frac{\mathrm{g}(\vec{r}_j, \vec{r}_i)}{\mathbf{g}_i^{\mathrm{H}} \mathbf{g}_i} \\ &= \frac{\exp\left(-jk\left\|\vec{r}_j - \vec{r}_i\right\|\right)}{\left\|\vec{r}_{j_0} - \vec{r}_i\right\| \left\|\vec{r}_j - \vec{r}_i\right\| \sum_{j=1}^{m} \left(\frac{1}{\left\|\vec{r}_j - \vec{r}_i\right\|^2}\right)}, \end{aligned} \tag{2.21}$$

$$\mathrm{g}^{\mathrm{IV}}\left(\vec{r}_j,\vec{r}_i\right)=\frac{1}{\sqrt{\mathrm{m}}}\frac{\mathrm{g}\left(\vec{r}_j,\vec{r}_i\right)}{\|\mathbf{g}_i\|}$$

$$=\frac{1}{\left\|\vec{r}_j-\vec{r}_i\right\|\sqrt{m\sum_{j=1}^{m}\left(\frac{1}{\left\|\vec{r}_j-\vec{r}_i\right\|^2}\right)}}\exp\left(-jk\left\|\vec{r}_j-\vec{r}_i\right\|\right). \tag{2.22}$$

The steering vector elements shown in Eqs. (2.19)-(2.22) provide four methods for obtaining the elements of the beamforming steering vector, $\mathbf{g}_i$, where $\mathfrak{g}_i$ is an $[m,1]$ steering vector with elements $\mathrm{g}\left(\vec{r}_j,\vec{r}_i\right)$, for each source-to-array element location. The third and fourth steering vector formulations result from the beamforming derivations of Eqs. (2.17) and (2.9), respectively. The goal of each steering vector is to both maximize the beamforming output at the correct source location and reproduce the correct source level at the source location. While none of the above steering vector formulations succeeds in both goals, they are formulated such that $\mathrm{g}^{\mathrm{I}}\left(\vec{r}_j,\vec{r}_i\right)$ and $\mathrm{g}^{\mathrm{IV}}\left(\vec{r}_j,\vec{r}_i\right)$ correctly maximize the beamforming levels at the correct source location, while $\mathrm{g}^{\mathrm{II}}\left(\vec{r}_j,\vec{r}_i\right)$ and $\mathrm{g}^{\mathrm{III}}\left(\vec{r}_j,\vec{r}_i\right)$ output the correct source levels at the source location. For the current study, the fourth formulation was chosen to more accurately estimate the source location. To rectify the source level estimates, the estimated source levels are again input into Eq. (2.13) and then scaled by a constant factor of $\|\mathrm{e}_{\mathrm{all}}\|/m$.

2.2.3 Advanced Beamforming Algorithm Examples

Many beamforming algorithms are available to handle different source configurations or array geometries. In this chapter, we focus primarily on algorithms designed for potentially correlated source configurations. CBF is a simple extension of the beamforming methodologies described in Section 2.2.1. FBF is a nonlinear technique to boost the source signals while

minimizing errors due to the beamforming process. The inverse techniques, GINV and HM build upon the generalized beamforming methodology discussed in 2.2.1.3 and incorporate regularization schemes. Finally, MACS is designed as a computationally efficient direct method for solving for potentially-correlated sources without first computing standard beamforming results as would be done using DAMAS-C. Each algorithm is explained here, and comparison are made in Section 2.2.4 for the methods and Section 2.2.5 for the regularization schemes of GINV and HM.

2.2.3.1 Cross Beamforming

Cross beamforming is a natural result of the beamforming methods development from Section 2.2.1. Interestingly, it was developed using the incoherent monopole assumption, although it produces a result that allows for partially correlated sources and therefore shares features of both the incoherent and coherent source beamforming derivations.

Starting from Eq. (2.9), the beamforming solution can be expanded by simultaneously including all steering vectors as columns of a steering vector matrix, $\mathbf{G_{SV}}$, where

$$\mathbf{G_{SV}} = \left[\frac{\mathbf{g}_{i=1}}{\|\mathbf{g}_{i=1}\|}, \ldots, \frac{\mathbf{g}_{i=\mathrm{m}}}{\|\mathbf{g}_{i=\mathrm{m}}\|}\right], \tag{2.23}$$

which when insert into Eq. (2.9) produces

$$\mathbf{Q_{CBF}} = \mathbf{G_{SV}^{H}}\ \mathbf{C}\ \mathbf{G_{SV}}, \tag{2.24}$$

where $\mathbf{C}$ is the cross spectral matrix. Equation (2.24) simultaneously solves Eq. (2.9) for each potential source location, $\vec{r}_i$, with results Q_{ii} along the diagonal of $\mathbf{Q_{CBF}}$. However, $\mathbf{Q_{CBF}}$ is an $[s, s]$ matrix and the off-diagonal elements are referred to as cross elements, $\mathbf{Q}_{\mathrm{CBF}_{i,i'}}$, where i and i' are the indices of $\mathbf{Q}_{\mathrm{CBF}}$ and correspond to source locations $\vec{r}_i$ and $\vec{r}_{i'}$. They represent the simultaneous steering of the array pressures to two locations along the source region, i.e.,

$$\mathrm{Q}_{i,i'} = \frac{\mathbf{g}_i^{\mathrm{H}}}{\|\mathbf{g}_i\|}\mathbf{p}\mathbf{p}^{\mathrm{H}}\frac{\mathbf{g}_{i'}}{\|\mathbf{g}_{i'}\|}. \tag{2.25}$$

The magnitude of the estimated CBF response relative to the corresponding individual source responses, $\mathbf{Q}_{\mathrm{CBF}_{i,i}}$and $\mathbf{Q}_{\mathrm{CBF}_{i',i'}}$, is large if there exists a degree of coherence between corresponding source locations. The physical representation of an example result, $\mathbf{Q}_{\mathrm{CBF}_{i,i'}}$, is shown in Fig. 2.2, where steering vectors from the array to source locations $\vec{r}_i$ and $\vec{r}_{i'}$ are used in conjunction. The solution of $\mathbf{Q}_{\mathbf{CBF}}$ is similar in form to the exact solution, $\mathbf{Q}_{\mathbf{MP}}$, in Eq. (2.17), CBF is developed from the incoherent monopole assumption in Section 2.2.1.2. Therefore, while the framework exists to indicate source correlation characteristics (e.g., cross elements), it must be stressed that it may not necessarily correctly identify those features.

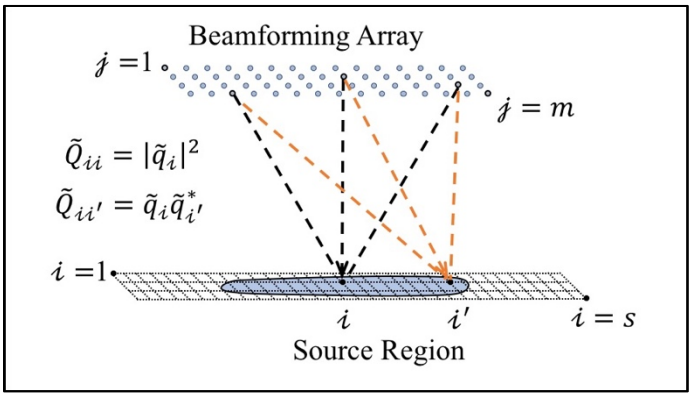

Fig. 2.2. Cross beamforming example.

In some circumstances, the geometry of the array in relation to the source is such that the deconvolution is desired to improve the resolution of the source information. In a similar manner as the application of DAMAS to conventional beamforming, DAMAS-C is an extension that is specifically designed for application to CBF. However, due to considerable number of linear equations to solve—on the order of s^4—this algorithm has limited use in practice. Deconvolution improves the beamforming results dependent on the array geometry (e.g., size of the array relative

to the source, array element density, etc.) and the proximity of the array to the source. In this study, the array geometry is chosen such that the addition of deconvolution does not appreciably improve the source resolution.

2.2.3.2 Functional Beamforming

Functional beamforming[48] is a method that improves the dynamic range of the CBF results by suppressing the sidelobe artifacts introduced in the beamforming process. The algorithm is a nonlinear technique that introduces an exponential adjustment parameter, η, to $\mathbf{C}$, The effect is to alter Eq. (2.24) so that

$$\mathbf{Q_{FBF}} = \left(\mathbf{G_{SV}^H C^{\frac{1}{\eta}} G_{SV}}\right)^{\eta}, \tag{2.26}$$

where the steering vector matrix was chosen using Eq. (2.24), although other choices from Eqs. (2.19)-(2.22) can instead be used. The positive definite nature of the cross-spectral matrix allows for the exponential to be carried out on the singular values of the SVD, as

$$\mathbf{C} = \mathbf{U}\begin{bmatrix} \sigma_1^{\frac{1}{\eta}} & 0 & 0 \\ 0 & \ddots & 0 \\ 0 & 0 & \sigma_M^{\frac{1}{\eta}} \end{bmatrix}\mathbf{U^H}, \tag{2.27}$$

where $\mathbf{U}$ is a matrix comprised of the eigenvectors of $\mathbf{C}$ along the columns. The outermost exponential of Eq. (2.26), $(\,)^{\eta}$, is calculated elementwise on the resultant matrix. The adjustment parameter can range in value from $1 \leq \eta < \square$, with $\eta = 1$ resulting in CBF. Dougherty[48] showed that when η is increased, the dynamic range of the beamforming results are improved while the levels at the source remain unaltered. For normalized steering vectors, if the dynamic range of the beamforming results is 10 dB—i.e., $\left\|\mathbf{g}_i^{\mathrm{H}}\mathbf{g}_i\right\|^2 = 0.1$—then if $\eta = 8$ the resultant dynamic range is theoretically $10\log_{10}(.1)^8 = 80$ dB.[48] In practice, Dougherty recommended empirically-

determined values of η between 50-400, to account for additional sources and noise. However, propagation errors from the steering vectors are amplified and a high η value may negatively affect the source estimates. A more conservative parameter of $\eta = 8$ was chosen to increase the dynamic range whilst avoiding larger exponentiation.

Because FBF is a nonlinear process, it is limited in its application scope. Deconvolution methods, such as DAMAS, that rely on linear propagation assumptions (i.e., linear filters) may not be combined with FBF results as reciprocity, the assumption that source-receiver configurations can be interchanged, is violated under the nonlinear process. In addition, while cross-beamform terms are output in Eq. (2.26), they are distorted by the algorithm. Consequently, attempts to use the FBF results to predict the field necessitate assuming the sources as incoherent monopoles.

2.2.3.3 Generalized Inverse Beamforming

Suzuki[47] developed an algorithm applicable to incoherent and coherent sources as well as other multipole sources such as dipoles. Instead of a least-squares cost function derivation [Eq. (2.13)], Suzuki solved a more generalized cost function using an L_p norm (where p is set to 1). The reasoning is that, considering a single monopole source of unit amplitude, the minimization of an L_2 norm cost function will favor a more distributed solution, say across two source locations since $\sqrt{\left(\frac{1}{2}\right)^2 + \left(\frac{1}{2}\right)^2} = \frac{1}{2} < \sqrt{1^2}$. Instead, an L_1 norm cost function is used. To solve this function, the problem is set up as an iteratively reweighted least squares algorithm (IRLS) and the solution is solved iteratively. Prior to solving, the cross spectral matrix is decomposed into its eigenvectors, and each eigenvector is solved individually. In addition, after each iteration, the solution space is truncated to remove potential source locations that are unnecessary or don't contain source

information in an effort to converge upon a more sparse solution. This technique is known as L_1 Generalized Inverse Beamforming (L_1-GIB).

The GINV method described by Dougherty[40] built upon the basic ideas of Suzuki, while solving a more simplified approach. Instead of solving an L_1 norm cost function, Dougherty solves Eq. (2.11) in a more direct method by taking the inverse of $\mathbf{G}$ using a singular value decomposition (SVD), where the decomposition is $\mathbf{G} = \mathbf{U}\,\mathbf{\Sigma}\,\mathbf{V^H}$. [40] The inverse, $\mathbf{G}^\dagger$, is calculated by taking the reciprocal of the diagonal singular values matrix, $\mathbf{\Sigma}$. The GINV method solves for the beamforming solution using the cross spectral matrix,

$$\begin{aligned} \mathbf{Q_{GINV}} &= \mathbf{G}^\dagger\,\mathbf{C}\,(\mathbf{G}^\dagger)^{\mathrm{H}} \\ &= (\mathbf{V}\,\mathbf{\Sigma^{-1}}\mathbf{U}^{\mathrm{H}})\,\mathbf{C}\,(\mathbf{U}\,\mathbf{\Sigma^{-1}}\mathbf{V}^{\mathrm{H}}) \end{aligned} \tag{2.28}$$

Unlike L_1-GIB, GINV does not solve for the eigenvectors individually, thus making this formulation simpler. In addition, the solution does not rely on a IRLS iterative approach, therefore requiring much less computation time. However, Dougherty does suggest a Gaussian smoothing operator to produce solutions that are more physically realistic instead of the more discrete solutions produced by L_1-GIB, which tends to compress and discretize the solution in the truncation-iteration process. The smoothing operator is added by altering the steering vector matrix such that $\mathbf{G} \rightarrow \mathbf{G}\mathfrak{L}$, where $\mathfrak{L}$ is the Gaussian smoothing norm with a length scale of a few grid points in the source region. The Gaussian blur was not used in this paper to further simplify the procedure.

While the SVD can successfully invert $\mathbf{G}$, doing so amplifies the small singular values under the reciprocation that are commonly associated with the measurement noise floor. To prevent the amplification of noise, a regularization process is necessary, which includes determining an appropriate lower limit in the singular values that describes the signal space. [17, 40]

All values below this limit are replaced with a lower limiting value to bound the amplification of less-pertinent features of the Green function matrix. The choice of cutoff levels can significantly alter the resultant field predictions, particularly in the low-level radiation regions. A more detailed look at the process of choosing the regularization parameter is given in Section 2.2.5, and a cutoff value of 2.33 dB below the largest singular value was chosen, which is similar to the choice of 1.4 dB that was empirically chosen by Dougherty.[40]

2.2.3.4 The Hybrid Method

The hybrid method (HM) is similar in function to GINV in that it attempts to solve the least-squares minimization problem [Eq. (2.13)] using a regularization approach.[60] However, the regularization is a modification over standard Tikhonov regularization. Traditional Tikhonov regularization improves the conditioning of $\mathbf{G}^{\mathrm{H}}\mathbf{G}$ by supplementing it with a penalization parameter, ν^2, along the diagonal entries as

$$\mathbf{q}_{\mathrm{Tikhonov}} = (\mathbf{G}^{\mathbf{H}}\mathbf{G} + \nu^2\mathbf{I})^{-\mathbf{1}}\mathbf{G}^{\mathbf{H}}\mathbf{p}, \tag{2.29}$$

where $\mathbf{I}$ is the identity matrix. The effect is similar to the regularization carried out in GINV, and methods to determine ν^2 include the Morozov discrepancy procedure and the generalized cross validation procedure.[83] However, in HM the penalization parameter is added to a square weighting matrix, and the solution to Eq. (2.11) then becomes

$$\mathbf{q}_{\mathrm{HM}} = (\mathbf{G}^{\mathbf{H}}\mathbf{G} + \nu^2\mathbf{L}^{\mathbf{H}}\mathbf{L})^{-\mathbf{1}}\mathbf{G}^{\mathbf{H}}\mathbf{p}, \tag{2.30}$$

where $\mathbf{L}$ is a beamforming regularization matrix,

$$\mathbf{L}^{-1} = \left[\mathrm{Diag}\left(\frac{\sqrt{\mathrm{diag}(\mathbf{Q}_{\mathbf{CBF}})}}{\sqrt{\|\mathrm{diag}(\mathbf{Q}_{\mathbf{CBF}})\|_\infty}}\right)\right]. \tag{2.31}$$

In Eq. (2.31), $\mathbf{L}^{-1}$ consists of a square matrix with elements formed from the individual source powers from $\mathrm{diag}(\mathbf{Q_{CBF}})$. Here, $\mathrm{diag}(\cdot)$ takes the diagonal elements of a matrix and $\mathrm{Diag}(\cdot)$ forms a diagonal matrix of these elements, $\|\cdot\|_\infty$ is the infinity norm, and $\sqrt{\cdot}$ is applied element-wise. The beamforming regularization matrix is an improvement to the standard regularization process because the Green function matrix is weighted by CBF source powers to add *a priori* information about the beamforming source locations to more selectively penalize the source region instead of the source-independent approach of classical Tikhonov. In fact, the incorporation of the beamforming results into $\mathbf{L}$ shares semblances with the L_p norm formulation in Ref. [47], although the current method does not require IRLS techniques to solve. Incorporating Eq. (2.31) into Eq. (2.30) and simplifying produces

$$\mathbf{q}'_{\mathrm{HM}} = \mathbf{L}^{-1}\left(\underline{\mathbf{G}}^{\mathbf{H}}\underline{\mathbf{G}} + \nu^2\mathbf{I}\right)^{-\mathbf{1}}\underline{\mathbf{G}}^{\mathbf{H}}\mathbf{p}, \tag{2.32}$$

where $\underline{\mathbf{G}} = \mathbf{G}\mathbf{L}^{-1}$, and $\mathbf{q}'_{\mathrm{HM}}$ is the estimated vector of source powers. Using Eq. (2.32), HM is developed such that

$$\mathbf{Q_{HM}} = \mathbf{q}'\mathbf{q}'^{\mathbf{H}} = \mathbf{L}^{-1}\beta\left(\mathbf{J}\,\underline{\mathbf{G}}^{\mathbf{H}}\right)\mathbf{C}\left(\underline{\mathbf{G}}\,\mathbf{J}^{\mathbf{H}}\right)\beta^*(\mathbf{L}^{-1})^{\mathbf{H}}, \tag{2.33}$$

where

$$\boldsymbol{J} = \left(\underline{\mathbf{G}}^{\mathbf{H}}\underline{\mathbf{G}} + \nu^2\mathbf{I}\right)^{-\mathbf{1}} \tag{2.34}$$

In the above, a scaling term, β, is included, where

$$\beta = \left\|\underline{\mathbf{G}}^{\mathbf{H}}\underline{\mathbf{G}} + \nu^2\mathbf{I}\right\|, \tag{2.35}$$

to compensate for the addition of regularization and ensure that the source estimated levels are correct. However, other techniques of scaling the source levels are discussed in Section 2.2.7. To determine v^2, Padois *et al.* conducted a regularization study using HM and found that by setting ν^2 to be at least five percent of the largest eigenvalue of $\mathbf{G}^{\mathrm{H}}\mathbf{G}$, the sound source level converged

to the correct levels, with the source levels being over-estimated for smaller regularization values. The five percent threshold was similarly chosen for this study. Other methods such as the Morozov discrepancy principle[83] and generalized cross validation can also be used.[84]

To improve upon the HM method, other square regularization matrices were tried in Eq. (2.34), as a substitute to the identity matrix shown. For example, scaled finite-difference approximations are commonly used in Tikhonov regularization,[85, 86] and a 2nd order difference operator is employed here, such that $\mathbf{I}$ in Eq. (2.34) is replaced with $\mathbf{L}_{\mathrm{FD}}^{\mathrm{H}}\mathbf{L}_{\mathrm{FD}}$, where

$$\mathbf{L}_{\mathrm{FD}} = \frac{1}{4}\begin{bmatrix} -1 & 2 & -1 & & & 0 \\ & -1 & 2 & 1 & & \\ & & \ddots & \ddots & \ddots & \\ 0 & & & -1 & 2 & 1 \end{bmatrix}. \tag{2.36}$$

It was found that the use of a difference operator was an improvement to the regularization scheme and improved the source estimates of Eq. (2.33). Section 2.2.5 explores the regularization choices made and compares those here with the parameters from GINV.

2.2.3.5 MACS

MACS is built upon the foundation of covariance matrix fitting (CMF) and a modified version designed for correlated sources, CMF-C.[49] To begin, CMF (and CMF-C) attempt to solve

$$\mathbf{Q}_{\mathrm{CMF}} = \arg\min_{\mathbf{Q}} \|\mathbf{C} - \mathbf{G}\mathbf{Q}\mathbf{G}^{\mathrm{H}}\|_F^2 \ \text{s.t.}\ \mathrm{Tr}[\mathbf{Q}] \leq \epsilon, \tag{2.37}$$

where the scalar ϵ is the sum of the eigenvalues of $\mathbf{C}$ and $\|\cdot\|_{\mathrm{F}}$ is the matrix Frobenius norm. In this case, $\mathbf{Q}$ is a diagonal matrix and is constrained such that its elements are nonnegative. This formulation sets up a convex quadratic problem that can be solved using software packages such as SeDuMi, a public-domain solver for optimization problems.[87] The CMF algorithm also assumes that the solution is sparse, i.e., the number of actual sources is much less than the total number of sources considered.

Because CMF is designed to only estimate the source powers (the diagonal elements of $\mathbf{Q}$), a generalization of CMF is necessary to obtain the cross terms of $\mathbf{Q}$ that contain information about the potential coherence that may exist between sources. CMF-C is an extension of CMF, where Eq. (2.37) is solved with the modification that

$$\begin{aligned} \mathbf{Q}_{\mathrm{CMFC}} &= \arg\min_{\mathbf{Q}} \|\mathbf{C} - \mathbf{G}\mathbf{Q}\mathbf{G}^{\mathrm{H}}\|_F^2 \text{ s.t.} \\ \mathrm{Tr}[\mathbf{Q}] &\leq \epsilon, \\ \mathbf{Q} &\succcurlyeq 0. \end{aligned} \tag{2.38}$$

Here, $\mathbf{Q} \succcurlyeq 0$ means that $\mathbf{Q}$ is a positive semidefinite matrix. Equation (2.38) is a convex semidefinite program and can also be solved using SeDuMi. However, the computational requirements of CMF-C increase exponentially (similar to those for DAMAS-C) because the number of potential sources grows from s to s^2, and CMF-C quickly becomes difficult to implement in practice.

To make the computation of CMF-C more feasible, MACS was developed, which introduces additional sparsity constraints to make the computation of Eq. (2.38) feasible when input into a software solver. In addition, the cost function is reduced to solving two unknown matrices iteratively and in an alternating fashion until convergence is reached.

The process is described here. First, the cross spectral matrix is decomposed in an Eigenvalue decomposition such that $\mathbf{C} = \mathbf{U}\boldsymbol{\Sigma}\mathbf{U}^{\mathrm{H}}$. Let $\mathbf{C}_{\hat{s}}$ be the cross spectral matrix with only the largest $\hat{s}$ eigenvalues kept, where $\hat{s} \ll s$. This is accomplished by substituting $\boldsymbol{\Sigma}$ with $\boldsymbol{\Sigma}_{\hat{s}}$ where $\boldsymbol{\Sigma}_{\hat{s}}$ is obtained by replacing eigenvalue entries that are smaller than the $\hat{s}$th entry (where the eigenvalues are assumed ordered from largest to smallest) with zeros. This becomes

$$\begin{aligned}\mathbf{C}_{\hat{s}} &= \mathbf{U}\begin{bmatrix}\boldsymbol{\Sigma}_{\hat{s}} & \mathbf{0}\\ \mathbf{0} & \mathbf{0}\end{bmatrix}\mathbf{U}^{\mathrm{H}}\\ &= \mathbf{U}_{\hat{s}}\boldsymbol{\Sigma}_{\hat{s}}\mathbf{U}_{\hat{s}}^{\mathrm{H}},\end{aligned} \tag{2.39}$$

where $\mathbf{U}_{\hat{s}}$ is $[s, \hat{s}]$ in size and comprised of the first $\hat{s}$ columns of $\mathbf{U}$. Next, we replace $\mathbf{Q}$ with a potentially-lower rank matrix, $\mathfrak{Q}$, of size $[s, \hat{s}]$ where $\mathfrak{Q}\mathfrak{Q}^{\mathrm{H}} = \mathbf{Q}$, thus ensuring that $\mathbf{Q}$ will be positive semidefinite. Finally, we recast $\mathbf{C}_{\hat{s}}$ as $\tilde{\mathbf{C}}\tilde{\mathbf{C}}^{H} = \mathbf{C}_{\hat{s}}$, where $\tilde{\mathbf{C}} = \mathbf{U}_{\hat{s}}\boldsymbol{\Sigma}_{\hat{s}}^{1/2}$. With these definitions, we can reformulate Eq. (2.38) as

$$\begin{aligned}\mathbf{Q}_{\mathrm{MACS}} &= \arg\min_{\mathfrak{Q}} \|\mathbf{C}_{\hat{s}} - (\mathbf{G}\mathfrak{Q})(\mathbf{G}\mathfrak{Q})^{\mathrm{H}}\|_F^2\\ &= \arg\min_{\mathfrak{Q}} \left\|\left(\tilde{\mathbf{C}}\mathfrak{B}^{\mathrm{H}}\right)\left(\tilde{\mathbf{C}}\mathfrak{B}^{\mathrm{H}}\right)^{\mathrm{H}} - (\mathbf{G}\mathfrak{Q})(\mathbf{G}\mathfrak{Q})^{\mathrm{H}}\right\|_F^2 \text{ s.t.}\\ &\|\mathfrak{Q}\|_F^2 \le \epsilon,\\ &\mathfrak{B}^{\mathrm{H}}\mathfrak{B} = \mathbf{I}.\end{aligned} \tag{2.40}$$

Accompanying $\tilde{\mathbf{C}}$ is an auxiliary variable, $\mathfrak{B}$, such that $\mathfrak{B}^{\mathrm{H}}\mathfrak{B}$ equals an identity matrix. Introducing this variable allows for the simplification of Eq. (2.40) to the more advantageous cost function:

$$\begin{aligned}\mathbf{Q}_{\mathrm{MACS}} &= \arg\min_{\mathfrak{B},\mathfrak{Q}} \left\|\tilde{\mathbf{C}}\mathfrak{B}^{\mathrm{H}} - \mathbf{G}\mathfrak{Q}\right\|_F^2 \text{ s.t.}\\ &\|\mathfrak{Q}\|_F^2 \le \epsilon,\\ &\mathfrak{B}^{\mathrm{H}}\mathfrak{B} = \mathbf{I},\end{aligned} \tag{2.41}$$

where the cost function now simultaneously estimates $\mathfrak{B}$ and $\mathfrak{Q}$. This is done by solving each in turn, and iterating through until convergence is reached. To further simplify, the Frobenius norm constraint on $\mathfrak{Q}$ can be relaxed to the L_1 norm to promote sparcity (i.e., an additional assumption that the solution will be sparse) such that the constraint becomes $\sum_i \sum_j |\mathfrak{Q}_{ij}| \le \sqrt{\beta s \hat{s}} = \zeta$. Like CMF and CMF-C, Eq. (2.41) is a second-order cone problem (SOCP) that can be solved iteratively using SeDuMi or a similar solver. This is done in a two-step process. First, an estimate of $\mathfrak{B}$ is

initialized ($\widehat{\mathfrak{B}} \to \mathbf{I}$), and Eq. (2.41) is solved for an estimate of $\mathfrak{Q}$ ($\widehat{\mathfrak{Q}}$). Next, for a given $\widehat{\mathfrak{Q}}$, $\widehat{\mathfrak{B}}$ is solved using the expression:[49]

$$\left\|\tilde{\mathbf{C}}\mathfrak{B}^{\mathrm{H}} - \mathbf{G}\mathfrak{Q}\right\|_F^2 = \delta - 2 \cdot \mathrm{Re}\left[\mathrm{Tr}\left(\tilde{\mathbf{C}}^{\mathrm{H}}\mathbf{G}\mathfrak{Q}\mathfrak{B}\right)\right], \tag{2.42}$$

where δ is an arbitrary scaler that is independent of $\mathfrak{B}$. We can decompose the matrix $\tilde{\mathbf{C}}^{\mathrm{H}}\mathbf{G}\mathfrak{Q}$ using a SVD to get $\tilde{\mathbf{C}}^{\mathrm{H}}\mathbf{G}\mathfrak{Q} = \mathbf{U}_{\mathfrak{B}}\mathbf{\Sigma}_{\mathfrak{B}}\mathbf{V}_{\mathfrak{B}}^{\mathrm{H}}$, it's singular value decomposition components, and therefore solve to update $\widehat{\mathfrak{B}}$ using $\widehat{\mathfrak{B}} = \mathbf{V}_{\mathfrak{B}}\mathbf{U}_{\mathfrak{B}}^{\mathrm{H}}$. With the updated $\widehat{\mathfrak{B}}$ we again repeat the process to solve for $\widehat{\mathfrak{Q}}$ and continue until $\widehat{\mathfrak{Q}}$ and $\widehat{\mathfrak{B}}$ converge. Once the two matrices have been estimated, the sources are solved using the estimated $\widehat{\mathfrak{Q}}$ by

$$\mathbf{Q}_{\mathrm{MACS}} = \widehat{\mathfrak{Q}}\widehat{\mathfrak{Q}}^{\mathrm{H}} \tag{2.43}$$

In practice, only a few iterations are required for convergence (e.g. 5 iterations), and MACS is computationally much faster than CMF-C because it takes advantage of the sparseness of sources relative to the number of microphone elements, m, and the number of potential source points, s. As a result, the number of significant eigenvalues of the cross-spectral matrix is generally much less than either the number of sources and the number of scanning points. The sparsity constraints that are introduced reduce the number of unknowns and significantly improve the computational time required to solve the problem. However, while the computation time may be much lower than CMF-C or DAMAS-C, it is still generally much higher than required for GINV or HM.

2.2.4 Comparison of Beamforming Algorithms

The previously described methods can generally be classified into two categories: those that are built using the incoherent source assumption, e.g. Eq. (2.9), and those that attempt to solve

the entire source distribution simultaneously under a potentially coherent source assumption, as in Eq. (2.17). The CBF and FBF methods are built assuming the incoherent source assumption, even though the means for estimating the source self-coherence are included in CBF. The GINV, HM and MACS methods solve for sources assuming potential source coherence exists. This is accomplished in various ways. For GINV and HM, a form of Tikhonov regularization added to the pseudoinverse solution of the least-squares cost function produces each respective solution. MACS, however, is solved by converging upon a solution in an iterative technique that solves a second-order cone problem using an optimization software package. The solving method for MACS can be more sensitive to small errors in the inputs or propagation terms, especially as the optimization solver searches for a global minimum to input the cost function.

In terms of implementation, CBF is the most straightforward to implement and a good starting point for any beamforming problem. FBF and GINV are also fairly straightforward, requiring a singular-value decomposition followed by minor adjustments to produce a result. The HM math is somewhat more complex due to the additional steps involved to produce the beamforming regularization matrix [Eq. (2.31)]. The regularization involved in GINV and HM can also present added complexity, although this is discussed in Section 2.2.5. MACS is fairly involved to implement, requiring multiple iterations to converge on a solution and an optimization solver. The iterations required also increase the computation time. In this example, a linear input array (50+ elements) and a linear potential source region (200 points) resulted in computation times that were not prohibitive (i.e., a few seconds per frequency on a standard desktop computer) for all methods except MACS, which took about twenty times longer.

2.2.5 Regularization Scaling

The choice of regularization was a significant factor in the performance of the HM and GINV method, as over-regularization or under-regularization would severely distort the beamforming results. The authors of GINV and HM gave guidelines for the determining of regularization, which in each case were based on empirical studies. Likewise, suitable regularization will depend, to some degree, on the specific application that determines the array and potential source location geometry as well as noise levels and other interferences. Thus, the following guidelines are given specific to the study here, although the trends should be applicable to further applications.

The regularization parameter of GINV, σ_{ref}, is used to prevent noise amplification when inverting the singular values matrix, $\mathbf{\Sigma}$ of $\mathbf{C}$. It is applied such that any singular values, $\sigma_i \leq \sigma_{\mathrm{ref}}$, are replaced by σ_{ref} prior to the inversion of $\mathbf{\Sigma}$. The choice of σ_{ref} is determined by considering the singular values of G, for which an example is shown in Fig. 2.3(a). The singular values, in this example, vary only slightly for at least the top thirty values, and thereafter they drop off quickly. The choice shown in Fig. 2.3(a) for a cutoff value is $\sigma_{\mathrm{ref}} = \sigma_1/1.71$, which is 2.33 dB less than the largest singular value. Values less than this cutoff are replaced with σ_{ref}.

The regularization in HM, however, is incorporated differently. In HM, regularization occurs on $\underline{\mathbf{G}}$, which has been weighted by the beamforming regularization matrix in Eq. (2.31). The singular values of this matrix are shown in Fig. 2.3(b) alongside those of $\mathbf{G}$. The blue-dotted line indicates the 5% threshold below the first singular value, which was suggested by Padois *et al.*[60] In this case, the regularization parameter does not replace lower singular values like for GINV, but it is added to the matrix in Eq. (2.32). In both cases, the regularization parameter value is slightly larger than the singular values that begin to decay exponentially.

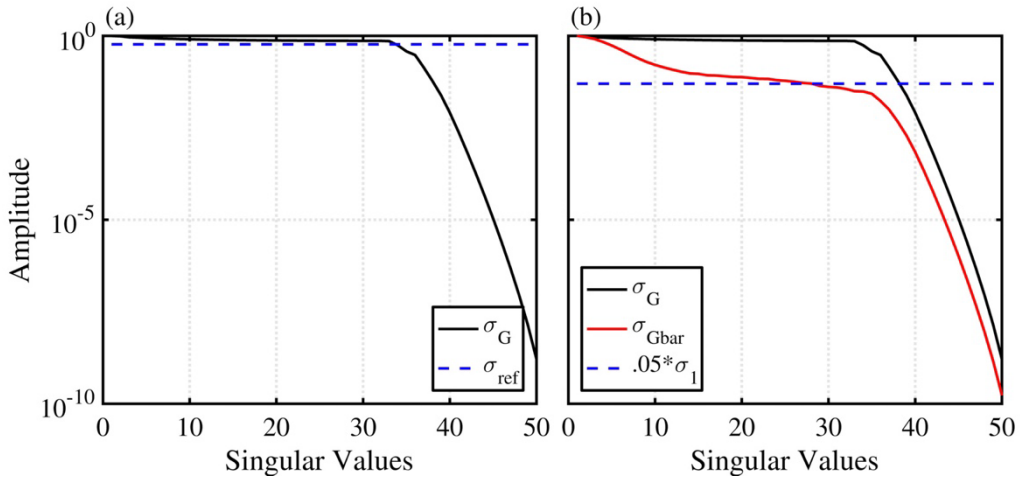

Fig. 2.3 (a) Singular values of Green function matrix, G. The blue-dotted line is the cutoff value in determining the regularization of GINV. (b) Singular values of G and $\underline{G}$ with the regularization parameter value suggested for HM (dotted line).

2.2.6 Beamforming-based Equivalent Source Model

A source model is propagated, by defining the Green function matrix, $\mathbf{G}_p$, similar to Eq. (2.12) that includes steering vectors for the desired locations in a field.[40] By propagating a given beamforming results matrix, $\mathbf{Q}$, the resultant cross spectral matrix of field pressures, $\mathbf{C}_p$, at those locations can by modeled using

$$\mathbf{C}_p = \mathbf{G_p}\,\mathbf{Q}\,\mathbf{G_p^H}. \tag{2.44}$$

Levels are calculated by taking the magnitude of the diagonal elements of $\mathbf{C}_p$ and converting to a decibel scale [i.e., $10\log_{10}(\cdot)$]. Furthermore, $\mathbf{C}_p$ includes both auto-spectral elements and cross-spectral elements to calculate the coherence properties of the field. For a reference location, $\vec{r}_{p_1}$, and another position $\vec{r}_{p_2}$, the coherence is calculated as

$$\gamma^2_{r_{p_1}r_{p_2}} = \frac{\left|\mathbf{C_p}(\vec{r}_{p_1},\vec{r}_{p_2})\right|^2}{\mathbf{C_p}(\vec{r}_{p_1},\vec{r}_{p_1})\mathbf{C_p}(\vec{r}_{p_2},\vec{r}_{p_2})}. \tag{2.45}$$

The ability to predict not only accurate levels but also correct coherence lengths using a beamforming-based equivalent source is an additional indicator of a beamforming methods' ability to estimate an extended, partially correlated source.

2.2.7 Scaling Source Estimates

Once beamforming results are calculated for each method, a standard technique for adjusting the levels is implemented to produce levels that, when averaged, agree with the average input measurements levels. Equation (2.44) is applied to a given beamforming results matrix, $\mathbf{Q}$, using the original propagation matrix, $\mathbf{G}$ from (2.12) to calculate an adjustment parameter, $\beta_{\mathbf{Q}}$, where

$$\beta_{\mathbf{Q}} = \frac{\mathrm{rms}\big(\mathrm{diag}(\mathbf{C})\big)}{\mathrm{rms}\big(\mathrm{diag}(\mathbf{G}\,\mathbf{Q}\,\mathbf{G}^{\mathbf{H}})\big)}. \tag{2.46}$$

In Eq. (2.46), $\mathrm{rms}(\cdot)$ is the root-mean square. The adjustment parameter calculates the mean-square difference between the predicted levels at the input array and the original inputs from the cross-spectral matrix. This is then used to update the beamforming results by $\mathbf{Q}_{\mathrm{update}} = \beta_{\mathbf{Q}}\mathbf{Q}$. This ensures that when considered as a source model, the levels predicted at the input array agree with the original measurement levels.

2.2.8 Extending Beamforming Bandwidth with UPAINT

The upper limit to the usable bandwidth for frequency-domain beamforming is set according to the spatial Nyquist frequency of a uniform input array. This is determined by solving for the frequency at which the array interelement spacing equals a one-half wavelength. Beamforming results above this limit introduce grating lobes, which are effectively spatially aliased estimates of the source properties. Where inverse and regularization methods are applied,

these grating lobes may interfere with the estimation process by redistributing energy from the true source estimate location to the grating lobes, or vice versa. To ameliorate the source estimates, a method was developed by Goates *et al.*[50] to increase the frequency bandwidth for the beamforming of broadband sources. A summary of the method is presented here, and a detailed description of the process is given in Ref. [50].

The unwrapped-phase array interpolation (UPAINT) method effectively creates a higher-density interpolated array to increase the spatial Nyquist frequency so that grating lobes do not interfere with the beamforming estimates. The UPAINT method accomplishes this by operating on both the frequency-dependent cross-spectra, $\mathbf{C}_{i_1,i_2}(f)$, of each microphone pair and the cross-spectral matrix of each frequency. First, the cross-spectral phase, $\mathbf{\Phi}_{i_1,i_2}(f)$, is unwrapped where

$$\mathbf{\Phi}_{i_1,i_2}(f) = \arg[\mathbf{C}_{i_1,i_2}(f)], \tag{2.47}$$

and i_1 and i_2 correspond to spatial locations $\vec{r}_{i_1}$ and $\vec{r}_{i_2}$. For each microphone pair, $\mathbf{\Phi}_{i_1,i_2}(f)$ is unwrapped to provide a smoothly-varying phase. This is performed by

$$\widetilde{\mathbf{\Phi}}_{i_1,i_2}(f) = \mathbf{\Phi}_{i_1,i_2}(f) + 2\pi \cdot \hbar(f), \tag{2.48}$$

where $\hbar(f)$ is an integer-valued function. As shown by Gee *et al.*[51] on near-field intensity measurements of laboratory-scale jet noise, this process is improved significantly using coherence-based methods to estimate the phase where noise may be present.[88] Once the unwrapped phase of each array microphone pair is determined, the magnitude, $\mathrm{abs}[\mathbf{C}(f)]$, and unwrapped phase, $\widetilde{\mathbf{\Phi}}(f)$, matrices form a UPAINT cross-spectral matrix. This cross-spectral matrix contains the magnitude of the cross-spectral matrix and unwrapped phase, which are distinct matrices that together form the standard version of the cross-spectral matrix. Having separated the components of the cross-spectral matrix by magnitude and unwrapped phase, each can be effectively interpolated because

both matrices are smoothly varying. Additional interpolation points are assigned and calculated as desired, and the interpolated components of the UPAINT cross-spectral matrix are then combined and input into the beamforming algorithm as a standard cross-spectral matrix. The corresponding array elements are updated with the additional interpolated locations and the beamforming results are produced. Because the array is interpolated—usually such that the interelement spacing corresponds to a spatial Nyquist frequency above the selected frequency—the beamforming results to not contain grating lobes that can interfere with the beamforming source estimates.

2.3 Multiple-Wavepacket Source Model

The purpose of this work is to evaluate five beamforming methods in a controlled numerical study that mimics the characteristics of the extended and partially coherent sources found in jet noise studies. A simplified source model is developed in this section, and methods are described for creating a simulated field. In Section 2.3.1, the source model characteristics are described. In Section 2.3.2, an example MWP source is described, which will be used to compare the performance of the beamforming method in Section 2.4. Finally, in Section 2.3.3 the accompanying radiation of the source example is provided, which mimics typical radiation found in jet noise studies.

2.3.1 Source Generation

Jet noise radiation has been described as distributed and partially correlated in nature.[9, 25, 26] In addition, the turbulence and hydrodynamic flow properties as well as the acoustic radiators of jet noise have been described as wavepacket-like, and wavepacket models have been an effective means of describing the turbulence flow and the radiation properties.[2] While attempts

have been made to relate the flow and acoustic radiation using wavepacket models,[3, 15] the acoustic radiation is treated independently in this study and modeled as a distributed wavepacket source. A wavepacket model is by nature a distributed source, however, additional steps are usually necessary to produce the features of partial coherence found in jet noise measurements. A prior study of an acoustic-based wavepacket model by Papamoschou[45] used a single wavepacket and a monopole to model the radiation of a subsonic jet. Papamoschou showed that the radiated levels estimated using a wavepacket and monopole agreed with the input measurements at a far-field array. However, neither the coherence of the wavepacket source nor the coherence of the radiation was considered. Furthermore, no additional validations were made to qualify the source model in the near or mid field. A more detailed model is pursued here in which the amplitude functions, as well as the partial coherence, of the wavepacket model are described. The model is be used in accompanying sections to produce a more complete radiation example.

Each wavepacket is modeled as an asymmetric-Gaussian function and represents a one-dimensional velocity source distribution. The velocity wavepacket distribution, w_{wpkt}, is modeled along an axis, z, by

$$w_{\mathrm{wpkt}}(z) = \begin{cases} a\exp\left(-b_1(z-z_{\mathrm{ref}})^2 + j\left(k_{\mathrm{peak}}z\right)\right), & z < z_{ref} \\ a\exp\left(-b_2(z-z_{\mathrm{ref}})^2 + j\left(k_{\mathrm{peak}}z\right)\right), & z \geq z_{ref} \end{cases}. \tag{2.49}$$

The peak amplitude of the distribution is located at z_{ref}, and the analytical function terms a, b_1 and b_2 are the amplitude, the growth rate and the decay rate, respectively. The wavepacket function is complex, and the complex argument depends on the peak wavenumber, k_{peak}. The peak wavenumber is related to the phase speed such that $k_{\mathrm{peak}} = 2\pi f/\overline{U}_c$, where $\overline{U}_c$ is the phase speed.

The wavenumber provides directionality to the wavepacket radiation, with the wavepacket directivity determined by

$$\phi = \pi/2 + \sin^{-1}(k_{\text{peak}}/k), \tag{2.50}$$

where k is the acoustic wavenumber and ϕ is the polar directivity of the wavepacket radiation (in radians), measured relative to the $-z$ direction. Azimuthally varying wavepackets have also been considered in prior mathematical formulations of wavepackets for modeling jet noise,[45, 89] although azimuthal symmetry is commonly considered, which is appropriate for some jet configurations dependent on the flow parameters and frequency,[23] and they are not included here as any axial array configuration will not detect azimuthal modes.

While radiated levels have been successfully mimicked using a single wavepacket,[18, 45] successful modeling of the coherence properties of the radiation has not been considered. For analytical wavepacket functions that use only a single wavenumber to describe the acoustic radiation, the coherence of the field is necessarily unity because the source is self-coherent. Jet noise fields, however, are not coherent fields but rather partially coherent, and, because jet noise is highly directional, the spatiotemporal characteristics are location dependent.[23, 90] The radiated field perpendicular to a jet flow along a sideline is generally characterized by very small coherence lengths corresponding to radiation from fine-scale turbulence structures, while the large-scale radiation structures produce large coherence lengths farther downstream in the field.[9] These varying coherence properties in the field are modeled in this chapter using multiple asymmetric-Gaussian wavepackets that share similar growth and decay parameters and that differ in relative amplitude and wavenumber selection.

2.3.2 Source Example

For this study, a selection of eleven wavepackets was chosen at a given frequency to provide sufficient variability in wavenumber selection for a partially coherent field, and the parameters of Eq. (2.49) were empirically determined to mimic jet noise directivity characteristics.[91] The individual wavepackets are shown in Fig. 2.4(a) for the case of 250 Hz. For each wavepacket, the wavepacket peak was positioned at $z_{\text{ref}} = 5.5$ m, and the growth and decay rates were fixed at 1 m^{-2} and 0.1 m^{-2}, respectively. The speed of sound, c, for the study is 343 m/s, and the individual wavepackets each differ by their phase speeds, U_c, which range from 250 m/s (subsonic) to 750 m/s (supersonic), with the center phase speed, $\overline{U}_c$, (i.e., 500 m/s) determining k_{peak}. The wavepackets produce radiation that propagates with a directivity ranging from 168° at $U_c = 350$ m/s to 117° at $U_c = 750$ m/s. In addition, two wavepackets contain subsonic phase speeds ($U_c \leq c$) such that their contribution to the field decays evanescently. The amplitude, a, of each wavepacket is assigned according to the difference between its phase speed the center phase speed such that the wavepacket at the center phase speed has the largest weighting. This produces radiation that is primarily directed according to $\overline{U}_c$ but also contains additional radiation contributions in alternate directions. A (normalized) normal distribution function, $f(U_c|\overline{U}_c, a_\sigma)$, is created with a mean of $\overline{U}_c$ and a frequency-dependent standard deviation, a_σ. The wavepacket amplitudes are drawn from the normal distribution by inputting each wavepacket phase speed into the function. For the case of 250 Hz, a_σ was set to $\overline{U}_c/5 = 100$ m/s to generate an overall radiation pattern that primarily contains directive radiation but that also contains cylindrical and omnidirectional radiation components for a smoothly-varying field.

The set of wavepackets, $\boldsymbol{W}_{\text{wpkt}}$, constitutes a multi-wavepacket (MWP) source model. Because each wavepacket radiates independently, the source self-coherence of the MWP model

along the z axis is shown in Fig. 2.4(b). The coherence is displayed such that the self-coherence is unity along the diagonal and coherence between locations in space are shown at off-diagonal points. In this example, the decay in coherence as a function of distance is similar regardless of the chosen reference location because the wavepackets are proportionally distributed over the z axis.

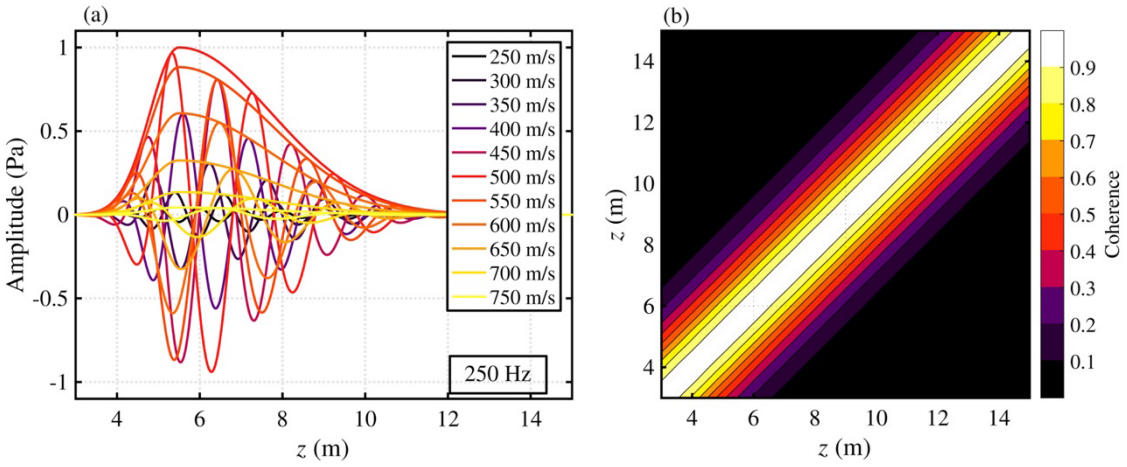

Fig. 2.4. (a) Individual wavepackets at 250 Hz that together constitute the one-dimensional source model. (b) Collective self-coherence of the MWP source distribution along the source axis.

The MWP source model is calculated for one-third octave frequencies from 40 Hz to 2000 Hz. The MWP model parameters of the six octave-band center frequencies contained in this range are given in Table 2.1, and parameters for the remaining frequencies are generally obtained via logarithmic interpolation. In each case, z_{ref} is constrained to be 5.5 m to match the measurement array reference point for a tactical full-scale engine measurement in Chapter 4. A set of eleven wavepackets is produced at each frequency, all of which share values of b_1 and b_2. Changes in the phase speed vary by frequency such that $\overline{U}_c$ is set to 400 m/s for $f \leq 125$ Hz, and it increases with frequency to 700 m/s at 1000 Hz. The corresponding U_c range is determined by $\overline{U}_c/2 \leq U_c \leq 3\overline{U}_c/2$. These values have been chosen based on results from a recent study by Neilsen *et al.*[92] to

model the level-educed large-scale turbulence radiation from jet noise as wavepackets. The growth, decay, and amplitude weighting parameters are also varied by frequency, with the values for each wavepacket set given in Table 2.1.

Table 2.1. Multi-wavepacket source model parameters.

Frequency (Hz)	U_c *(m/s)*	a_σ *(m/s)*	b_1	b_2
63	200-600	80	0.25	0.025
125	200-600	80	0.5	0.05
250	250-750	100	1	0.1
500	300-900	120	2	0.2
1000	350-1050	140	4	0.4
2000	400-1200	160	8	0.8

The overall amplitude distribution of each MWP source model is shown in Fig. 2.5(a) for the octave center-band frequencies, where each has been normalized by the peak level. Each MWP set has a growth and decay rate such that the source size contracts with increasing frequency, and previous beamforming,[39, 93] intensity-based,[27] and holography[29] estimates of jet noise source characteristics have displayed similar trends.

The frequency-dependent coherence properties are also considered using a convenient measurement means. Because coherence is dependent on a reference location,[90] coherence lengths provide a way to summarize the spatial variation in the coherence.[94] Coherence length, L_{γ^2}, is generally defined as the distance from a reference location over which coherence, $\gamma^2 \geq 0.5$. Here, it is specifically the shortest distance from the reference location to a point at which $\gamma^2 \leq 0.5$. Whereas previous definitions of L_{γ^2} are defined in terms of an axial direction from the reference location, the current definition can be extended to multiple dimensions. In addition, this definition is an improvement in cases where single-direction coherence lengths are undefined because coherence does not drop below 0.5 within the observational region (e.g., near the edge of a

measurement array). The variation of $L_{\gamma^2}(z)$ for example MWP source models is shown in Fig. 2.5(b). As was shown for the MWP source coherence at 250 Hz in Fig. 2.4(b), the coherence is self-consistent across the entirety of the source region. The coherence lengths also vary with frequency from about 5.7 m at 63 Hz to about 0.6 m at 1000 Hz—approximately 1-2 wavelengths. Whereas a single wavepacket would be perfectly coherent across the source (i.e. undefined L_{γ^2}), the finite coherence of the MWP source model generates a sound field with coherence properties similar to those expected for a jet noise measurement.[90]

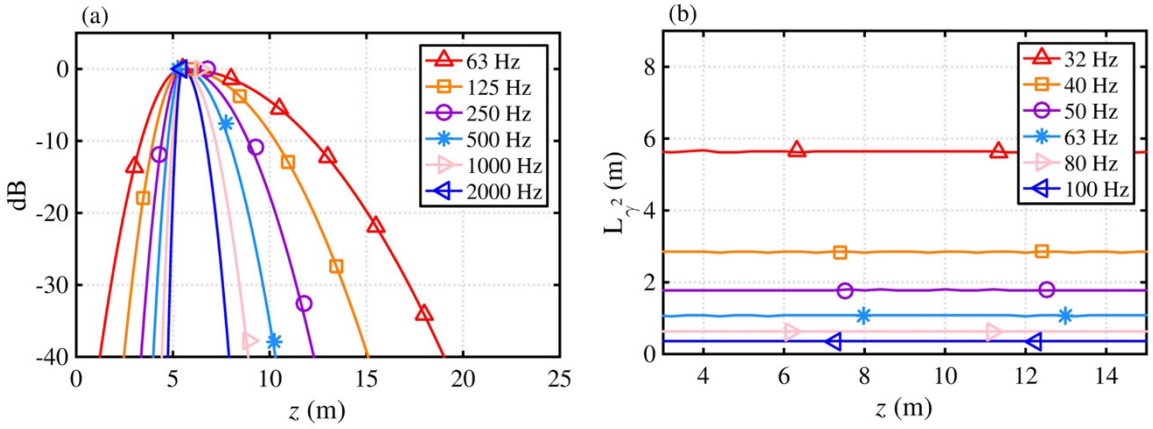

Fig. 2.5. (a) Overall source distribution levels and (b) corresponding coherence lengths for octave frequencies of the MWP source model.

2.3.3 Source Radiation

The MWP source model is used to generate a radiation field, which is used input into the beamforming methods in Section 2.4.1 and to validate the beamforming-based source models in Section 2.4.2. The model is positioned in a free-field environment along the z axis as shown in Fig. 2.6. Two arrays are positioned in the vicinity of and coplanar with the reconstruction region where the source distribution is located. The 50 element "beamforming array" is positioned similar to a ground-reference array geometry from a recent full-scale jet noise measurement.[24] This array spans 30 m in length and individual microphone locations are separated by 0.61 m. In addition,

the "far-field arc" is placed with a radius of 100 m from the origin, with 91 elements spaced in one degree increments. Finally, a dotted-line box in Fig. 2.6 marks the near-field region, where radiation levels are calculated.

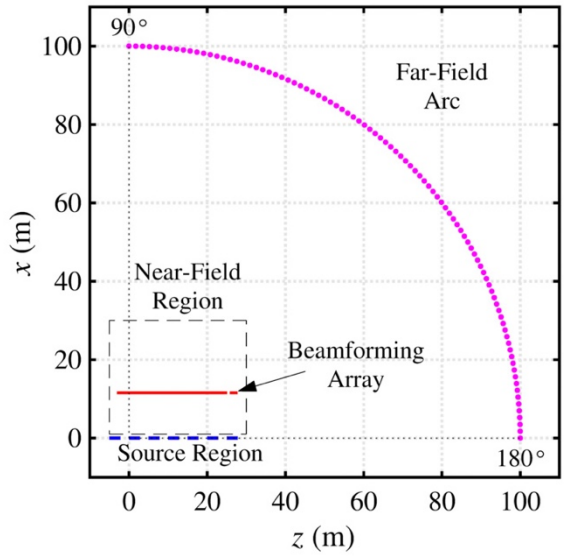

Fig. 2.6. Measurement setup schematic.

The sound fields generated by the MWP source models are shown in Fig. 2.7 for frequencies of 63 Hz, 250 Hz and 1000 Hz. The MWP source model radiation is designed to mimic jet noise radiation characteristics. Consequently, a strong radiating main lobe radiates with a directivity that turns upstream with increasing frequency, as dictated by the wavepacket parameters in Table 2.1. In addition, the main lobe of the radiation becomes more compact with increasing frequency. These calculations provide qualitative agreement in level with the radiated levels that Wall *et al.*[29] showed for holography reconstructions in the near field of a full-scale jet, thus indicating that the MWP model radiation levels are suitable in mimicking jet noise radiation for the current study.

The radiated levels are also simulated at the beamforming array and shown in Fig. 2.8(a). For each frequency case, the peak directivity angle—the angle at which the largest radiation levels

are directed—is spanned by the array geometry. However, the very gradual roll-off in level for 63 Hz and 125 Hz relative to the level roll-off at other frequencies indicates that the radiation may not be sufficiently spanned by the array. These constraints are generally present for full-scale array measurements of jet noise. In Section 2.4, the beamforming array calculations are used as input for the various beamforming methods, and the constraints that the array geometry places on the input information—particularly at frequencies below 125 Hz—produce practical circumstances under which to compare the performance of each beamforming algorithm to estimate the MWP source model.

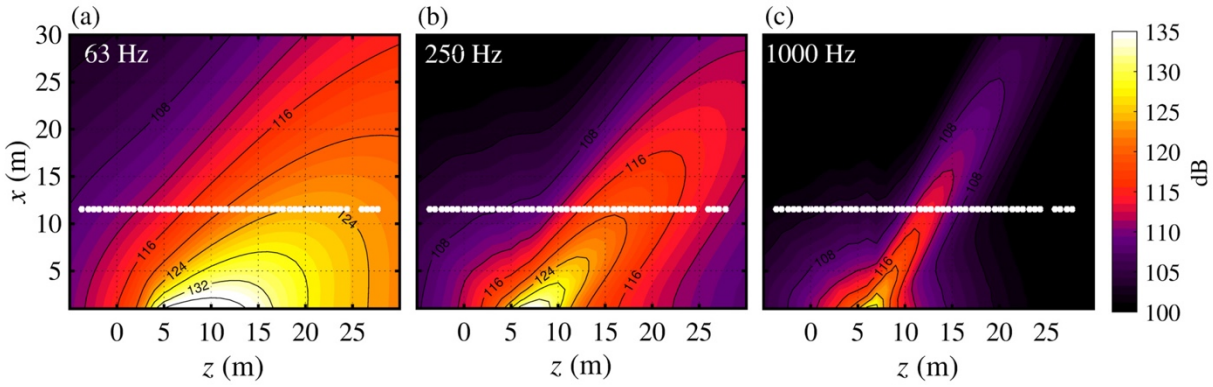

Fig. 2.7. Radiated levels from MWP source distributed along the z axis at (a) 63 Hz, (b) 250 Hz and (c) 1000 Hz.

In addition to levels, L_{γ^2} is calculated at the beamforming array at each frequency in Fig. 2.8(b). These coherence lengths are related to the temporal characteristics of the radiation and show that the field is partially coherent. The coherence lengths are largest in the downstream regions of the array because the direction of propagation is shallower for the MWP source, relative to the axis of the beamforming array. Thus, there is less separation—in an angular sense—between array elements at the edges of the array that creates increases in L_{γ^2} that are strictly a function of geometry.[95] The coherence lengths seem to be primarily associated with the geometric spreading of the source, with the largest lengths boosted by the grazing incidence of the radiation across the

array at far downstream locations. In addition, discontinuities in the coherence lengths are present towards the $-z$ end of the array (e.g., for 63 Hz at $z = 5$ m) where L_{γ^2} transitions between the smaller of the two possible coherence length calculations, whether measured in the $-z$ or $+z$ direction from the reference location. There are also local maxima or turning points in the L_{γ^2} calculations that correspond with the maximum levels, particularly for frequencies above 250 Hz. These peaks, corresponding to the maximum levels, were seen by Wall *et al.*[95] using a similar beamforming array to measure tactical noise.

The radiation levels and coherence properties from the MWP source model are also calculated at the far-field arc in Fig. 2.8(c) and Fig. 2.8(d). In Section 2.4.2, beamforming-based equivalent source models (ESM) are used to predict the radiation, and these level and coherence calculations provide a benchmark with which to compare the estimates. In addition, the coherence calculations, θ_{γ^2} are done as a function of angle in Fig. 2.8(d).

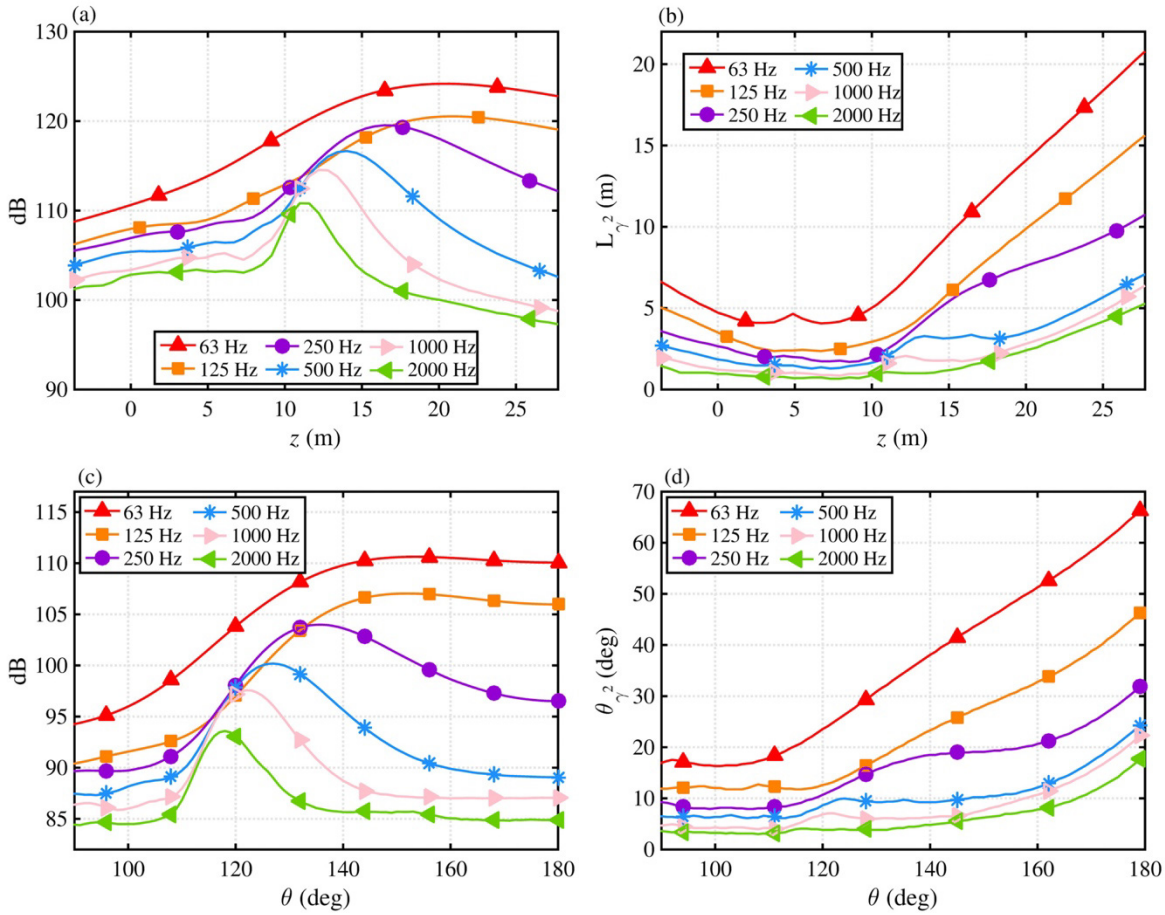

Fig. 2.8. Radiated levels from each MWP source model at the (a) beamforming array and (c) far-field arc. The coherence lengths are measured (b) as L_{γ^2} at the beamforming array and (d) as θ_{γ^2} at the far-field arc.

2.4 Application of Beamforming Methods

The five cross beamforming methods described in Sec. 2.2 are applied to sound simulated by the MWP source model at the beamforming array. These beamforming results are compared to the MWP source levels and coherence properties in Section 2.4.1. In Section 2.4.2, each beamforming result is treated as a source model and used to predict radiated levels and coherence. The results are compared to the near- and far-field benchmarks from the MWP source model

radiation. The comparisons illuminate the advantages and constraints for each beamforming method when used to estimate a distributed and partially coherent jet noise source.

2.4.1 Reconstruction Results

The MWP source-modeled calculations at the beamforming array [Fig. 2.8(a) and Fig. 2.8(b)] are used as input to the beamforming algorithms. The normalized beamforming results for each algorithm described in Section 2.2 are shown for the 63 Hz, 250 Hz, and 1000 Hz cases in Fig. 2.9. The MWP source-modeled levels (benchmarks) are shown using a black solid line, and results from CBF, GINV, HM, MACS, and FBF results are also given. At 63 Hz, the main lobe of each beamforming result captures the general features of source levels, although some methods (e.g., FBF) underestimate the top 6 dB of the source distribution while others (CBF and GINV) overestimate. At 250 Hz, all methods estimate at least the top 6 dB of the source distribution to within about 1 dB error, although thereafter the source distribution is overestimated to varying degrees. The CBF results diverge from the benchmark distribution first, followed by the GINV and then MACS results. There are low-level secondary lobes that appear for the CBF and GINV results below about 20 dB from the peak level. The HM and FBF results match the source distribution to within 1 dB for levels at most 20 dB down from the peak level.

The results at 1000 Hz include beamforming results that are caused by grating lobes. Because the spatial Nyquist frequency of the beamforming array is 280 Hz, beamforming results at higher frequencies suffer from grating lobes. While the additional ‘ghost’ sources are present in the results, the reconstruction of the original distribution is unaffected provided that the grating lobe effects do not overlap with the main lobe. However, in the case of the HM results, the regularization method can boost the levels of grating lobes while decreasing the levels of the actual source distribution, as shown in Fig. 2.9(c), resulting in a greater average error between the source

benchmark and the HM estimates. While not shown here, these grating lobes also interfere with the generation of equivalent source models by creating additional sources that propagate incorrectly, creating large errors between the MWP radiation levels and those predicted by the beamforming-based source models.

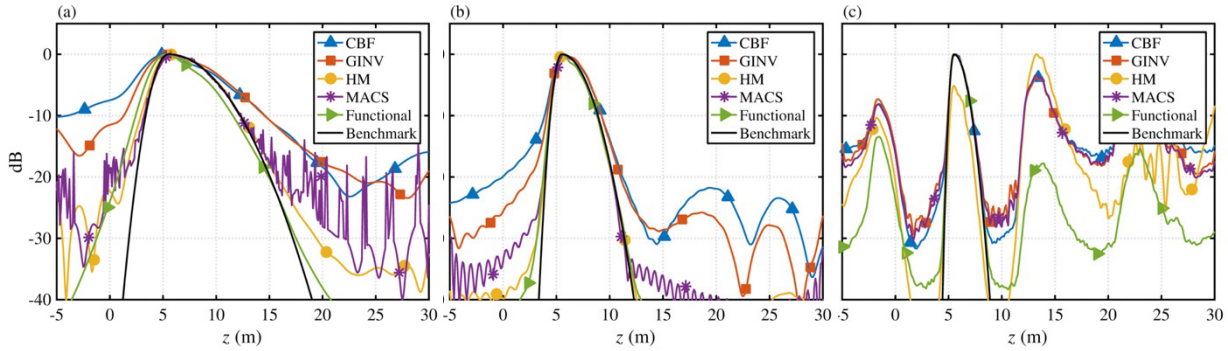

Fig. 2.9. Normalized beamforming level results of the source distribution for (a) 63 Hz, (b) 250 Hz, and (c) 1000 Hz, plotted alongside the benchmark levels.

To remedy the errors caused by grating lobes, the UPAINT method is applied to the processing of the cross spectral matrix and the corresponding beamforming results at 1000 Hz are shown in Fig. 2.10(a). With the UPAINT processing applied, the grating lobes are removed and the beamforming results have significantly improved for the CBF, GINV and HM methods. The source distribution is accurately estimated to within 1 dB for levels at most 20 dB down from the peak level. The source region estimates outside of the actual source distribution region, while relatively low-level, are much more noisy compared to the results without the UPAINT method applied. In addition, FBF results underestimate the source distribution levels, and MACS is unable to accurately estimate the source distribution and instead contains large estimated levels at the edges of the reconstruction region. In summary, the UPAINT method is a significant improvement for the CBF, GINV and HM results by removing grating lobes and by improving the source distribution estimate, but it degraded the estimate of the source for FBF and MACS.

The average error between the MWP source model and the estimated levels from each beamforming method is shown in Fig. 2.10(b) for one-third octave center frequencies from 40 Hz to 2000 Hz. The average decibel error is calculated by averaging over the difference, in decibels, of the beamforming results and the benchmark levels. Prior to the calculation for a given frequency, each beamforming result is normalized such that the peak level is unity (0 dB). Next, any beamforming or benchmark levels in the source region that are less than -20 dB are set to -20 dB to only consider relevant information above this threshold. The average errors are plotted in solid lines, and results above 280 Hz that used the UPAINT method are shown in solid lines while the dotted lines represent the average errors for results that do not use UPAINT.

For results that do not use UPAINT processing, the average errors are generally the lowest near the design frequency of the array, particularly for CBF and GINV errors. The MACS results show average errors below 1 dB for frequencies between 63 Hz and 250 Hz, while the average errors of FBF are below 1 dB from about 63 Hz to beyond 1000 Hz. The average errors of HM are the lowest overall for frequencies below the spatial Nyquist frequency. Beyond this frequency, however, HM and nearly all the methods suffer from grating lobe interference and the average errors grow from about 2 dB average error at 500 Hz to about 5 dB at 1000 Hz. Interestingly, the FBF average errors are not strongly affected by the grating lobes, and it can be seen in Fig. 2.9(c) that even though grating lobes are present in the FBF results, they are between 15-20 dB down from the peak level—while grating lobes in the other beamforming results are higher—and the source distribution estimate is accurate to within 1 dB for levels at most 30 dB down from the peak level.

When the UPAINT method is applied for frequencies above the spatial Nyquist frequency, the average errors are lower for every beamforming method and UPAINT processing results in

improvements for CBF, GINV and HM, although the overall performance of FBF and MACS results is degraded somewhat. With the UPAINT method, average error of HM results is below 1 dB throughout the entire frequency range, and CBF and GINV average errors are below 1dB for all frequencies past the spatial Nyquist frequency. The larger average errors for MACS when UPAINT is applied is a result of the large 'ringing' effect and inability of the method to properly estimate the source, although because there are no grating lobes the average errors are still lower than the results without UPAINT applied. The FBF average errors are also lower than the corresponding results without UPAINT because of the removed grating lobes, even though the source distribution is underestimated as seen in Fig. 2.10(a).

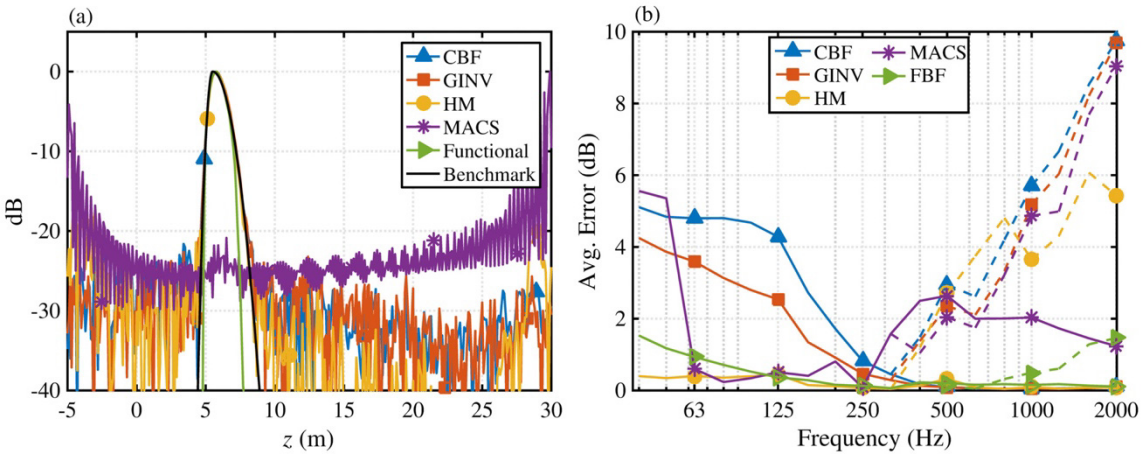

Fig. 2.10. (a) Normalized beamforming level results for 1000 Hz source distribution using UPAINT processing (b) Average level-based errors (in dB) of the beamforming results across the source distribution axis for all frequencies. The dashed lines represent the errors if UPAINT is not applied to the results.

The coherence properties of the beamforming results are also calculated for the case of 250 Hz and the beamforming source coherence lengths are shown in Fig. 2.11(a). The L_{γ^2} results are calculated across the reconstruction region, although source coherence length results are expected to be unreasonable outside of the region where the source levels are significant, and these regions are shaded in gray to mark the 20 dB down cutoff points of the source from the peak level—a

reasonable range over which accurate beamforming source properties are desired. The benchmark coherence length, shown in solid black, is uniform across the source region. In the region of interest, L_{γ^2} is estimated to within about 0.3 m of the correct values on average for the GINV, HM and MACS results. The CBF results are accurate to within about 0.5 m on average although they overestimate the values, and FBF is unable to calculated L_{γ^2} values because of the nonlinear process used to generate the results. For this reason, FBF is not a suitable method when source coherence is important, which is necessary for generating an equivalent source model to predict the field levels and coherence.

The average L_{γ^2} error is shown across multiple frequencies in Fig. 2.11(b). The average L_{γ^2} error is calculated by averaging the absolute difference between the benchmark values and those estimated by the beamforming results in the region of interest described above. In this case, grating lobes present beyond the spatial Nyquist frequency do not interfere with the coherence length results because only the region over which the MWP source is greater than -20 dB is considered, unless those grating lobes interfere at this location. The FBF results indicate the average errors that would be expected assuming the sources were incoherent, and serve well for comparison with the average errors of the other beamforming results. The GINV and CBF average errors are typically higher than even the FBF average errors because of the methods tendencies to overpredict the L_{γ^2} values. Coherence in this instance is overpredicted because of a significant point-spread function that bleeds source information over a larger space than it occupies. The MACS processing is designed to remove the point-spread function and the MACS average coherence results are generally lower than those of CBF and GINV. However, MACS also overpredicts L_{γ^2} values significantly below about 100 Hz, which roughly corresponds with the

inability of the method to correctly predict the source levels in Fig. 2.11(b). The HM average errors are also low, even below 63 Hz where MACS average errors are large, and the errors between MACS and HM are roughly on par with each other between 125 Hz and 315 Hz, although the lower average errors of the MACS results between 80 Hz and 160 Hz may be indicative of the overprediction of the HM values due to the point-spread function.

Above the spatial Nyquist frequency, the average L_{γ^2} error is shown both for results with and without the UPAINT method applied. Because the wavelengths are smaller at higher frequencies the overall average errors are smaller. However, the average errors are slightly lower for the methods where UPAINT is not applied. Because UPAINT is an interpolation process, small errors in the interpolated phase are amplified in the beamforming process because of its reliance on the coherent addition of input data. While the difference between the average errors with and without the UPAINT method applied is small (partially owing to the smaller wavelengths) it will most likely have a small effect on the resultant equivalent source models.

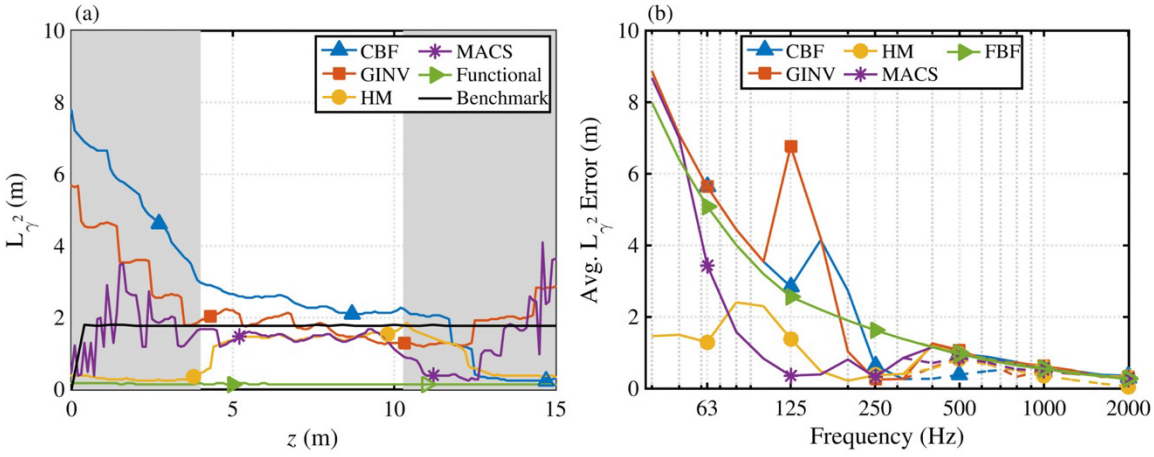

Fig. 2.11. (a) Beamforming-based coherence length of the source distribution at 250 Hz, plotted alongside the benchmark beamforming results. (b) Average error of the coherence length measured from the beamforming results for all frequencies. The dashed lines higher than the spatial Nyquist frequency (280 Hz) represent errors if UPAINT is not applied to the results.

Although UPAINT adversely affects the average coherence errors, its improvements on the source region estimates are significant. The UPAINT processing for frequencies above the spatial Nyquist frequency removes the adverse effects of grating lobes when used as a source model that otherwise produce 'ghost' sources that significantly interfere with the correct radiation estimates. The proceeding beamforming results used to generate equivalent source models will include UPAINT processing. In addition, FBF results will not be considered as a source model because of its inability to generate coherent source information necessary for the purpose.[48]

2.4.2 Beamforming Results as Equivalent Source Models

In addition to source estimation capabilities, the beamforming results can be used as an equivalent source model to predict the radiation properties if they estimate the source self-coherence as well as the levels. In many cases, this prediction field is limited to the aperture spanned by the beamforming array. The beamforming-based equivalent source models (hereafter referred to as "beamforming source" models) are verified by propagating to the beamforming array array to predict the levels and coherence lengths as in Eq. (2.44) and Eq. (2.45). The average level errors, calculated by averaging over the absolute decibel level difference, between the beamforming array calculations and those predicted by the beamforming sources are shown in Fig. 2.12(a). The average level errors are very low for HM and MACS up to the spatial Nyquist frequency, with average errors <0.1 dB. For frequencies above 280 Hz, the average errors of HM and MACS are higher although they remain within about 1 dB average error. This is also true of the GINV errors, although they are overall slightly higher for frequencies below the spatial Nyquist—a probable result of the larger average errors in the beamforming source estimates relative to HM and MACS. The CBF average errors are larger, with up to 2 dB average error. The

improvement of the regularized beamforming algorithms and MACS over the CBF results to validate the levels at the array shows the utility of these methods.

The average predicted coherence length errors at the beamforming array are shown in Fig. 2.12(b). The errors of the CBF predicted coherence lengths are generally greatest, with average errors up to about 3 m. The average predicted errors using the other three methods are much lower, with most average errors falling to within 0.5 m, which is approximately the interelement spacing of the beamforming array. The results show that both the predicted coherence lengths and levels are validated using each equivalent beamforming source model shown here and that the regularized beamforming algorithms and MACS are an improvement to the CBF-based source model.

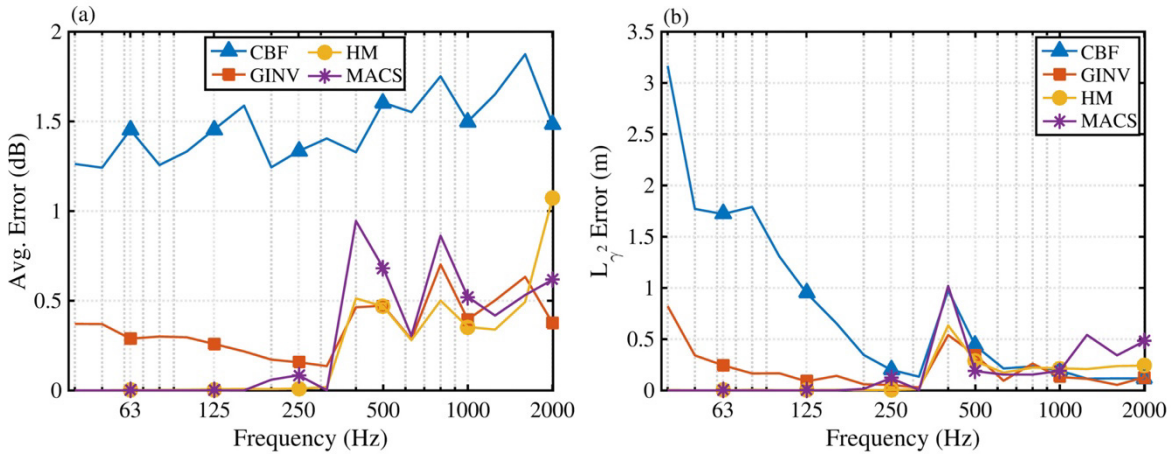

Fig. 2.12. (a) Average level errors (in dB) and (b) average coherence length errors (in m) at beamforming array between beamforming-based source models and the MWP source calculations.

Having validated the predictive capabilities of the beamforming source models, the field levels from the MWP source are predicted in the near-field region using each beamforming source. As an example, the HM predicted levels are shown in Fig. 2.13(a-c) at 63 Hz, 250 Hz and 1000 Hz for a field that is coplanar with the reconstruction and measurement arrays. The levels show strong agreement with the benchmark levels in Fig. 2.7, and the difference (in dB) between the

predicted and measured levels is shown in Fig. 2.13(d-f). In this case, errors are all within ± 1 dB except for small region at 250 Hz and 1000 Hz that are either between the beamforming array and the source region, or that are farther beyond the beamforming array in the $-z$ or $+z$ direction. Because the beamforming source is produced using beamforming array inputs, it predicts radiation that propagates through the beamforming array. This is generally the case of all beamforming sources. In some cases—e.g., at 63 Hz in Fig. 2.13(d)—the levels are accurately predicted even for propagating waves that do not traverse the beamforming array. This is likely a function of the beamforming methods ability to completely represent the source in a global sense, and requires that sufficient information about all sources is received at the beamforming array. For example, if an additional source were to radiate primarily in the $-z$ direction, outside of the region spanned by the beamforming array, it would likely not be estimated in the beamforming results and consequently the propagation related to that source would not be accurately represented. In this instance, a majority of the MWP source radiation propagates to the beamforming array and, consequently, the beamforming source predicted levels between the reconstruction region and the beamforming array are predicted to within ± 1 dB errors.

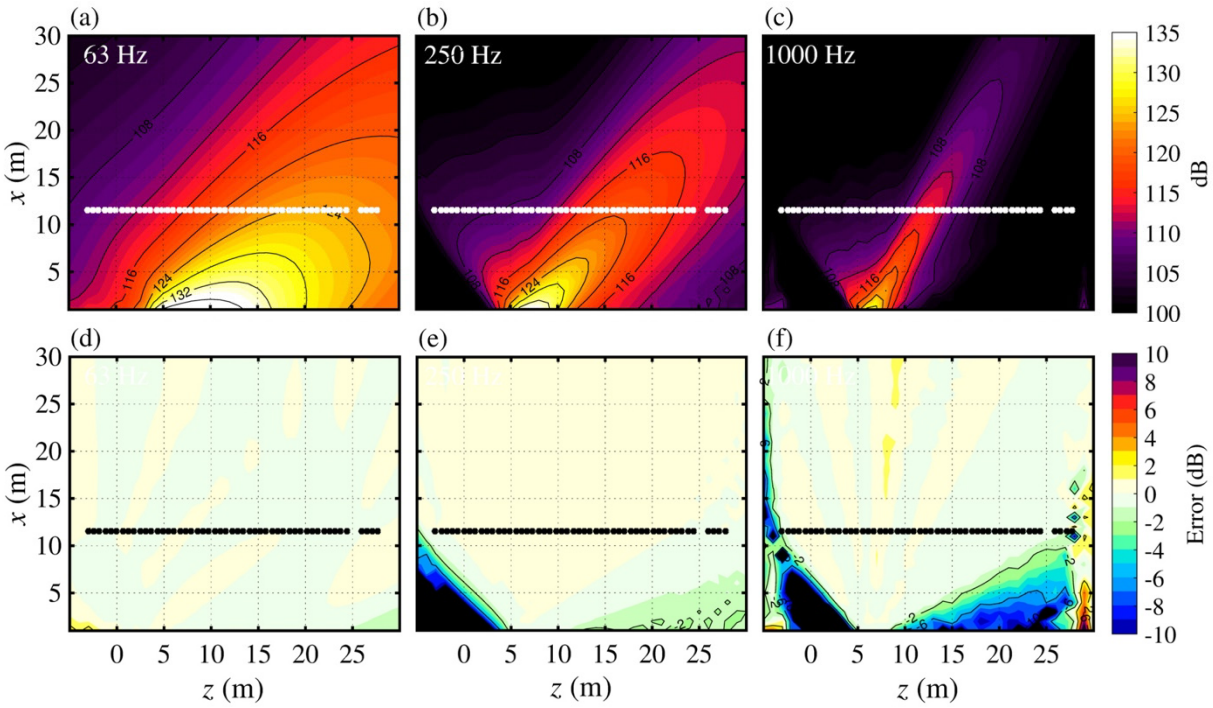

Fig. 2.13. Predicted radiated levels using HM based source model at (a) 63 Hz, (b) 250 Hz, and (c) 1000 Hz. Decibel level errors compared to radiated levels from source are shown in (d-f) for respective frequencies.

By comparing the predicted field levels using the beamforming sources to those calculated by the MWP source in the near-field region, the average field level errors, calculated in the same manner as for Fig. 2.12(a), are calculated and shown in Fig. 2.14 over multiple one-third octave frequencies. Apart from the MACS average field errors, the average errors of the beamforming-source predicted levels are similar below and above the spatial Nyquist frequency of the measurement array. This is the result of the UPAINT method to remove the grating lobes, which also adversely affects the MACS predicted levels. However, even without the UPAINT method the MACS average field level errors would remain high due to the contamination of the grating lobes. The average errors are within about 2 dB for the CBF values, while those of GINV are between 1-2 dB. The HM values provide the lowest overall errors, ranging between 0-2 dB across the frequency range and particularly low for frequencies below the spatial Nyquist frequency. The

results show the advantage of the HM method when predicting the field levels using an HM-based beamforming source.

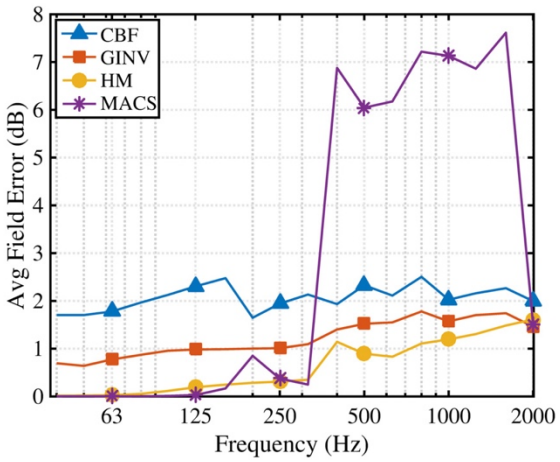

Fig. 2.14. Average field errors from radiated levels of beamforming-based source models.

To complement the near-field predictions, the beamforming source models are used to predict the levels and coherence lengths at the far-field arc. The predicted levels are shown alongside the benchmark calculations at the far-field arc in Fig. 2.15(a) for the case of 250 Hz. The benchmark levels (shown as a solid black line) smoothly vary and peak in level at about 135°. Each predicted level follows this trend and closely matches the benchmark levels to within 1-3 dB for predictions below about 150°, but because the measurement array does not capture the radiation for angles larger than about 150°, the predicted levels generally underestimate the benchmark calculations. The MACS and HM-predicted levels, however, estimate even the large angle radiation to within 3 dB. While these results may be promising, the cause of the successful beamforming estimates at these angles is not straightforward. One explanation is that the beamforming source model was generated using a low-wavenumber source model that coincidentally predicts the radiation globally, as was seen in Fig. 2.13(a). Whether the source model was produced because of the robustness of a given beamforming model or as a matter of

coincidence according to the chosen regularization value is unclear. The average error of the predicted levels at the measurement arc are shown in Fig. 2.15(b) using each beamforming source model for multiple one-third octave center frequencies. The trends of the average level errors are very similar to those seen in the average near-field level errors in Fig. 2.14.

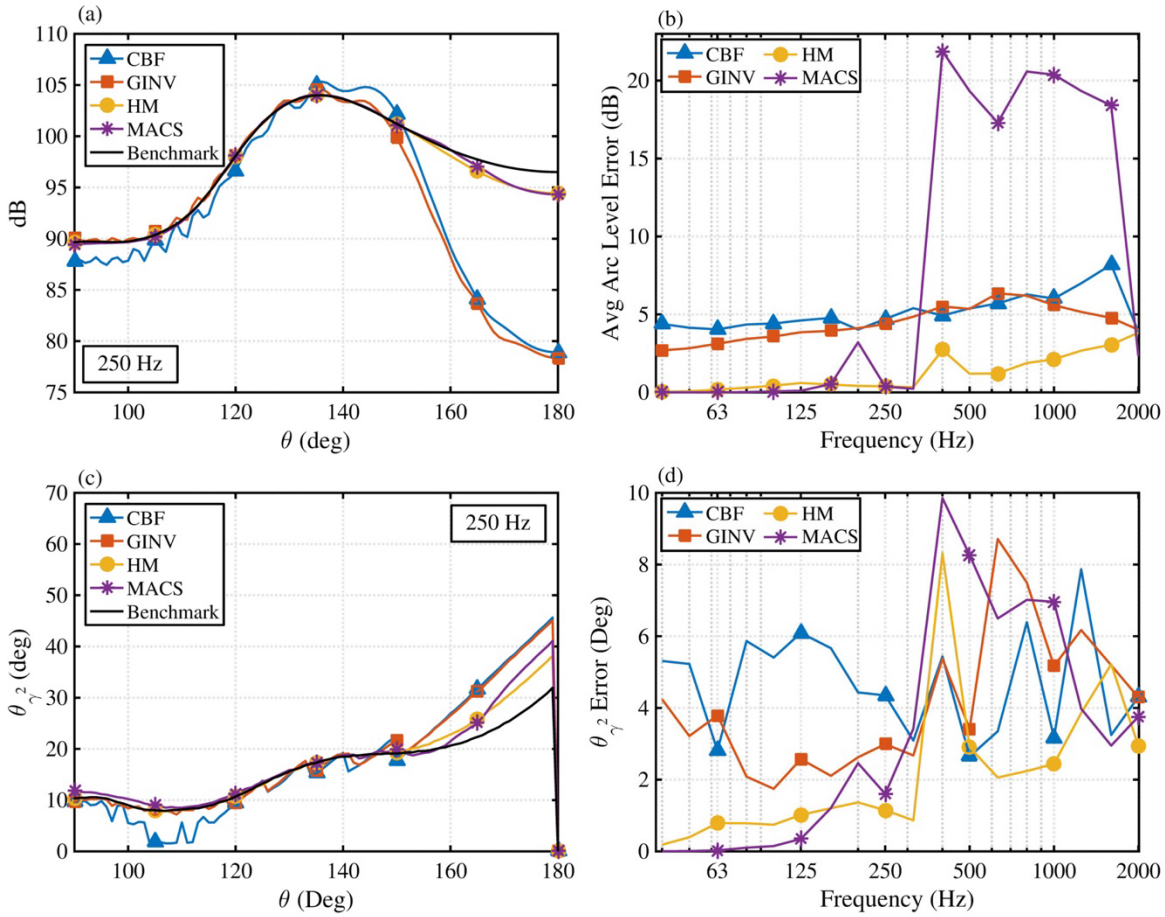

Fig. 2.15. (a) MWP calculated levels [in dB] and (c) θ_{γ^2} values [in deg] between beamforming-source predicted levels at the far-field arc at 250 Hz. (b) The corresponding average level errors [in dB] and (d) average θ_{γ^2} error [in deg] between MWP calculated levels and predicted levels for one-third octave center frequencies.

The predicted coherence lengths at the far-field arc are shown in Fig. 2.15(c) for the case of 250 Hz. Because coherence is calculated over the arc where measurements are one degree apart, θ_{γ^2} is given in degrees, which is a better generalization of the coherence lengths for a far-field measurement given that they do not depend on the distance from the source. Each method

successfully predicts the benchmark θ_{γ^2} values across the measurement arc, with errors of only a few degrees in the region where radiation levels are most significant and up to $15°$ at the extreme angles of the array. Interestingly, the predicted coherence lengths agree with benchmark values to within about $15°$, even at angles that are beyond the aperture of the input array ($> 150°$), while the predicted levels at these angles deviate by as much as 15 dB. This is most likely the result of the coherence values being highly affected by the grazing-incidence effect, discussed in Section 2.3.3, where in this case the source is seen end-on for large far-field angles.

The average error of θ_{γ^2} values predicted by each beamforming source is shown in Fig. 2.15(d) over the considered frequency range. The average θ_{γ^2} errors fall within $6°$ for frequencies below the spatial Nyquist frequency, and errors as low as $0.1 - 1.5°$ in the same frequency range for the HM average θ_{γ^2} errors. Above the spatial Nyquist frequency, the average errors are more varied, most likely because of the increased phase error resulting from the UPAINT processing. These average error values range between $2 - 10°$ and the error trends do not match those seen in Fig. 2.15(b) for average level-based errors. While the results are more varied, particularly at higher frequencies, the HM results generally outperform the results of the other beamforming methods, like the results for the level-based analysis in Fig. 2.15(b). Additionally, the coherence-based analysis features an additional interesting layer of information beyond results produced from only a level-based analysis.

2.5 Concluding Discussion

Multiple beamforming-based methods have been compared to estimate the source characteristics of an extended, partially correlated source distribution. The focus of this chapter is

directed towards comparing and validating beamforming methods for application to sources that exhibit various degrees of self-coherence, e.g., jet noise sources. A numerical study has been performed using a multiple-wavepacket (MWP) source distribution designed to mimic the partially correlated nature of jet noise. Measurements using a linear array near the source distribution are applied to cross-beamforming (CBF), generalized inverse beamforming (GINV), hybrid method (HM) the mapping of acoustic correlated sources (MACS), and functional beamforming (FBF).

Each method is successful in reconstructing the source distribution levels at least 6 dB down from the peak level for frequencies below, near, and above the design frequency of the array (i.e., spatial Nyquist frequency), although there are significant differences in the individual algorithms performance. Below and near the array design frequency, CBF and GINV overpredict the source levels while MACS, FBF and HM results produce more accurate results. For example, the HM and FBF results at the array design frequency produce results accurate to within 1 dB for levels at most 20 dB down from the peak level. Above the array design frequency, grating lobes are introduced that can interfere with the beamforming results and that create 'ghost' sources that produce corrupt field radiation predictions when the beamforming results are treated as a source model. The UPAINT method is an interpolation method that can be applied to broadband source measurements to increase the usable bandwidth of an array. With the UPAINT processing applied, the grating lobes vanish and the average level errors between the source and beamforming results are greatly reduced. The UPAINT interpolation process also adds small phase-errors and more sensitive algorithms such as MACS are adversely affected. However, the UPAINT method extends the usable bandwidth of the array to at least seven times the original spatial Nyquist frequency. Using UPAINT, the HM method produces the lowest level errors below and above array design frequency. The self-coherence is also compared between the beamforming results and the MWP

source, and the HM results provide the best overall performance across multiple frequencies. In addition, FBF is unable to estimate the source self-coherence due to its nonlinear algorithm, which renders it unable to accurately produce a beamforming-based source model.

In addition to the source properties, the beamforming results are treated as an equivalent source model to predict the levels and coherence properties of the radiation. While FBF cannot be used in this manner, the approach to treat the remaining beamforming results as source models is straightforward. When re-radiated to the (input) beamforming array, the average level errors from the GINV, HM and MACS are much lower than the corresponding errors of the CBF estimates. While the frequency-dependent CBF average level errors range from 1.3-1.8 dB, the HM average errors are less than 0.1 dB up to the array design frequency and about 0.5-1.0 dB for higher frequencies tested. The MACS average errors at the beamforming array are on par with the HM errors, while GINV average errors are slightly higher. The estimated coherence lengths show similar trends seen by the estimated levels: the average coherence length error of the HM results was best overall with average errors under 0.5 m, and the GINV and MACS values were generally on par with HM results although slightly higher. Thus, the improvement of the beamforming-based equivalent source models is pronounced using the more advanced regularization beamforming methods as opposed to simply CBF.

The beamforming-based equivalent sources are also used to estimate the levels and coherence properties of the near-field region and the far-field arc. The predicted levels in the near-field region are shown below, near and above the array design frequency using the HM-based source. Compared to the radiation calculated using the MWP source, the beamforming-based source agrees to within ± 1 dB across most of the region and captures the salient features of the source. Regions that are not spanned by the beamforming array, however, are not well predicted

by the beamforming source model. In a comparison between the different beamforming-based source models, the MACS and HM models predict the near-field and far-field levels generally to within 1 dB average error of the calculated levels below the array design frequency. Above this frequency, the HM method continues to produce the best performance while the MACS results drop in performance below CBF and GINV, owing to its inability to successfully converge on the correct beamforming results with the UPAINT method applied. Similar trends are also seen for the coherence-based average errors in the far field predictions.

The general conclusions are as follows:

1. HM, MACS, and FBF produce the best level-based performance for estimating the source levels below the array design frequency.
2. Above the array design frequency, all methods produce larger source level errors owing to grating lobes. After applying the UPAINT method, all methods except MACS and FBF produce high-quality source level estimates that area free of grating lobes. MACS is unable to converge on the source using UPAINT.
3. MACS and HM are the best performers in predicting the source self-coherence while FBF is unable to do so because of its nonlinear process.
4. HM and MACS outperform CBF and GINV in terms of performance to predict the near-field and far-field levels and coherence properties for frequencies below the array design frequency.
5. HM continues to perform well above the array design frequency with UPAINT applied, although MACS errors are significantly higher.

Overall, the HM results showed the best overall performance when considering both source properties and equivalent source model capabilities.

Future work to further improve beamforming methods for application to distributed and self-coherent sources will continue to reduce the errors in the source predictions as well as the radiation properties of the source. A common difficulty of the regularization methods is the proper selection of a penalization parameter. While the methods shown here have regularization methods that provide adequate results, additional work to formalize the different techniques incorporated in GINV, HM and other inverse methods should provide improved performance over a larger frequency range and/or for measurements with a worse signal-to-noise ratio. A more advanced method derived from a combination of these techniques may further improve the beamforming results. Finally, additional steering function formulations, whether from multi-pole type sources as described in L_1 generalized inverse beamforming or using spherical harmonics as used in HELS.[47, 96] Improvements in the beamforming methods should aid in the successful reproduction of the acoustic phenomena associated with distributed sources such as those present in jet noise, and they provide a valuable predictive tool to estimate the corresponding radiation in an effective manner.

Chapter 3

Spatiotemporal Correlation Analysis of Jet Noise from a High-Performance Military Aircraft

3.1 Introduction

This chapter is modified from a 2016 paper published in the AIAA Journal under the same title.[90] The purpose of the work is to provide a detailed characterization of the correlation and coherence properties of tactical jet noise measurements that are used as input to advanced beamforming methods in Chapter 4. In addition, a preliminary investigation of the source levels and coherence properties was performed. An understanding of the measurements is used to guide the beamforming study in Chapter 4, including the subarray study in Section 4.3.3, and the source coherence estimates provide a framework for the more detailed source coherence analysis in Section 4.3. While results here are provided for the intermediate and afterburner engine conditions, this work was also presented at the *21st AIAA/CEAS Aeroacoustics Conference* in Dallas, TX, and the corresponding conference paper contains additional results for the military engine condition.[97]

Correlation analyses of near-field acoustical data from supersonic tactical aircraft engines provide key insights into the noise field variation as a function of location and engine power. Furthermore, because jet noise source characteristics are imprinted on the radiated sound field,[9] the spatiotemporal features found in the pressure field complement spectral analyses by providing a more complete understanding of the acoustic source, thereby assisting those who seek to more accurately replicate these environments analytically, numerically, and experimentally. For example, both two-point, space-time pressure correlation functions[23, 75, 98, 99] and the shape of single-point autocorrelation functions have been used to distinguish between the fine versus large-scale nature of the jet noise radiation.[9, 100] These measurements have also been used to provide spatiotemporal length scales, either broadband[9] or band-limited,[94] which are useful in validating and improving jet noise models.[17, 101, 102] Consequently, the correlation results presented in this paper for full-scale tactical engine noise extends the growing number of laboratory and computational jet studies that use auto (single-point) and cross (two-point) correlation functions of the acoustic field to obtain not only valuable information of the spatial structure of the noise field, but also insights into the noise sources found within the turbulent jet plume.

Previous experiments have used correlation analyses to relate pressure-field measurements to source phenomena. Early work by Clarkson,[103] Fuchs,[104, 105] Maestrello,[106] Fisher *et al.*[28] and Ribner,[107] as well as more recent work by Tam *et al.*[9] have suggested the autocorrelation function has significant negative loops when large-scale structure noise dominates the spectrum. This was verified by Harker *et al.,*[100] who calculated autocorrelation functions defined by Tam's large and fine-scale similarity spectra[108, 109] and showed that the autocorrelation function of the large-scale similarity spectrum contains significant negative loops. Viswanathan *et al.*[23] used an extensive conical array of microphones to calculate near-field correlation measurements of a laboratory-

scale, heated supersonic jet. They determined that a large coherent region existed, at least two potential core lengths downstream and beyond the maximum radiation region, as well as a single mechanism responsible for the generation and radiation of noise to the peak radiation sector. Kumar *et al.*[110] showed how the temporal width of the far-field correlation measurements broadened as a laboratory-scale jet was operated at under, ideally and over-expanded conditions. Liu *et al.*[111] calculated cross correlations as part of an analysis of numerical pressure fields resulting from simulations of perfectly expanded and underexpanded jets. They found that while the broadband shock-associated noise (BBSAN) could be identified in the cross correlation, the autocorrelation distribution gives a more precise end location of the BBSAN. Correlation analyses, including the works of Panda *et al.*[25] and Papamoschou *et al.*[16] have also been applied to measure the correlation of pressure measurements in the acoustic field to the jet flow properties. The results of these prior correlation studies indicate that field characteristics can provide insights into source characteristics.

In this chapter, spatiotemporal correlation and coherence analyses of sound measured in the vicinity of a static tactical aircraft are presented to provide an improved characterization of the noise radiation and to provide a benchmark case for comparing against modeling and laboratory-scale experiments. An introduction to correlation methods is followed by a short description of the experiment. Auto and cross correlation functions of the pressure field from an array of ground-based microphones in the vicinity of a tactical aircraft at intermediate and afterburner condition are presented to investigate the broadband features of the sound field. Some of the full-scale jet noise correlation features are not exhibited in previous laboratory-scale jet studies. To investigate these features further, a complementary study of the coherence of the noise at select frequencies is presented to provide additional insights and allow for comparison between field properties and

related source properties obtained using beamforming methods. Findings yield a more complete picture of tactical jet noise characteristics and highlight features of noise from high-performance military aircraft that have not yet been replicated in laboratory-scale jets.

3.2 Methods

A short description of the methods for each of the correlation and coherence analyses applied to the tactical jet noise data is provided in this section. First, definitions of the auto and cross correlation functions are followed by coherence spectrum and coherence lengths definitions. Finally, a cross beamforming and deconvolution algorithm called DAMAS-C is briefly described and a method for extracting an estimated source coherence from the DAMAS-C output is summarized.

3.2.1 Correlation

The single-point correlation (autocorrelation) functions are studied to understand the temporal scales over which the waveform is correlated and the evolution of these properties in space. In addition, two-point correlation (cross-correlation) functions provide a look at the spatiotemporal variation in the correlation properties as well as estimates of correlation length scales. The correlation between two waveforms is defined as[59]

$$R_{xy}(\tau) = E[x(t)y(t+\tau)] \tag{3.1}$$

where the expectation value, $E[\cdot]$, of a signal, $x(t)$, with a signal, $y(t)$, delayed by time, τ. The autocorrelation function, $R_{xx}(\tau)$, is the inverse Fourier transform of the autospectral density and there is, therefore, a single autocorrelation function that corresponds to a given spectrum. This property permitted the development of similarity autocorrelation functions from Tam's fine and

large-scale similarity spectra.[100] Similarly, the cross correlation function, $R_{xy}(\tau)$, and the cross-spectral density form a Fourier transform pair. Although the correlation and the spectrum technically contain the same information, using one or the other can be beneficial in examining different trends in the sound field. For example, correlation may be used to more easily identify waveform periodicities and obtain spatiotemporal length scales and phase speeds. On the other hand, coherence (a normalized form of the squared cross spectrum), is useful for extracting the spatial phase relationships of the field as a function of frequency. In this paper, all correlation functions are normalized by the maximum correlation value, i.e. as correlation coefficients, such that $\left|R_{xy}(\tau)\right|^2 \leq R_{xx}(0)R_{yy}(0)$. In this study, a temporal or spatial correlation length is defined as the time or distance over which $\max\left[R_{xy}(\tau)\right] > 0.5$.

To facilitate comparison of temporal decay rates of $R_{xy}(\tau)$ and better identify low-level features, the envelope function of the correlation coefficient is employed. The envelope function is defined as[59]

$$A_{xy}(\tau) = \left[R_{xy}^2(\tau) + \tilde{R}_{xy}^2(\tau)\right]^{1/2}, \tag{3.2}$$

where $\tilde{R}_{xy}(\tau)$ is the Hilbert transform of the correlation function. Since $A_{xy}(\tau)$ is positive semidefinite, it can be plotted on a logarithmic (decibel) scale to more clearly observe low-amplitude features not visible in $R_{xy}(\tau)$. Additionally, the envelope function is useful to more consistently quantify differences in the temporal decay rate of $R_{xy}(\tau)$ for various locations around a jet or for jets of different scales and conditions. Instead of relying on an interpretation of negative loops in the autocorrelation to define a temporal or spatial correlation scale,[9] $A_{xy}(\tau)$ provides the magnitude of the temporal correlation and can be used to compare the temporal decay of fundamentally different autocorrelation functions (e.g. $A_{xy}(\tau) > 0.5$).[100]

3.2.2 Coherence

The coherence between a reference microphone and other ground-array microphones indicate the spatial extent over which individual frequency components of the jet noise are related and allows for additional investigation of features seen in a broadband cross correlation analysis. The frequency-dependent coherence function is defined as

$$\gamma_{xy}^2(f) = \frac{\left|G_{xy}(f)\right|^2}{G_{xx}(f)G_{yy}(f)}, \tag{3.3}$$

where the cross-spectral measurement $G_{xy}(f)$, relating signals $x(t)$ and $y(t)$, is normalized by the respective autospectra and therefore bounded between 0 and 1. In a manner similar to the correlation analyses, a spatial coherence length, $L_{\gamma^2}(z_1, f)$, is defined as the length over which there is significant coherence. In this paper, it may be defined as the distance at which the coherence, $\gamma_{xy}^2(f)$, of a reference signal at z_1 drops below 0.5 when compared to adjacent measurements, z_i, in the upstream direction.[94]

3.2.3 Source Coherence via Beamforming

Beamforming measurements have been used in multiple contexts in efforts to reconstruct source properties from jet noise radiation.[15, 35, 39, 41] Using phased arrays, pressure measurements provide equivalent source reconstructions by defining a source distribution region in the vicinity of the jet plume. Generally, beamforming analyses assume a distribution of incoherent simple sources. However, more advanced beamforming algorithms have been developed to successfully reconstruct spatially distributed sources with varying degrees of spatial coherence.[40, 58, 93] One such algorithm is an extension of the deconvolution and mapping of acoustical sources (DAMAS[42]) algorithm, known as DAMAS-C,[43] which is favorable for jet noise studies because of partial

coherence over the source region as a function of frequency. A detailed description of the DAMAS-C algorithm can be found in Ref. [43]. Since flow parameters and refraction effects are not incorporated in the beamforming model presented, an equivalent source region is obtained. Of importance here, however, is our use of DAMAS-C to provide an estimate of source coherence within the source reconstruction region. While source level can usually be obtained as a function of space and frequency using traditional beamforming methods, DAMAS-C also determines a relationship in level and phase between two source locations, where $X_{z_1 z_2}(f)$ represents the DAMAS-C output due to the likelihood of sources at locations z_1 and z_2 along the jet centerline generating the measured pressure field. The algorithm is applied to each frequency component individually, and the coherence, $\gamma^2_{z_1 z_2}$, may be shown to be related by the corresponding beamforming outputs:

$$\gamma^2_{z_1 z_2}(f) = \frac{\left|X_{z_1 z_2}(f)\right|^2}{X_{z_1 z_1}(f) X_{z_2 z_2}(f)}. \tag{3.4}$$

Thus, in addition to obtaining an estimated source region, the spatial properties of the equivalent source coherence can also be obtained. In spite of this advantage, DAMAS-C has not been widely used because of its high computational expense, which requires on the order of N^4 operations, where N is the number of beamforming reconstruction points. For the current work, a one-dimensional source distribution along the nozzle centerline axis, similar to other equivalent line-source models,[28, 35] is chosen with a 0.3 m spacing (~$0.5D_j$) between each scan point such that the algorithm run time for each frequency was reduced from days to minutes.

3.3 Experiment

In this section, details of the tactical jet noise measurement[24] that are pertinent to the correlation and coherence analyses are provided. In addition, although engine operating parameters are not available, a discussion is included of how these results may possibly relate to published jet noise studies for known operating conditions.

3.3.1 Full-scale Measurement and Analysis

Noise measurements were made of a tactical aircraft that was tied down on a concrete runup pad. One of the aircraft engines was operated at four engine conditions [idle, intermediate (INTER), military (100%, MIL), and afterburner (150%, AB)] while the other was held at idle. A linear array of 50 GRAS 6.35-mm and 3.18-mm Type 1 microphones, spanning 30 m, was placed on the ground 11.6 m from the centerline of the jet axis, as shown in Fig. 3.1(a). The ground array element spacing was 0.61 m. Each measurement was taken for 30 seconds at either a 48 kHz or 96 kHz sampling rate, depending on the engine condition tested, and each resultant waveform was divided into time-waveform blocks of 2^15 samples each with 50% overlap. A Fourier transform was applied to each block after a Hanning-window correction was applied, and cross-spectral calculations were averaged over the blocks to obtain cross-spectral density elements.

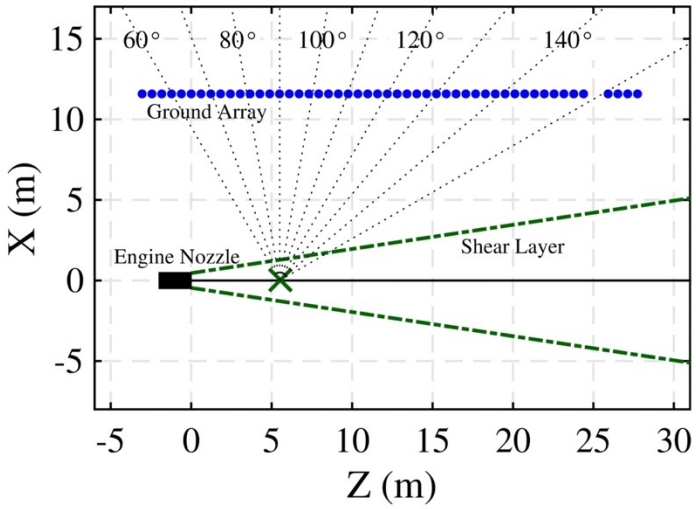

Fig. 3.1. Experimental Setup. Schematic of ground-based microphone array (blue dots) in the vicinity of an tactical aircraft.

The one-third octave (OTO) band spectra of the measurement at intermediate and afterburner engine operation conditions are shown as a function of position, z, along the ground-based array in Fig. 3.2, and the averaged overall sound pressure levels (OASPL) across the array are plotted alongside. An extensive analysis of the spectral variation along the array, including contributions due to large and fine-scale turbulent structures, is contained in Ref. [91]. The spectral comparisons show evidence that a combination of fine- and large-scale mixing noise exists over most of the spatial aperture at intermediate engine power, with the levels associated with the large-scale contributions remaining relatively flat. On the contrary, at afterburner condition, there is a more abrupt transition from fine- to large-scale contributions and a rapid increase in level due to Mach wave radiation.

Also of importance here are the variations in peak frequency at each engine condition as a function of z. Sound to the sideline, defined as $4\text{ m} < z < 6\text{ m}$, and upstream ($z < 4\text{ m}$) exhibits spectra that are broad in nature and generally contain a higher peak frequency content (approx. 800 – 1200 Hz). Farther downstream, the peak frequency drops to between 100-200 Hz and the

spectral shapes narrow and become more haystack-like. Across most of the array, the spectral shape has a single peak frequency, as has been observed for laboratory-scale jets.[15, 23] However, some locations exhibit a double-peaked spectral shape that appear as the peak shifts between two discrete frequencies. Such a transition region exists at both MIL and AB in approximately the $12\text{ m} < z < 15\text{ m}$ range where two dominant frequencies exist in the spectra. Neilsen *et al.*[112] has described how the presence of dual spectral peaks is not accounted for by the analytical similarity spectral shapes given by Tam *et al.*[108, 109] and also discussed how these peaks are not present in existing laboratory-scale measurements. The reason for the double peaks in the military jet aircraft spectra is currently under investigation.[13, 113] Note that a similar double peak has been observed in F-35 AA-1 data[114] and in far-field tactical jet noise data,[55] well below ground interference nulls caused by elevated microphones, so this feature appears to be a characteristic of current-generation tactical aircraft noise spectra at high engine powers.

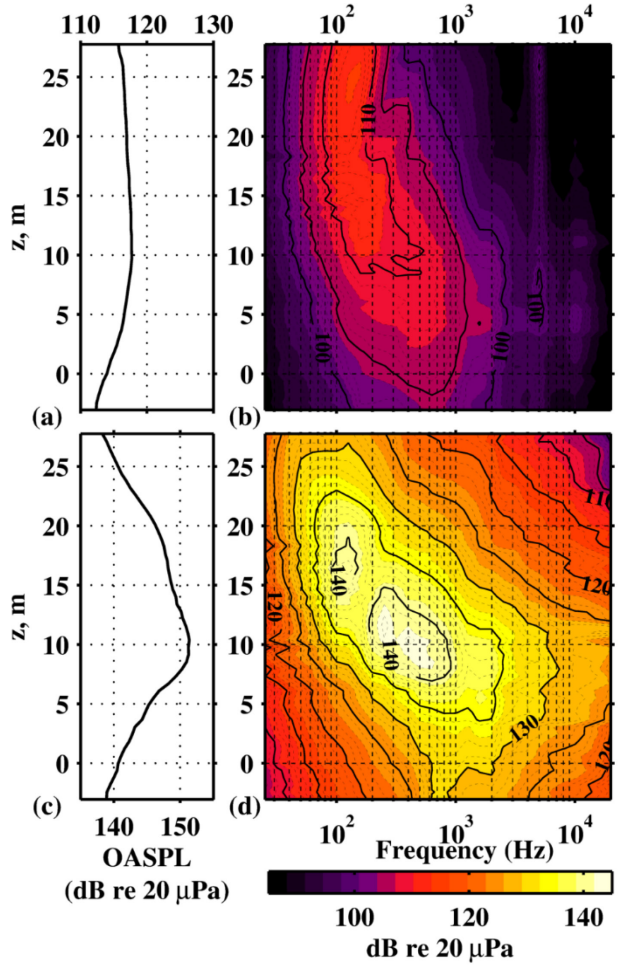

Fig. 3.2. Overall and one-third octave band sound pressure levels. Overall levels and one-third octave band spectra for each of the 50 ground-based microphones located 11.6 m to the sideline of a tactical aircraft when one engine was operated at (a-b) intermediate and (c-d) afterburner engine power.

3.3.2 Comparison to Similar Experiments in the Literature

The correlation and coherence analyses add further dimensionality to prior jet noise characterizations from this high-performance tactical aircraft. Previous investigations of a similar tactical jet noise dataset include near-field acoustical holography,[115, 116] vector intensity,[117] beamforming,[93] equivalent source modeling,[92, 118] and similarity spectra analyses.[91, 112] These studies have improved understanding of military jet noise environments and elucidated both similarities and differences with laboratory-scale jets. Because the jet nozzle exit conditions for

the full-scale engine are not available, a complete scaling with laboratory studies is not possible. However, some basic scalings can be performed that establish a regime for this experiment and allow for connections with laboratory-scale phenomena.

Three scalings that potentially allow for, at the very least, phenomenological comparisons with laboratory-scale jets include jet noise classification based on maximum radiation angle, scaling of peak Strouhal number in the maximum radiation direction, and geometric scaling based on nozzle diameter. First is the question of radiated overall directivity. As the convective Mach number of a heated jet transitions from subsonic to supersonic, the peak radiation angle shifts from 150° (re engine inlet) forward. For the intermediate engine condition here, the overall radiation angle is approximately 150°, suggesting the jet noise may be treated as being radiated from a convectively subsonic source. For the afterburner case, however, the maximum radiation angle is approximately 125°,[55] indicating a convective Mach number of approximately 1.7-1.8. Note that these classifications are strengthened by a similarity spectra analysis[91] of the same dataset. The analysis revealed a gradual transition between fine and large-scale similarity spectra with increasing angle for intermediate power and a much more abrupt transition for afterburner. These similarity spectral trends were consistent with those of Tam *et al*.[9] for convectively subsonic and supersonic jets.

Although the engine jet conditions are unavailable, the derived convective Mach number range exceeds prior scale-model engine tests. Greska[119] presented results from a laboratory jet that matched the operating conditions of the F404 engine, with a resulting far-field radiation angle of 130°. Baars *et al.*[120] described near-field correlation measurements of a heated supersonic jet that approximated the conditions of the F414 engine,[121] resulting in the maximum overall level radiated at 135°. Other jet experiments, not intended to match tactical jet engines, but with maximum

directivities in the 130-135° range were Krothapallli *et al*.[122] and Baars and Tinney.[123] The former experiment was with a highly heated jet with conditions similar to the scaled F404/F414 engine tests, whereas the latter was with an unheated, Mach 3.0 jet. Three laboratory-scale experiments with the convective Mach number required to produce a 125° peak far-field angle are noteworthy. Greska experimentally showed that the maximum directivity angle for supersonic jets shifted to 125° as temperature increased to beyond 1300K for a jet Mach number of 1.3 and 1000K for Mach 1.5 and Mach 1.8. The measurements of Seiner *et al.*[124] exceeded these jet velocities and temperatures, resulting in peak directivities at slightly lesser angles. Of particular relevance to this study, Viswanathan *et al.*[23] made near and far-field correlation measurements of a heated supersonic jet with convective Mach number 1.69. Both the studies of Viswanathan *et al.* [23] and Baars *et al.* [120] will be described further as part of the data analysis.

The other potential scalings are related to frequency and geometry. For the afterburner case, the peak frequencies along the maximum radiation angle number are between 125-250 Hz. Prior engine tests where the supersonic jet conditions were available—for the F404 engine by Greska[119] and an advanced tactical engine by Schlinker *et al*.[41]—the peak Strouhal number is approximately 0.15-0.3. This suggests a frequency-to-Strouhal number scaling of approximately $1.2 \cdot 10^{-3}$ Hz^{-1}. Regarding geometric scaling, Tam and Zaman[125] suggest nonround nozzles may be considered as a round nozzle with equivalent area. Consequently, an approach to geometric scaling would be to treat the current engine nozzle with a hydraulic diameter of 0.6 m.[116, 118] These scalings, of course, have considerable uncertainty. Consequently, figures in this paper will be presented in terms of dimensional length and frequency units; references to scaled units will be considered in the discussion as appropriate.

3.4 Analysis and Discussion

We first present a broadband analysis of full-scale jet correlation measurements using auto and cross correlation techniques in Section 3.2.1 to obtain temporal and spatial waveform characteristics. This provides a general overview of the spatial variation in the waveform features and associated correlation lengths. Because many features within jet noise are frequency-dependent, the correlation investigation is augmented by a coherence analysis in Section 3.2.2, which provides spatial scales of frequency-separated elements. The resulting field coherence maps provide estimates of the coherence lengths as functions of frequency and position for both engine conditions. Finally, because the connection between the field and source coherence is also of interest, equivalent source coherence measurements are obtained using the DAMAS-C beamforming algorithm and compared with the corresponding field coherence measurements.

3.4.1 Correlation Analysis

The broadband nature of turbulent mixing noise is studied most easily using time-domain correlation analyses.[2] Previous work on laboratory-scale data provides a backdrop against which these correlation analyses are compared to indicate both the similarities and differences that exist between lab-scale and full-scale jet noise.

3.4.1.1 Autocorrelation Measurements

Several previous laboratory studies have used features of pressure autocorrelation functions to argue for the existence of large-scale and fine-scale turbulent structures as distinct sources of jet mixing noise. Tam *et al.*[9] state two arguments to distinguish between the two sources. First, the width of the peak in the autocorrelation is considerably narrower to the sideline than in the aft direction. This argument was used by Kumar *et al.*[110] and by Tam *et al.*[9, 98] to indicate that

large-scale turbulent structures generated the noise at the aft angles and that the randomness at sideline angles is indicative of fine-scale structures. However, it has been shown[100] that the autocorrelation function width is strongly dependent on the spectral peak frequency and scaling of the temporal axis by peak frequency causes the gross differences in the width of the autocorrelation function to disappear. Thus, the autocorrelation function width is not intrinsically related to the nature of the jet noise field and a more careful analysis is required. The second argument by Tam *et al*.[9] is that the existence of negative loops (dips) in the autocorrelation at aft angles indicates the presence of partially correlated noise from the large-scale turbulent structures. Harker *et al.*[100] confirmed this to be true by demonstrating that the negative loops are present in the autocorrelation function obtained from the analytical similarity spectrum associated with the large-scale structures. A limited analysis of the autocorrelation of select waveforms indicated the presence of negative loops at downstream distances, similar to those seen in lab-scale cases.[9, 98, 110] However, there are features in the full-scale data that are not seen in the laboratory-scale cases.

Across the ground-based microphones in the vicinity of the aircraft, the autocorrelation functions show significant variation. As examples of the features seen at different locations, R_{xx} curves are shown in Fig. 3.3 for AB and microphones located at $z = 4$, 12, and 26 m along the ground array. The left column displays the correlation as a function of delay time, τ, similar to Fig. 14 in Tam *et al.,*[9] while those in the right column have been scaled by peak frequency: $\eta = \tau \cdot f_{\text{peak}}$. The initial positive peaks of the scaled autocorrelation functions have nearly the same width, but the widths of the Hilbert transform-based envelopes, $A_{xx}(\eta)$, shown as dashed lines, illustrate the different natures of the sound measured at these three locations. The envelope for the sideline location ($z = 4$ m) has a narrower width, due to the broad spectrum and small-amplitude ringing that may result from BBSAN, given the similarity with the "wriggles" observed for an aerospike

nozzle operated at off-design conditions by Kumar *et al.*[110] At z = 26 m, the single set of deep negative loops in R_{xx} broadens A_{xx}, matching the observations of Tam *et al.*[9] for radiation dominated by large-scale noise. However, in the region of maximum OASPL, at z = 12 m, there are two sets of negative loops, which results in a different shape for A_{xx} beyond $\eta > 1$. This is a feature that has not been reported for laboratory-scale jet noise studies. Overall, the differences in the autocorrelation functions in Fig. 3.3 imply that the noise signal characteristics vary at these three downstream distances.

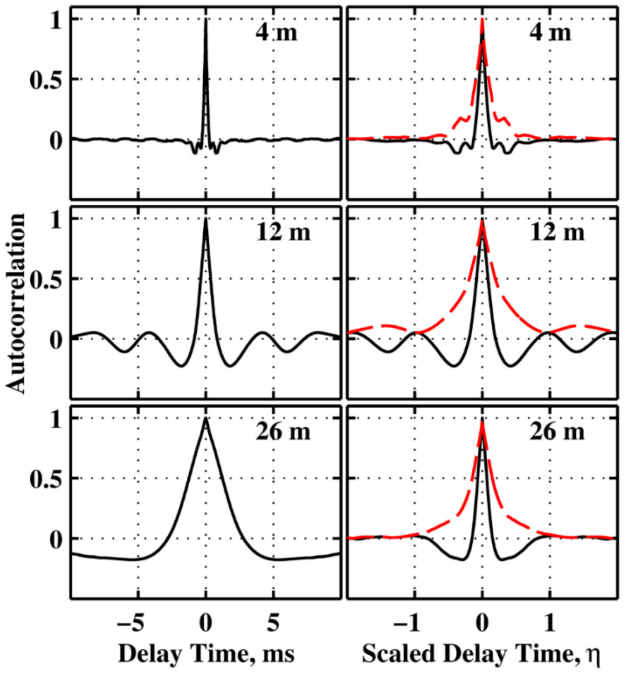

Fig. 3.3. Autocorrelation functions at different ground-based microphones for AB. The corresponding downstream distances are indicated on the individual frames. $R_{xx}(\tau)$ is shown on the left. The time-scaled versions, $R_{xx}(\eta)$, are on the right, in which the spatial variation in the peak frequency has been removed, and autocorrelation envelopes, $A_{xx}(\eta)$, are overlaid on each as dashed lines.

The presence of these same features in the autocorrelation functions and envelopes over the entire 30 m spatial aperture reveals distinct transition regions between the types of signals for both intermediate (Fig. 3.4) and afterburner (Fig. 3.5) engine conditions. At afterburner, in Fig. 3.5, for locations with $z < 9$ m, there is only low-level ringing in the autocorrelation outside the

peak region. When viewed in the time-scaled envelopes, the ringing corresponds to appreciable correlation, particularly for measurements in the sideline region. For z = 9–13 m, the second set of negative loops leads to significant correlation over much greater values of η. It is important to note that this region corresponds to the maximum OASPL measured across the array, as seen in Fig 3.2(c), but slightly upstream of the dominant dual peak region in Fig. 3.2(d). For $z > 13$ m, the single set of negative loops is the only feature of significance outside the peak region. From the autocorrelation envelopes for the afterburner case, it can be seen that once the peak frequency dependence is removed from the scaling, the relative temporal length of the negative loops does not increase significantly with downstream distance, suggesting an invariant nature to the noise. Note that similar features are shown for military power in Ref. [97], i.e., it is not solely an afterburner phenomenon.

To investigate if these autocorrelation characteristics are unique to high engine powers, they can be compared to the analysis for intermediate power that was shown in Fig. 3.4. The map of $R_{xx}(\tau)$ shows the lack of negative loops to the sideline with a gradual increase in depth in the downstream direction, but other distinguishing features are easier to see in $A_{xx}(\eta)$, which is shown on a decibel scale. There is less ringing for z = 7 m at intermediate than at afterburner, which is consistent with the hypothesis that the ringing at afterburner is due to BBSAN. For 7 m $< z <$ 11 m in Fig. 3.4, there is perhaps evidence of the double negative loops, albeit at levels about 10 dB down from the peaks. Farther downstream, the relative width of the envelope continues to increase indicating that the relative temporal width of the single negative loops increases with distance downstream. This increase could be related to end-fire effects because of the large spatial aperture being considered. Thus, the fact that this broadening of the envelope is not observed at afterburner

is even more meaningful: the signals received at the farthest downstream distances at afterburner have less evidence of the large-scale turbulent structures than those at z between 13 and 20 m.

To summarize the results of the autocorrelation analysis, the current full-scale-results show both the similarities and differences with laboratory-scale jet noise. The presence of negative loops downstream, which are more quantifiable using envelope functions, helps to distinguish between large and fine-scale turbulent mixing noise and ringing in the upstream direction may be indicative of BBSAN at both scales. However, in between these two spatial regions, the double loops are unique to the full-scale jet noise case and although present at both engine conditions, they are significantly stronger at high engine powers.

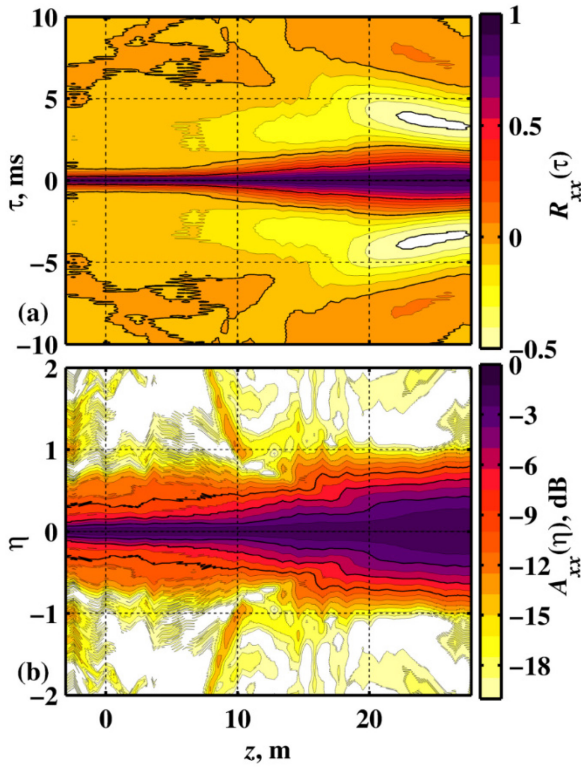

Fig. 3.4. Autocorrelation function as a function of downstream distance, INTER. (a) $R_{xx}(\tau)$ at ground-based array for intermediate engine condition. (b) The corresponding envelope functions, $A_{xx}(\eta)$ shown on a decibel scale

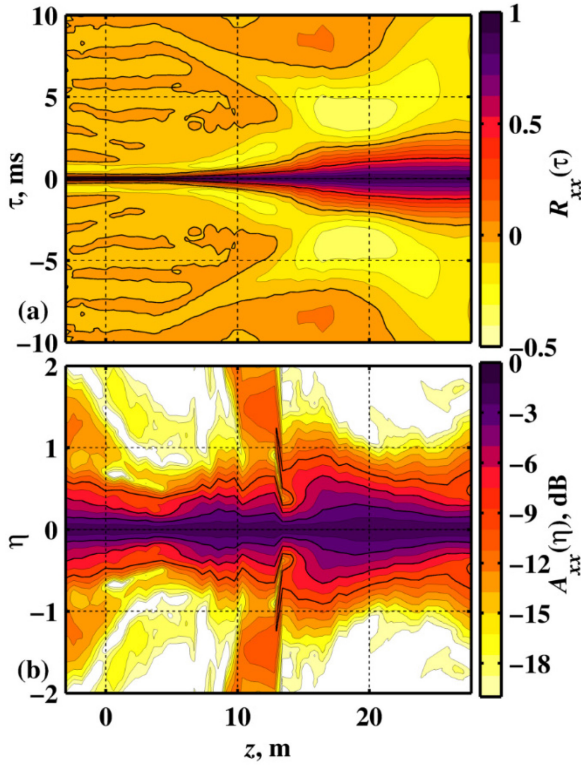

Fig. 3.5. Autocorrelation function as a function of downstream distance, AB. Similar to Fig. 3.4 but at afterburner engine condition.

3.4.1.2 Cross-correlation Analysis

Some of the first studies to look at the spatial distribution of acoustic pressure cross correlations were Clarkson's[103] and Maestrello's[106] work with subsonic jets. Clarkson explored the differences in the correlation for the hydrodynamic near field and the geometric near and far fields. Maestrello produced two-point space-time correlation maps (correlograms) over a distant sphere to illustrate the usefulness of acoustic pressure correlations in quantifying the broadband features of the jet noise. Maestrello's goal was to use the phase-preserving cross correlation functions as an inverse problem for identifying source characteristics. Although his conclusions were not universally accepted,[107] Maestrello concluded that the lack of correlation at angles to the side of the nozzle exit were indicative of incoherent sources and that larger regions of high cross

correlation peaks for angles closer to the jet axis were indicative of a more coherent source downstream than near the nozzle exit.

The cross correlation of the acoustic pressure field has been used in recent years to show support for the two-source model of jet noise proposed by Tam *et al*.[109] based on the presence of uncorrelated fine-scale turbulent structures radiating to the sideline and partially correlated large-scale turbulent structures responsible for the Mach wave radiation in supersonic jets. The angular variation in cross correlations for a wide variety of subsonic and supersonic laboratory jets have confirmed what Maestrello originally observed: for angles close to the jet axis, there is relatively high correlation. Conversely, for sideline angles, the peak cross correlation values drop off rapidly.[8, 9, 23, 75, 99] A study by Ahuja *et al*.[75] has shown the same trends for a nozzle of a variety of shapes, including a rectangular nozzle with an aspect ratio of 8. These overall features have appeared to be relatively independent of the jet velocity for measurements in the acoustic far field.[23]

Analysis of the cross correlation functions from the 50 ground-based microphones provides the unique opportunity to examine if the noise in the vicinity of the aircraft exhibits similar temporal and spatial evolution as laboratory jets or, if like autocorrelation analysis, there are significant differences. Examples of the normalized cross correlation coefficient, R_{xy}, are displayed for afterburner in Fig. 3.6 for reference microphones at z = 4, 12, and 26 m and the closest four microphones on either side. There is essentially no correlation (R_{xy} < 0.1) between the microphone at z = 4 m and neighboring microphones that are 0.6 m away. At z = 12 m, which is within the maximum OASPL region, the peaks in the cross correlation fall off more gradually and exhibit a second set of negative loops, similar to the autocorrelation. At z = 26 m, the maximum values of cross correlation are significantly greater, and the cross correlation functions

are broader and contain a single negative loop, similar to the findings of previous studies. As with the autocorrelation, some of the broadening in the cross correlation as downstream distance increases is caused by the decreasing peak frequency. However, because the cross correlation involves two signals, the most meaningful frequency scaling to correct for the change in peak frequency has not yet been determined.

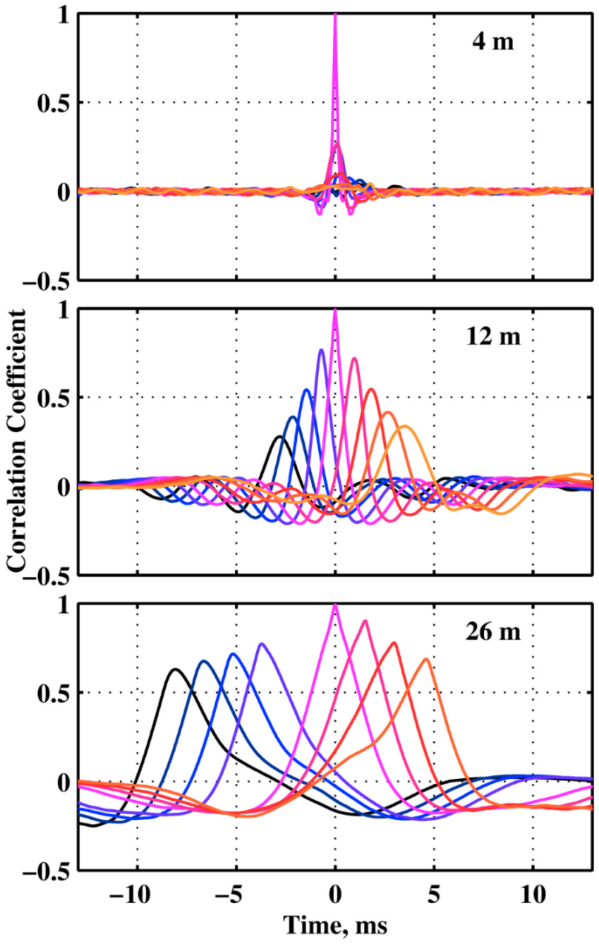

Fig. 3.6. Autocorrelation and neighboring cross-correlation functions at AB. Reference microphones along the ground-based array are located at downstream distances of 4, 12, 26 m. Microphone spacing is 0.6 m (2 ft), except for one 1.2 m (4 ft) gap (seen in the bottom plot).

The spatiotemporal interdependence between the recorded signals can be seen in correlograms that have been calculated across the entire array, relative to the same three reference

microphones. The correlograms are shown in Fig. 3.7 for intermediate power and Fig. 3.8 for afterburner engine condition. As with the autocorrelation, the use of the Hilbert transform-based envelopes of the cross correlation allows the correlograms to be plotted on a logarithmic scale, facilitating identification of low level features. At intermediate (Fig. 3.7), the magnitude and extent of the region of large correlation in $A_{xy}(\tau)$ increases when the reference microphone is located farther downstream. However, for all three reference locations (z_{ref} = 4, 12 and 26 m), there is appreciable correlation across the array, indicating partially correlated noise exists across the entire 30 m aperture. This is likely due to the large spatial region over which the large-scale turbulent mixing noise contributes significantly to the signals, as shown via spectral decomposition in Ref. [91]. The turning points with zero slope in Fig. 3.7 mark the region at which acoustic energy is traveling perpendicular to the array and the transition between upstream and downstream radiation. For the intermediate case, this turning point occurs between z = 0 and 5 m in all three correlograms, suggesting the overall source location is close to the nozzle exit (< 8 D_j, where D_j is the jet nozzle diameter length) . In addition, the slope of the correlation functions at downstream locations is relatively constant, indicative of planar wavefronts crossing the array with an apparent directivity of 145 -150°. This directivity is consistent with a heated, convectively subsonic jet.[41] Constant downstream slope for a space-time correlogram across a linear array was used previously to calculate phase speed across a linear array located near an unheated jet.[120]

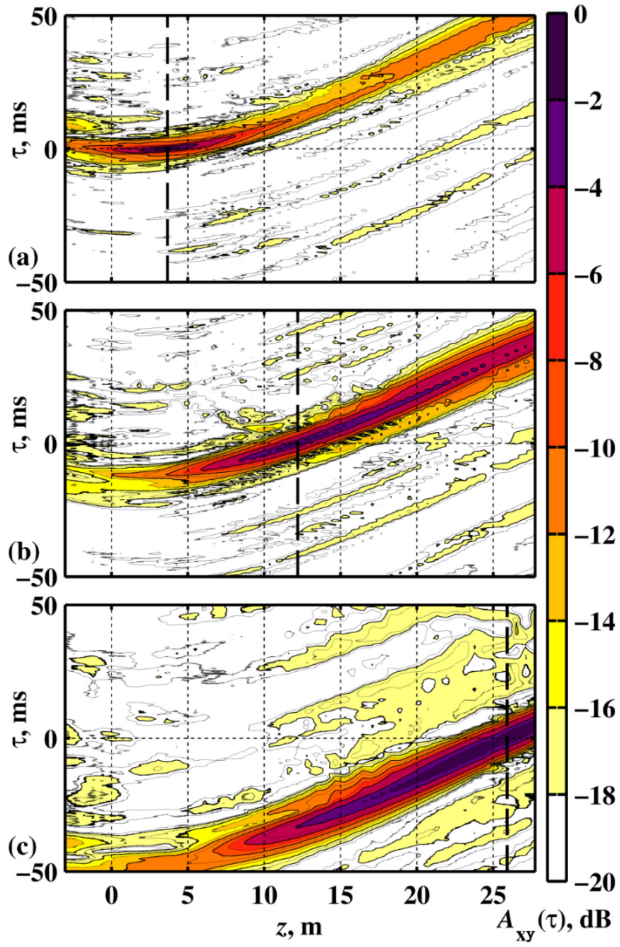

Fig. 3.7. Envelope-based cross correlograms, INTER. Envelopes of the cross correlation, $A_{xy}(\tau)$, between a single mic (dashed black line) and the other 49 microphones along the ground based array at intermediate power.

The correlograms for the afterburner in Fig. 3.8 vary greatly from those seen in the intermediate case. The high correlation region depends greatly on the location of the reference microphone, z_{ref}. When z_{ref} = 4 m [Fig. 3.8(a)], there is little cross correlation with the other locations and a relatively compact turning point (3 m < z < 5 m), both of which are indicative of uncorrelated noise dominating the noise radiation in this region. The turning points for downstream reference microphones are more extended, 3 m < z < 7 m, and the slope of the region of large correlation is not constant but continues to increase, both of which could be indicative of the extended nature of the source. Note that changing cross correlogram slopes have been previously

used within the hydrodynamic near field to estimate the decay rate of convective velocities along the shear layer.[120]

Additional correlogram features are present for downstream reference microphones at afterburner that are not observed at the sideline or at any locations in the intermediate case or in laboratory studies. When z_{ref} = 12 m, within the region of maximum OASPL between 10-15 m [see Fig. 3.8(b)], there is essentially no correlation with the upstream locations (z < 5 m), and a relatively large aperture of high correlation in the downstream direction. In addition, there are striations in the cross correlations near z_{ref} = 12 m and at the farthest downstream locations. This splitting of the region of high correlation is seen more clearly in Fig. 3.8(c). The signals recorded in the region of maximum OASPL have significant correlation with the signal at z_{ref} = 26 m at two different time delays. The slopes of the two curves in the array correspond to two sets of waves with discretely different phase speeds propagating through the array, resulting in different far-field directivities. This dual directivity has been noted in other studies of similar tactical data.[13, 91, 117] Tam and Parrish[113] have postulated that one of these sources is associated with indirect combustion noise and the other with large-scale turbulent mixing noise. However, it may be significant to note that, in the correlograms, both branches appear to have turning points at z~5 m suggesting that the apparent overall origins of both the noise sources are at least that far downstream.

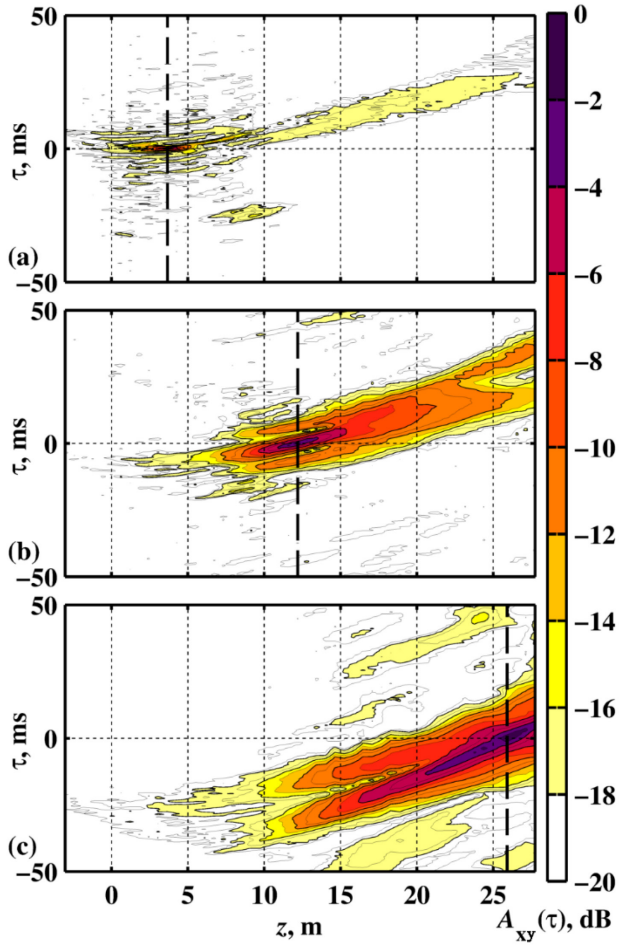

Fig. 3.8. Envelope-based cross correlograms, AB. ***Similar to Fig. 3.7 but at afterburner.***

The differences between intermediate and afterburner are also evident in the spatial distribution of the maximum cross correlation coefficients between all 50 microphones. To facilitate discussing the features of the peak correlation values, correlation lengths are defined as the distances over which $R_{xy} > 0.5$, shown by the bold contour line in Fig. 3.9. Considering intermediate power in Fig. 3.9(a), the small correlation lengths at sideline locations indicate the presence of relatively uncorrelated noise, with correlation increasing in the downstream direction. This behavior is phenomenologically similar to laboratory-scale jets,[9, 23] but acoustical cross-correlation lengths appear not to have been quantified for laboratory jets previously. For afterburner, however, the spatial distribution of the peaks of the correlation functions has

somewhat different features. First, for $z_{\mathrm{ref}} < 7$ m, the correlation lengths are less than the microphone spacing of 0.6 m, and are overall shorter than for intermediate, even beyond $z_{\mathrm{ref}} = 20$ m, where the peak frequency for afterburner begins to dip below intermediate. Viswanathan *et al*.[23] noted a reduction in peak correlation by nearly 50% as Mach number increased from a convective Mach number of 1.05 to 1.69 for highly heated jets, so these results are not surprising. However, the cause for the dip in correlation length at around $z_{\mathrm{ref}} = 22$ m for Fig. 3.9 is undetermined. It corresponds to a relatively rapid change in OASPL in that region, so perhaps could represent a transition away from the dominant Mach wave radiation region to other large-scale radiation phenomena that dominate beyond 25 m downstream. However, corroborative experiments are required to verify this hypothesis.

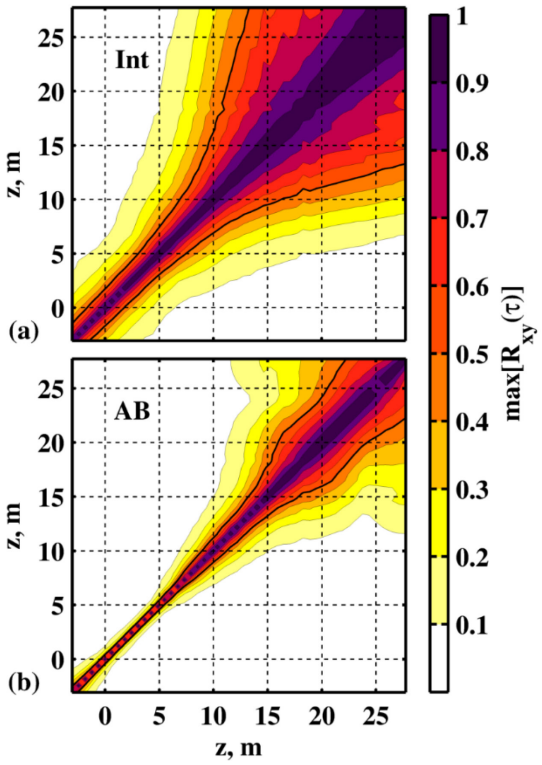

Fig. 3.9. Maximum cross correlation coefficients. The maximum cross-correlation coefficients are obtained from ground-based array measurements between all 50 microphones for (a) intermediate and (b) afterburner conditions.

3.4.2 Coherence Analysis

Coherence is useful to characterize the directivity and propagation of jet noise data based on frequency-dependent characteristics and thereby directly complements the correlation analyses. The coherence across the linear array, located in the geometric near field of the aircraft, is used to explore the properties of the sound field. In addition, a cross beamforming technique yields an estimate of the coherence properties of an equivalent one-dimensional source located along the jet centerline. A comparison between the field coherence and the estimated source coherence provides additional insight of the jet noise dependent on the engine condition.

3.4.2.1 Field Coherence

Previous coherence studies of laboratory scale jets provide a background against which the full-scale coherence can be evaluated. For example, Baars *et al.*[120] calculated the coherence spectra at multiple reference locations for a heated, supersonic jet. They showed high spatial coherence across a linear array in the hydrodynamic near field, with coherence lengths, L_{γ^2}, up to $7D_j$, particularly at frequencies associated with Mach wave radiation. Work by Viswanathan *et al.*[23] showed both the azimuthal and axial variation of coherence as a function of frequency for heated subsonic and supersonic jet noise conditions. While sideline coherence lengths were small, they found a large coherent region about two potential core lengths downstream that was about $15D_j$ in length and which demonstrated high azimuthal coherence. Further work done by Ahuja *et al.*[75] showed the coherence of subsonic and supersonic unheated jets in the far field. They found, similar to Viswanathan and similar correlation studies, that for both subsonic and supersonic cases there are high degrees of coherence in the downstream direction and incoherent noise in the sideline and

upstream direction at most frequencies. However, they also observed non-negligible coherence between sideline and downstream measurements for $\mathrm{St} < 0.1$, where St is the Strouhal number.

In this study, coherence analyses of intermediate and afterburner power conditions are presented, which show both similarities and differences with the lab-scale measurements previously described. In addition, coherence lengths show effects of different mixing noise contributions in the measurements as the fine-scale and large-scale turbulent mixing noise have short and long coherence lengths, respectively. These coherence length estimates near the aircraft across downstream distance, frequency, and engine condition can enhance jet noise prediction models and design of measurement arrays.

Coherence calculations have been performed for the ground-based array as described in Section 3.2 and are shown at OTO band center frequencies for reference locations $z_{\mathrm{ref}} = 4$, 12, and 26 m in Fig. 3.10 for intermediate power and Fig. 3.11 for afterburner power. For both engine conditions, the coherence spectra for $z_{\mathrm{ref}} = 4$ m [Figs. 3.10(a) and 3.11(a)] is highly symmetric spatially in the upstream and downstream directions, with the exception of frequencies below 50 Hz. This low-frequency observation agrees with the findings of Baars *et al.*[120] for a laboratory scale-engine experiment. When the reference microphone is placed in the region of maximum OASPL, (located at about 10-25 m at INTER and 10 m at AB), the coherence transitions dramatically to be highly coherent at most frequencies below 400 Hz ($\mathrm{St} < \sim 0.5$) in the downstream direction, although the region of high coherence does not extend in the upstream direction. Thus, for example, the 100 Hz coherence lengths at intermediate condition in Fig. 3.10(b) extend up to 15 m in the downstream direction, but only about 5 m in the upstream direction. This highly self-coherent region, ascribed to the large-scale radiation features, has been observed by Baars *et al.*[120] for a supersonic heated jet and by Viswanathan *et al.*[23] for both subsonic

and supersonic heated jets. However, this large downstream coherence region is most dominant for frequencies below 400 Hz, as, similar to sideline measurements, the coherence is much more spatially symmetric at higher frequencies. The afterburner case shares similar general features with the intermediate case, except that L_{γ^2} values progressively decrease as the engine power increases. The distinguishing features in the spatial dependence of coherence length across engine conditions are few: the onset of high L_{γ^2} values at afterburner occurs slightly upstream compared to the intermediate case—consistent with the idea that large-scale structure radiation shifts upstream with the increase in engine power (convective Mach number),[24] and at $z_{\mathrm{ref}} = 26$ m [Fig 3.11(c)], the coherence at 100 Hz is markedly low at afterburner for unknown reasons.

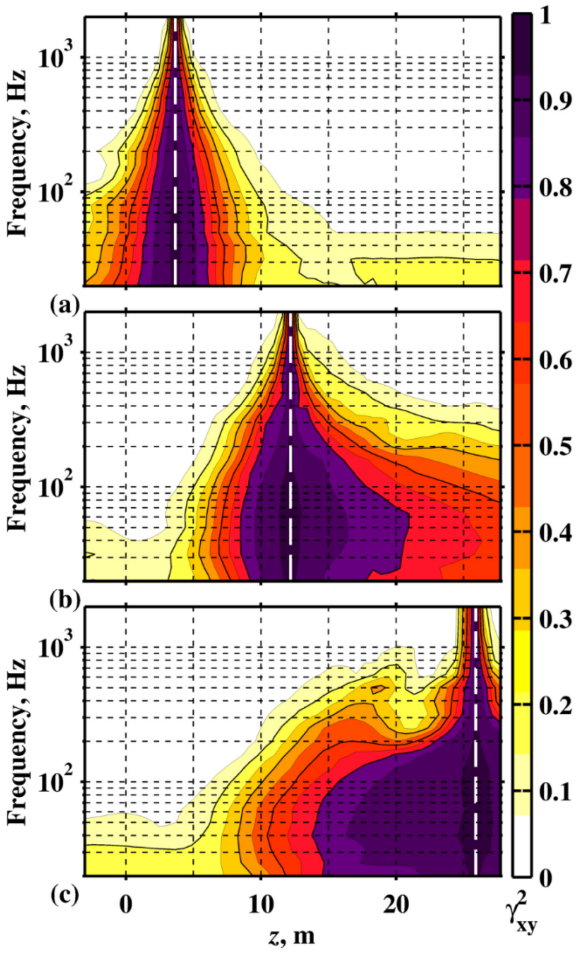

Fig. 3.10. Coherence spectra for select references at INTER. Coherence spectra calculated across the ground-based array for intermediate engine condition relative to three reference microphones at (a) 4 m, (b) 12 m, (c) 26 m. Solid contour lines are incremented by 0.2.

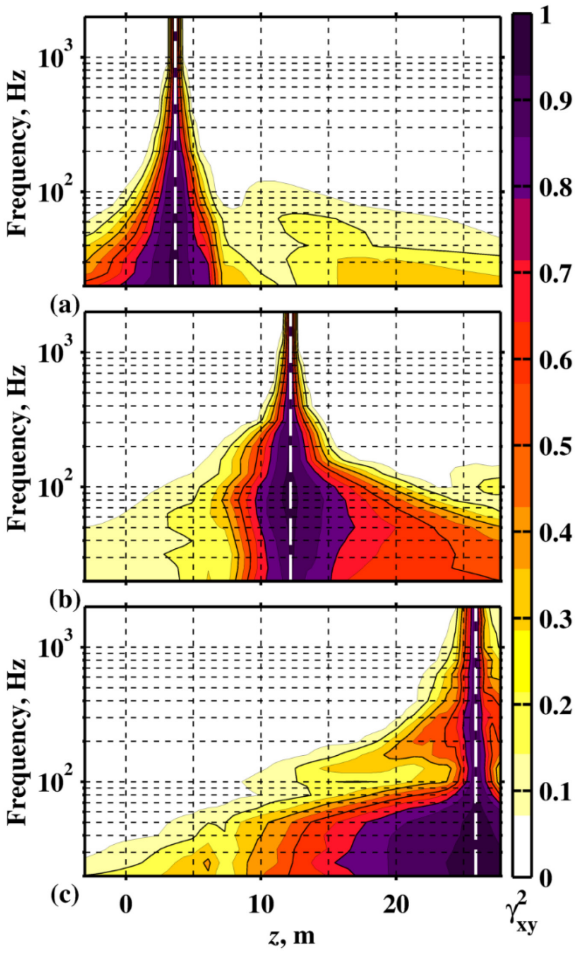

Fig. 3.11. Coherence values across the ground-based array for select references at AB. Similar to Fig. 3.10, except at afterburner.

The spatial coherence characteristics shown in Fig. 3.10 and Fig. 3.11can be summarized using coherence lengths, which quantify the spatial and frequency-dependent variation in the coherence of the sound field. These are shown in Fig. 3.12, with $L_{\gamma^2}^{-}$ representing the coherence lengths in the upstream direction relative to the reference position. Due to the way the coherence length is calculated, good estimates of upstream coherence lengths are not available when the array does not extend sufficiently far to capture the location at which $\gamma^2(f) \leq 0.5$. These regions are indicated by gray in the figure. As seen in the previous figures, coherence lengths generally decrease with increasing engine condition, and they are generally largest in the downstream

direction where large-scale structure turbulent mixing noise dominates. The coherence lengths also highlight less obvious features in sound field. For example, for both engine conditions, the variation in $L_{\gamma^2}^-$ is seen to be very pronounced for frequencies below 200 Hz and changes rapidly for $z_{\mathrm{ref}} > 10$ m. This corresponds to the regions where the maximum overall levels occur, as shown in Fig. 3.2, and where the spectral shapes are well described solely by the large-scale turbulent structure similarity spectrum.[91] In the afterburner case, a small increase in $L_{\gamma^2}^-$ values is visible, between $125\ \mathrm{Hz} < f < 400\ \mathrm{Hz}$ and at $z_{\mathrm{ref}} = 11 - 12$ m. Considering spectral levels in Fig. 3.2, this corresponds to the dominant spectral features across the array between $200 < f < 500$ Hz. Thus, the coherence lengths of the primary radiation at these frequencies are significant, although much lower in comparison with coherence lengths farther downstream [e.g. $L_{\gamma^2}^-(125\ \mathrm{Hz})$ at $z_{ref} = 17$ m] In addition, a transition region exists where $L_{\gamma^2}^-$ values indicate a dip in coherence lengths. At both engine powers, this dip occurs for $40\ \mathrm{Hz} < f < 125$ Hz and at z_{ref}~7-8 m, dependent on frequency. It was previously shown that a combination of the fine-scale and large-scale similarity spectra is necessary to represent the measured spectra in this region.[91] In addition, the frequencies at which the dip in coherence length occurs coincides with the locations where the two spectra are equal contributors to the spectral levels.

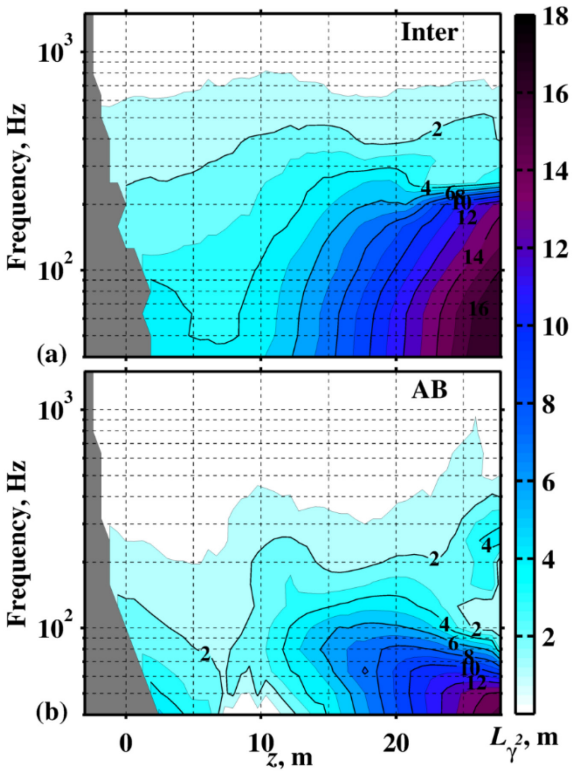

Fig. 3.12. Spatial coherence lengths. Coherence lengths, $L_{\gamma^2}^{-}$, for (a) intermediate and (b) afterburner power. Contour colors are spaced at 1 m increments with solid lines at 2 m increments. Grayed out portions are areas where the array aperture was insufficient to calculate the coherence length.

To further investigate the spatial variation in coherence lengths near the peak frequency, the coherence at two particular frequencies is examined at afterburner condition between all microphones on the ground-based array in Fig. 3.13. Coherence plots are oriented such that self-coherence (nominally unity) occurs along the diagonal, and coherence between two distinct locations can be found along the off-diagonal elements. Shown alongside the coherence maps are the corresponding sound pressure levels across the array at each frequency. The largest levels generally correspond to locations with the longest coherence lengths. However, this does not seem to be the case in the upstream direction. At 100 Hz, a narrower spatial extent of significant correlation is located at $z = 6 - 7$ m, separating larger coherence lengths in the far downstream and the upstream direction. This is also present at 200 Hz, although more difficult to observe. In

this region, the SPL increases with z, but the coherence lengths unexpectedly decrease to a minimum value. The minimum coherence levels may result from the interference of competing independent sources. Previous work showed that the spectral shapes along the ground-based array change from matching the general features of the fine-scale similarity spectrum to those of the large-scale similarity spectrum over a transition (or combination) region that occurs over $z = 5 - 7$ m for frequencies below 400 Hz.[91] The presence of similar levels of the independent fine-scale and large-scale turbulent mixing noise would account for the drop in coherence in this transition region. Thus, the independent signals would be responsible for increasing overall levels and yet decreasing coherence lengths in this region. While some have recently discounted the two-source model of jet noise[8, 9] in favor of continuous source models, such as a wavepacket ansatz, the similarity spectra fit performed independently nevertheless explains the otherwise discrepant effects seen here in the coherence at the sideline.

In addition to the large spatial coherence related to the Mach-wave radiation, there is a secondary region of large spatial coherence in the far downstream region of the array ($z > 20$ m), visible in Figs. 3.13(b) and 3.13(d). At 100 Hz, the spatial extend of this region extends up to 15 m, although coherence levels are lower ($0.1 < \gamma^2 < 0.4$) compared with the 200 Hz measurements ($0.1 < \gamma^2 < 0.7$) where the spatial extent is smaller (about 5 m). Interestingly, this region is also separated from the coherence associated with Mach wave radiation by a region of low spatial coherence, similar to the effect seen at $z =$ 6-7 m, suggesting an independent signal radiating in the far downstream direction. Tam *et al.* [113] argued that farther aft of the Mach wave radiation, there is evidence in the spectral data of radiation from an additional source in the afterburner condition for these frequencies. This needs to be the subject of further study. There is also evidence related to the dual-spectral peaks at this engine condition seen in Fig. 3.13(d) as an additional

narrowing of the correlation lengths for $15\ \text{m} < z < 20\ \text{m}$. The previous cross-correlation analysis showed evidence corresponding to two radiating sources with different directivities at afterburner. This is related to the dual spectral peaks that are seen in Fig. 3.2 and that are just visible in the levels in Fig. 3.13(c). While these two features are relatively self-coherent, coherence between the two peaks is only minimally significant. These radiators may thus be independent and associated with two incoherent sources. The coherence relating these features is explored in greater detail through holography analyses in Ref. [13].

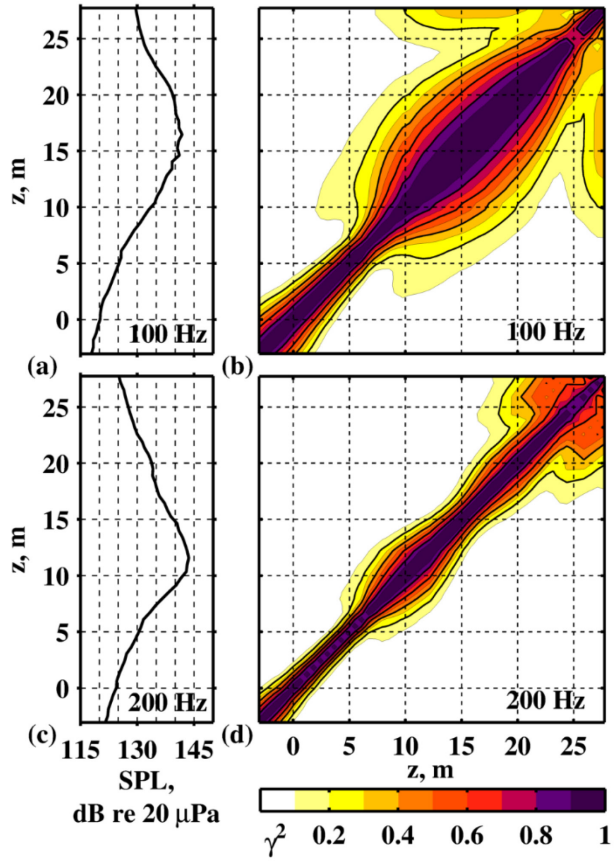

Fig. 3.13. Spatial coherence for select one-third octave band center frequencies at AB. Sound pressure measurements and corresponding coherence values across the ground-based array as a function of position at afterburner power for (a-b) 100 Hz and (c-d) 200 Hz.

3.4.2.2 Source Coherence Analysis

The analyses thus far have characterized the correlation and coherence properties of the acoustic field, which provides insights about the nature of the source. However, source-related characteristics can be obtained more directly from pressure data, even in the absence of flow information. For example, Baars *et al.*[120] used a linear microphone array located within the hydrodynamic near field of their F414-simulated jet to show a significant decrease in the convective (phase) speeds between $11 - 20\ D_j$ downstream of the nozzle exit, which they attributed to the decay of large-scale turbulent structures. Others have shown direct correlation between the flow and acoustic field. For example, Papamoschou *et al.*[16] found significant correlation between beamformed far-field acoustic pressure and jet shear layer optical deflectometry measurements in the mixing region and outside the hydrodynamic layer. Panda *et al*.[25] correlated far-field acoustical pressure with jet density and velocity measurements for subsonic and supersonic unheated jets at laboratory-scale. They found that correlation between density and velocity parameters was greatest in the downstream radiation, corresponding to large coherent structures.

The prior studies show direct links between the correlation properties of the radiated acoustic field and the source. Here, in the absence of flow data, the coherence properties of the source are obtained by beamforming the ground-array pressure measurements to the jet centerline. Because the DAMAS-C algorithm used (see Section 3.2) makes no assumptions on the degree of source correlation, source coherence properties can be calculated as part of the analysis. The source coherence maps are shown in Fig. 3.14 for intermediate power and Fig. 3.15 for afterburner at 100 and 200 Hz, with the beamformed source levels plotted alongside. Coherence values are only shown for estimated source amplitudes within 12 dB of the maximum reconstructed level. The diagonal elements of the coherence maps represent the self-coherence at each reconstruction

location, which by definition is unity. The off-diagonal elements, $\gamma^2_{z_1 z_2}$, represent the coherence between equivalent sources located at positions z_1 and z_2 along the jet centerline.

There are a number of noteworthy features in the source coherence results in Figs. 3.14 and 3.15. First, generally speaking, the calculated source coherence contracts with increasing frequency as well, similar to the trends seen in the field measurements. At 100 Hz, the spatial aperture of significant coherence is particularly large at both engine conditions, with source coherence lengths ($\gamma^2 > 0.5$) that span 5-6 m (8-10 D_j) for the afterburner case within the peak source region. This lends merit to efforts to produce self-coherent, e.g. wavepacket, models to characterize the radiation in the large-scale radiation regions. Second, the dual radiation lobe for afterburner at 200 Hz that produced two coherent regions in Fig. 3.14 has resulted in a single broad source region with maximum coherence in the 5- 9 m range. Recent holography source reconstructions for the current aircraft have shown that the dual radiation lobe in the field collapses to a single source region, but which extends over multiple axial coherence lengths.[126]

A final feature of note in the beamforming source coherence maps in Figs. 3.14 and 3.15 is the fact that for both engine conditions, the region of maximum coherence is downstream of the maximum amplitude, with the difference being greater for intermediate than afterburner. This could be possibly related to the laboratory-scale findings of Viswanathan *et al.*,[23] who showed that for their test with convective Mach number 1.69 (thus approximating afterburner here) the radiation far downstream was most correlated with near-field measurements between 13-31 D_j. Jordan and Colonius[2] later countered these conclusions, suggesting that tracing their results back to the centerline results in a coherent source region that was both farther upstream and smaller. The conflicting views merit a further look. In the Viswanathan *et al.* test, the peak overall directivity of the jet was approximately 125° and the region of maximum correlation was in the

135°-150° range. Although correlation is a broadband quantity, the tie between the aft angles and the downstream location suggests that the high correlation is due to low frequencies, i.e. $\mathrm{St} < 0.1$ that have downstream source origins relative to the overall dominant radiation region. However, ray-tracing their results back to the centerline would, as Jordan and Colonius pointed out, contract their results.

For the results here, we recall that 100-200 Hz is in the peak-frequency range of the spectrum in the maximum radiation direction for both engine conditions. At afterburner, these frequencies are believed to fall in the St~0.15-0.3 range, not the low frequencies that Viswanathan *et al.* were likely considering. Through ray tracing, the maximum directivity angles can be used to relate the levels at the ground array and the source, but they can also be used to show that the maximum coherence at a given frequency does, in fact, appear downstream of the maximum source level. These results, and the fact that the difference is greater for intermediate than for afterburner, can be explained with a two-source model of jet noise—a relatively compact, uncorrelated source region and an extended, correlated source region, like the fine and large-scale structures described by Tam *et al*.[9] The field analyses already have distinguished between fine and large-scale behavior, showing relatively uncorrelated noise to the sideline and correlated noise downstream. For each frequency, however, the source regions will overlap, thus producing a maximum level that may result upstream of the maximum coherence, which is dominated by the extended source producing the downstream radiation. The fact that the spatial difference is greater for intermediate than afterburner would then be attributed to the fact that the fine and large-scale contributions are more equal for intermediate than for afterburner, which was shown previously through a similarity spectra analysis.[91]

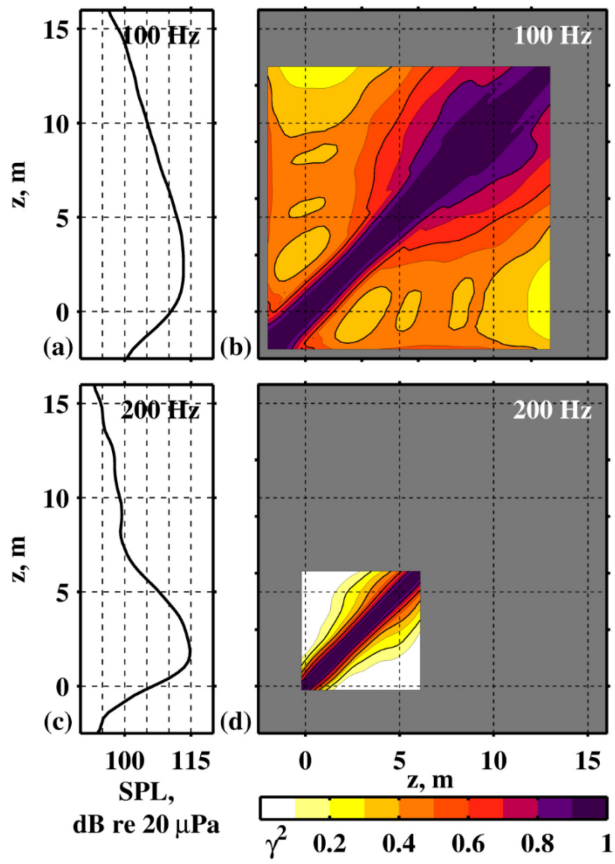

Fig. 3.14. Equivalent Source Coherence from DAMAS-C at INTER. The beamforming levels and corresponding coherence of the equivalent sources reconstructed by DAMAS-C for intermediate power at (a-b) 100 Hz and (c-d) 200 Hz. The horizontal and vertical axes are in meters, and the color represents coherence level, incremented at intervals of 0.1. Grayed out regions represent regions not displayed of the coherence where the maximum corresponding source levels (along the diagonal) were below 12 dB from the peak level.

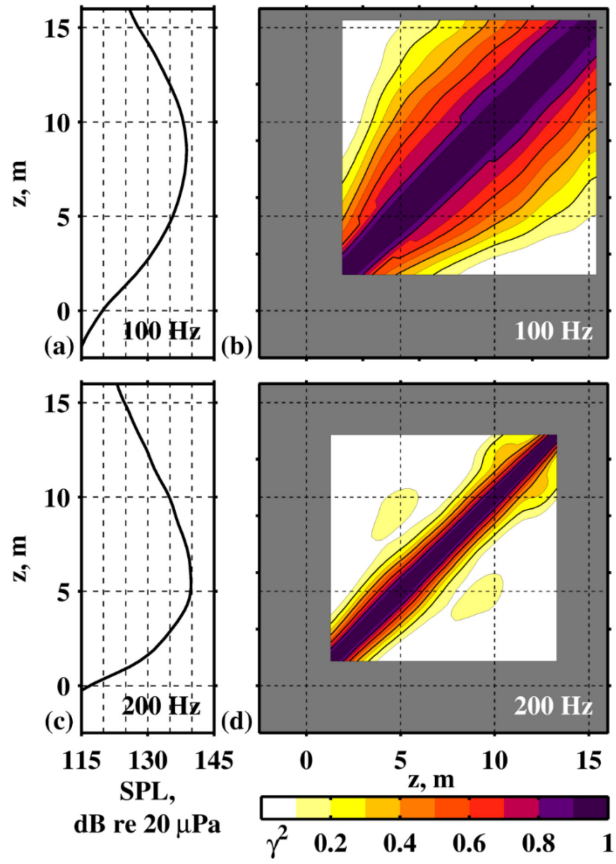

Fig. 3.15. Equivalent Source Coherence from DAMAS-C. Similar to Fig.3.14, except at afterburner.

3.5 Conclusion

A detailed time-waveform analysis of jet noise from a high-performance military aircraft has been completed. Correlation and coherence analyses have been presented from ground-array data collected in the vicinity of a tethered tactical aircraft with a single engine operated at intermediate and afterburner engine conditions. Comparison of the combined analyses with previously published studies have confirmed that many of the basic properties of laboratory jets are phenomenologically the same as those observed for noise from the current study. All the analyses indicate that the noise radiated at intermediate power seems to behave largely like a

heated, convectively subsonic jet with uncorrelated, fine-scale turbulent mixing noise to the sideline and with a smooth transition to more correlated, large-scale mixing noise downstream. However, for the afterburner jet, the analyses contain features that have not been observed for laboratory-scale jets.

The fundamental differences between the correlation functions of high-power full-scale and convectively supersonic laboratory-scale jets appear in the region of maximum overall sound pressure level. Autocorrelation functions reveal a secondary set of negative loops in this region, whereas laboratory-scale jets have only shown no loops to indicate fine-scale noise or a single set of loops to indicate noise associated with large-scale structures. In the cross correlation analyses, the dominant features in the correlograms appear to split around and downstream of the dominant radiation direction, thus corresponding to multiple phase-speeds across the array. Both analyses are indicative of multiple, mutually incoherent radiating sources with distinct directivity patterns that contribute to the sound radiation in the region of maximum overall level, resulting in dual-peaked spectral shapes and dual directivity lobes.

Two complementary coherence studies have also been presented. First, the field coherence spectra and corresponding coherence lengths found at intermediate and afterburner exhibit properties similar to those observed for laboratory-scale jets, with a reduction in coherence length at frequencies where there are believed to be nearly equal contributions from fine and large-scale structures.[91] For the afterburner case, however, there are additional increases and reductions in coherence length in the downstream direction, especially around 200 Hz, that appear to indicate multiple mutually incoherent sources. Second, one-dimensional, equivalent source coherence properties at the jet centerline have been developed from the DAMAS-C beamforming algorithm. It has been shown for both engine conditions that the maximum source coherence occurs

downstream of the maximum source level, which indicates that, as observed across the measurement array, the maximum source level region is comprised of both uncorrelated and correlated sources and that the correlated source dominates farther downstream.

In conclusion, the cumulative results have provided a deeper understanding of jet noise characteristics for a high-performance military aircraft and provided connections to phenomena shown in the literature. The differences seen for the full-scale case may motivate further laboratory and computational investigations into understanding the physical mechanisms that result in these differences. Matching the coherence and correlation properties of the field, in addition to spectral levels, will result in more complete jet noise models and possibly point toward efficient noise reduction strategies.

Chapter 4

Phased-array Measurements of Full-scale Military Jet Noise

4.1 Introduction

4.1.1 Background

Phased-array techniques, e.g., beamforming, bring a unique perspective to jet-noise-source characterizations. While computational fluid dynamics (CFD)[81, 127] and particle image velocimetry (PIV)[2] studies are useful to model or measure the turbulence, it is difficult to relate the flow properties to the corresponding acoustic radiation.[3] Beamforming techniques instead rely on the acoustic radiation to estimate the corresponding sources and thereby complement the flow-field investigations. The standard beamforming techniques have had limited success to estimate jet noise source properties, [35, 41, 128] however, beamforming methods have additional considerations to be effective.

While much has been done in beamforming jet noise studies using more traditional beamforming methods, the investigations are limited by the standard beamforming assumption

that the source is a distribution of incoherent monopoles. Because jet noise sources contain components that are distributed and partially correlated in nature,[2, 9, 43] standard beamforming results can produce misleading source locations and levels.[40, 81] The beamforming incoherent monopole assumption results from solving for potential sources independently of one another. More general beamforming methods instead solve for the potential sources simultaneously (see Section 2.2.1). Example methods include the hybrid method (HM),[60] L_1 generalized inverse beamforming (L_1-GIB) and its derivatives (e.g., GINV),[40, 47] LORE modified for coherent sources,[69] and covariance matrix fitting for correlated sources (CMF-C and MACS).[49, 64] In addition, these methods provide information about the self-coherence along a distributed source, which is useful to study the source composition, including its phase speed. The results can also be used as an equivalent source model to predict the levels and coherence properties of the radiation.

In addition to the choice of beamforming method, the measurement array geometry requires consideration. While far-field measurements can be used as inputs to beamforming methods, the beamforming results are significantly improved when the array spans the source distribution and is placed in the geometric near field.[37, 40] For instance, the source resolution (i.e., the Rayleigh criterion[40]) approximately scales with the measurement distance and as the inverse of the array length so that the resolution is improved an array is placed nearer the source region.[129] In many circumstances, linear arrays are used in lab-scale[39] and full-scale environments,[24] both to span the jet noise source and to feasibly capture the salient features of the jet noise. [41, 44, 77] In practical considerations, the relatively low element count and ability to span large jet noise sources makes linear arrays suitable for jet noise experiments. In this chapter, a generalized beamforming method is applied to measurements of jet noise from a tactical aircraft along a linear uniform array,

and the beamforming results are used to estimate the source distribution properties, including the coherence characteristics.

4.1.2 Beamforming in Jet Noise Studies

Previous beamforming studies have shown limited success to characterize full-scale jet noise, although limited data exists due to the difficulties associated with procurement and controlled test environments. Phased-array methods are particularly useful in full-scale applications, where the direct measurement of flow parameters is difficult due to the heated, turbulent nature of the flow field.[41, 56, 77] While some studies have used more conventional beamforming techniques,[39] many have expanded upon the incoherent monopole assumption of conventional beamforming. Venkatesh *et al.*[35] proposed an integration beamforming method to account for the distributed nature of the source but without explicitly considering source correlation integration. Schlinker *et al.*[41] applied this method using phased-array measurements from a ground-based array of a supersonic tactical engine. The 30-element 3.9 m array measurements, positioned in the maximum radiation region, were input into the beamforming method and produced relatively consistent source estimates in terms of peak location and extent. However, the limited aperture prevented a more detailed perspective. Brusniak *et al.*[77] produced an extensive dataset with multiple arrays—including a polar array, multiple parallel linear arrays and a multi-arm spiral—to measure jet noise sources at the nozzle exit and downstream of a full-scale commercial grade engine. The linear arrays spanned about 27 m in length and contained 181 microphones for a dense spacing near the jet mixing noise. Using traditional beamforming, they found that, while the polar array was useful for limited low-frequency jet noise source estimates and for characterizing the core and fan noise, the linear array was most appropriate to estimate the turbulent mixing noise properties. Measurements from the two arrays were compared for

consistency, and conventional beamforming results along the jet centerline were obtained. They found that the use of small subarrays and extreme array steering angles to estimate source component characteristics potentially produced erroneous results. However, the traditional beamforming methods may have impaired the source characterizations.

More advanced beamforming techniques applied to full-scale jet noise measurements have provided increased capabilities and produced improved results of the acoustic source properties. Dougherty and Mendoza[56] applied advanced beamforming and deconvolution techniques [i.e., the deconvolution approach for the mapping of acoustic sources (DAMAS)[42] and CLEAN for spatial source coherence (CLEAN-SC)[58]] to engine and jet noise beamforming results using measurements from a 100-foot-radius polar arc array near a Honeywell Tech977 engine. They showed that the deconvolution improves the beamforming results by providing a higher resolution image of the source levels as well as a reduction in sidelobes levels. Michel and Funke[44] developed a method to model full-scale jet engine noise that can be used to spatially separate the contributions from the radiating sources (e.g., aft fan, core and jet noise). They used linear array measurements of a full-scale turbofan engine and applied their method to successfully predict the far field radiation level contributions from each of the components. In addition, Padois *et al.*[46] tested HM and briefly compared this with DAMAS and CLEAN-SC on a full-scale aero-engine. When DAMAS was applied in addition to this hybrid method, the iterative deconvolution results converged more quickly and required fewer iterations. Although each full-scale test has analyzed source level properties, a limited full-scale source coherence analysis has only recently been performed by Harker *et al.*[90] In addition, an in-depth characterization of the source levels and coherence properties is lacking, particularly for tactical engines. In addition, more advanced

beamforming methods, including those studied in Chapter 2 can potentially improve the source property estimates.[40, 44, 46, 48, 49]

4.1.3 Overview

The focus of this chapter is to understand the source characteristics of turbulent mixing noise from an installed tactical aircraft engine by applying an advanced beamforming method to the noise measured on a linear microphone array in the mid field of the jet. The HM[60] was found to outperform many similar beamforming methods in Chapter 2 and is applied here to both remove array effects and to measure the extent of source self-coherence. In addition, the unwrapped phase interpolation (UPAINT) method—recently developed for interpolating levels and phase information along the measurement array—is applied to extend the usable frequency bandwidth beyond the spatial Nyquist frequency without adverse grating lobe effects.[50, 51] The beamforming results are validated with a Rayleigh integral to compare the predicted sound pressure levels with those measured at various points in the mid field of the jet.

The beamforming results provide insight into the source levels and coherence properties of the full-scale, heated jet. The results form a source cross-spectral matrix (SCSM) that is useful to understand the frequency-dependent directivity of the maximum radiation. The SCSM also provides a means to estimate the source self-coherence along the source distribution. In addition, an analysis of the sideline and downstream noise sources is performed to understand the respective source levels and coherence properties corresponding to large and fine-scale radiation structure spectra.[91] Finally, beamforming results are generated for additional engine conditions. Each condition is validated by comparing estimated field levels to mid-field measurements, and a comparison of the engine-condition-specific results shows how the source levels and coherence properties vary. The level and coherence analyses of the jet-noise beamforming results provide

insight into the tactical jet noise radiation and serve as a benchmark for similar lab-scale and computational studies.

4.2 Methods

The large length scales of turbulent mixing noise from a tactical engine produces partially-correlated radiation requiring a partially correlated source model. Beamforming algorithms based on a potentially-coherent source distribution provide a means of investigating and modeling source correlation features. A numerical validation study in Chapter 2 comparing cross beamforming,[42], functional beamforming,[48] HM, GINV and MACS techniques found that all methods were successful in estimating the source levels to some degree. HM, however showed the best overall performance in estimating the source levels and coherence properties and was selected as the method most suitable for the current problem. A summary of HM is presented in Section 4.2.1, and a more detailed review is provided in Section 2.2.3.4. In addition, the UPAINT method is described in Section 4.2.2, which extends the usable bandwidth of the array measurements when used as beamforming inputs. Additional information on UPAINT is given in Section 2.2.8. The comparisons in Chapter 2 provide validation and understanding of the beamforming algorithms, especially when the source characteristics are unknown.

4.2.1 Review of Hybrid Method

The assumptions of an incoherent monopole source distribution are relaxed when the source distribution is solved for as a system of equations. Assuming m measurement points and s potential source locations, the hybrid method (HM) attempts to solve a least-squares minimization problem from

$$\mathbf{p} = \mathbf{G}\,\mathbf{q}, \tag{4.1}$$

where the vector of array acoustic pressures, $\mathbf{p}$, for a given frequency, f, is $[m, 1]$ in size, and the vector of complex source strengths, $\mathbf{q}$, is $[s, 1]$. The Green function matrix, $\mathbf{G}$, is comprised of steering vectors along the columns such that

$$\mathbf{G} = [\mathbf{g}_{i=1} \quad \cdots \quad \mathbf{g}_{i=s}], \tag{4.2}$$

and accounts for the free-field monopole propagation from each source to each array element. In Eq. (4.2), each steering vector, $\mathbf{g}_i$, is comprised of steering elements from the potential source location, $\vec{r}_i$, to each array element location. To solve Eq. (4.1), a Moore-Penrose pseudoinverse is commonly employed coupled with a regularization approach.[60, 82] However, the HM regularization is a modification over standard Tikhonov regularization. Traditional Tikhonov regularization improves the conditioning of $\mathbf{G}^{\mathrm{H}}\mathbf{G}$ by supplementing it with a penalization parameter, ν^2, along the diagonal entries as

$$\mathbf{q}_{\mathrm{Tikhonov}} = (\mathbf{G}^{\mathbf{H}}\mathbf{G} + \nu^2\mathbf{I})^{-\mathbf{1}}\mathbf{G}^{\mathbf{H}}\mathbf{p}, \tag{4.3}$$

where $\mathbf{I}$ is the identity matrix and ν^2 is the penalization parameter and is determined by various means, including the Morozov discrepancy principle and generalized cross validation.[83] However, in HM the penalization parameter is added to a square weighting matrix, and the solution to Eq. (4.1) then becomes

$$\mathbf{q}_{\mathrm{HM}} = (\mathbf{G}^{\mathbf{H}}\mathbf{G} + \nu^2\mathbf{L}^{\mathbf{H}}\mathbf{L})^{-\mathbf{1}}\mathbf{G}^{\mathbf{H}}\mathbf{p}, \tag{4.4}$$

where $\mathbf{L}$ is a beamforming regularization matrix,

$$\mathbf{L}^{-1} = \left[\mathrm{Diag}\left(\frac{\sqrt{\mathrm{diag}(\mathbf{Q_{CBF}})}}{\sqrt{\|\mathrm{diag}(\mathbf{Q_{CBF}})\|_\infty}}\right)\right]. \tag{4.5}$$

In Eq. (4.5), $\mathbf{L}^{-1}$ consists of a square matrix with elements formed from the individual source powers from $\mathrm{diag}(\mathbf{Q_{CBF}})$. Here, $\mathrm{diag}(\cdot)$ takes the diagonal elements of a matrix and $\mathrm{Diag}(\cdot)$ forms a diagonal matrix of these elements, $\|\cdot\|_\infty$ is the infinity norm, and $\sqrt{\cdot}$ is applied element-wise. The beamforming regularization matrix is an improvement to the standard regularization process because the Green function matrix is weighted by CBF source powers to add *a priori* information about the beamforming source locations to more selectively penalize the source region instead of the source-independent approach of classical Tikhonov. In fact, the incorporation of the beamforming results into $\mathbf{L}$ resembles the L_p norm formulation in Ref. [47], although the current method does not require iteratively reweighted least squares techniques to solve. Incorporating Eq. (4.5) into Eq. (4.4) and simplifying produces

$$\mathbf{q}'_{\mathrm{HM}} = \mathbf{L}^{-1}\left(\underline{\mathbf{G}}^{\mathbf{H}}\underline{\mathbf{G}} + \nu^2\mathbf{I}\right)^{-\mathbf{1}}\underline{\mathbf{G}}^{\mathbf{H}}\mathbf{p}, \tag{4.6}$$

where $\underline{\mathbf{G}} = \mathbf{G}\mathbf{L}^{-1}$, and $\mathbf{q}'_{\mathrm{HM}}$ is the estimated vector of source powers. Using Eq. (4.6), HM is developed such that

$$\mathbf{Q_{HM}} = \mathbf{q}'\mathbf{q}'^{\mathbf{H}} = \mathbf{L}^{-1}\beta\left(\mathbf{J}\,\underline{\mathbf{G}}^{\mathbf{H}}\right)\mathbf{C}\left(\underline{\mathbf{G}}\,\mathbf{J}^{\mathbf{H}}\right)\beta^*(\mathbf{L}^{-1})^{\mathbf{H}}, \tag{4.7}$$

where $\mathbf{C}$ is the cross-spectral matrix of the array pressures, $\mathbf{p}$, and

$$\boldsymbol{J} = \left(\underline{\mathbf{G}}^{\mathbf{H}}\underline{\mathbf{G}} + \nu^2\mathbf{I}\right)^{-\mathbf{1}} \tag{4.8}$$

In the above, a scaling term, β, is included, where

$$\beta = \left\|\underline{\mathbf{G}}^{\mathbf{H}}\underline{\mathbf{G}} + \nu^2\mathbf{I}\right\|, \tag{4.9}$$

to compensate for the addition of regularization and ensure that the source estimated levels are correct. To determine ν^2, Padois *et al.* conducted a regularization study using HM and found that by setting ν^2 to be at least five percent of the largest eigenvalue of $\mathbf{G}^{\mathrm{H}}\mathbf{G}$, the sound source level converged to the correct levels, with the source levels being over-estimated for smaller

regularization values. The five percent threshold was similarly used in this study. This threshold corresponds to the value for which eigenvalues of $\underline{\mathbf{G}}$ that are below this threshold are orders of magnitude lower (i.e., near the noise floor of the measurement; see Section 2.2.5). For frequencies at or below the array spatial Nyquist frequency of the array, this recommendation was appropriate. However, above the spatial Nyquist frequency of the array it was found that the 5% eigenvalue threshold would overpredict the value at which the eigenvalue drop occurred. An attempt to more precisely determine the threshold value was made by determining the significant eigenvalues of $\underline{\mathbf{G}}$. For example, the threshold can be estimated by determining the last eigenvalue for which

$$\mathrm{abs}\left(d\boldsymbol{\lambda}_{\underline{\mathbf{G}}}/dx\right) > \mathrm{std}\left(\mathrm{abs}\left(d\boldsymbol{\lambda}_{\underline{\mathbf{G}}}/dx\right)\right)/2, \tag{4.10}$$

where $d\boldsymbol{\lambda}_{\underline{\mathbf{G}}}/dx$ takes the finite difference along, $\boldsymbol{\lambda}_{\underline{\mathbf{G}}}$, which are the eigenvalues of $\underline{\mathbf{G}}$, and $\mathrm{abs}(\cdot)$ and $\mathrm{std}(\cdot)$ are the absolute value and standard deviation operators, respectively. Equation (4.10) was determined empirically and—for frequencies at or below the array spatial Nyquist frequency—produces ν^2 values that are approximately those found using the recommendation of Padois *et al.* However, above the array spatial Nyquist frequency, the ν^2 better correspond to a turning point at which the eigenvalues of $\underline{\mathbf{G}}$ are significantly less than the standard deviation. While more robust methods for determining this threshold are available, Eq. (4.10) was sufficient for the current study.

4.2.2 Review of UPAINT Algorithm

The upper limit to the usable bandwidth for frequency-domain beamforming is set according to the spatial Nyquist frequency of a uniform input array. This is determined by solving for the frequency at which the array interelement spacing equals one-half wavelength. Beamforming results above this limit introduce grating lobes, which are effectively spatially

aliased estimates of the source properties. Where inverse and regularization methods are applied, these grating lobes may interfere with the estimation process by redistributing energy from the true source estimate location to the grating lobes, or vice versa. To ameliorate the source estimates, a method was developed by Goates *et al.*[50] to increase the frequency bandwidth for the beamforming of broadband sources. A summary of the method is presented here, and a detailed description of the process is given in Ref. [50].

The UPAINT method effectively creates a higher-density interpolated array to increase the spatial Nyquist frequency so that grating lobes do not interfere with the beamforming estimates. It accomplishes this by operating on both the frequency-dependent cross-spectra, $\mathbf{C}_{i_1,i_2}(f)$, of each microphone pair and the cross-spectral matrix of each frequency. First, the cross-spectral phase, $\mathbf{\Phi}_{i_1,i_2}(f)$, is determined for each element of $\mathbf{C}$, where

$$\mathbf{\Phi}_{i_1,i_2}(f) = \arg[\mathbf{C}_{i_1,i_2}(f)], \tag{4.11}$$

and i_1 and i_2 correspond to array elements at $\vec{r}_{i_1}$ and $\vec{r}_{i_2}$, respectively. Next $\mathbf{\Phi}_{i_1,i_2}(f)$ is unwrapped for each microphone pair to provide a smoothly-varying phase. This is done using a coherence-based unwrapping procedure described in Ref. [88], which was implemented previously on lab-scale rocket measurements for intensity-based measurements.[51] The resultant unwrapped phase matrix, $\widetilde{\mathbf{\Phi}}(f)$, contains the unwrapped phase of each array microphone pair. Together, the magnitude matrix, $\mathrm{abs}[\mathbf{C}(f)]$, and $\widetilde{\mathbf{\Phi}}(f)$ form the two components of the UPAINT cross-spectral matrix. The separated the cross-spectral matrix, i.e., the magnitude matrix and the unwrapped phase matrix, are smoothly varying and hence can be interpolated. Additional interpolation points are assigned and calculated to increase the spatial Nyquist frequency of the array. The interpolated components of the UPAINT cross-spectral matrix (magnitude and phase) are then combined and

input into the beamforming algorithm as a standard cross-spectral matrix. The corresponding array elements are updated with the additional interpolated locations and the beamforming results are produced. Because the array is interpolated—usually such that the interelement spacing corresponds to a spatial Nyquist frequency above the selected frequency—the beamforming results to not contain grating lobes that can interfere with the beamforming source estimates.

4.3 Results

The HM method and UPAINT described in Section 4.2 are applied to noise measurements taken of a full-scale tactical engine. The experimental setup is described in Section 4.3.1. In Section 4.3.2, measurements from a ground-based linear array are input to the HM method to estimate the source characteristics and the UPAINT method is applied for frequencies above the spatial Nyquist frequency of the input array. These are validated by comparing mid-field measurements with those estimated using the beamforming results as an equivalent source model. The estimated source properties are analyzed using a beamforming-based source cross-spectral matrix, including the convective phase-speed across the source and an analysis of the source self-coherence properties. In Section 4.3.3, a subarray analysis reveals the source levels and coherence properties associated with radiation perpendicular to the jet noise flow, as well as the source properties related to the maximum radiation region. Finally, Section 4.3.4 provides an analysis of the beamforming results as a function of engine condition using two additional engine conditions, and the results are compared to the engine condition reported in Section 4.3.2.

4.3.1 Experiment

Noise measurements were taken of an installed full-scale tactical engine (see Fig. 4.1). One of the engines of the tethered aircraft was operated at three engine conditions while the other was held at idle. An array of 50 GRAS 6.35-mm and 3.18-mm microphones was placed on the ground 11.6 m from the centerline of the jet axis. As shown in Fig. 4.1, the ground array element spacing was 0.61 m—except for a small gap in the array towards the downstream end—and the array spanned 30 m. Because of the near-grazing incidence of the sources on the array at the location of the gap, no effort was made to interpolate measurements at this location (except as done using UPAINT above the spatial Nyquist frequency). Using a separate array of 18 microphones, with a 6 inch interelement spacing, ten nonsynchronous measurements were taken along the scanning array line at locations marked by the triangles in Fig. 4.1. For each of the scans, measurements were also taken at the ground array. Each measurement was taken for 30 seconds at either a 48 kHz or 96 kHz sampling rate, depending on the engine condition tested, and each resultant waveform was divided into time-waveform blocks of 16384 samples each with 50% overlap. Due to the consistency of the measurements (see Fig. 8 of Ref. [24]), the ten ground array measurements were appended to form a single 300 second measurement. A Fourier transform was applied after each block was filtered by a Hanning window, and cross-spectral calculations were averaged over the blocks to obtain cross-spectral density elements. This provided a cross spectral matrix, $\mathbf{C}$, for each frequency to input into the beamforming methods. Whereas some studies apply a diagonal deletion to $\mathbf{C}$ to reduce microphone self-noise,[34] particularly for cases when flow noise is present, this was not applied here as the source measurement levels were on the order of at least 30 dB higher than background and flow noise levels and the inclusion of the diagonal elements was found

to improve beamforming results. A detailed description of the experiment is found in Ref. [24], and the spectral variation of the measured sound as a function of angle is shown in Ref. [91].

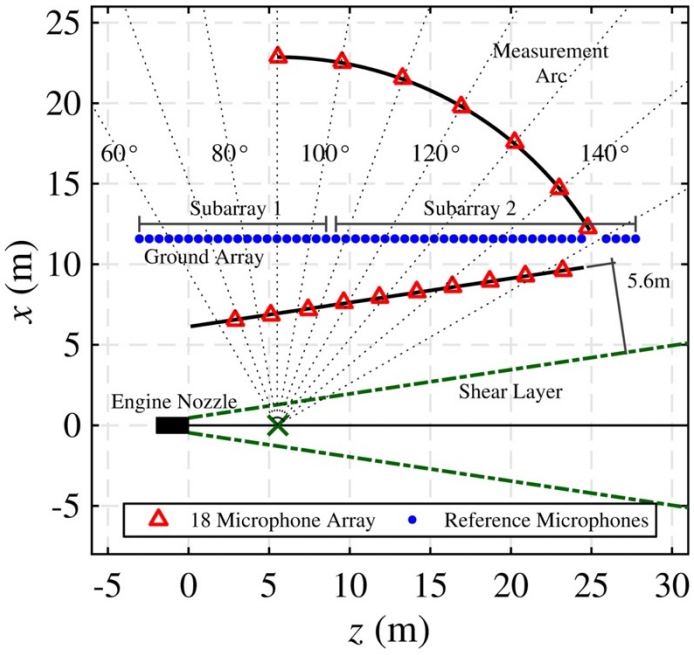

Fig. 4.1. Schematic of the experimental setup. A ground-based array of 50 microphones is shown with blue dots and the 18-element scanning array measured at locations marked by red triangles.

One-third octave (OTO) band levels of the measurements at the ground-based measurement array are given in Fig. 4.2 for three engine conditions, namely intermediate (INTER), military (MIL; 100% Engine Thrust Request [ETR]) and afterburner (AB; 150% ETR). In each case, the maximum radiation varies with frequency and shifts upstream—towards the sideline—with increasing frequency. The main radiation lobe at INTER is primarily located far downstream at 100 Hz and does not seem to be fully captured by the array, while peak levels at 400 Hz are at a position of about $z = 8$ m. At MIL, the peak levels are about 30 dB higher than INTER, and two distinct radiation lobes—a primary lobe and a secondary—are present in the ground array data, centered at $z = 20$ m and 125 Hz and $z = 12.5$ m and 500 Hz, respectively. These radiation lobes extend many meters spatially as well as across multiple one-third octave bands. In addition to the

multiple lobes, the narrowband F-35A measurements also show evidence of broadband shock-associated noise (BSAN) visible at $-3\ m < z < 2$ m and peaking in level at 500 Hz. Similarly, the OTO results here show higher levels in the same region, albeit at 800 Hz and less discernable. At AB in Fig. 4.2(c), the results are like the MIL spectra, except that the levels are about 4-6 dB higher overall, and the peak level locations are farther upstream. The primary lobe is shifted upstream to about z =17.5 m. Like the narrowband results in Ref. [130], evidence of multiple lobes—especially a third lobe at $z = 10$ m and 500 Hz—and BSAN to the sideline is also present. The additional lobes are located are about 2 m further to the sideline compared to the lobes at MIL. In Section 4.3.2, the measurements taken at MIL are used as beamforming inputs, and the INTER and AB measurements are considered in Section 4.3.4.

The OTO band results are reported here to better compare with similar tactical studies.[13, 41, 91] However, narrowband power spectral densities were recently reported of an F-35A engine at MIL power in the vicinity of the engine.[130] Using a 32 m long linear ground array approximately parallel to and about 9 m from the shear layer, they showed many similar features in the spectral data as those shown here, including a primary lobe at about 100 Hz and $z = 20$ m from the nozzle. However, they also found that multiple distinct lobes are evident between 150 and 800 Hz, including at 230 Hz and $z = 13$ m and 350 Hz and $z = 10$ m. Although difficult to resolve, it is possible that additional lobes may also be present in corresponding narrowband spectra of the current study, as a small null within the secondary lobe at 300 Hz suggests there might be. The origins of these multilobe features are under investigation. It has been hypothesized that they are the result of shock cells interacting with turbulence structures,[29, 130] the effects of combustion noise (particularly at AB),[113] and the effect of high temperatures to separate Mach wave and large-scale structure radiation.[10]

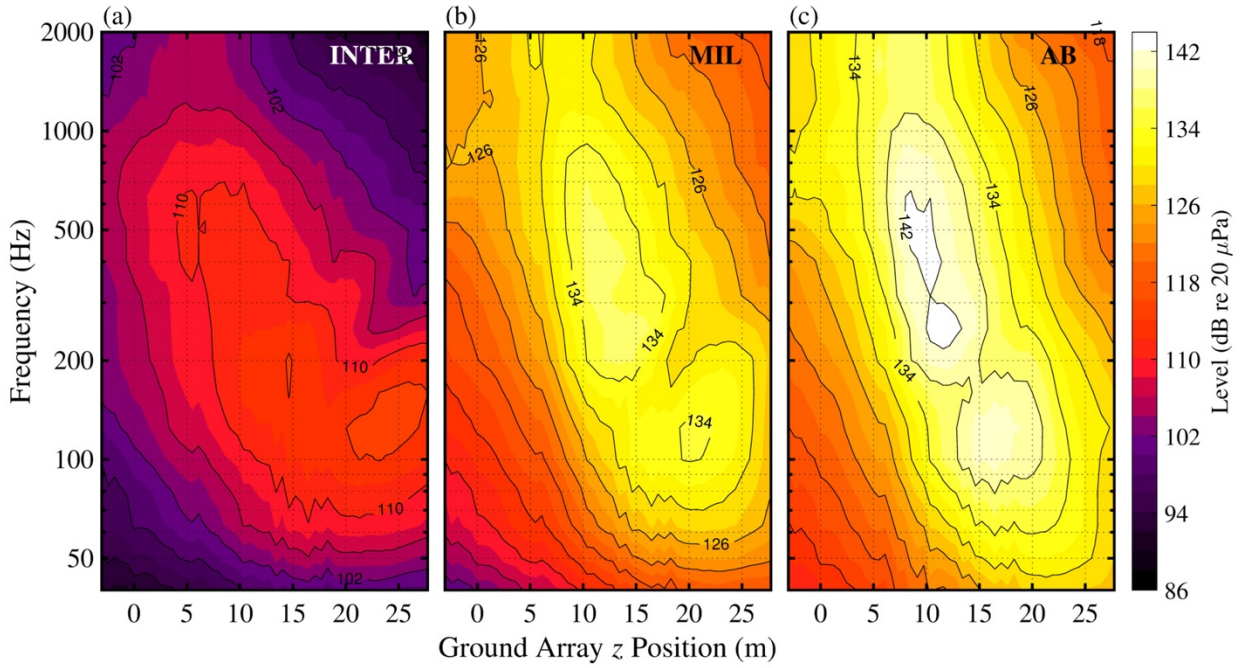

Fig. 4.2. One-third octave band levels at (a) INTER (b) MIL, and (c) AB engine condition along the ground-based measurement array.

4.3.2 Beamforming at Military Power

The pressure measurements at MIL engine power, shown in Fig. 4.2(b), are used as inputs for HM beamforming to yield estimated source characteristics as a function of frequency. These results, shown in Fig. 4.3(a), are distributed across the axis of the jet centerline (at the nozzle height of 1.9 m), shown as a black solid line in Fig. 4.1. The reconstruction grid density is 10 cm for all beamforming results, and the 40 Hz to 2000 Hz OTO center-band results were obtained by summing over appropriate 5.9 Hz narrowband results. Colored areas represent the absolute source strength density levels, and white contour lines are overlaid in 3 dB increments to represent the levels normalized by the frequency peak level. The source strength density estimates have units of a volume velocity per unit meter along the jet centerline, and they are shown in dB using an arbitrary reference of $10^{-3}\,\mathrm{m}^3/\mathrm{s}$. As seen in lab-scale and full-scale beamforming measurements,[37, 39, 56] as well as for acoustical holography[29] and vector-intensity-based source

estimates,[27] the source distribution shifts upstream and the extent of the source diminishes with increasing frequency. These effects are best visualized using the white 3 dB down contour lines in Fig. 4.3(a). Schlinker *et al.*[41] showed beamforming source estimates of a full-scale military engine using measurements taken in the maximum radiation direction with a compact 3.9 m ground-based array. They applied the integration beamforming approach of Ventakesh *et al.*,[35] and found that the maximum source location is centered approximately 4-6 nozzle diameters (D) downstream for frequencies between 250 Hz and 400 Hz. Using an approximate nozzle diameter of about 0.6 m (see Section 3.3.2), the results here at MIL are centered between 6-8 D, which is slightly farther downstream than they predicted. Thus, this dataset produces a source slightly farther downstream along the jet centerline than previously seen in full-scale tactical measurements. In addition, a primary and secondary lobe are visible in the source estimates, similar to the features seen in the spectral measurements at the ground array. The primary lobe peaks at 8 m at 100 Hz, and the secondary lobe peaks at about 5 m at 250 Hz. The source extent greatly contracts and shifts upstream between these two features. While the gradual shift and contraction of the source is usually observed, this discrete transition region between the two lobes has only been observed in similar tactical source estimates using acoustical holography.[29] The measurement array used in this study has a spatial Nyquist frequency at about 280 Hz, due to the 0.61 m interelement spacing, and grating lobes begin to interfere with the source estimates above this frequency.

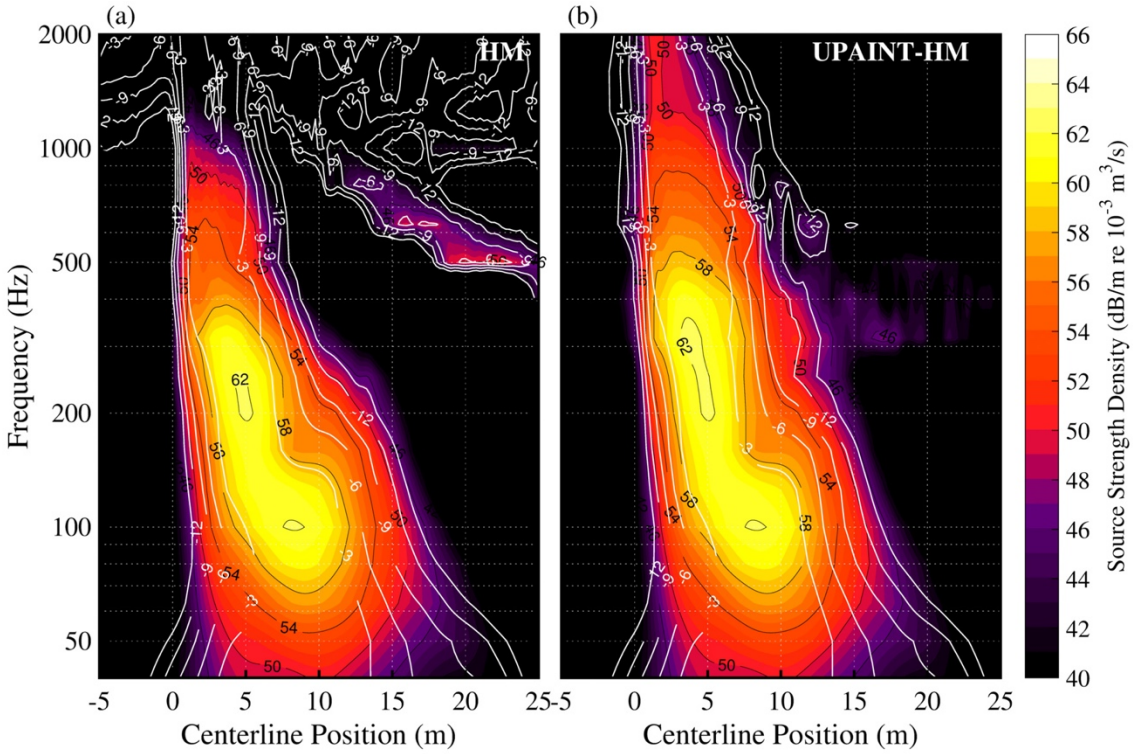

Fig. 4.3. (a) Beamforming results of tactical aircraft at MIL engine condition using (a) HM and (b) UPAINT-HM that were applied to ground array data and steered to jet center axis. The colors and black contour lines indicate absolute levels and the white contour lines indicate the levels relative to the maximum level of each one-third octave band.

To increase the usable bandwidth of the measurement array for beamforming studies, the UPAINT method was implemented, which provides the ability to spatially interpolate the phase of $\mathbf{C}$ by unwrapping the phase spectrum of each individual measurement. The HM and UPAINT-HM beamforming results are shown alongside each other in Fig. 4.3. Without UPAINT, grating lobes appear in the results [of Fig. 4.3(a)] above about 400 Hz and progress towards the main lobe with increasing frequency. In addition, the source levels decline with increasing frequency as the HM algorithm distributes the energy of the main lobe to the additional grating lobes. The normalized contour lines that are overlain in white show the source extent as a function of level, relative to the peak level. For example, the 6 dB down contour lines show that without UPAINT the grating lobes significantly affect the main source distribution above 1000 Hz. In addition, the source contracts

significantly past the spatial Nyquist frequency. In Fig. 4.3(b), UPAINT processing was applied to all frequencies above the spatial Nyquist frequency (>280 Hz). Furthermore, for a small band of frequencies just above the spatial Nyquist frequency (i.e., 280-550 Hz), a supplemental spatial unwrapping of the phase of $\mathbf{C}$ was necessary to remove additional artifacts. Noise within the CSM is believed to strongly affect the UPAINT algorithm so as to not remove the grating lobes within this frequency range. However, the spatial unwrapping seems to improve the results.

With UPAINT and the additional spatial unwrapping applied at select frequencies, the grating lobes effects in the HM results are not present in the UPAINT-HM source estimates. The source extent and location of UPAINT-HM results, measured using the normalized 6-dB down contour lines, are qualitatively similar to the HM results, although some differences do exist. For example, as measured using the 6 dB contour lines, the source extent of the UPAINT-HM results is slightly larger than those of HM—e.g., the UPAINT-HM extent at 800 Hz is about 7.5 m compared to the corresponding HM extent of 5.5 m. Further study is necessary to definitively quantify the source extent as the HM source extent may be contracted due to aliasing while the UPAINT process may be enlarging the source extent slightly. However, because the UPAINT-HM results remove the extraneous grating lobes shown in the HM results, they can be used as an equivalent source model above the spatial Nyquist frequency to provide estimates of the radiation.

A validation of the UPAINT-HM results is performed by treating the beamforming-based source results as an equivalent source model (ESM). Using a Rayleigh integration, the ESM predicts radiation along the scanning array, where additional measurements were taken. The spectral level measurements are shown in Fig. 4.4(a). Unlike the ground-based measurements, the scanning array measurements were taken at a height of 0.38 m above a concrete surface, thus creating an interference null that is present in the data beginning at 700 Hz at the upstream edge

of the array and that shifts up in frequency to about 2000 Hz and centered at $z = 17$ m. When predicting the radiation, an image source of the ESM was used to mimic the effects of the ground reflection, and the ESM and image ESM levels were each reduced by 6 dB to account for the added image source. The predicted levels are shown in Fig. 4.4(b), and the error between the measured and predicted spectral levels is provided in Fig. 4.4(c). There is good agreement between the measured and predicted levels overall, particularly for frequencies between 100-500 Hz where errors are mostly less than 2 dB. The predicted levels errors are underpredicted below 100 Hz by about 2 dB. Above 500 Hz, large errors are shown that are related to the interference null patterns. The predicted levels greatly underpredict the levels along the interference null, in some cases more than 10 dB. Because the ESM and image ESM are line source distributions, they do not adequately represent the more complex patterns created by a volume source interacting with a hard surface, although it can be assumed that a more volumetrically distributed ESM would produce similar interference nulls as measured. Overall, the predicted levels agree with those measured and confirm the beamforming-based source estimates to predict radiation properties.

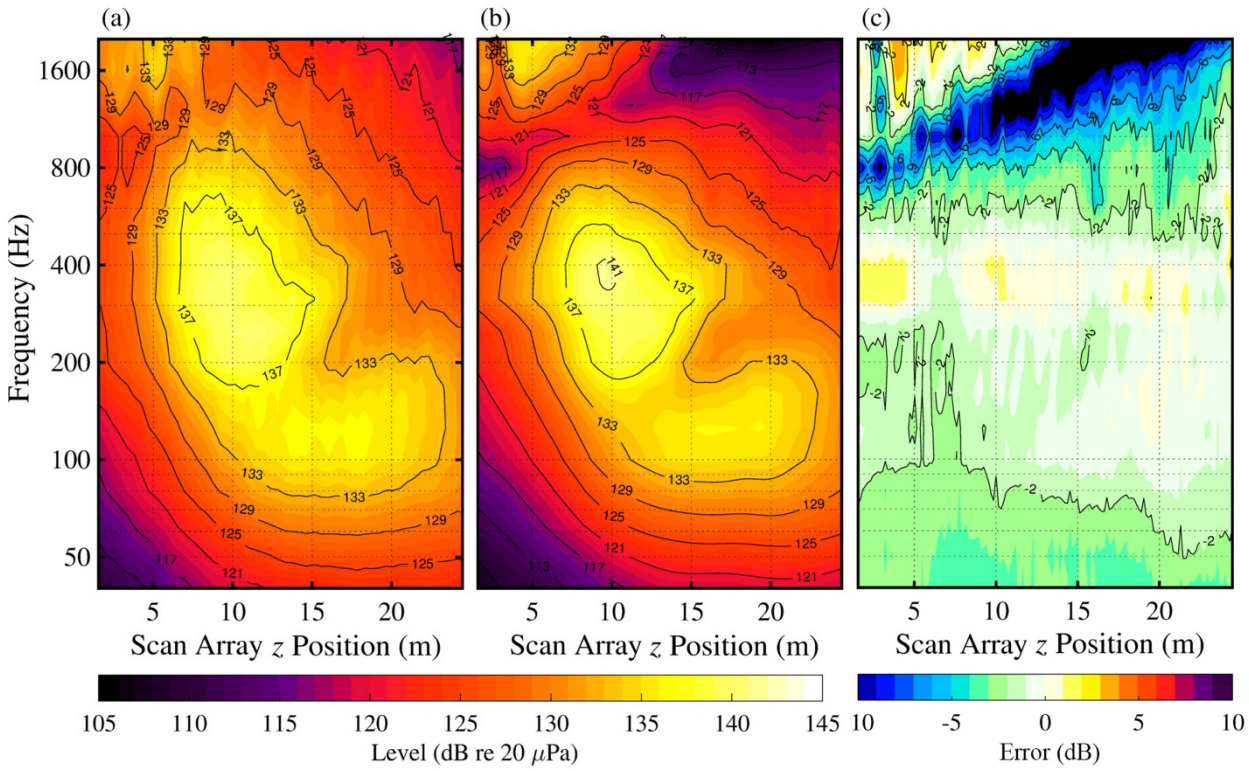

Fig. 4.4 (a) One-third octave band level measurements at scanning array, (b) predicted levels from beamforming-based source model, and (c) the errors of the estimated levels to measurements.

In addition to analyzing levels, the HM produces a source cross spectral matrix (SCSM) that can lend insights into phase of the equivalent acoustic source. To provide examples, the unwrapped phase, referenced to the peak level location, is shown in Fig. 4.5(a-b) for 100 Hz and 200 Hz. The slope of the unwrapped phase is related to the phase speed—and consequently the directivity—of an equivalent propagating wave across the source distribution. In Fig. 4.5(a), a reference line is plotted alongside the phase with a dashed black line and represents a -1.28 rad/m slope. If considered as a convective phase speed of the source, this would correspond to a plane wave propagating with a directivity of 135°, measured relative to the engine inlet, for the conditions at 100 Hz. The slope of this reference line closely resembles the phase of the beamforming results between about $0\ \text{m} \leq z \leq 15\ \text{m}$, coinciding well with the source extent—

overlaid on the figure for convenience—down to about 15 dB from the peak level. Thus, the directivity of the beamforming radiation in the peak source level location is about 135° at 100 Hz. A similar analysis at 200 Hz [Fig. 4.5(b)] shows that a reference line with a slope of -2.07 rad/m matches the slope of the beamforming phase near the peak level location, corresponding to a directivity of 125°. The slope of the beamforming phase, however, only matches the reference line to within the top 3 dB of the source region. Outside of this region, the beamforming phase is steeper for lower values of z and more gradual for higher z values. Thus, at 200 Hz the radiation is not as uniformly directional as found at 100 Hz, which is confirmed by the additional spectral features in the ground-based array measurements. Additionally, the phase changes directions for $z > 15$ m, corresponding to source levels < 15 dB below the peak level, which is an erroneous processing artifact of the unwrapping process.

These examples show that the SCSM can be used to estimate the prominent radiation directivity at which the beamforming results would radiate if treated as an equivalent source. An estimate of the SCSM directivity as a function of frequency is given in Fig. 4.5(c). This was calculated as in the examples of 100 Hz and 200 Hz by matching the slope of the SCSM phase in the vicinity of the peak source levels. The plotted directivity indicates that the directivity is primarily $135°$ for frequencies up to 125 Hz, and a rapid transition to a $125°$ directivity at 200 Hz and a gradual shift to about $120°$ at 1000 Hz. The directivity agrees with the peak spectral level locations in Fig. 4.2(b), which are relatively fixed up to 125 Hz before transitioning rapidly upstream at about 160 Hz and then which gradually shift slightly further upstream with frequency above 200 Hz. Du and Morris[89] showed results of the beamforming source phase using traditional delay-sum beamforming on a numerical jet noise model, although they did not estimate the phase speed.

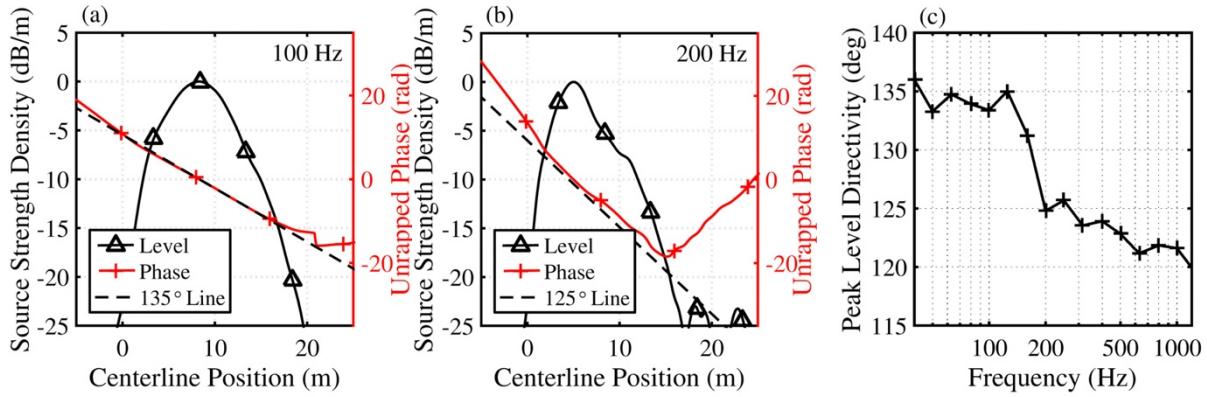

Fig. 4.5. The beamforming levels at (a) 100 Hz and (b) 200 Hz are shown, and the unwrapped phase of the source is calculated relative to the maximum source level location and overlaid on the beamforming level plots. (c) The unwrapped phase in the vicinity of the peak beamforming levels is used to calculate the source directivity.

The SCSM also provides an estimate of the source self-coherence, which is shown in Fig. 4.6(a-c) for frequencies of 100, 200, and 500 Hz. The source coherence identifies the nature of the source as a coherent, partially-coherent or incoherent distribution. The corresponding beamforming levels (the diagonal entries of the SCSM) are shown in Fig. 4.6(d-f). In each case, dashed lines are overlaid on the coherence plot and beamforming levels plot to show the point at which the normalized beamforming levels are 12 dB down from the peak level. The dashed-line box helps to separate coherence results where the levels are significant from those that may be contaminated by noise, and the 12 dB threshold level was empirically selected. The source coherence is a function of frequency and higher frequencies show less self-coherence across the source distribution. At 100 Hz, the source coherence, measured at the peak level location, extends at least 4 m in either direction, with coherence values of ≥ 0.5. This encompasses over 50% of the 12 dB down source extent and characterizes a highly self-coherent source with salient features that can be described using relatively few independent sources. However, at 200 Hz and 500 Hz, the coherence decays quickly in space. The coherence drops below 0.5 within 1-2 m of the peak level location at 200 Hz, and within under 1 m from the peak level location at 500 Hz. However, the

source distribution lengths, as defined by the 12 dB down lines, extend about 12 m and 9 m for each respective frequency. Because low coherence across a source distribution is indicative of multiple independent sources, multiple partially coherent sources are required in a source model to produce source properties like the results shown here, particularly above 200 Hz.

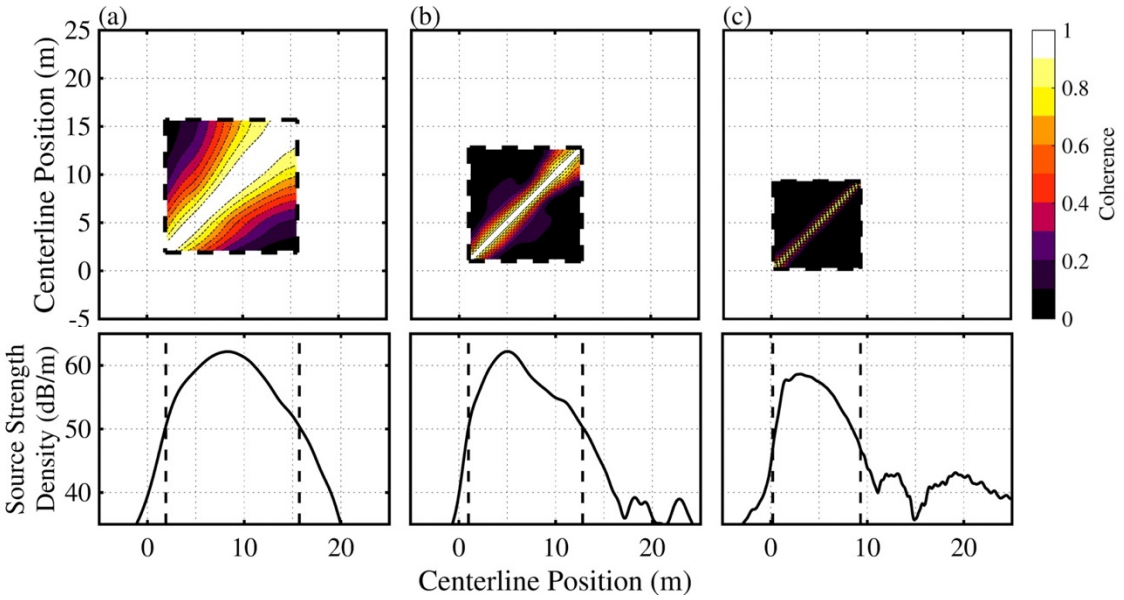

Fig. 4.6. Beamforming-based source coherence and corresponding levels for (a) 100 Hz, (b) 200 Hz and (c) 500 Hz. The dashed box indicates the region of the highest 12 dB of the source region.

To more readily quantify source coherence properties, a coherence length, L_{γ^2}, is defined, which is the smallest spatial distance, measured from a reference location, to a point where coherence drop below 0.5. This provides a convenient way to express coherence properties over a range of frequencies and spatial reference locations. The coherence lengths of the results shown in Fig. 4.6 are calculated and given in Fig. 4.7. At each frequency, the coherence calculations are limited to reference locations within the top 12 dB of the corresponding beamforming source levels, shown by the dashed line. The coherence lengths vary significantly as a function of frequency. L_{γ^2} values exceed 8 m below 50 Hz, although they are less than 1 m above 400 Hz. At $z = 13$ m, the L_{γ^2} values peak for a given frequency, which is about 4 m farther downstream than

the peak level locations for frequencies below 125 Hz, and even farther still for frequencies above 125 Hz. This local peak in L_{γ^2} may indicate a source that is spatially separated from other sources that are present in the peak level region, as the increased L_{γ^2} values generally do not extend past the peak source level locations. However, within the peak level locations, which varies from about $z = 9$ m at 100 Hz to $z = 4$ m at 300 Hz, the coherence lengths are more consistent as a function of space.

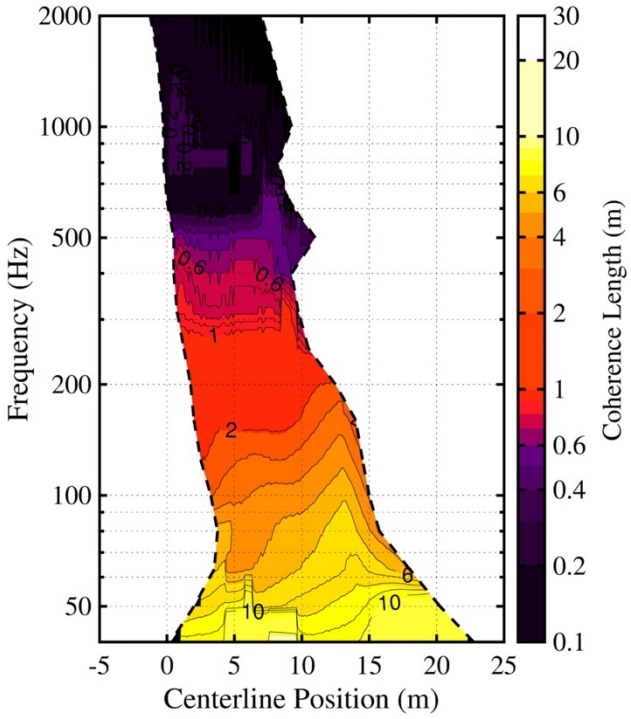

Fig. 4.7. Source coherence lengths (L_{γ^2}) calculated for beamforming results at MIL engine condition.

4.3.3 Subarray Beamforming Analysis

The prior results utilized the entire measurement aperture as input to the beamforming methods to find a corresponding equivalent source distribution. Because the radiation is spatially distributed in the jet noise field, a decomposition of the noise using subarrays may yield unique source properties and insights. For example, Neilsen *et al.*[91] characterized tactical jet noise using

fine and large-scale structure (FSS and LSS) similarity spectra. They found that at MIL engine condition, fine-scale similarity spectra represent the dominant radiation features for directivities up to about 100° ($z = 7.5$ m) and large-scale similarity spectra represent the dominant radiation levels farther downstream. Therefore, the goal of this section is to characterize the radiation in regions that were described by Neilsen *et al.* to comprise the fine and large- scale radiation features, both in terms of levels and source coherence properties.

The measurement array is subdivided into two parts, consisting of the first twenty elements to the sideline of the jet (-3.0 m $< z <$ 8.5 m) and the remaining thirty elements located farther downstream (9.1 m $< z <$ 27.7 m). The $z = 8.5$ m division point corresponds to the location of lowest coherence length measurements along the array in Section 3.4.2.1. The low coherence field coherence lengths at this point indicate a possible transition point between two or more independent sources of similar strength. In addition, this location was found by Neilsen *et al.*[91] to mark the approximate transition region from the FSS similarity spectra to that of the LSS.

Measurements from each subarray are applied separately to UPAINT-HM beamforming to estimate the source properties, and the frequency-dependent levels are shown in Fig. 4.8. The beamforming results of the sideline subarray ($z \leq 8.5$ m) show a source that remains nearly stationary, with the source location moving from 2.8 m at 100 Hz to 2.0 m at 800 Hz . The source extent gradually contracts in size with increasing frequency from about 6.1 m (1.8 λ) at 100 Hz to about 3.3 m (7.7 λ) at 800 Hz, as measured from the 3 dB down contours of the peak level. In contrast, the peak location of the beamforming source from the downstream subarray varies much more with frequency, progressing upstream from 8.5 m at 100 Hz to 4.9 m at 800 Hz. The source extent remains nearly constant, varying from 5.3 m (1.5 λ) at 100 Hz to 5.5 m (12.8 λ) at 800 Hz, although the source extent may be slightly enlarged due to the UPAINT processing (see Section

4.3.2). In addition, the source extent and peak location undergoes a sharp transition at 100-200 Hz similar to the one seen in Fig. 4.3 where the extent contracts by 1.2 m and the peak level location shifts upstream by 3.3 m. A grating lobe also exists at 500 Hz, centered at $z = 20$ m, which was not entirely removed in the UPAINT process and which slightly modifies the results.

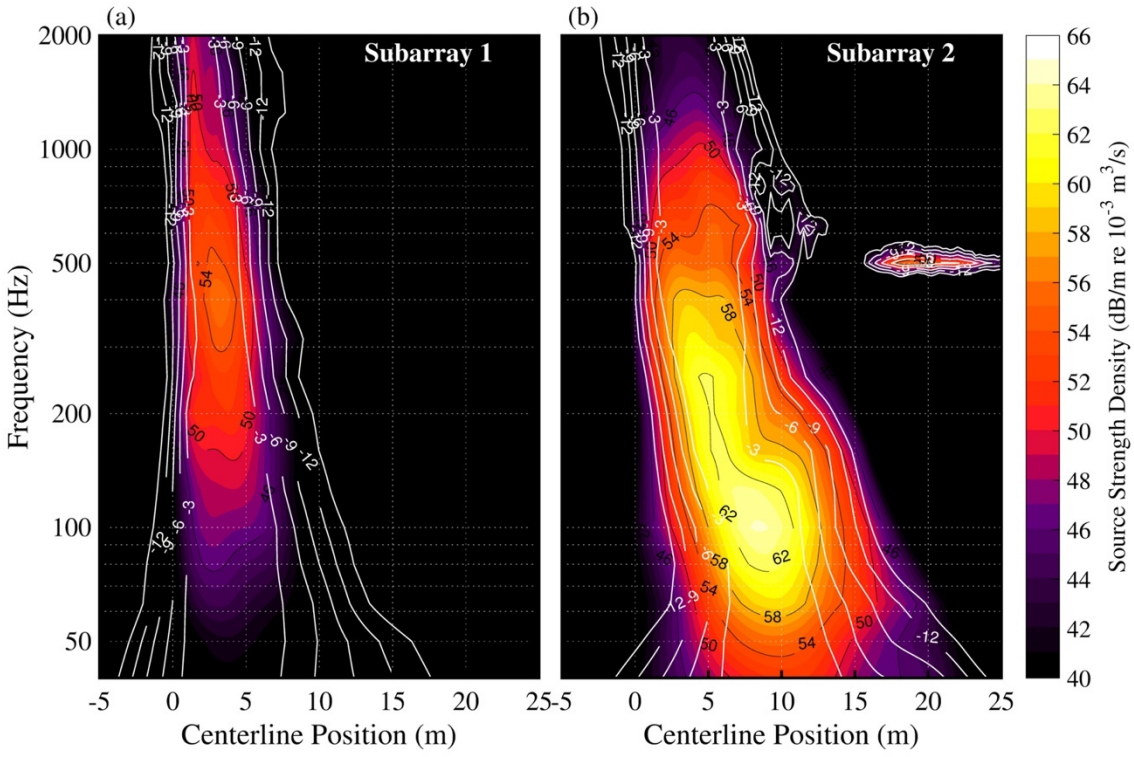

Fig. 4.8. Beamforming results at MIL engine condition using subarrays of (a) microphones 1-20 [$z \leq 8.5$ m; sideline] and (b) microphones 21-50 [$z > 8.5$ m; downstream].

Using the source cross-spectral matrix results of the two subarray beamforming datasets, the source coherence is obtained from which the L_{γ^2} values are calculated. The L_{γ^2} values corresponding to the beamforming results from the sideline subarray in Fig. 4.9(a) are about 2 m at 100 Hz, about 1 m at 200 Hz, and much less than 1 m at 500 Hz. The L_{γ^2} values from the downstream array in Fig. 4.9(b) are generally more than double those of Fig. 4.9(a) for a given frequency. Values of L_{γ^2} are between 3-6 m at 100 Hz, 1-2 m at 200 Hz and just under about 1 m at 500 Hz. The L_{γ^2} values below 100 Hz from the downstream array are particularly larger than

for values that used the sideline array. These results show that the coherence values are low for the sideline-subarray source estimates, even for frequencies below 100 Hz, relative to the downstream-subarray source L_{γ^2} values.

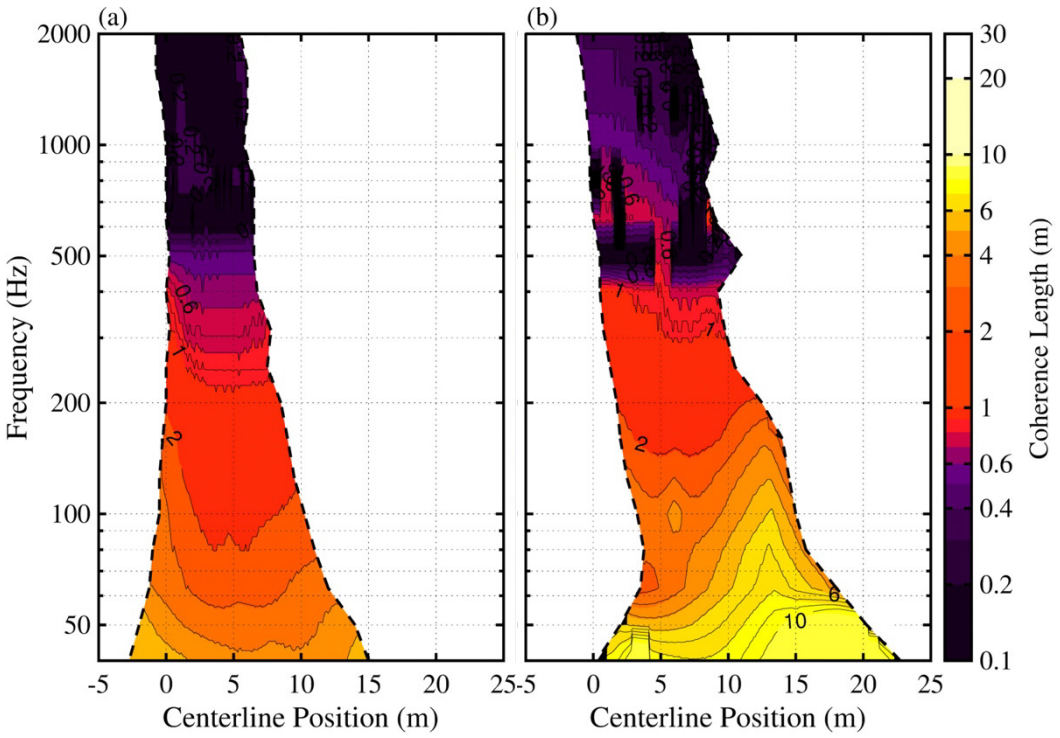

Fig. 4.9. Source L_{γ^2} values calculated from beamforming results using subarrays of (a) microphones 1-20 [$z \leq 8.5$ m; sideline] and (b) microphones 21-50 [$z > 8.5$ m; downstream].

The spectral decomposition of Neilsen *et al.*[91] to separate the radiation into two sources was used to guide the subarray designs and, thus, highlight the differences between the sources in terms of level and L_{γ^2} values. They showed that while the fine-scale spectral radiation levels are highest between 500 Hz-3000 Hz, and do not strongly vary as a function of radiation angle, the large-scale similarity spectral radiation peaks in value between 100-500 Hz and radiates most prominently for directivities of 110-140°. In terms of level, the dominance of the downstream-subarray source levels for frequencies below 500 Hz and the relatively larger role of the sideline-subarray source above 500 Hz confirms these trends for the sources.

The frequency- and level-dependent trends separating the two sources are also evidenced by Stout *et al.,*[27] who measured the acoustic intensity vectors in the mid field of a tactical full-scale engine. They noted a dramatic shift in the angular span of the peak radiation between 100-300 Hz. In addition, the radiation span shifted from 120-130° at 100 Hz to 110-120° at 300 Hz. The frequency at which this shift occurs in radiation angle corresponds to the transition region between 100-200 Hz in Fig. 4.8(b). In addition, Stout *et al.* showed that the angular span of the peak intensity vectors increased significantly above 500 Hz and was more omnidirectional. The angular span increased from about a 15° spread at 500 Hz to over 35° at 2 kHz. The beamforming source levels from the sideline and downstream subarrays show that the source levels from the sideline subarray peak at about 500 Hz. In addition, the relative amplitude of the sideline-based source estimates increases with respect to that of the downstream subarray with increasing frequency. This is consistent with the findings of Stout *et al.* and suggests that spread in directivity of the vector intensity results above 500 Hz is the result of more omnidirectional radiation that is preeminently observed along the sideline.

The coherence analysis shows the differences of the subarray source estimates beyond the level-based findings. The relatively low L_{γ^2} values from the sideline-based source relative to those from the downstream-based source indicate that the downstream-radiating sources are much more spatially distributed and correlated compared to the sideline radiation. The source level and coherence results suggest that the source estimated by the first subarray characterizes more omnidirectional, incoherent sources whereas the secondary subarray source is comprised of much more distributed and correlated sources with radiation directive towards high aft angles, in support of a two-source jet noise model interpretation.[9]

4.3.4 Engine Condition Analysis

The preceding analyses were for the tactical engine operating at MIL engine condition. In this section, the beamforming results that use the full ground array as input are used to analyze two additional engine conditions, namely intermediate (INTER) and afterburner (AB; 150% ETR), to understand the engine-specific source level and coherence characteristics. A comparison of the tactical engine conditions with laboratory-scale jets was provided in Section 3.3.2 and includes jet noise classifications based on maximum radiation angle, scaling of peak Strouhal number in the maximum radiation direction, and geometric scaling based on nozzle diameter. It was found that for the INTER engine condition the overall radiation angle of approximately 150° suggests the jet noise may be treated as being radiated from a convectively subsonic source. For the AB case, however, the maximum radiation angle is approximately 125°, indicating a convective Mach number of approximately 1.7-1.8. These results corroborate similar findings for heated supersonic jet measurements that approach settings found in typical full-scale tactical jet measurements.[23, 119, 120, 122-124]

The beamforming-based source estimates are calculated for INTER and AB engine conditions using UPAINT-HM, and results are shown in Fig. 4.10. At INTER, the source distribution is closer to the origin and the extent is smaller as compared to the MIL beamforming source estimates. The levels peak between 100-200 Hz at about 3.2-3.7 m, and although there is a large shift in the peak location in this region, the dip in level between the two frequencies is not clear as seen at MIL. In contrast, the frequency-dependent source extents at AB condition are generally larger and located farther downstream of the nozzle exit. The transition region in the AB results between 100-200 Hz is evident. The trends between the engine conditions provide similar findings as for additional analyses of comparable jet noise studies. For example, Stout *et al.*[27]

estimated the source distribution location using ray-tracing from vector intensity methods and found that the AB source distribution was located about 1 m farther downstream and that the source width dimensions were about 1 m smaller than for the MIL vector intensity results. In addition, he observed a source transition region at about 200 Hz where the source levels transitioned about 3-4 m upstream from 100 Hz to 300 Hz in both engine cases. A comparison with the beamforming results shows many similarities, as a transition region is seen in both MIL and AB beamforming level results, as the peak source level location shifts about 2-3 m in the upstream direction in both engine cases.

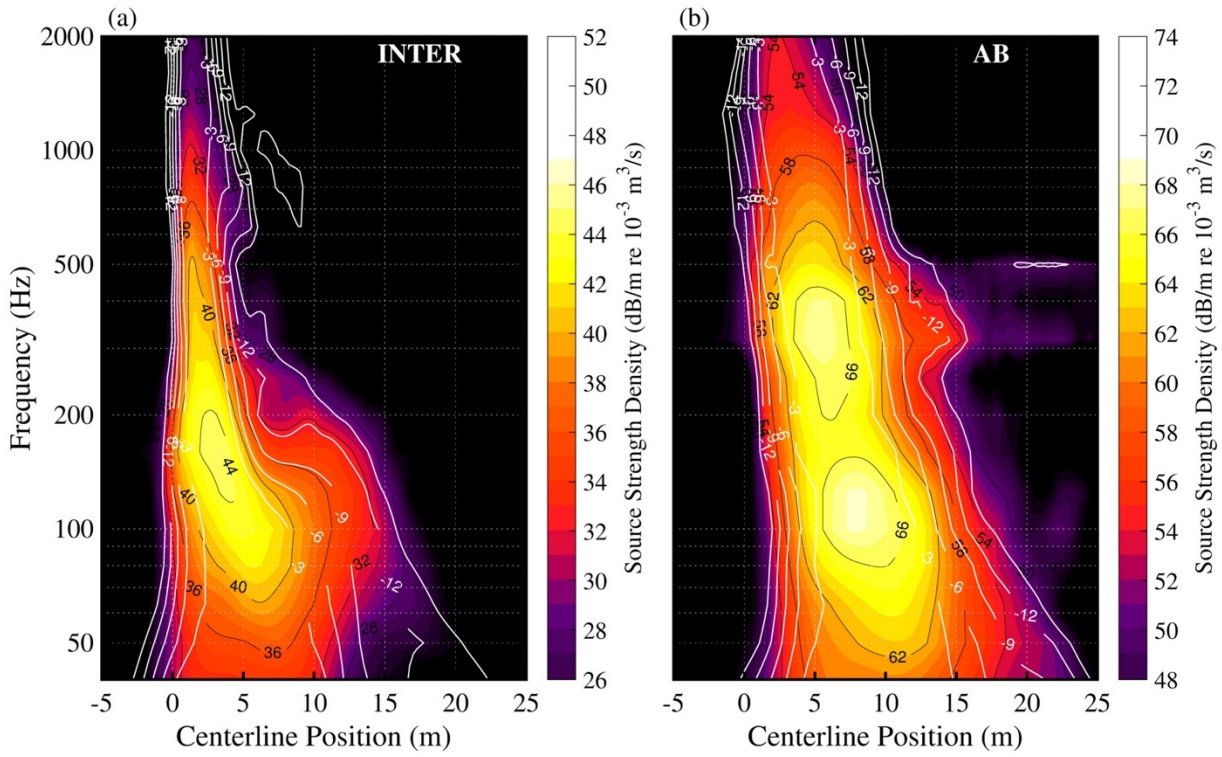

Fig. 4.10. Beamforming results at (a) INTER and (b) AB engine conditions.

In addition to the intensity analysis results of Stout *et al*., Wall *et al.*[29] used multisource, statistically-optimized near-field acoustical holography (M-SONAH) to estimate the pressure levels at the source distribution for INTER, MIL and AB conditions. A comparison of the

beamforming and holography results is shown in Table 4.1. The peak location and extent of the source estimates is provided for each engine condition and between the beamforming-based and holography-based results. Because the holography results were given as pressure estimates along the jet lip line (~0.3 m from the jet centerline), a Rayleigh integration of the beamforming results was performed to predict the lip line levels. The results of both methods generally show that peak location moves downstream and the source extent enlarges with increasing engine condition. The peak locations and source level distributions of the two methods are within 1.0 m for the three frequencies shown, apart from the peak level location at INTER at 100 Hz where the results deviate by nearly 4 m. However, the holography results in this case show higher variation, particularly below 100 Hz, of the peak level location, suggesting that the peak location becomes more ambiguous at these frequencies. In addition, the holography results were truncated according to the reconstruction uncertainty at the INTER condition, and a lower bound is given. At 100 Hz, the source extent, as measured using the 3 dB down locations from the peak level, varies by only about 1.0 m between engine conditions from INTER to AB in the beamforming results, although the peak location shifts 2.3 m farther downstream. At 200 Hz and 500 Hz, both results show that the peak location and extent follow predictable trends where the source extent becomes more compact and shifts towards the engine nozzle with increasing frequency.

Table 4.1. Comparison of source estimates between engine conditions for the peak location and spatial aperture over which the UPAINT-HM beamforming and the M-SONAH output (from Ref. [29]) is within 3 dB of the maximum. Results are in meters.

	100 Hz		200 Hz		500 Hz	
UPAINT-HM Beamforming						
Engine Condition	Peak	3 dB Width	Peak	3 dB Width	Peak	3 dB Width
INTER	6.4	7.0	3.1	3.6	1.9	2.0
MIL (100% ETR)	8.7	7.0	5.4	4.1	3.9	5.1
AB (150% ETR)	8.7	6.3	6.5	5.8	4.7	5.9
M-SONAH						
Engine Condition	Peak	3 dB Width	Peak	3 dB Width	Peak	3 dB Width
INTER	2.5	>5.5	2.0	3.0	1.5	>2.2
MIL (100% ETR)	7.3	7.4	5.0	4.9	3.0	4.0
AB (150% ETR)	8.2	8.2	6.0	5.8	4.9	5.0

The beamforming and holography analyses were performed for similar tactical measurements, providing a comparison of the two methods. Whereas beamforming results produce source strength density estimates, the holography results are given in terms of pressure and require the subsequent propagation of the beamforming results for a direct comparison. The holography results relied on scanning array measurements, which were taken nonsynchronously, and used ground array measurements as a reference to stitch the results together into partial fields.[131] These partial fields together constitute the entire scan measurement plane and are self-coherent and mutually incoherent. However, the quality of the partial-field decomposition process is a function of the reference array geometry and its proximity to the scan plane. For example, original scanning energy is lost when the coherence between the scanning measurements and reference array diminishes, particularly for high-frequency components. In these cases, the holography reconstructions lack sufficient energy to adequately represent the radiation and predict the source. The beamforming results, however, instead use the ground-based array as input and avoid the need to use the partial-fields. In addition, both methods suffer from effects of aliasing above the spatial Nyquist frequency. The recent addition of UPAINT to the HM results allows for an extension of

the results up to seven times past the 280 Hz design frequency of the ground array. Because the UPAINT processing is independent of the beamforming method, future work could also be done to apply it to holography techniques as well.

Additional analyses of the beamforming results as a function of engine conditions are provided in Fig. 4.11, where the L_{γ^2} values are shown for the INTER and AB conditions. In Fig. 4.11(a), the INTER L_{γ^2} values show much more variation as a function of reference position compared to those of MIL in Fig. 4.7 or AB in Fig. 4.11(b), including a dip in the L_{γ^2} results to < 2 m at 100 Hz and about $z = 3$ m. The L_{γ^2} values at INTER farther downstream are much higher, with values approaching 6 m at 100 Hz. At AB, the L_{γ^2} results show less variation as a function of reference location. For example, L_{γ^2} values range between about 2-4 m at 100 Hz across the source region, marked by the 12 dB down locations of the beamforming levels.

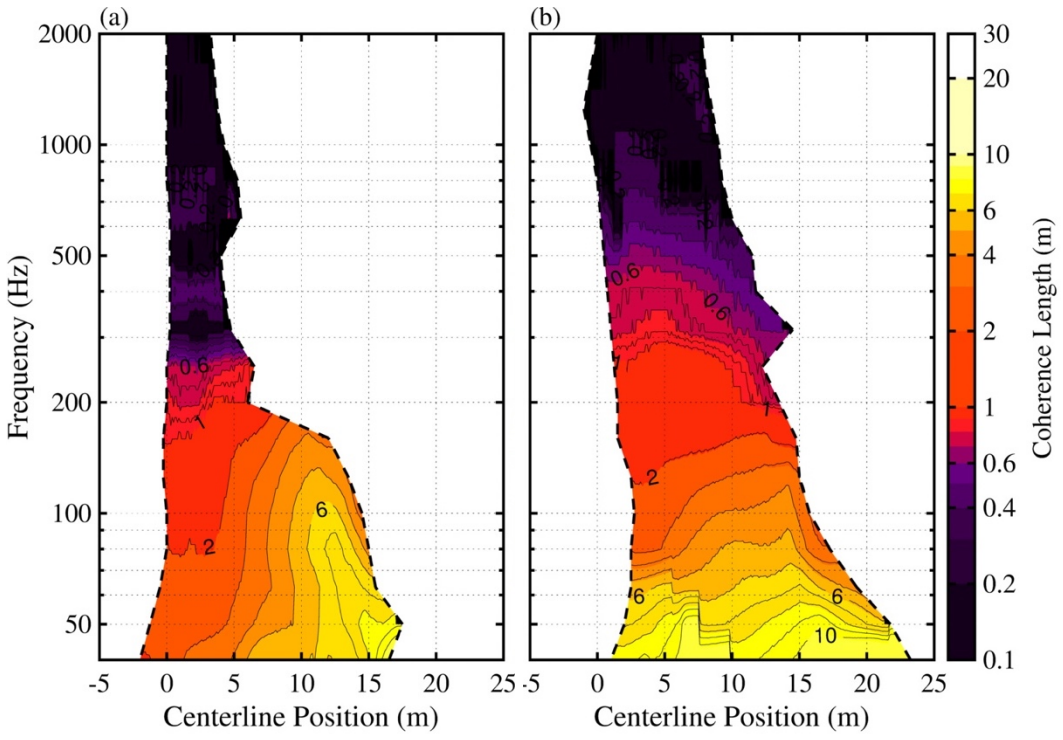

Fig. 4.11. Source L_{γ^2} values for (a) INTER and (b) AB engine conditions.

There are a few noteworthy comparisons of the L_{γ^2} values between engine conditions. Interestingly, the AB L_{γ^2} values are generally less than those at MIL. For example, at MIL the L_{γ^2} values at 100 Hz range from 3-5 m, which are about 1 m larger than at AB. Furthermore, the INTER L_{γ^2} values are even larger than those at MIL for centerline positions of $z > 10$ m. These L_{γ^2} values are highest in both conditions at $z = 12 - 13$ m, suggesting a similar mechanism that is responsible for the large values. However, L_{γ^2} values greater than 8 m are present in the MIL (and AB) results between 50-60 Hz regardless of the reference location, whereas they are only present in the INTER data at locations downstream beyond $z = 10$. In all cases, however, the source extent, measured using the 12 dB down levels shown by dashed lines, exceeds the coherence length values for a given frequency. In the context of a single distributed, coherent source, the L_{γ^2} value will be at least as large as the source size in the absence of noise. If multiple independent, distributed sources are present and overlapping, the L_{γ^2} value will decrease according to their relative strengths. Thus, in the context of the various engine condition analyses, the limited L_{γ^2} values within source region signify that multiple partially-correlated sources comprise the source. However, for frequencies below 60 Hz at MIL and AB, the L_{γ^2} are sufficiently high to suggest that one source radiates significantly more than any other potential contributors.

4.4 Conclusion

Phased-array methods have been successfully applied to measurements of a full-scale tactical engine at multiple operating conditions using a linear measurement array in the mid field of the acoustic radiation. The hybrid (beamforming) method (HM) was selected from results of a numerical study of a distributed source model performed in Chapter 2. It was found that the robust

nature of HM produced source estimates that smoothly varied with frequency. In addition, the unwrapped-phase array interpolation (UPAINT) method interpolates across the measurement levels and phase values to artificially increase the perceived array measurement density to remove negative effects caused by grating lobes. When applied to the jet noise beamforming results, it extended the source level estimates up to seven times above the array spatial Nyquist frequency by significantly reducing the adverse effects of grating lobes.

The beamforming source distribution at military engine condition (MIL) has been used to estimate the source self-coherence. At 100 Hz, the source has been shown to be highly self-coherent, while at 200 Hz and 500 Hz, the source coherence confirms that multiple independent sources would are required to adequately model the source at this frequency. These results have been shown in terms of coherence lengths (L_{γ^2}) to more efficiently represent the data. The phase speed has also been estimated using the beamforming-based source estimates, which can be used to determine the primary directivity of the source, and results corroborate similar acoustic vector intensity-based studies.[27]

In addition, the source has been further decomposed by beamforming separately using subarrays consisting of twenty sideline microphones and of thirty microphones located further downstream. This is motivated by a similarity spectra analysis of tactical radiation that suggests independent sideline- and downstream-radiating components.[91] The source estimated using the first subarray was centered at about 2.5 m and did not significantly vary with increasing frequency. However, the source estimated using the downstream subarray showed a source that varied in location and extent with frequency, and much of the overall radiation was included in this subarray-based source. The beamforming source levels from the sideline subarray peak at about 500 Hz and the relative amplitude of this source increases with respect to that of the downstream subarray

suggest that the source estimated by the first subarray characterizes an omnidirectional-type source whereas the secondary subarray source is much more directive towards high radiation angles. In addition, an analysis of the coherence properties resulting from the two subarrays reveals that the downstream-based source properties contain coherence lengths that are generally about double the values of the sideline-derived source for a given frequency. The level and coherence results point to a sideline radiation model that radiates omnidirectionally and which is derived of multiple independent sources, whereas downstream radiation is much more directed and generated with higher amplitude sources that are more self-coherent, consistent with a two-source jet noise model.[9]

Finally, source estimates were calculated along the jet centerline for three engine conditions ranging from intermediate (INTER) to full afterburner (AB). The source extent and peak level locations were compared with analyses of a comparable tactical measurement using near-field acoustical holography and vector intensity methods. In a direct comparison of the jet lip line pressure estimates using the holography reconstructions and beamforming results revealed that the estimated peak source locations and extents were nearly all within 1 m for the frequency cases tested at all engine conditions. A coherence analysis revealed that the coherence lengths at AB are generally less than those at MIL for a given frequency as well as for INTER towards the jet nozzle. Thus additional partially-correlated sources are required to adequately model these engine conditions. However, the INTER and MIL L_{γ^2} values were distinctly higher for distances greater than 12 m from the nozzle. This finding indicates the preeminence of a source distribution in this region that exists for both engine conditions.

This work characterizes the one-dimensional source estimate of a full-scale jet noise source. The beamforming results, when considered as an equivalent source model, constitute a

full-order model. However, an analytical reduced-order model of the beamforming results could similarly be used that could provide a more physically-intuitive model framework. For example, axial wavepackets have been used to represent the turbulent, hydrodynamic, and acoustic jet noise properties provide a suitable model to decompose the beamforming results.[2] Further phased-array work to characterize the azimuthal variation of the source is expected to provide additional insights to the source self-coherence as well as the azimuthal variation as engine condition and frequency vary. These efforts will provide better understanding of the source characteristics of tactical jet noise, thus allowing for improved models to predict the radiation.

Chapter 5

Beamforming-Based Wavepacket Model for Noise Predictions of Tactical Aircraft

5.1 Introduction

5.1.1 Background

Wavepacket models provide a reduced-order, analytical and physical framework for describing acoustic, hydrodynamic, and turbulence-related features of jet noise.[2] They are defined as advecting disturbances that are correlated over distances exceeding the integral scales of turbulence and have been used to describe the Mach wave radiation of supersonic jet noise[2, 45] as well as subsonic noise.[18] Many studies have focused modeling the turbulent wavepackets to describe the jet physical behavior.[2, 19, 132, 133] However, because of the harsh environment and hot, fast flows in the vicinity of full-scale jet noise measurements, the jet acoustic wavepacket properties are most easily analyzed using pressure measurements of the radiated field. Additionally, Towne *et al.*[3] found that the dominant turbulence wavepackets and those of the acoustic radiation were nearly uncorrelated. Acoustic phased array methods, such as beamforming,

can be used to estimate equivalent wavepacket descriptions of the source, which can predict the radiation in terms of level and coherence, without the need to measure the source directly.[37, 41, 56]

5.1.2 Equivalent Acoustic Wavepacket Models in Jet Noise Studies

Although not numerous, there are studies that provide context for acoustically modeling jet noise using wavepackets. Suzuki and Colonius[15] modeled the instability waves of near-field subsonic jet noise using an eigenfunction approach to beamforming. Kœnig *et al*[18] decomposed far-field noise measurements of a subsonic cold laboratory jet using an orthogonal decomposition of the pressure field into a single modal component, which they compared to the radiation of a wavepacket model. Papamoschou[45] showed that one wavepacket per frequency could adequately describe the measured far-field levels for lower frequencies and in the peak radiation direction. Du and Morris[89] applied conventional beamforming to simulated far-field jet noise data to obtain the acoustic complex pressure at the jet lipline, which was then decomposed using a wavepacket model for Strouhal numbers of 0.3 and 0.6. When compared to the simulated far-field pressure measurements, the estimated pressure field from the first wavepacket mode showed general agreement. Reba *et al.*[17] measured the hydrodynamic pressure field and fit the amplitude and correlation measurements to Gaussian-shaped wavepackets of the first two azimuthal modes. When used to predict acoustic levels, each wavepacket model showed good agreement with acoustic measurements in the peak radiation region. Cavalieri *et al.*[134] found that the axisymmetric acoustic wavepacket of a subsonic lab-scale jet is more strongly coupled to the jet velocity than higher-order azimuthal acoustic wavepackets. They predicted the source size to be 6-8 D in length and developed a model of the high-angle (measured relative to the jet inlet) downstream radiation. Additional work by Maia *et al.*[135] incorporated wavepacket self-coherence in a subsonic lab-scale jet study and showed that educed wavepackets of particle image velocimetry measurements that

included coherence decay more accurately estimated the radiated levels. They also found that a decomposition of the modeled radiated levels indicated roughly ten modes were required to capture the top 10 dB of the radiated energy. These studies have shown that levels of the sound field have been shown to be reasonably reproduced, particularly for the downstream radiation, using a few wavepackets. However, these studies have not attempted to model the radiated coherence properties using wavepacket models, and modeling both radiation levels and coherence necessitates a more complete jet noise source model. Additionally, few, if any, studies have modeled full-scale jet noise using acoustic wavepackets, particularly for tactical jet engine noise.

5.1.3 Overview

In this chapter, a multiple-wavepacket (MWP) source model of the noise radiation from a high-performance tactical aircraft is developed using HM beamforming results at the jet centerline. The resultant frequency-dependent ESM predicts both the levels and temporal properties (via the coherence) of the corresponding radiation.[17, 78] The HM algorithm that includes regularization,[60] described in Section 2.2.3.4, is used to produce frequency-domain beamforming results. These results were analyzed in detail in Chapter 4. However, the beamforming results are generally given in an inefficient, nonintuitive way that requires the full matrix solution to adequately describe the source reconstruction. A method to decompose the matrix solution into a concise model, consisting of a minimal number of wavepackets identified by a few parameters, is desired.

The MWP model, which is used to produce complex, extended source reconstructions over a wide frequency range, is described in Section 5.2. In addition, a numerical case study is also provided in Section 5.2.3 to show the method's benefits and limitations. In Section 5.3, beamforming ESMs of tactical jet noise measurements are used as inputs to produce MWP models. These MWP models are validated using benchmark jet noise measurements in the near and mid

fields. In addition, an optimization study guides the selection of the number of wavepackets for a given frequency. Finally, an engine condition analysis is performed to assess the variability of the MWP model as a function of engine power. It is shown that the reduced-order MWP model provides a simplified analytical framework that captures the salient radiation features as well as the field coherence properties observed in full-scale jet noise measurements. The models also provide physical insight into the equivalent acoustic source characteristics as they vary with frequency and engine condition.

5.2 Methods

In this section, a reduced-order model of beamforming-based jet noise predictions is developed. First, pressure measurements from a microphone array near an acoustic source are used as inputs to the HM beamforming algorithm, and the beamforming results produce an ESM. The beamforming-based source model is then used to create a reduced-order MWP model, which provides a simplified analytical framework and allows for extensions to other similar-typed sources. Others have attempted to model array measurements as wavepackets, including Kœnig *et al.*[18] as well as Papamoschou.[45] These studies modeled far-field measurements as a single wavepacket and included an additional component to model the residual energy. These methods were successful in modeling the far field radiation levels at the respective measurement input locations. To build upon these studies, the HM algorithm is used, which is capable of modeling source levels and coherence properties, and multiple axial wavepackets are incorporated into the source model. The MWP model is then used to predict the levels and coherence properties of the acoustic field. A numerical example is provided in which a multiple wavepacket source is used to illustrate the process and effectiveness of the beamforming and MWP model.

Unlike traditional far-field beamforming methods where the source-to-array distance is much larger than the array dimensions, beamforming in the geometric near field can lead to improved resolution.[42] However, the level of improvement is determined by the choice of reconstruction locations, the array geometry and dimensions relative to the source size, and the frequency under consideration. In this study, the array design is chosen to be sufficiently dense to produce high-resolution estimates of the source distribution without the need for deconvolution methods. In addition, the array spans the source region such that resolution across the source region is approximately uniform, although additional complications can arise from more directional sources. The array measurements are used as inputs to the Hybrid method (HM), which is described in Section 2.2.3.4. Additionally, the UPAINT method is applied to the array measurements to increase the usable bandwidth of the array for frequencies multiple times higher than the spatial Nyquist frequency. This process is described in Section 2.2.8. The beamforming results comprise the full-order source model, and they are decomposed into an MWP model. The method for determining the multiple wavepackets is detailed in Section 5.2.1. In Section 5.2.2, the methods for estimating the sound levels and coherence properties using the MWP model is given. Finally, a case study is given in Section 5.2.3 where array calculations from a numerical source model are used to as inputs to produce an MWP model. The benchmark model and MWP model are compared in terms of the wavepacket properties and their corresponding radiation levels.

5.2.1 Wavepacket Source Model

The HM beamforming results produce a full-order matrix solution of the original sources. However, when describing a distributed, partially correlated source, the number of elements in the beamforming source CSM, $\mathbf{Q}_{\mathrm{HM}}$, is s^2, where s is the number of source reconstruction locations, $\vec{r}_{i=1\ldots s}$. This number can be both large and excessive. Previous studies have shown the

effectiveness of an analytical wavepacket model to efficiently predict jet noise levels within the dominant radiation lobe using very few wavepacket models, although in many cases only a single wavepacket is used.[18, 45, 89] A single wavepacket model produces infinite coherence in both the source and corresponding radiation—contrary to the observed finite coherence lengths in actual jet noise. Reproducing the temporal features (i.e., coherence) of the field requires a more complex model, and an analytical MWP model provides the capability to describe the finite coherence lengths present both in the source model and in the radiated field.

The MWP model is generated from the HM beamforming results, which are decomposed through an iterative process, and each analytical wavepacket is projected onto the beamforming results to extract the wavepacket's amplitude and phase contribution. Each step is summarized in Fig. 5.1, and an explanation of each step follows. In addition, an example decomposition is provided in Section 5.2.3.

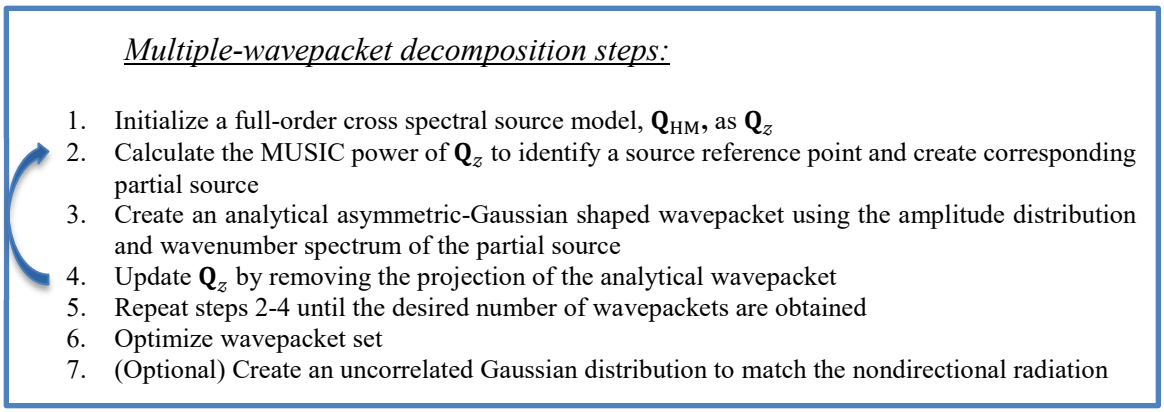

Fig. 5.1 Multiple wavepacket model creation process.

5.2.1.1 Initialization

The beamforming results matrix, $\mathbf{Q}_{\mathrm{HM}}$, is treated as a full-order model, and the goal of the wavepacket decomposition is to produce a reduced-order model, $\mathbf{Q}_{\mathrm{MWP}}$. First, the wavepacket

decomposition process is initialized by setting $\mathbf{Q}_z = \mathbf{Q_{HM}}$. The matrix $\mathbf{Q}_z$ is a running residual matrix from which the wavepackets are obtained.

5.2.1.2 Calculate MUSIC Power

The process of decomposing $\mathbf{Q}_z$ into a system of wavepackets is done iteratively, extracting one wavepacket at a time. First, the MUSIC (Multiple Signal Classification)[136] power algorithm is applied to $\mathbf{Q}_z$ to identify a source location. A summary of the MUSIC algorithm is presented here, and additional information is found in Ref. [136]. The noise subspace of $\mathbf{Q}_z$ is calculated using an eigendecomposition, such that

$$\mathbf{Q}_z = \mathbf{W}\,\mathbf{\Lambda}\,\mathbf{W}^{\mathrm{H}}, \tag{5.1}$$

where the unitary matrix, $\mathbf{W}$, is the set of singular vectors, and $\mathbf{\Lambda}$ is a diagonal matrix with the singular values comprising the diagonal. The singular vector matrix can be written $\mathbf{W} = [\mathbf{w}_1, \mathbf{w}_2, \dots, \mathbf{w}_s]$, where $\mathbf{w}_p$ are the singular vectors. A signal subspace of $\mathbf{Q}_z$ is defined by assuming the first ℓ singular vectors span the space. The corresponding residual subspace is then formed by defining

$$\mathbf{R} = \sum_{p=\ell+1}^{s} \mathbf{w}_p \mathbf{w}_p^{\mathrm{H}}. \tag{5.2}$$

Here, ℓ is set to 1 so that only the space spanned by the largest singular vector is considered.

The goal of the MUSIC algorithm is to determine the spatial distribution of the equivalent source that contains the largest percentage of coherent field energy. This is accomplished indirectly by searching for a spatial position that contributes least to the residual subspace, $\mathbf{R}$. A trial vector $\mathbf{u}_i$, representing a trial source location at $\vec{r}_i$, is assumed such that $\mathbf{u}_i = [0 \dots 0\ 1\ 0 \dots 0]^{\mathrm{T}}$, with the vector having a value of 1 at index i. The MUSIC power is then defined as

$$\mathbf{P}_{\mathbf{MUSIC}_i} = \frac{1}{\mathbf{u}_i^{\mathrm{H}}\,\mathbf{R}\,\mathbf{u}_i}. \tag{5.3}$$

Note that if the trial vector is equivalent to a singular vector in the signal subspace, $\mathbf{P}_{\mathbf{MUSIC}_i} \to \infty$. The MUSIC power estimates the most likely source position as the highest value of $\mathbf{P}_{\mathbf{MUSIC}_i}$, and the index i_{ref}, with corresponding location at $\vec{r}_{i_{\mathrm{ref}}}$, is chosen as the signal reference location.

Using the source reference location, $\vec{r}_{i_{\mathrm{ref}}}$, a partial source is extracted from $\mathbf{Q}_z$. The i_{ref}th row of $\mathbf{W}$ is chosen, corresponding to the i_{ref}th element of each singular vector as $\boldsymbol{v} = \left[\mathbf{w}_{1,i_{\mathrm{ref}}}, \mathbf{w}_{2,i_{\mathrm{ref}}} \ldots \mathbf{w}_{s,i_{\mathrm{ref}}}\right]$. This vector is multiplied by $\mathbf{W}$ and scaled by the i_{ref}th diagonal element of $\mathbf{Q}_z$. The product of $\boldsymbol{v}$ and the singular vector matrix, when scaled by the corresponding source level, extracts a partial source, $\boldsymbol{q}$, from $\mathbf{Q}_z$, such that

$$\boldsymbol{q} = \frac{\mathbf{W} \cdot \boldsymbol{v}^{\mathrm{H}}}{\sqrt{\boldsymbol{Q}_{z_{i_{\mathrm{ref}},i_{\mathrm{ref}}}}}}. \tag{5.4}$$

The partial source, $\boldsymbol{q}$, is an $[s,1]$ vector comprised of the portion of $\mathbf{Q}_z$ that exhibits coherence with a source located at $\vec{r}_{i_{\mathrm{ref}}}$. If only a single source located at $\vec{r}_{i_{\mathrm{ref}}}$ were present and the measurement was noiseless, then $\boldsymbol{q}\boldsymbol{q}^{\mathrm{H}}$ would be equivalent to $\mathbf{Q}_z$. Conversely, if high levels of additional signals and/or noise contributed to $\mathbf{Q}_z$, then $\boldsymbol{q}$ would only contain a portion of the energy of $\mathbf{Q}_z$.

5.2.1.3 Create Analytical Asymmetric-Gaussian Shaped Wavepacket

The extracted partial source, $\boldsymbol{q}$, is itself an equivalent source derived from the beamforming results that can be used to create a corresponding analytical wavepacket. If the potential source locations are distributed linearly, the shape of $\boldsymbol{q}$, in many cases, has similarities with that of an

asymmetric-Gaussian function—which are related to underlying wavepacket-like source properties[2]—with the functional form,

$$\boldsymbol{q}_{\mathrm{wpkt}}(z) = \begin{cases} a\exp\left(-\dfrac{4\ln 2\left(z - z_{i_{\mathrm{ref}}}\right)^2}{c_1^2} + j\left(k_{\mathrm{peak}}z\right)\right), & z < z_{i_{\mathrm{ref}}} \\ a\exp\left(-\dfrac{4\ln 2\left(z - z_{i_{\mathrm{ref}}}\right)^2}{c_2^2} + j\left(k_{\mathrm{peak}}z\right)\right), & z \geq z_{i_{\mathrm{ref}}} \end{cases}. \tag{5.5}$$

The analytical wavepacket function is defined by a, c_1 and c_2 that determine the partial source amplitude, the growth rate and the decay rate, respectively. Equation (5.5) is a function of the spatial variable, z, along the source region and $z_{i_{\mathrm{ref}}}$ is the component of $r_{i_{\mathrm{ref}}}$ along the source distribution dimension (i.e., z axis). The amplitude is set such that the peak of the magnitude of $\boldsymbol{q}_{\mathrm{wpkt}}(z_{i_{\mathrm{ref}}})$ is unity ($a = 1$). Because the wavepacket is asymmetric, the growth rate, c_1, is an 'equivalent' measure of the full-width half maximum value for the upstream ($z < z_{i_{\mathrm{ref}}}$) portion of the wavepacket. It is obtained by doubling the width from the peak at $z_{i_{\mathrm{ref}}}$ to the closest location in the $-z$ direction from the peak at which the amplitude is half of the maximum. The decay rate, c_2, for the second part of the wavepacket is obtained in similar fashion, except the width is measured from $z_{i_{\mathrm{ref}}}$ to the location in the $+z$ direction at which the amplitude is half of the maximum.

The wavepacket function is complex, and the complex argument is dependent on the peak wavenumber, k_{peak}, of the partial source's corresponding wavenumber spectrum. The wavenumber spectrum of the partial source is obtained by taking a discrete spatial Fourier transform of $\boldsymbol{q}$. The wavenumber corresponding to the maximum value of the spectrum determines

k_{peak}. The wavepacket fitting process provides an analytical representation that requires a minimal number of parameters, which can be obtained from $\boldsymbol{q}$.

5.2.1.4 Update $\mathbf{Q}_z$ by Removing Projection of the Analytical Wavepacket

While the analytical wavepacket, $\boldsymbol{q}_{\text{wpkt}}$, is representative of the corresponding partial source, $\boldsymbol{q}$, it only contains a portion of its energy and radiative properties, and the extent that the wavepacket model relates to $\mathbf{Q}_{\boldsymbol{z}}$ is unclear. A Graham-Schmidt process[137] is therefore performed using the eigenvectors of $\mathbf{Q}_{\boldsymbol{z}}$ and $\boldsymbol{q}_{\text{wpkt}}$ to obtain the span of $\boldsymbol{q}_{\text{wpkt}}$ and the corresponding residual, which are used to update $\mathbf{Q}_z$. The current cross spectral source matrix is decomposed as

$$\begin{aligned}\mathbf{Q}_{\boldsymbol{z}} = \mathbf{W}\,\boldsymbol{\Lambda}\,\mathbf{W}^{\mathrm{H}} &= \left(\mathbf{W}\,\boldsymbol{\Lambda}^{\frac{1}{2}}\right)\left(\boldsymbol{\Lambda}^{\frac{1}{2}}\,\mathbf{W}^{\mathrm{H}}\right) \\ &= \left(\mathbf{W}\,\boldsymbol{\Lambda}^{\frac{1}{2}}\right)\left(\mathbf{W}\;\boldsymbol{\Lambda}^{\frac{1}{2}}\right)^{\mathrm{H}} \\ &= \boldsymbol{\mathcal{W}}\,\boldsymbol{\mathcal{W}}^{\mathrm{H}}\end{aligned} \tag{5.6}$$

where singular values, σ_p, that comprise the diagonal of $\boldsymbol{\Lambda}$ are used to scale $\mathbf{w}_p$, which are the singular vectors of $\mathbf{Q}_{\boldsymbol{z}}$ (i.e., the columns of $\mathbf{W}$). This produces scaled singular vectors, $\boldsymbol{\mathcal{w}}_p$, such that $\boldsymbol{\mathcal{w}}_p = \sqrt{\boldsymbol{\sigma}_p}\,\mathbf{w}_p$. A Graham Schmidt process is then carried out on each of the scaled singular vectors,

$$\boldsymbol{\mathcal{w}}_{p,\text{rem}} = \boldsymbol{\mathcal{w}}_p - \frac{\boldsymbol{q}_{\text{wpkt}}^{\mathrm{H}}\boldsymbol{\mathcal{w}}_p}{\boldsymbol{q}_{\text{wpkt}}^{\mathrm{H}}\boldsymbol{q}_{\text{wpkt}}}\,\boldsymbol{q}_{\text{wpkt}}. \tag{5.7}$$

The remainder vectors are combined into a matrix, $\boldsymbol{\mathcal{W}}_{\text{rem}} = [\boldsymbol{\mathcal{w}}_{1,\text{rem}}, \boldsymbol{\mathcal{w}}_{2,\text{rem}}, \ldots \boldsymbol{\mathcal{w}}_{s,\text{rem}}]$, and a remainder matrix of $\mathbf{Q}_z$ is obtained,

$$\mathbf{Q}_{\boldsymbol{z},\text{rem}} = \boldsymbol{\mathcal{W}}_{\text{rem}}\boldsymbol{\mathcal{W}}_{\text{rem}}^{\mathrm{H}}. \tag{5.8}$$

The Graham-Schmidt process removes the projection of the wavepacket from the current cross spectral source matrix, and a new CSM is obtained.

5.2.1.5 Repeat to Obtain Desired Number of Wavepackets

The process of obtaining an additional analytical wavepacket is repeated by setting $\mathbf{Q}_{z+1} = \mathbf{Q}_{z,\mathrm{rem}}$ and proceeding from a recalculation of the MUSIC power (Section 5.2.1.2). The required number of wavepackets for a given reduced-order model is dependent on the number of sources present. For jet noise, the source spans many meters and many coherence lengths, depending on the frequency of interest. A discussion on the adequate number of wavepackets is provided for jet noise measurements in Section 5.3.5.

5.2.1.6 Optimize Set of Wavepackets

The wavepacket analytical functions, $\boldsymbol{q}_{\mathrm{wpkt}}$, provide a representative framework for the observed acoustic radiation from jet noise. However, because the analytical wavepackets only approximately model their corresponding partial sources, $\boldsymbol{q}$, the derived wavepacket set does not produce an orthogonal wavepacket basis. To best optimize the wavepacket set and assign amplitudes to each wavepacket, an optimization problem is cast as a linear set of equations, with the d wavepackets forming the columns of a wavepacket matrix, $\mathbf{Q}_{\mathrm{wpkt}} = \left[\boldsymbol{q}_{\mathrm{wpkt},1}, \boldsymbol{q}_{\mathrm{wpkt},2} \ldots \boldsymbol{q}_{\mathrm{wpkt},d}\right]$. The solution to

$$\mathbf{Q}_{\mathrm{wpkt}}\, \boldsymbol{\mathcal{C}} = \boldsymbol{\mathcal{W}}_0, \tag{5.9}$$

is desired, where $\boldsymbol{\mathcal{W}}_0$ refers to the solution of the first iteration of Eq. (5.6), and $\boldsymbol{\mathcal{C}}$ is a $[d, s]$ coefficient matrix containing the contributions of each analytical wavepacket to describe the scaled singular vectors. If the number of singular values comprising the signal space of $\boldsymbol{\mathcal{W}}_0$ is known, fewer than s vectors can be used in Eq. (5.9) as appropriate. The solution to Eq. (5.9) is obtained using a Moore-Penrose pseudoinverse,[40] and Tikhonov regularization is also applied for the coefficient matrix to ensure stability.[46] With regularization added, the solution to Eq. (5.9) is

$$\boldsymbol{\mathcal{C}} = \left(\mathbf{Q}_{\mathrm{wpkt}}^{\mathrm{H}}\mathbf{Q}_{\mathrm{wpkt}} + \delta\mathbf{I}\right)^{-1}\mathbf{Q}_{\mathrm{wpkt}}^{\mathrm{H}}\boldsymbol{\mathcal{W}}_0. \tag{5.10}$$

The identity matrix, **I**, is scaled by a penalization parameter, δ, which is determined here using the Morozov discrepancy principle, although generalized cross validation can also be used.[83] Having determined the coefficients describing the analytical wavepacket contributions, the reduced order scaled singular vectors are

$$\boldsymbol{\mathcal{W}}_{\mathrm{red}} = \left[\mathbf{Q}_{\mathrm{wpkt}}\,\boldsymbol{c}_1, \mathbf{Q}_{\mathrm{wpkt}}\,\boldsymbol{c}_2, \ldots, \mathbf{Q}_{\mathrm{wpkt}}\,\boldsymbol{c}_s\right], \tag{5.11}$$

where the coefficient vector, $\boldsymbol{c}_p$, is the pth column of $\boldsymbol{\mathcal{C}}$ and describes the contribution of each wavepacket to $\boldsymbol{w}_p$ in Eq. (5.9). The reduced-order MWP model is then calculated as

$$\mathbf{Q}_{\mathrm{MWP}} = \boldsymbol{\mathcal{W}}_{\mathrm{red}}\boldsymbol{\mathcal{W}}_{\mathrm{red}}^{\mathrm{H}}. \tag{5.12}$$

The reduced-order MWP model represented by Eq. (5.12) is a source CSM like the beamforming results, $\mathbf{Q}_{\mathrm{HM}}$, and can be treated like its full-order counterpart to predict the levels and coherence properties of the source and radiated field. However, the MWP model provides an analytical framework that decomposes the full-order results of $\mathbf{Q}_{\mathrm{HM}}$ to only the parameters that describe the wavepackets. In addition, the model methodology provides flexibility where a large number of wavepackets are necessary to adequately reproduce the full-order model results, especially as the frequency is varied. It also provides for a connection across frequency-dependent MWP models. However, while MWP models are obtained for multiple frequencies, a frequency-independent MWP model would require a clear connection between each wavepacket contribution in the MWP model across the frequency range. Therefore, the frequency-independent MWP model is not treated in this present study.

5.2.1.7 Create Uncorrelated Distribution for Nondirectional Radiation

The reduced-order MWP model characterizes the dominant wavepacket-like radiation of the beamforming-based ESM. In many cases, additional radiation is also present which is not wavepacket-like and, therefore, is more difficult to model using solely wavepacket contributions. In the case of jet noise, sideline radiation is typically described as the product of fine-scale structures (FSS) that radiate in an omnidirectional manner from multiple uncorrelated sources.[9] These FSS sources often require a significant number of additional wavepackets to effectively model the radiation. Instead, the addition of an uncorrelated distribution can augment the MWP model by characterizing the FSS-like radiation contributions.

Starting from Eq. (5.5), the uncorrelated distribution (UD) is assumed to be shaped as a symmetric Gaussian function ($c_{1,\mathrm{UD}} = c_{2,\mathrm{UD}}$) with $k_{\mathrm{peak}} = 0$ and centered at $b_{\mathrm{UD}} = z_{i_{\mathrm{max}}}$, where $z_{i_{\mathrm{max}}}$ is the location along the beamforming source distribution corresponding to the maximum amplitude of the beamforming results. While the UD model was not found to be especially sensitive to the width of the Gaussian function, the full-width half maximum value of the distribution is defined as three wavelengths, with a minimum value of 3 m. This choice was found to produce radiation that balances spherical and cylindrical spreading and imitates a compact yet finite UD.

The amplitude of the distribution is determined by matching the original levels at the measurement array, $\mathbf{p}$, to those predicted by the MWP model and the additional UD model in an iterative process. Starting with a distribution, $\boldsymbol{q}_{\mathrm{UD}}$, the amplitude of the UD model is initialized at unity. This distribution is added to the MWP model by placing the squared elements of the distribution along a diagonal matrix to create a CSM of the uncorrelated distribution with off-

diagonal elements set to zero. This produces the source cross spectral model for the MWP and UD as

$$\mathbf{Q}_{\mathrm{MWP+UD}} = \mathbf{Q}_{\mathrm{MWP}} + \mathrm{Diag}\left[\boldsymbol{q}_{\mathrm{UD}}^{\mathbf{2}}\right]. \tag{5.13}$$

The MWP+UD model is used to predict the levels at the original measurement array as $\mathbf{p}_{\mathrm{pred}}$, and the process for predicting the levels is described in Section 5.2.2. The error between $\mathbf{p}_{\mathrm{pred}}$ and $\mathbf{p}$ is calculated for a subsection of the measurement region where the MWP model underpredicts the levels, e.g., perpendicular to the jet at the sideline where fine-scale turbulent mixing noise is the primary contributor. The error is calculated as

$$\epsilon_{\alpha} = \frac{1}{r}\sum_{j=1}^{r}\left(\frac{\left|\mathbf{p}_{\mathrm{pred},j}\right|}{\left|\mathbf{p}_{j}\right|} - 1\right), \tag{5.14}$$

where the predicted and measured levels at the subset of r measurement locations determine the amplitude adjustment parameter, ϵ_{α}. The error is calculated for the αth iteration and the distribution amplitude, a_{UD}, is then updated as

$$a_{\mathrm{UD},\alpha+1} = a_{\mathrm{UD},\alpha}(\epsilon_{\alpha} - 1) \tag{5.15}$$

A new $\boldsymbol{q}_{\mathrm{UD}}$ is calculated and the process is repeated until $\mathbf{p}_{\mathrm{pred}}$ converges on $\mathbf{p}$ to determine a_{UD}. The process for determining the UD amplitude only uses the original input array levels, and the resultant UD model can then be used in conjunction with the MWP model to predict field levels elsewhere.

Whereas wavepackets are effective for modeling the high-amplitude, directive radiation, the UD model produces omnidirectional radiation to more easily model uncorrelated radiation components. In many cases the salient radiation features are captured by the wavepacket model, leaving higher-order residual components to be modeled using the UD. For example, Kœnig *et*

al.[18] modeled far-field measurements using a single wavepacket (the first and and showed that the residual radiation was comprised of multiple additional partial fields. In addition, Morgan *et al.*[118] modeled tactical jet engine noise using a correlated Rayleigh source distribution and an uncorrelated distribution. They found that the relative amplitude of the UD model to the correlated source distribution increased with frequency and for lower engine powers. Conversely, a larger percentage of the radiation was modeled by the correlated source distribution for lower frequencies and higher engine powers. While neither study examined coherence properties, the MWP model and UD model both provide means for estimating the source and radiation coherence characteristics that are otherwise difficult to model using a single wavepacket.

5.2.2 Field Predictions

Where source benchmarks are not available, the ability of the source model to predict field characteristics determines the model's effectiveness and reliability. The source model, $\mathbf{Q}$, is propagated for each of the methods by defining a new Green function, $\mathbf{G}_a$, that includes steering vectors for additional locations[40]. The CSM of field pressures, $\mathbf{C}_a$, at the desired locations can by modeled using

$$\mathbf{C}_a = |\mathbf{G}_a \mathbf{q}|^2 = \mathbf{G}_a \, \mathbf{Q} \, \mathbf{G}_a^{\mathbf{H}}. \tag{5.16}$$

Levels are calculated by taking the magnitude the diagonal elements of $\mathbf{C}_a$ and converting to a decibel scale. Equation (5.16) is also referred to as a Rayleigh integration.

Furthermore, $\mathbf{C}_a$ provides the necessary information to calculate the coherence properties of the field. For reference location, $\vec{r}_{j_1}$, and another position $\vec{r}_{j_2}$, the coherence is calculated as

$$\gamma^2_{j_1,j_2} = \frac{\left|\mathbf{C}_{a\,j_1,j_2}\right|^2}{\mathbf{C}_{a\,j_1,j_1}\mathbf{C}_{a\,j_2,j_2}}. \tag{5.17}$$

Because coherence is dependent on a reference location,[90] coherence lengths provide a means of summarizing the spatial variation in the coherence.[94] Coherence length, L_{γ^2}, is defined as the shortest distance from a reference position to a location where coherence drops below 0.5. The ability of MWP models obtained from beamforming methods to predict L_{γ^2} values is an important measure of the methods' success when applied to an extended, partially correlated source to produce a more complete source model of the radiation.

5.2.3 Wavepacket Decomposition Using a Numerical Source

To understand the capabilities and demonstrate the procedure of the wavepacket decomposition process, a numerical case study is presented for a single frequency. An axisymmetric source distribution consisting of six asymmetric-Gaussian wavepackets is chosen, and the magnitude and real part of the wavepackets are shown in Fig. 5.2(a). Each wavepacket is spatially distributed along the $+z$ axis and each contains unique parameters for various amplitudes, growth and decay rates, and peak locations. In addition, the peak wavenumber of each wavepacket varies such that the radiation directivity ranges from 95-135°—measured from the $-z$ axis—and the directivities are assigned sequentially such that the largest directivity corresponds to the wavepacket that peaks farthest from z=0 m. In addition, the growth and decay rates and relative amplitudes of each wavepacket are varied to distinguish them. The complete parameter set of the wavepacket source model is given in the left column of Table 5.1.

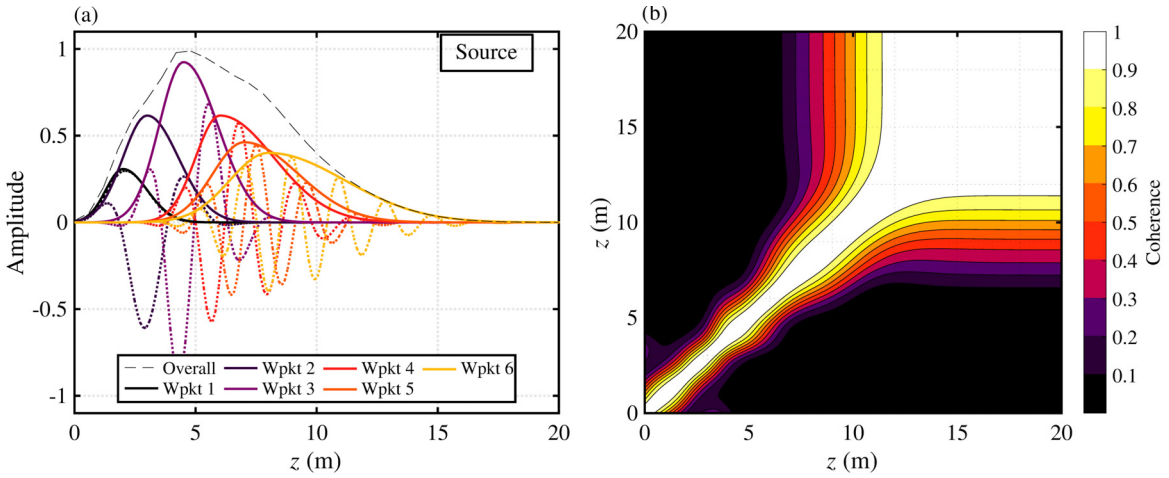

Fig. 5.2. (a) Numerical one-dimensional source model created using asymmetric-Gaussian-shaped wavepackets and (b) corresponding source coherence

In Fig. 5.2(b), the source coherence across the distribution is given, with the self-coherence shown along the diagonal and off-diagonal elements representing the coherence between two respective locations along the z axis. The source self-coherence varies as a function of position with coherence lengths that are small for $z < 9$ m, corresponding to regions where multiple wavepackets significantly overlap. Regions outside of this indicate where a single wavepacket source is the primary source.

The source distribution is aligned along the z-axis to mimic the jet noise setup shown in Fig. 5.3(a), with the setup assumed to lie in a free space environment. The array consists of 50 elements shown by blue dots. The array geometry mirrors the experimental setup described in Section 5.3.1. The corresponding simulated field level calculations are shown in Fig. 5.3(b), and the radiation pattern is meant to simulate the jet noise directivity as seen in Section 4.3.2 for the case of 250 Hz.

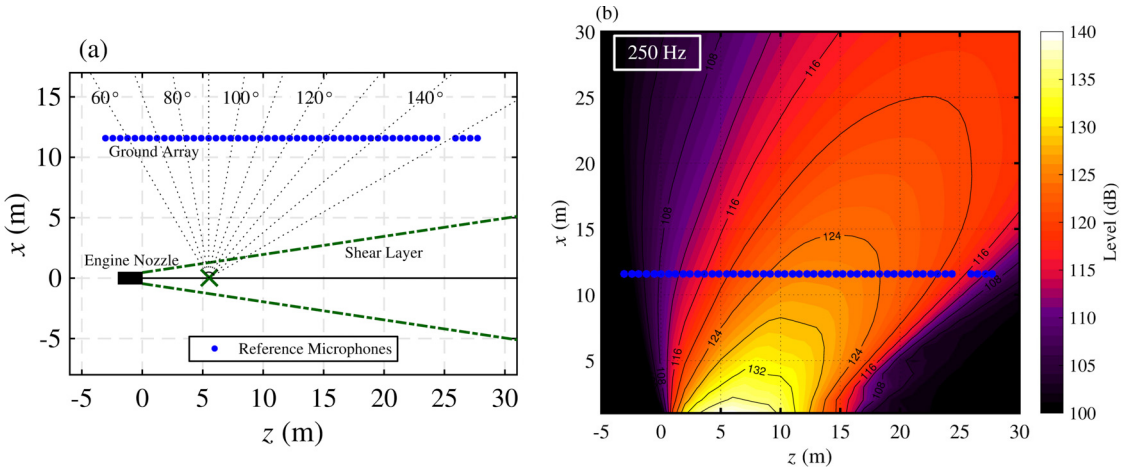

Fig. 5.3. (a) Numerical case geometry, with the source distributed along the z axis and (b) the corresponding simulated field levels.

The simulated array pressures are used as inputs to the HM to estimate the source CSM. The levels of the beamforming estimate (hereafter referred to as beamforming levels) are shown alongside the original overall source levels in Fig. 5.4. In this example, the regularization was chosen using the method used in Section 2.2.5, except that the regularization parameter was chosen to be 0.005% of $\boldsymbol{\lambda}_{\underline{\mathbf{G}}_1}$ to better match the current noise floor, where $\boldsymbol{\lambda}_{\underline{\mathbf{G}}_1}$ is the largest singular value of $\underline{\mathbf{G}}$ in Eq. (4.10). The estimated levels match the benchmark source distribution to within 1-2 dB over locations where the levels are within 20 dB of the peak level, with the level differences growing outside of this region, particularly for $z > 12$ m. Because the wavepacket that peaks at 8 m radiates with a directivity of 135°, some of the radiation is not entirely captured by the input array, and the resultant beamforming levels are slightly underestimated. However, the large majority of the source is accurately represented and provides a strong foundation from which the MWP decomposition process can take place.

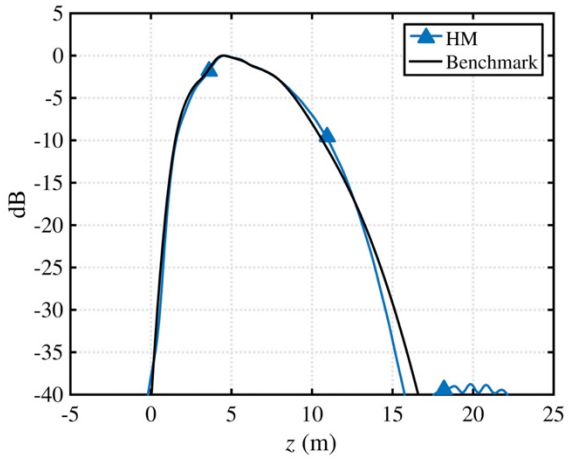

Fig. 5.4. Numerical source level estimate using HM beamforming, plotted with the original overall levels of the numerical source.

Next, the MWP decomposition process is performed, as described in Section 5.2.1. Each analytical wavepacket is determined in an iterative process until the desired number of wavepackets is reached, which in this case is chosen as six to compare with the original wavepacket source. For each iteration, the MUSIC power of the beamforming-based source CSM is calculated, and the location corresponding to the highest MUSIC power value is selected. From this location, a corresponding partial source is extracted. The real part and magnitude of the partial sources, $\boldsymbol{q}$, for each wavepacket iteration are shown in solid black in Fig. 5.5. Having created a partial source corresponding to the highest MUSIC power location, an analytical asymmetric-Gaussian function is fit to the partial source, $\boldsymbol{q}_{\mathrm{wpkt}}$, by using $\boldsymbol{q}$ to define the parameters in Eq. (5.5). The analytical wavepackets are shown in solid red in Fig. 5.5. Generally, the analytical function represents a significant portion of the partial source, although secondary peaks in the partial source are not usually well represented. The projection of this analytical function is removed from the beamforming-based source CSM and the process is repeated until six wavepackets are extracted. The ordering of the extracted wavepackets is based on the largest

MUSIC power selection process, and the wavepackets shown in Fig. 5.5 are reordered based on their peak level locations to compare with the original wavepacket parameters in Table 5.1.

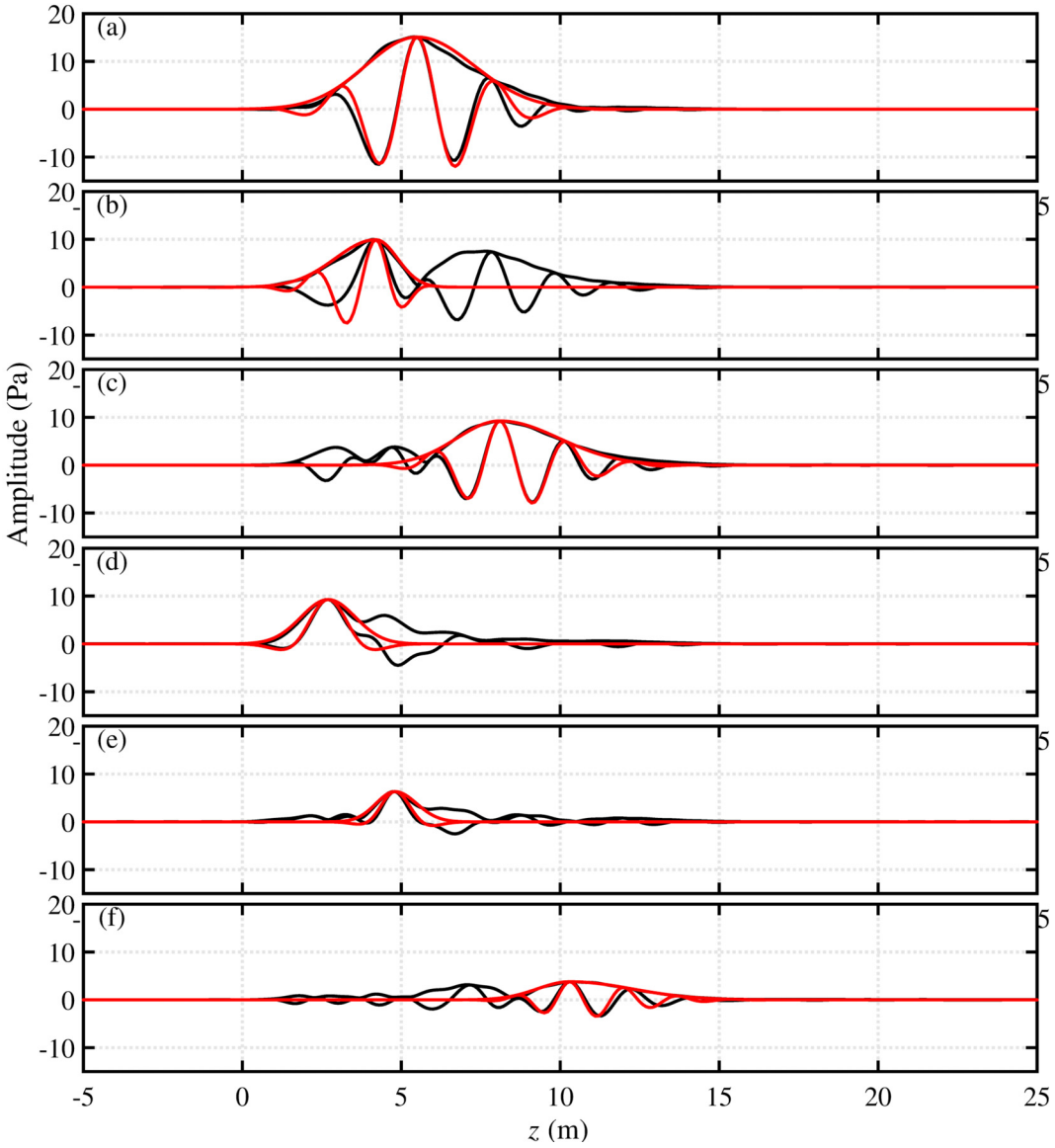

Fig. 5.5. Wavepacket decomposition technique to iteratively extract analytical wavepackets from partial sources.

Table 5.1. Input wavepacket parameters for numerical model using six asymmetric-Gaussian wavepacket functions, and resultant wavepacket fitting parameters from decomposition of beamforming results

Wavepacket Parameter (Wpkts 1-6)	*Numerical Wavepacket*	*Decomposed Wavepacket*
Amplitude (a)	0.33	0.61
	0.67	0.66
	1.00	0.42
	0.67	1.00
	0.50	0.61
	0.43	0.25
Center Location ($z_{i_{ref}}$)	2.0	2.7
	3.0	4.2
	4.5	4.8
	6.0	5.5
	7.0	8.1
	8.0	10.3
Growth Rate (c_1)	1.67	1.81
	2.35	1.48
	2.35	2.16
	2.35	1.31
	3.04	1.42
	3.72	1.65
Decay Rate (c_2)	2.35	1.81
	3.04	2.02
	3.33	2.02
	5.27	1.25
	5.27	1.22
	7.44	1.19
Wavenumber (k_{peak}) / Directivity Angle	0.40 / 95°	1.49 / 109°
	1.57 / 110°	3.20 / 134°
	2.29 / 120°	1.83 / 114°
	2.63 / 125°	2.51 / 123°
	2.94 / 130°	2.97 / 130°
	3.24 / 135°	3.66 / 143°

The analytical wavepackets are optimized in a least squares process and the resultant MWP model derived from the beamforming results is shown in Fig. 5.6 with corresponding parameters given in Table 5.1. The beamforming-based MWP model is shown in Fig. 5.6(a) and the numerical source is again shown in Fig. 5.6(b) for convenience. The combined MWP levels closely match those of the numerical source, although the individual wavepackets vary in shape and level from the original source wavepackets. For example, the largest source wavepacket amplitude is Wpkt 3

[in Fig. 5.6(b)], while the MWP's highest amplitude wavepacket is Wpkt 4 [in Fig. 5.6(a)]. In addition, the shapes of each wavepacket vary between the original and decomposed wavepackets. These effects are quantified in Table 5.1, where the resultant parameters associated with the MWP model are shown in the right column alongside those of the original wavepackets. Wpkt 6, for instance, peaks at $z = 8$ m and has growth and decay parameters of of 3.72 and 7.44, respectively for the source. The corresponding MWP parameters are 1.65 and 1.19 for the growth and decay values, indicating a wavepacket that decays more quickly than that of the source. This wavepacket also peaks at 10.3 m, which is 2.3 m farther downstream than the corresponding source wavepacket. The directivities (wavenumber) of the wavepackets, however, are more similar. All but the first two corresponding wavepackets have directivities that vary by less than 10°.

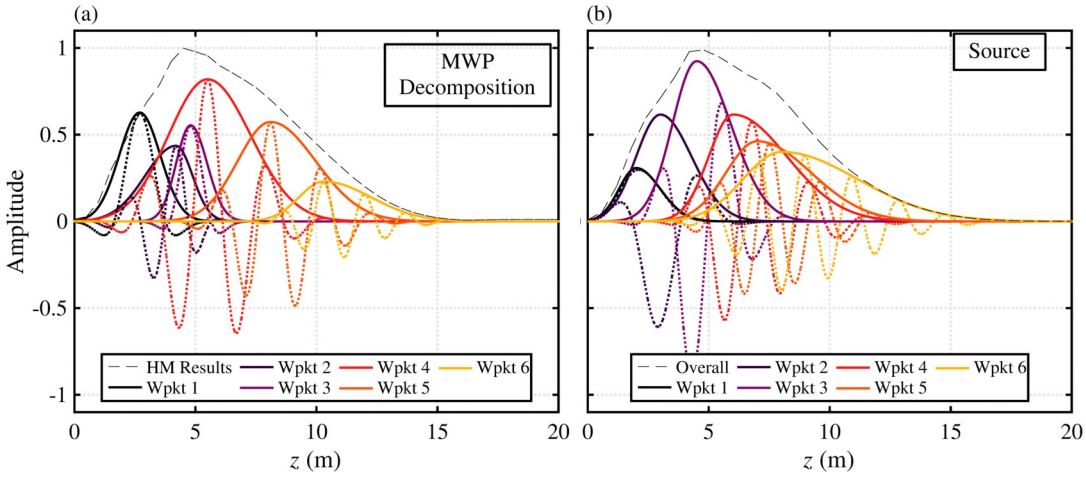

Fig. 5.6. (a) Beamforming results from measurements at ground-based array with corresponding wavepacket amplitude decompositions, and (b) the benchmark multiple-wavepacket source model.

The source coherence of the MWP model is also estimated and shown in Fig. 5.7(a), and the error of the estimate with respect to the benchmark coherence shown in Fig. 5.2(b) is given in Fig. 5.7(b). The estimated source coherence shows strong agreement with the numerical source coherence values, particularly for $4 \text{ m} < z < 8 \text{ m}$, which is where the highest source levels are

found. For $z < 4$ m, the coherence is overpredicted and indicates that there is not enough overlap between independent wavepackets in this region. Conversely, the coherence is slightly overpredicted near $z = 10$ m, indicating that there is too much overlap between independent wavepackets. Overall, the source coherence errors are within 0.1 over much of the source region, which shows that the MWP model sufficiently characterizes the source coherence.

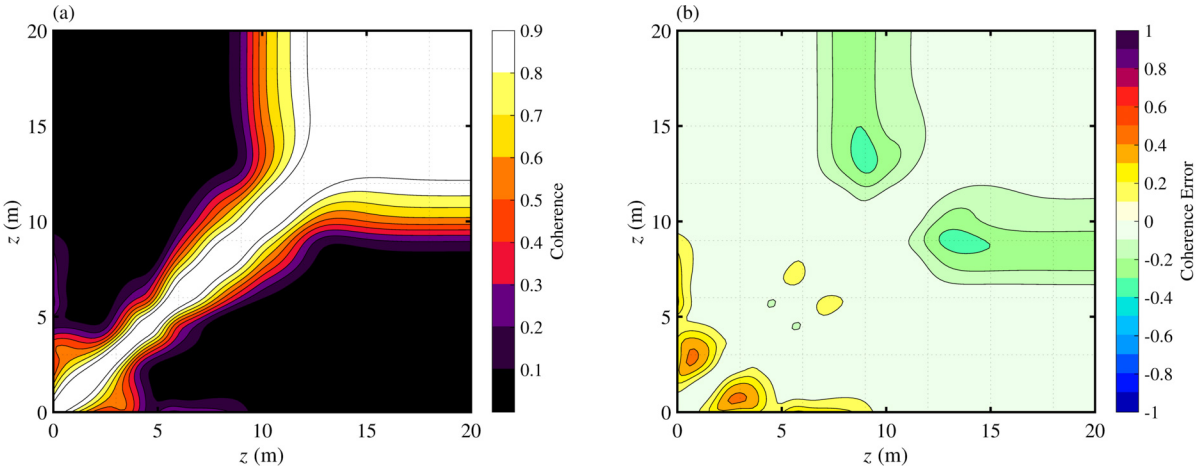

Fig. 5.7 (a) Predicted source coherence using the MWP model and (b) the coherence difference between the predicted coherence and benchmark coherence values shown in Fig. 5.2(b).

To compare the predictive capabilities of the MWP model, it is treated as an ESM and the radiated field levels are predicted using a Rayleigh integration [see Eq. (5.16)]. The estimated levels are shown in Fig. 5.8(a), and the error, in decibels, between the original and estimated levels is shown in Fig. 5.8(b). The estimated levels closely resemble those of the numerical source with errors that are generally within 1 dB of the simulated radiation levels except for the extreme upstream and downstream regions. The radiation that traverses the array at $z < 0$ m is underestimated. Because the first wavepacket in the numerical source radiates with a directivity of 95°, the radiation is underestimated in this region as the closest associated directivity in the MWP results is 109°. In addition, the levels of the radiation that propagates downstream beyond the array

are significantly overestimated. This result is due to the inability of the beamforming results to accurately predict the radiation beyond the array aperture and is a common shortcoming of beamforming (see Section 2.4.2). Further investigation in extrapolation methods may mitigate this result.[29]. However, the overall results highlight the effectiveness of the MWP model to adequately estimate the field.

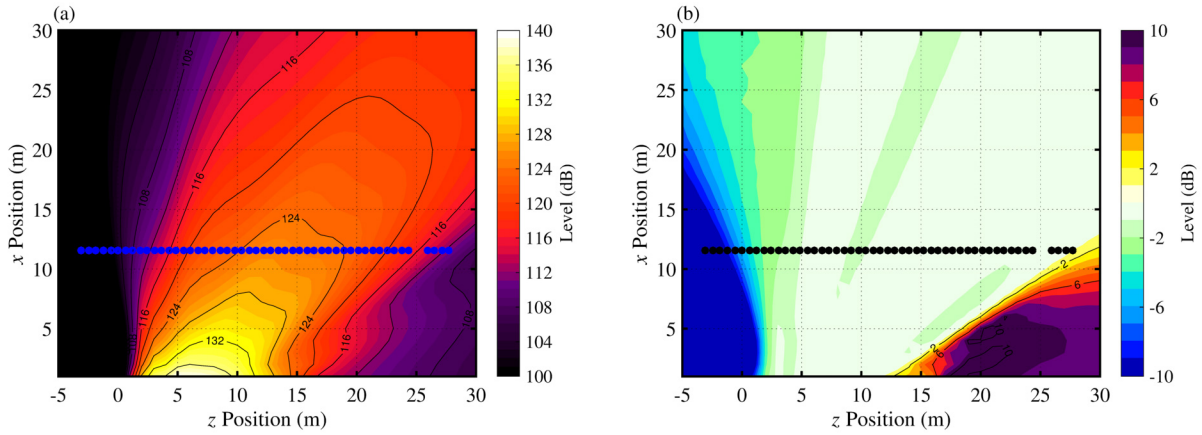

Fig. 5.8. (a) Predicted field levels using the MWP model and (b) the level difference, in dB, between the predicted MWP levels and simulated benchmark levels shown in Fig. 5.3(b).

The numerical case study highlights the capabilities and limitations of the MWP decomposition process. While the individual extracted wavepackets in the MWP model do not generally share similar properties with the numerical source in terms of their growth rate, decay rate and amplitude, they were found to have connections in terms of their center location and associated wavenumber. In particular, the directivities of the highest amplitude wavepackets were found to be within 3° of each other. In addition, the MWP model showed agreement with both the overall levels and the source coherence properties of the numerical source, and the estimated radiation levels generally agreed with the simulated levels to within 1 dB. Therefore, while many of the individual wavepacket features were not extracted, the MWP was successfully capable of representing the numerical source in terms of its cumulative properties, e.g., source level and

coherence and radiation properties. In addition, the MWP model simplified the beamforming results into a reduced-order model with a similar number of partial sources as found in the numerical source. In Section 5.3, the same beamforming and MWP decomposition process is applied to array measurements of full-scale jet noise data to produce a reduced-order model and extract the salient features of the ESM and corresponding predicted radiation.

5.3 Experimental Results

The methods described in Section 5.2 are used to analyze data taken from a full-scale turbofan engine. Measurements taken at a linear array are used as inputs to the HM beamforming algorithm to produce a full-order beamforming source model in Section 5.3.2. The MWP decomposition technique is applied to the beamforming measurements in Section 5.3.3 and the MWP model is analyzed. In Section 5.3.4, the beamforming source model and MWP model are used to predict radiation levels at the scan array and measurement arc, and the results are compared with the benchmark measurements. In addition, the coherence measured along a linear array is compared to predictions from the beamforming and MWP models. The predicted radiation of the MWP model is analyzed to show that key radiation features are well-represented. In Section 5.3.5, the required number of wavepackets in the MWP model is analyzed to adequately represent radiation level and coherence properties. Section 5.3.6 extends the MWP model analysis to include additional engine power configurations, showing the changes in the radiation properties as well as the requirements and resultant changes of the MWP model.

5.3.1 Experiment

Noise measurements were collected in the vicinity of an installed, full-scale turbofan engine at four engine conditions ranging from idle to afterburner. A planar microphone array arranged in an 18 x 5 rectangular grid pattern with 15 cm inter-element spacing was moved to multiple locations shown by triangles in Fig. 5.9(a). In this paper, only the microphones closest to the ground (0.38 m) are used from each planar array measurement, and they are referred to as the scan array, located 5.6 m from and parallel to the estimated shear layer. The same planar array, when placed at polar angles in the mid field between 90° and 148° (relative to the nozzle inlet) is referred to as the measurement arc. Each planar array measurement is collected at a radial distance of 23 m from the microphone array reference position, located 5.5 m downstream of the nozzle exit. The measurement arc is comprised of measurements from a single row of microphones, located at a height of 1.60 m, that are taken from each planar array measurement. A separate 50-microphone ground-based array recorded measurements simultaneously, for reference, during each planar microphone array measurement. As shown in Fig. 5.9(a), the ground array element spacing is 0.61 m, and the array spans 30 m. A detailed description of the experiment is found in Ref. [24].

The MIL condition data is analyzed in Sections 5.3.2-5.3.5, and Section 5.3.6 revisits the methods and procedures for additional engine conditions. The one-third octave levels at the ground-based array are shown in Fig. 5.9(b) for MIL engine condition (100% engine thrust request [ETR]). At this engine condition, two primary radiation lobes are present in the ground array data, centered at $z = 12.5$ m and 400 Hz and $z = 20$ m and 125 Hz. These radiation lobes extend many meters spatially as well as across multiple third-octave measurements. A more detailed analysis of the spectral variation of the measured sound as a function of angle is provided in Ref. [91]. While

jet-nozzle exit conditions are not available, Harker *et al.*[90] estimated an appropriate frequency-to-Strouhal-number (Sr) scaling of approximately $1.2 \cdot 10^{-3}$ Hz^{-1}, such that the frequency range reported here is approximately $0.05 \leq Sr \leq 2.4$.

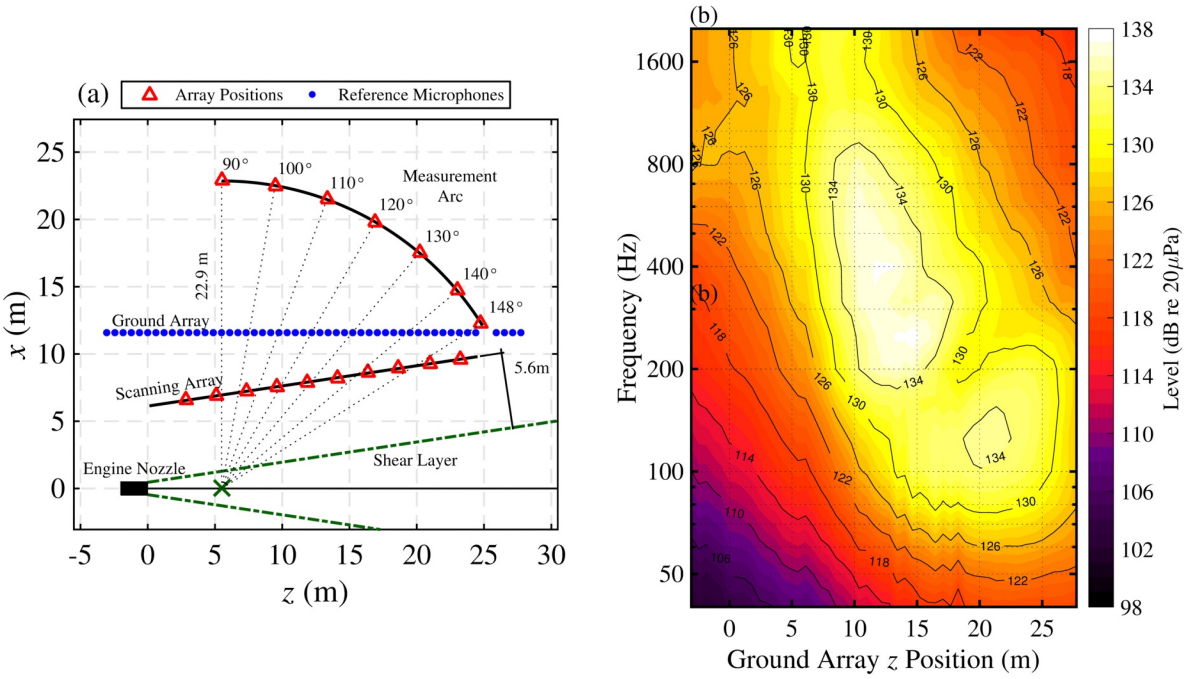

Fig. 5.9. (Left) Schematic of the experimental setup. Red triangle locations represent measurement positions of the 90-microphone planar array, and a ground-based array of 50 microphones are shown with blue dots. (Right) The one-third octave band levels at MIL engine condition along the ground array show evidence of a dual lobe.

5.3.2 Beamforming Results

The HM is applied to the ground-based array measurements shown in Fig. 5.9 to obtain beamforming equivalent source strength results along the jet centerline. The one-third-octave beamforming results, shown in Fig. 5.10(a), are obtained by summing over narrowband beamforming results at 6 Hz intervals within the band. In addition, the unwrapped phase interpolation method (UPAINT) was applied to array measurements in the frequency range above the spatial Nyquist frequency (280 Hz). The UPAINT method interpolates the levels and phase of the CSM prior to its input to beamforming to remove grating lobes and improve the array

performance for frequencies up to seven times higher than the spatial Nyquist. This method is described in Section 4.2.2 and the HM beamforming results are compared with and without the UPAINT processing in Section 4.3.2. The HM results below the spatial Nyquist frequency and the UPAINT-HM results above this frequency will hereafter be simply referred to as the HM results. To note, while the UPAINT method provides improved results above the spatial Nyquist frequency, some low-level processing artifacts remain in the source level estimates that can be observed for frequencies of 300-600 Hz for approximately $z > 12$ m.

The HM results show a large, distributed source region that peaks in amplitude for frequencies between 100-400 Hz. Liu *et al.*[10] used LES simulations to show that for highly heated jets the acoustic pressure levels at the jet lipline are affected by the radiation efficiency and turbulent kinetic energy corresponding to a given frequency. In particular, they showed that for simulations of a heated jet with afterburner-like conditions and with jet velocity of Mach 1.5, frequencies that correspond to subsonic convective phase speeds ($Sr \leq 0.1$) radiated inefficiently, while higher frequencies ($Sr \geq 0.1$) radiated with more efficient supersonic convective speeds. In addition, they found that the axial pressure distribution along the lipline of their simulations was greatest for $0.04 \leq Sr \leq 0.3$. They concluded that these observations explained the far-field radiation levels, which were greatest for $0.1 \leq Sr \leq 0.3$. This frequency range is approximately the range of frequencies at which the peak levels of the current study are found, both in the beamforming results in Fig. 5.10(a) as well as from the measured spectral levels in Fig. 5.9(b).

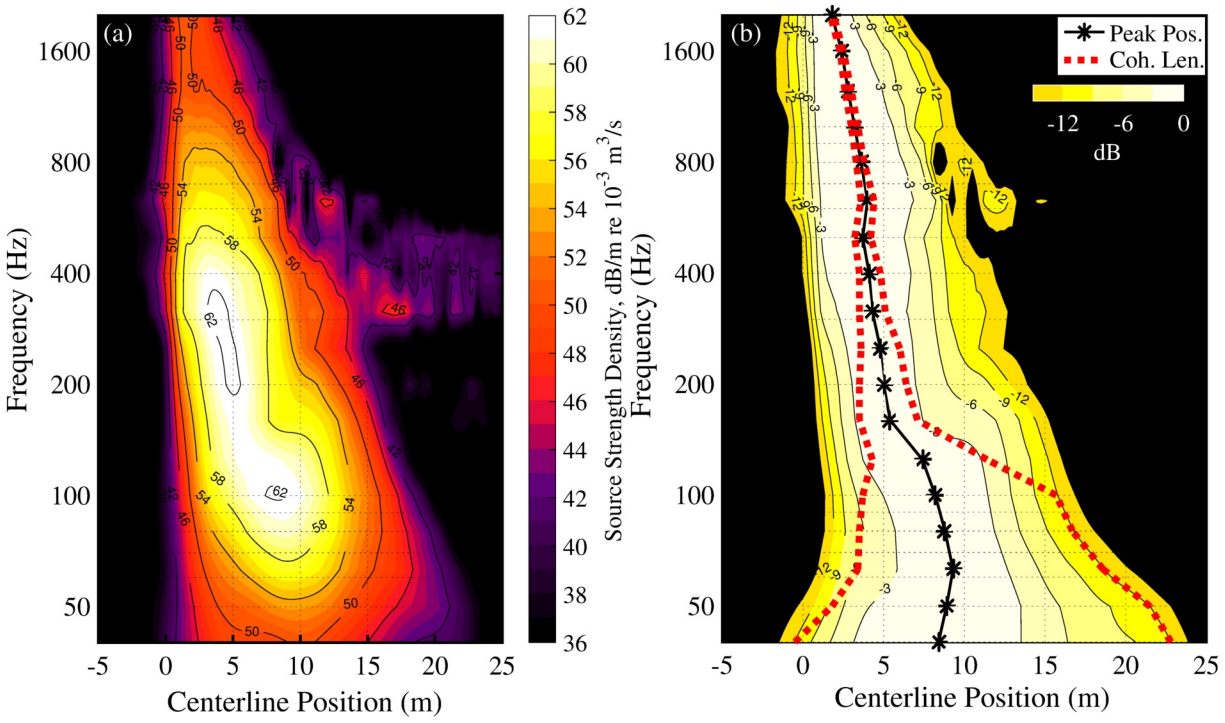

Fig. 5.10. Beamforming results at jet centerline shown (a) in absolute levels and (b) relative to the maximum level of each one-third octave band. The location of the maximum level at each frequency is indicated with an asterisk, and the coherence region over which coherence exceeds 0.5 relative to the peak beamforming level location is also delineated with a red dashed line.

The frequency-dependent beamforming results are also plotted relative to their respective maximum levels in Fig. 5.10(b) to more clearly show the beamforming source distribution. The source region extends many meters downstream of the nozzle (located at $z = 0$ m) with the peak locations marked by the black asterisks. A common report of prior beamforming studies of jet noise—including those using LES-simulations,[61] laboratory[37, 39] and full-scale experiments[41, 56]—is the gradual decrease in source size as well as the upstream-shifting peak level location with increasing frequency. The contraction in source size here agrees with previous findings and, as measured in Fig. 5.10(b) using the 3 dB-down contour lines, the source distribution reduces from 10.4 m at 40 Hz to 2.5 m at 2000 Hz. When adjusted by wavelength, however, the source distribution increases steadily from 1.2λ at 40 Hz to 14.3λ at 2000 Hz. The beamforming results

shown in Fig. 5.10(b) are scaled by wavelength in Fig. 5.11. These results are qualitatively consistent with measurements from Schlinker *et al.*[41] They found that for an uninstalled full-scale supersonic exhaust stream engine, the source width—measured using beamforming results using the 3 dB-down points from the maximum level—increased by about a factor of six from 250 Hz to 2000 Hz when scaled by wavelength. The source width of the results of Fig. 5.11, as scaled by wavelength, increase by nearly a factor of five over the same frequencies range. In addition, while the peak level location, $z_{peak}(f)$, shifts towards the nozzle with increasing frequency, when scaled by wavelength this distance increases gradually. The peak location shifts from 8.4 m (1.0λ) at 40 Hz to 5.0 m (2.9λ) at 200 Hz and even more pronounced for higher frequencies [e.g., 1.8 m (10.3λ) at 2000 Hz]. Lee and Bridges[128] found that for a heated supersonic jet with a jet diameter (D) of 2 inches, a jet Mach number of 1.57 and a temperature ratio of 2.7, the peak beamforming levels peaked between 13 z/D at $Sr = .05$ and 2 z/D at $Sr = 2.4$. These values are consistent with the change in peak location in Fig. 5.10(b), although the ratio of the shift in the peak level location between 40 Hz and 2000 Hz is slightly larger in the lab-scale experiment (6.5 compared to 4.7 for the present engine condition).

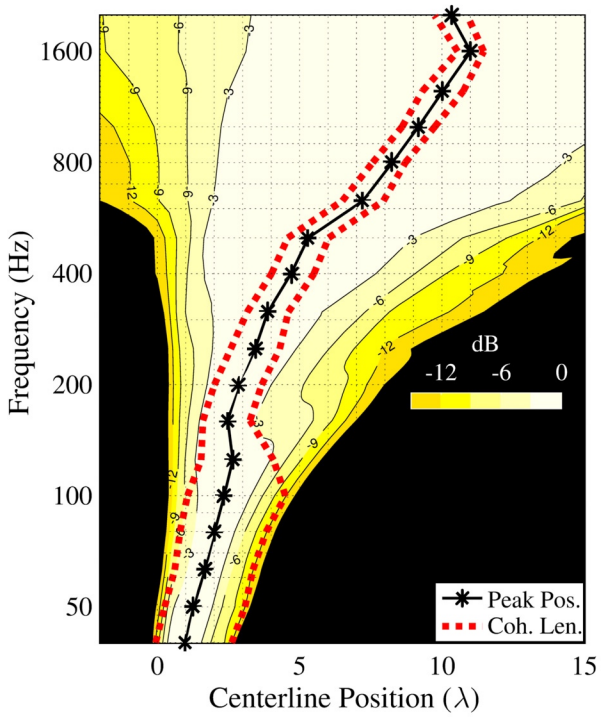

Fig. 5.11 Scaled beamforming results at jet centerline as shown in Fig. 5.10(b), but the axial distance is scaled by wavelength with 0λ corresponding to the nozzle exit location.

The coherence of the beamforming results is also calculated using Eq. (5.17) (replacing $\mathbf{C_a}$ for $\mathbf{Q}$). The locations at which coherence drops below 0.5, as measured relative to the frequency-dependent peak beamforming level locations, are marked by red dashed lines in Fig. 5.10(b) and Fig. 5.11. As defined in Section 5.2.2, the closest distance between a reference location (the peak level location) and these coherence lines for a given frequency is referred to as the coherence length, L_{γ^2}. The L_{γ^2} values at frequencies below 160 Hz are on the order of about 1 λ (3-9 m) and the locations at which coherence drops below 0.5 roughly coincide with the 12 dB down lines of the beamforming results in Fig. 5.10(b). However, L_{γ^2} values at and above 160 Hz are only about 0.5-0.8λ ($\leq$ 1.7m). The source L_{γ^2} values as well as source size and peak level location suggest a transition region separating phenomenological distinctions in the source characteristics. This transition region has appeared in other studies of full-scale jet engines as well. Stout *et al.*[27] noted

a dramatic shift between 150-250 Hz in the estimated source location using an vector intensity-based approach. The source region shifted from 5-8 m to 3-5 m from the nozzle exit in this transition region. Wall *et al.*[29] showed a split in the reconstructed equivalent source distribution in this region using an advanced acoustical holography technique. They also observed that the peak source level location also shifted from about 7 m to about 5 m downstream from the nozzle exit. Above 160 Hz, the increased source size (in terms of wavelength) and decreased coherence lengths demonstrate that multiple partially-correlated sources are required to appropriately model the source distribution.

5.3.3 Wavepacket Decompositions

From the equivalent beamforming-based source reconstructions in Fig. 5.10, MWP source models are developed for six wavepackets using the techniques described in Section 5.2. The decomposed MWP models are shown in Fig. 5.12(a-c) for 500, 200 and 100 Hz, which represent above, in, and below the transition region in the beamforming source results. The beamforming levels are shown as a solid black line, with the MWP overall level shown in a gray dotted line, and the six individual wavepackets are shown as dashed color lines. Overall, the combined level of the MWP model shows good agreement with the beamforming results, particularly at 100 Hz. However, the low-level beamforming results are not represented by the MWP model, and the individual wavepacket peaks become more evident at 500 Hz. In addition, an individual wavepacket level will exceed the overall levels in some instances. This results from the partially-coherent addition of the wavepackets and the ensuing potential for constructive and destructive interferences. While methods are implemented in Section 5.2.1 to produce the fewest number of wavepackets that reproduce the beamforming results, each wavepacket is finite in shape and, thus, its associated wavenumber spectrum is continuous. Therefore, some overlap occurs between the

various wavepackets in the wavenumber domain and allows for interference. The individual wavepackets are therefore not orthogonal, and the degree of interference is a function of the spatial separation between the wavepackets.

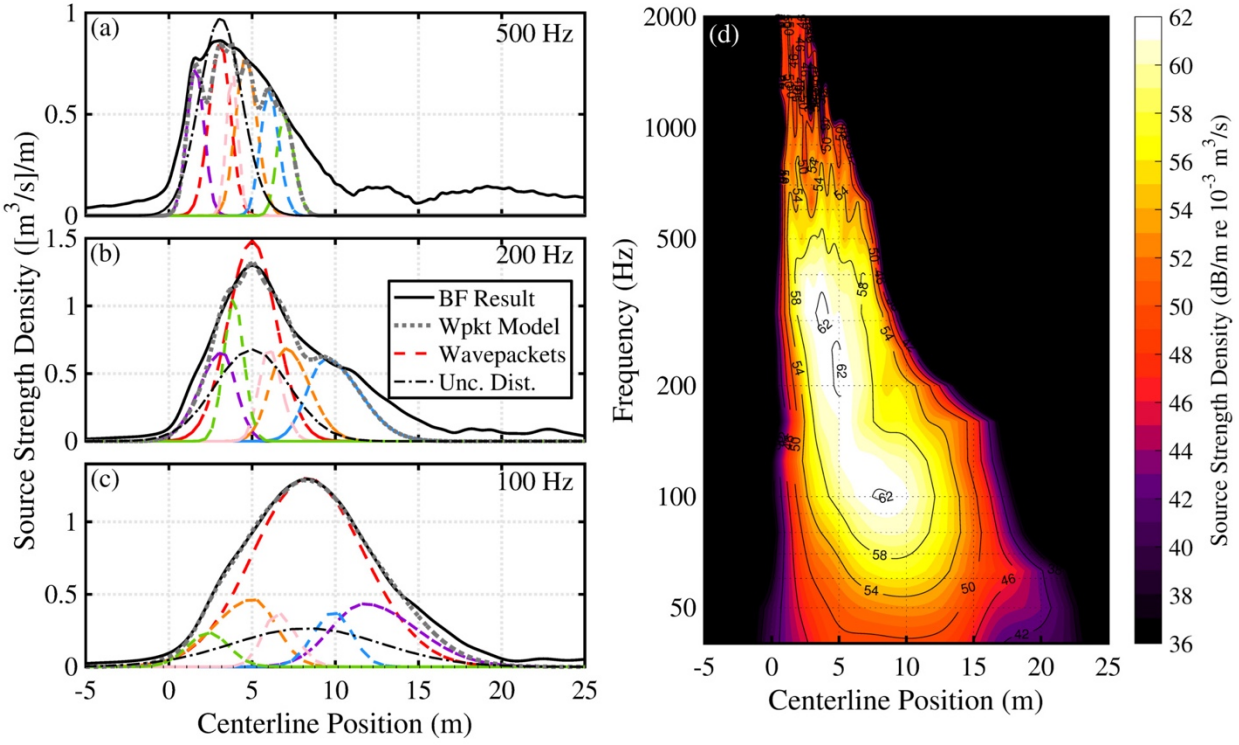

Fig. 5.12 Wavepacket examples at (a) 500 Hz, (b) 200 Hz, and (c) 100 Hz using six wavepackets are shown with the beamforming source strength and resultant MWP model levels. A UD is also plotted as a dash-dot line alongside each result. (d) Combined levels of the frequency-dependent MWP models are shown along jet centerline.

The combined levels of the MWP models are shown in Fig. 5.12(d) for each of the one-third-octave, with the MWP model at each frequency corresponding to the combined levels in Fig. 5.12(a-c). The results share many of the salient features seen in the beamforming results in Fig. 5.10(a), particularly for levels which are within the top 12 dB of the peak level for each frequency. Levels below this, however, are underpredicted by the MWP model, including regions far upstream or downstream of the main source region. This may not necessarily be problematic, as the low-level beamforming results are typically less consequential and the physical interpretation

of levels below the top 12 dB may have higher errors from the HM and UPAINT processing. In addition, results above 500 Hz become jagged, as the individual wavepacket contributions are more visible to the combined levels as seen in Fig. 5.12(a). These errors, produced by the reduced order of the MWP model may become large for sufficiently high frequencies, and an optimization study to determine a sufficient number of wavepackets for a given frequency is explored in Section 5.3.5.

Low-order models have been shown by Papamoschou[45] and by Koenig *et al.*[18] to be somewhat effective in describing the Mach wave radiation in far-field predictions, although they often do not entirely reproduce the radiated levels. This is solved by either increasing the order of the model (e.g., adding additional wavepackets) or by including a compensatory source. For an example of the latter, Papamoschou[45] included an additional monopole source to his single wavepacket model to boost the sideline radiation. While the effect of additional wavepackets on the source model is explored in Section 5.3.5, a UD is also applied to augment the reduced-order MWP model. It is shown in Fig. 5.12(a-c) with a dash-dot line. The UD is calculated to match the levels measured along the sideline ($-2\ \mathrm{m} \leq z \leq 5\ \mathrm{m}$) of the input array as explained in Section 5.2.1.7. Due to the uncorrelated nature of this distribution, individual components that comprise the uncorrelated distribution add incoherently and, thus, produce overall levels that are less than those of the correlated distribution. A similar finding was noted by Morgan *et al.*,[118] who found that while the uncorrelated distribution levels were usually higher than the correlated source levels, they accounted for a much lower percentage of the radiated energy.

5.3.4 Estimated Field Levels and Coherence

An ESM allows for an efficient means to estimate and characterize the level and coherence information of the radiation field. To validate the beamforming-based ESM (hereafter referred to

as beamforming model) and the MWP model previously described, the estimated levels at the ground array, the scan array and the measurement arc are considered. A Rayleigh integral is used to predict the levels as described in Section 5.2.2. In addition, while the input array was located at the ground, the scan array and measurement arc were at heights of 0.38 m and 1.60 m, respectively. To compensate for the additional ground-based interference patterns, an image source is modeled and it is propagated, together with the original source model, to predict the radiated levels at the scan array and measurement arc. The image source properties are identical to those of the original source, except that the height is mirrored about the ground plane. In addition, a test case is also included in which the uncorrelated Gaussian distribution is used to augment the wavepacket model. Measurements at the ground array, the scan array and the measurement arc are compared to the estimated levels using the three methods at 100 Hz, 200 Hz and 500 Hz in Fig. 5.13. In each plot, the measurements are represented by black triangles, and the predicted levels from the beamforming source model are shown by red squares. The orange circles and purple asterisks represent the predicted levels from the MWP model and MWP model with the UD (MWP+UD model), respectively. The estimated levels from the beamforming source model and the MWP model show good agreement at all three measurement locations, within 2 dB at most locations for all frequencies, with two notable exceptions. First, the estimated levels of the MWP model along the sideline ($z < 5$ m) in many cases underestimate the measurement levels by as much as 15 dB or more. This is best seen on the measurements from the ground array, which extends up to about 4.5 m farther upstream than the scan array and about 7 m farther than the measurement arc. The addition of the uncorrelated distribution in the MWP+UD model boosts the sideline levels such that they are within measurement levels to within 2 dB throughout. Second, the predicted levels at the scan array and the measurement arc at 500 Hz are slightly larger, up to 5 dB (discounting the

sideline). While the UD addition improves the sideline levels, the levels farther downstream are still slightly underpredicted as compared to the beamforming model estimates. In this case, additional wavepackets beyond the six used for the MWP model here may be necessary for improved results.

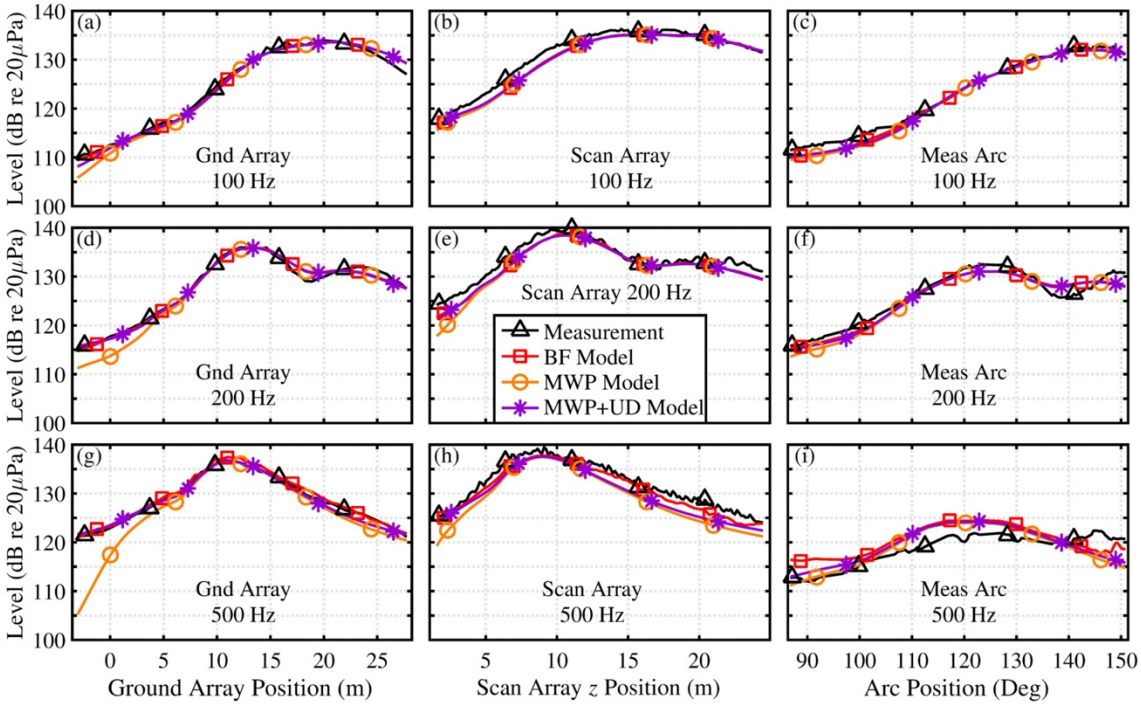

Fig. 5.13. Comparisons of measurements and predicted levels for (a-c) 100 Hz, (d-f) 200 Hz and (g-i) 500 Hz at (left) the ground array, (middle) the scan array, and (right) the measurement arc. The predictions are made using a beamforming model, an MWP model, and an MWP+UD model.

The capabilities of the beamforming model and wavepacket model to estimate the field levels extend beyond the 100 Hz, 200 Hz and 500 Hz examples, as shown in Fig. 5.13. The one-third octave spectra from 40 Hz to 2000 Hz at the measurement arc are shown in Fig. 5.14(a). In addition, the estimated levels using the MWP model and the MWP+UD model are given in Fig. 5.14(b-c), respectively, and the errors of these estimated levels when compared to measurements are given in Fig. 5.14(d-e). The measurements show two strong radiation lobes, one centered about 145° at 125 Hz, and the other centered at about 125° at 250 Hz. In addition, features above 400 Hz

are present that are not found in the corresponding ground array measurements [Fig. 5.9(b)]. A path difference comparison between a source located at $z = 5.5$ m along the jet centerline and a corresponding image source reflected about the ground plane was conducted. It predicts that interference nulls should be present at the measurement arc for frequencies of 600 Hz and 2000 Hz. Consequently, while there appears to be a third radiation lobe, centered at 130° and 1000 Hz, this may simply be a result of the interference nulls. However, the two lobes present below 500 Hz are not the result of ground interference patterns, as they are also present in the ground-based measurements in Fig. 5.9(b). The size and frequency bandwidth of the two lobes are considerable, expanding many degrees in either direction and spanning multiple third-octave bands. The multilobe features seen at 200 Hz in Fig. 5.13(f) are more apparent here and seem to be formed from contributions from both lobes. In the radiation from both MWP and MWP+UD models, the key features of the radiation are present.

As shown in Fig. 5.14(d-e), the predicted levels using the MWP model show agreement with the measurements with errors less than 3 dB over most the measurement arc and across the frequency bandwidth, with notable exceptions along the regions where the interference nulls are believed to be located. In addition, the errors to the sideline range from 1-8 dB owing to the difficulty of wavepackets to predict sideline radiation, where short coherence lengths shown in Section 3.4.2.1 indicate radiation from multiple independent sources. The addition of the uncorrelated distribution in the MWP+UD model significantly boosts the sideline levels so that the errors are reduced from 1-8 dB errors at the sideline (discounting the interference null errors) to about 1-2 dB along the upstream edge of the measurement arc. At 315 Hz and 400 Hz, however, the errors along the sideline increase with the UD addition. The cause is unknown, although it may

be an overestimation of the beamforming ESM levels, related to the additional spatial unwrapping applied in addition to the UPAINT processing at these frequencies.

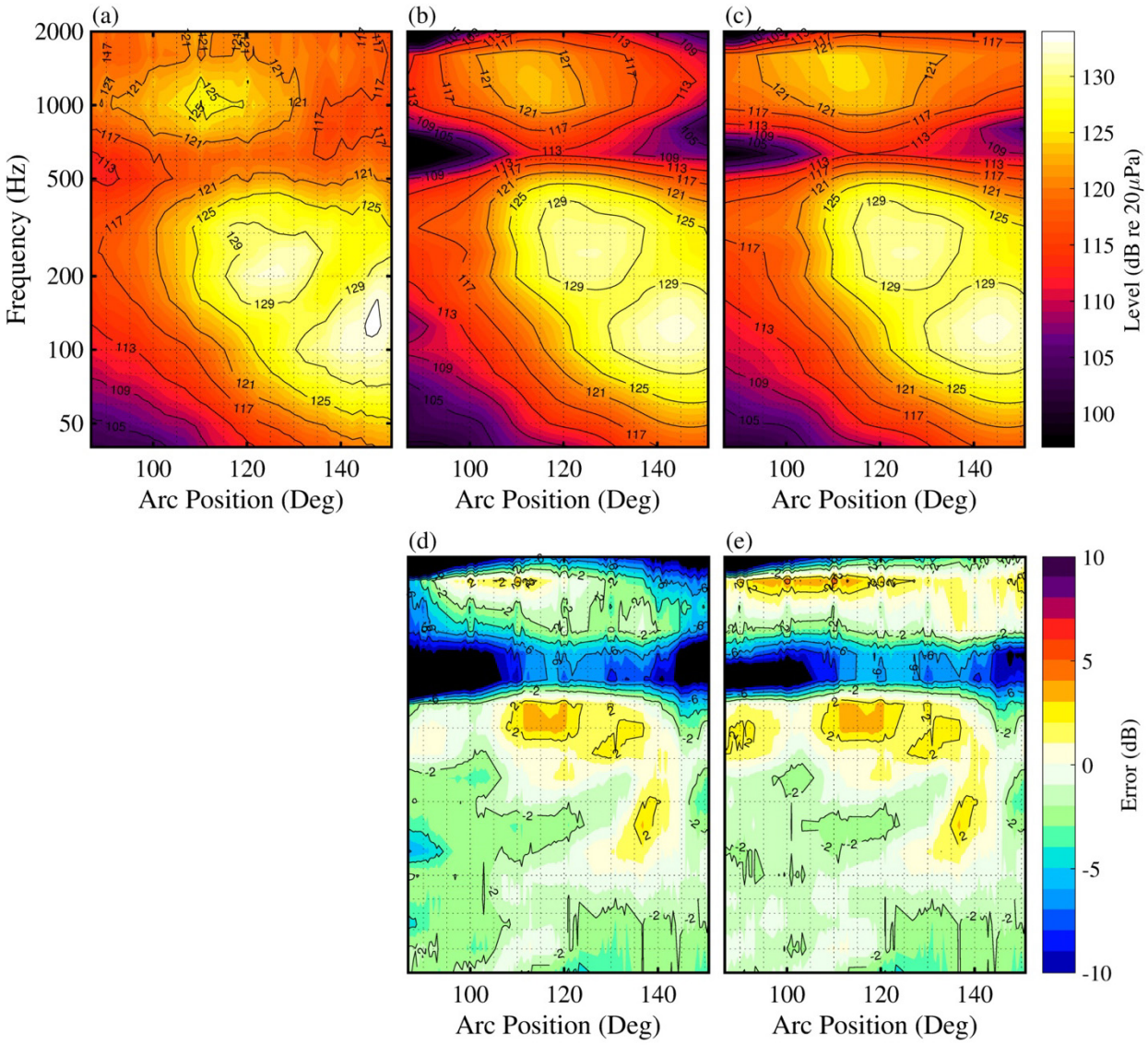

Fig. 5.14. (a) Measured levels at 22.9 m arc, and predicted levels from (b) MWP model and (c) MWP+UD model. The errors of the estimated levels to measurements for (d) the MWP model and (e) the MWP+UD model are also given.

To better visualize the acoustic radiation, the beamforming model, MWP model, and MWP+UD model, having been validated in the available measurement regions shown in Fig. 5.13, are used to estimate the acoustic radiation near the MIL power engine on a horizontal plane at

ground height for frequencies of 100 Hz, 200 Hz and 500 Hz in Fig. 5.15. Because the ESMs are based on ground array measurement inputs, the estimated levels are only assumed to be accurate for radiation contained within the white dashed lines. The lines coincide with the approximate aperture of the ground-based array and the jet centerline at 0 m for the upstream line and 20 m for the downstream, approximating the source region of the jet noise sources. This is only an approximate region of certainty, as the jet noise sources vary greatly in directionality with respect to source position and frequency. The field is propagated along the ground plane to better visualize the radiation without the inclusions of constructive and destructive interferences. The results show that all three models produce similar fields in the maximum radiation regions, which highlights their consistency and the capabilities of the reduced order model to capture the key characteristics of the full-order beamforming model. The primary deviation between the models lies in the sideline radiation of the MWP model, which significantly underpredicts the levels produced by the beamforming model. The MWP+UD model boosts the levels at the sideline to those like the beamforming results.

The radiation at 200 Hz also helps to better visualize the multilobe directivity pattern of the jet noise. Wall *et al.*[13] used acoustical holography to predict the radiated levels for similar test conditions. They showed that while the levels for holography were reconstructed at a height of 1.9 m and ground interference patterns were present in the results, the radiation lobes show agreement in directivity and in terms of level, after accounting for the increase of pressure for ground level predictions. They found that with increasing frequency, the relative levels between the multilobe features changed such that the levels of the more upstream lobe increased with frequency, while the levels of the lobe radiating farther downstream decreased.

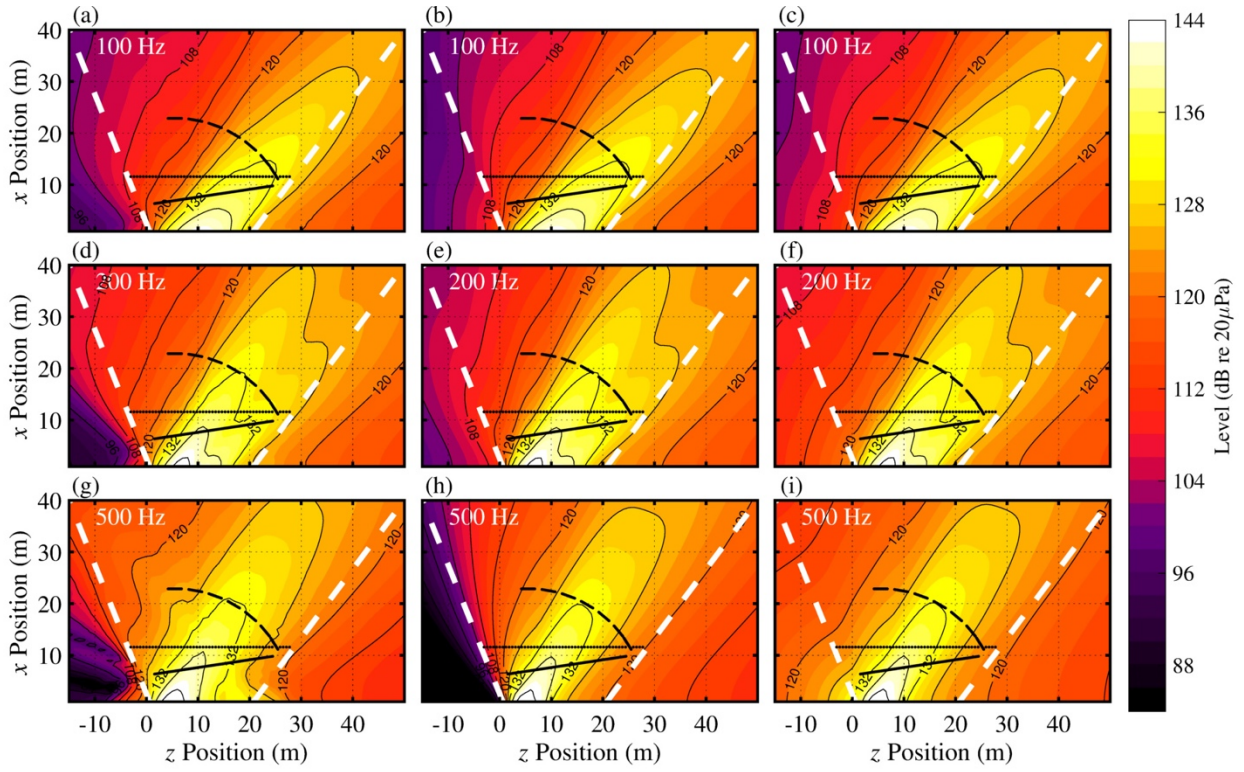

Fig. 5.15. Predicted levels across a horizontal plane with jet centerline on *z* axis. Cases for (a-c) 100 Hz, (d-f) 200 Hz, and (g-h) 500 Hz are shown using (left) a beamforming model, (middle) an MWP model, and (right) an MWP+UD model. The white-dashed lines represent the approximate aperture spanned by the ground-based array.

The multilobe features seen in the measurements in Fig. 5.14 and from the predicted radiation in Fig. 5.15 are well represented using the MWP model. Each wavepacket in the MWP model is associated with a wavenumber, derived from the wavenumber spectrum of its associated partial source, and the wavenumber produces radiation with a specific directivity. By viewing the individual contributions of the wavepackets, the reproduction of the multilobe phenomenon is better understood, and field level predictions from several components of the multiple-wavepacket model at 200 Hz are plotted in Fig. 5.16. In this example, the first few wavepackets contribute most to the multilobe radiation. The first wavepacket radiates at an angle of about 123° and predicts the primary lobe. The second wavepacket comprises the secondary lobe with a directivity of 139°.The third wavepacket is not associated with the two main lobes and comprises residual energy

with a slightly more downstream radiation angle of 152°. Wall *et al.*[13] found that, for 200 Hz, the radiation was reducible into two partial fields, plus a residual. The peak levels of the first wavepacket were about 6 dB higher than those of the residual. Their results are corroborated by this reduction. For example, the remaining wavepackets are necessary to reconstruct any residual energy of the two lobes, as well as upstream and downstream lower-level contributions. In addition, the difference, in peak level, between the first and third wavepackets is about 7 dB. Wall *et al.* also concluded that the coherence between the radiation of the two lobes was low. They suggested that two overlapping partial sources, each with a characteristic phase speed, were responsible for the radiation. The MWP source model provides evidence that overlapping sources with differing phase speeds could indeed generate multilobe radiation patterns.

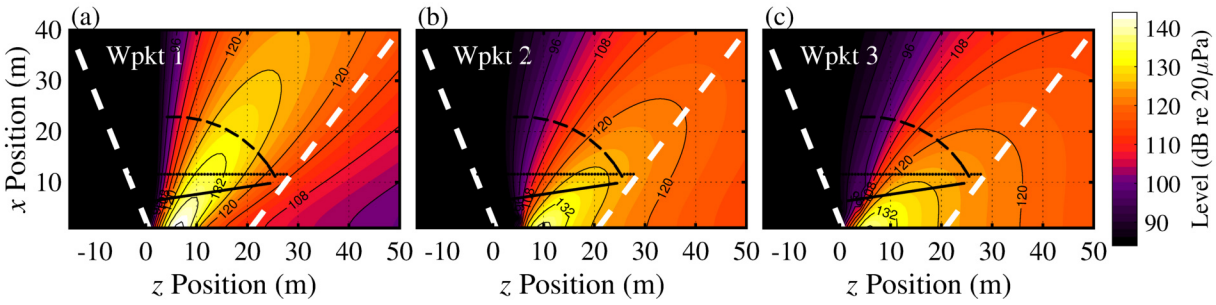

Fig. 5.16. Individual wavepacket contributions of the multiple-wavepacket model at 200 Hz.

In many circumstances, the primary wavepacket comprises most of the radiated acoustic energy, particularly for frequencies below about 125 Hz. A comparison of the first wavepacket shapes across frequencies, when normalized and scaled by wavelength, are shown in Fig. 5.17. Each primary wavepacket spans multiple wavelengths (corresponding to several meters, depending on the wavelength) and, when scaled by wavelength, the wavepackets are only slightly asymmetric in shape. The length and shape of the primary wavepacket supports findings by Reba *et al.*,[138] who used radiation from a single Gaussian-shaped wavepacket to model pressure

measurements near the shear-layer of a heated, supersonic, lab-scale jet. They noted that the correlation length scales of the wavepacket source extended several nozzle diameters.

While there are some small differences across frequencies, the primary wavepacket shapes are, for the most part, self-similar. When scaled by wavelength, the primary wavepackets in Fig. 5.17 grow in width with frequency, from 40-125 Hz. The wavepacket asymmetry is most prominent for these frequencies, owing to the fact that the primary wavepacket comprises the majority of the energy for frequencies up to 125 Hz. Beyond 125 Hz the scaled primary wavepackets show appreciable self-consistency with a wavepacket width of 2.0 ± 0.3 wavelengths measured at the full-width half maximum, and are nearly symmetrical in shape. The length of the wavepackets is surprising considering that the beamforming results of the source distribution from Fig. 5.11—when scaled by wavelength—show that the source width nearly triples over the same frequency bandwidth. This result suggests that the relative importance of the nonprimary wavepackets increases with frequency and that the combination of these wavepackets, when spatially distributed, comprise the source distribution. It also highlights the self-similarity across frequencies of the dominant radiation features. It is interesting to note that the fluctuation of the coherence, while varying in Fig. 5.11, does not seem to significantly affect the individual wavepacket sizes.

The directivities of each wavepacket are also provided in the legend of Fig. 5.17. They show that the directivity of the first wavepacket steadily shifts from 133° to 136° as frequency increases from 40 Hz to about 160 Hz. Thereafter a transition occurs and the directivity of the primary wavepacket shifts to angles closer to the sideline. The trend then continues and the directivity shifts downstream from 123° to 130° from 200 Hz to 315 Hz. These shifts to higher angles, followed by ever decreasing jumps to lower angles continues up to 2000 Hz. The transition

in directivity between 160 Hz and 200 Hz shows the shift in relative energy between the downstream and upstream radiation lobes, and it makes clear the subtler trend that with increasing frequency the directivity of each of the multilobe radiation features shifts downstream. The transition in directivity between multilobe radiation features, as well as the trend of the radiation to larger angles with increasing frequency is also shown by Wall *et al.*[130] in the predicted jet noise radiation from a static F-35 aircraft at MIL power using an advanced near-field acoustical holography technique. Using narrowband spectra, they showed that the two large multi-lobe features could actually be further decomposed into at least four distinct lobes. While only two lobes are visible in the one-third octave spectra in Fig. 5.9(b), corresponding narrowband spectra may yield similar findings.

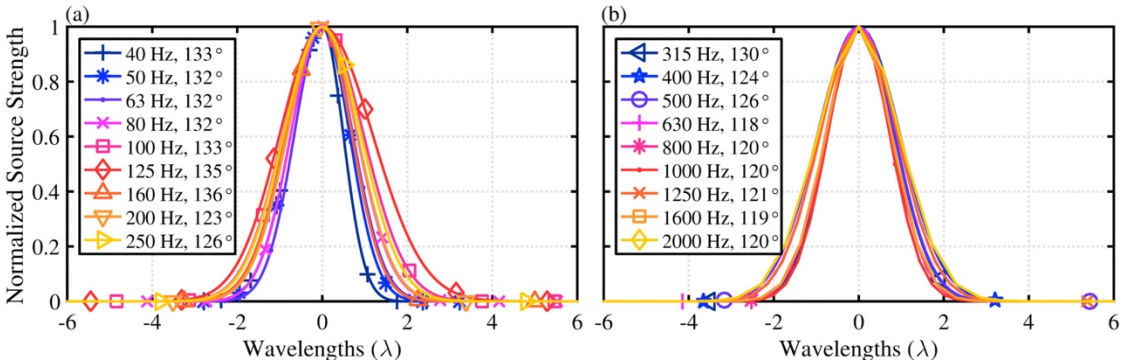

Fig. 5.17. Primary wavepacket shape that have been normalized and scaled by wavelength for one-third octave frequencies.

Whereas a single wavepacket model cannot correctly reproduce the coherence properties of the acoustic radiation and struggles to reproduce radiation at all angles,[18, 45] the MWP model produces a field with finite coherence properties. Ground array coherence calculations were used to compare the predicted coherence properties of the field using the MWP and MWP+UD source models. The results of the calculated and predicted coherence at 100, 200 and 500 Hz are shown in Fig. 5.18. Coherence is shown such that the self-coherence for each plot is shown along the

diagonal, with a value of unity, and the off-diagonal elements represent coherence between two corresponding measurement locations along the ground array. The L_{γ^2} values are generally largest in the region where the direction of maximum radiation traverses the ground array, at about z =10-25 m downstream. At 100 Hz, the calculated coherence lengths are greatest in the maximum radiation region [see Fig. 5.9(b)]. At 200 Hz, however, the multilobe radiation produces two spatial regions over which there is high coherence and a neck in the coherence map between the regions. The coherence is much lower across the array at 500 Hz, with L_{γ^2} values in the maximum radiation region not exceeding about 1 m.

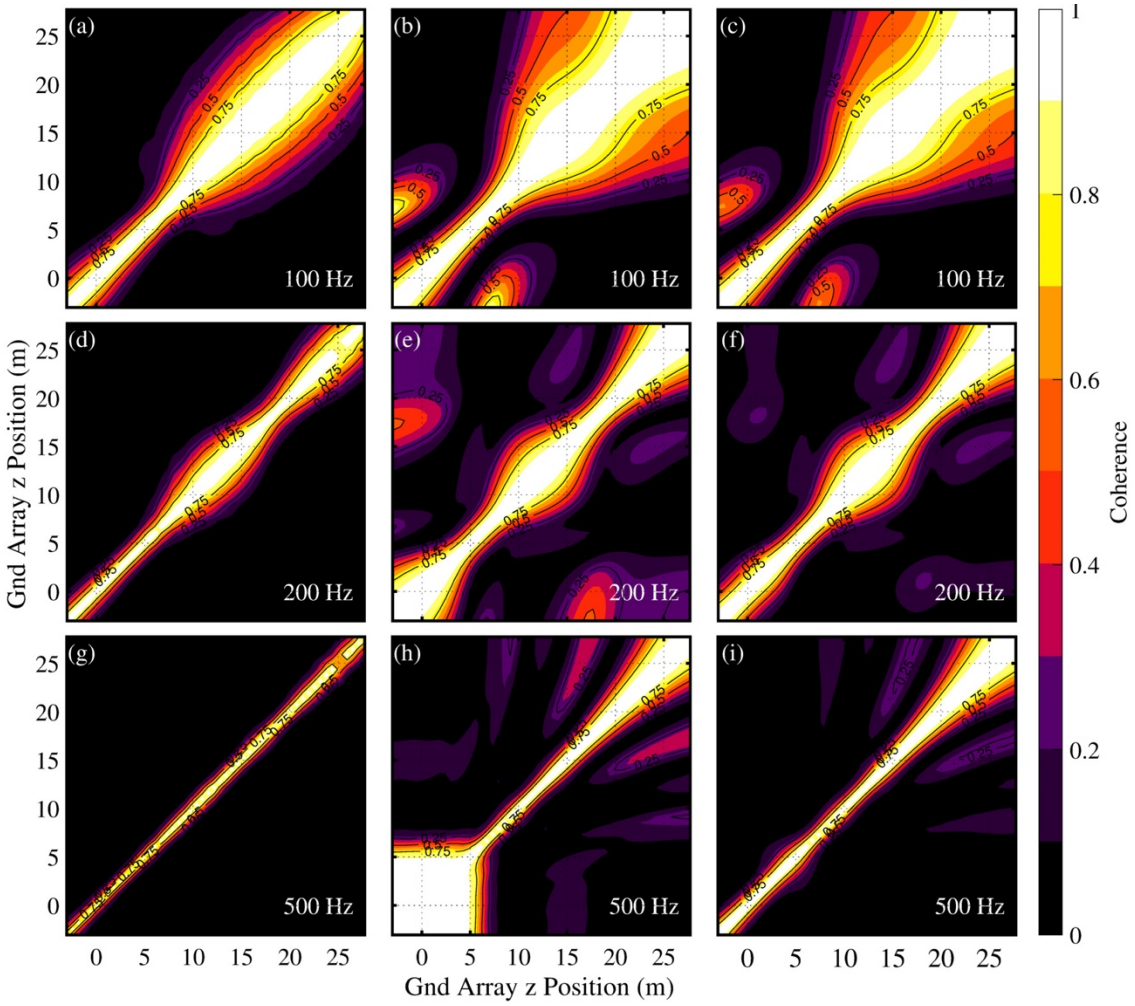

Fig. 5.18. Coherence values at the ground array for (a-c) 100, (d-f) 200, and (g-i) 500 Hz. The calculated coherence is shown (left), as well the predicted values using (middle) the MWP model and (right) the MWP+UD model.

The coherence is estimated at each of these frequencies using both the MWP and the MWP+UD reduced-order models. In the case of coherence estimated by the MWP model, the qualitative features found in the calculated coherence maps are present, although the coherence values are generally overestimated. For example, the coherence predictions for $z < 5$ m are greatly overestimated and bear no resemeblance to the calculated coherence. In addition, coherence predictions for $z > 20$ m are also overestimated, and additional lobes in the coherence are visible at $z = 7$ m at 100 Hz and $z = 17$ m at 200 Hz that are not present in the coherence calculations

from the array measurements. Thus, while the L_{γ^2} values will approximate those calculated from measurements, the additional artifacts indicate the regions where there are an insufficient number of independent sources to better estimate the coherence. Additional wavepackets reduce the overestimation of the coherence in most regions across the measurement array, although a large number of wavepackets may be necessary to adequately reproduce the short coherence lengths to the sideline (see Ref. [97]), likely resulting from the fine-scale structure radiation identified by Neilsen *et al.*[91] using similarity spectra. The MWP+UD model incorporates the additional distributed uncorrelated source and the corresponding predicted coherence, shown in the right column of Fig. 5.18, improves the overestimated coherence, particularly for the sideline predictions. It also reduces the overestimation of the coherence farther downstream along the measurement array, although the result can be further improved by increasing the number of wavepackets in the MWP model. With a sufficient number of wavepackets, the inclusion of both directive wavepackets and an uncorrelated distribution allows for the accurate prediction of coherence properties both to the sideline and within the maximum radiation region where large-scale structure radiation is present.

The coherence calculations and predictions were made at the input array. Coherence predictions at additional locations will further validate the MWP capabilities. However, whereas the ground array was a synchronous measurement, measurements at the scan array and measurement arc are comprised of nonsynchronous measurements, and calculating coherence values across these arrays therefore requires additional considerations and are not included in the present study.

5.3.5 Optimizing the Wavepacket Model

In the preceding analyses, six wavepackets were chosen for the MWP and MWP+UD models, regardless of frequency. This is not necessarily the optimal number of wavepackets, as fewer wavepackets might be sufficient to accurately describe the radiation, particularly at lower frequencies. In contrast, additional wavepackets may be needed for higher frequencies. To gain a sense of the required number of wavepackets for each frequency, the decibel level differences between MWP predicted and measured levels at both the scan array and the arc—shown in Fig. 5.14(d) for the measurement arc—are averaged for each frequency. These results are averaged in a dB sense in order to equally weight the radiation levels along the array, instead of weighting the errors by the peak levels as occurs using a squared-pressure average. The errors are calculated for a variable number of included wavepackets, from one to ten, and the average errors are shown in Fig. 5.19(a-b) for the scan array and the measurement arc, respectively. In these plots, the horizontal axis shows the number of wavepackets used in the multiple-wavepacket model for a given frequency, and the colored contour lines provide the average error of the model. In addition, the average error of the beamforming model predicted levels is shown at the far right of each plot. As additional wavepackets are added, the errors should converge to those of the beamforming model. From the results, it is shown that by using six wavepackets, the average level errors at the scan array vary between 1-4 dB for frequencies below 400 Hz. As frequency increases, the required number of wavepackets to produce similar errors increases, and beyond 1000 Hz, errors exceeding 10 dB can result even when ten wavepackets are used. These high errors are primarily due to the increased difficulty of the MWP model to accurately estimate the sideline radiation with increasing frequency. At the measurement arc, which is located slightly farther downstream and does not include a significant portion of the sideline radiation, the errors are more consistent with frequency.

Except for the errors at frequencies of 600 Hz and 2000 Hz that correspond to errors from the interference nulls, six wavepackets is sufficient to produce level estimates with average errors generally between 1-4 dB.

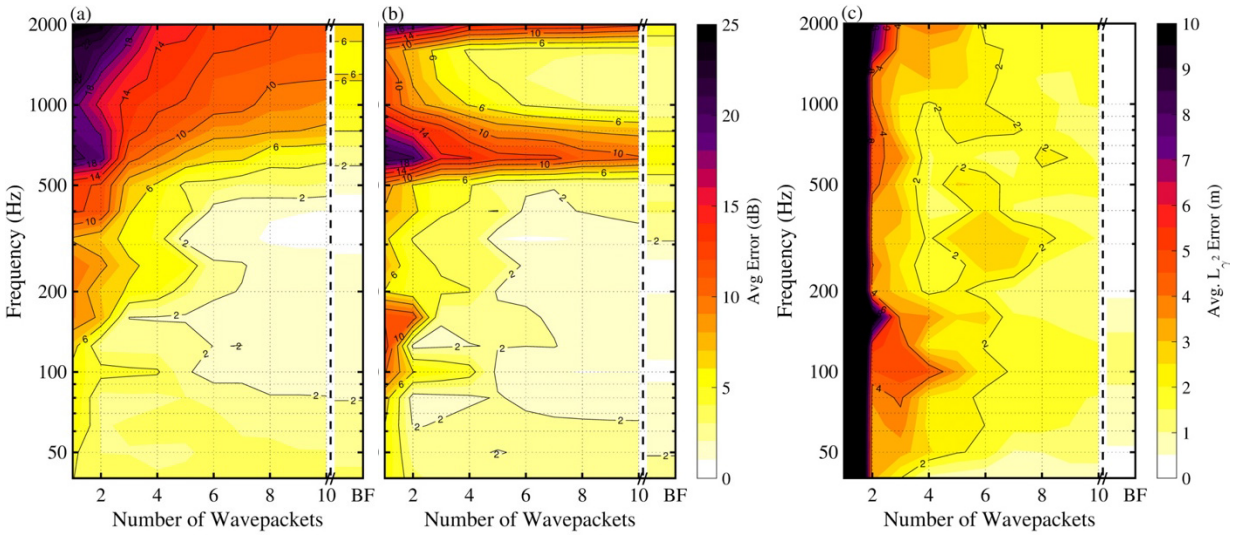

Fig. 5.19. Average error of MWP model predicted levels to (a) the scan array measurements and (b) the arc measurements. (c) The average error, in meters, of coherence length from wavepacket models and beamforming results to coherence calculations at the ground array. In each plot, the predicted levels and coherence length errors for each respective data of the beamforming results is plotted to the far right.

The predictions of the field coherence using the MWP model are also affected by the included number of wavepackets as using too few results in an overestimate of the coherence values as shown in Fig. 5.18. To compare the capability of the MWP model to predict the coherence properties of the field, the L_{γ^2} values are calculated at the ground array and compared to the predicted L_{γ^2} values using the MWP model. The L_{γ^2} values are calculated for every microphone reference position along the measurement array. The average error of the L_{γ^2} values is plotted as a function of the number of wavepackets used in the wavepacket model in Fig. 5.19(c). The L_{γ^2} values are very large (i.e., a limiting value) when only one wavepacket is used because the calculated coherence for a single source will be unity between all measurement positions.

Using six wavepackets, the average L_{γ^2} errors range up to 2.9 m. If instead, ten wavepackets are used, the additional wavepackets improve the average L_{γ^2} errors, which are reduced to less than 2.0 m. In terms of wavelength, these errors therefore increase with frequency such that errors at 100 Hz correspond to about 0.5λ, while errors at 1000 Hz are large at about 4.4λ.

While the main lobe and large amplitude features are well represented using the MWP model, the majority of the average estimated radiation level errors and average L_{γ^2} value errors, shown in Fig. 5.13, are due to poor results to the sideline of the jet. To improve the sideline errors, the MWP+UD model was used, and the average errors the level estimates to the measurements are shown for the scan array and measurement arc in Fig. 5.20(a-b), respectively. Like Fig. 5.19(a-b), the horizontal axis shows the chosen number of wavepackets, and the level of the UD was adjusted for each case to best match the sideline levels at the measurement array. The inclusion of the UD reduces errors at all frequency bands, particularly for frequencies above 500 Hz at the scan array. For example, the average error at 2000 Hz using six wavepackets drops from about 13 dB to less than 7 dB at the scan array. In addition, errors are significantly reduced for models using less than three wavepackets, such that a three wavepacket MWP+UD model produces errors under 3 dB average errors for frequencies under 500 Hz at both arrays.

The estimates of L_{γ^2} at the ground array were also improved using the WPKT+UD model, and the average L_{γ^2} error of the estimated coherence lengths to the calculations derived from the measurements are shown in Fig. 5.20(c). When compared to Fig. 5.19(c), the coherence length calculations are significantly improved by the inclusion of the uncorrelated distribution, particularly for models that include fewer than four wavepackets, and the effects are mostly noticeable when using between 1-3 wavepackets in the wavepacket model. Here, the

improvements in the average L_{γ^2} errors are pronounced because of the improved coherence length predictions at the jet sideline.[9] The inclusion of additional wavepackets can also improve the sideline errors, although, provided the MWP model captures the salient level and coherence radiation features, the UD model is a more efficient means of modeling the residual energy.

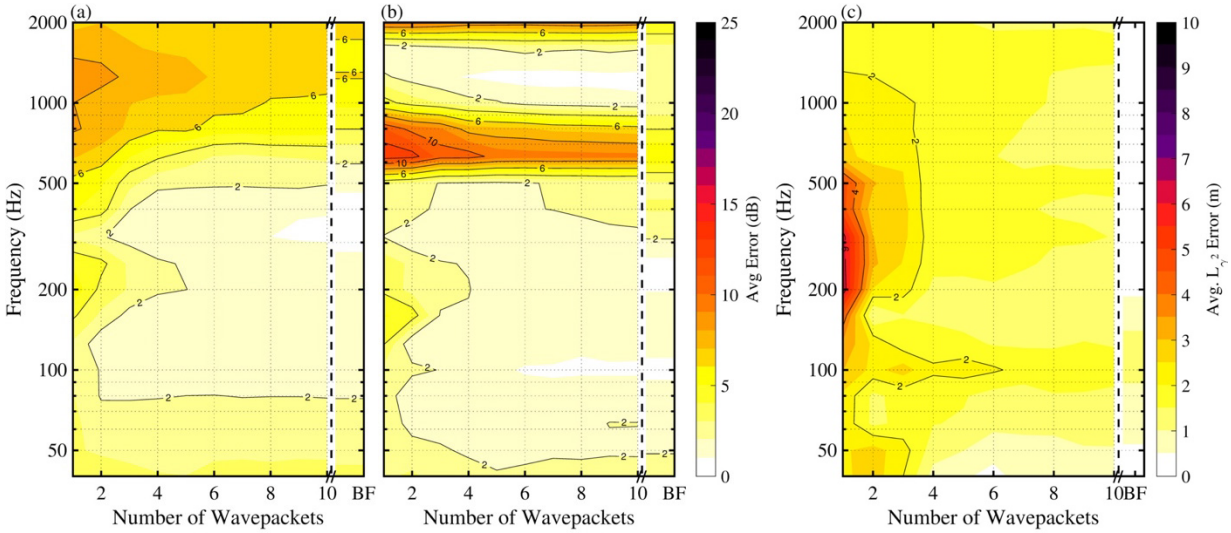

Fig. 5.20. Average dB error of predicted levels from MWP+UD model to (a) the scan array measurements and (b) the arc measurements. (c) The average error, in wavelengths, of coherence length estimated using MWP+UD model to coherence calculations at the ground array.

5.3.6 Engine Condition Analysis

Previous results were shown for MIL engine condition (100% ETR). In addition to this condition, both intermediate (INTER) and afterburner (AB; 150% ETR) conditions were measured at the ground array, scan array and measurement arc. The variation in temperature and jet velocity necessitates additional consideration of the MWP models to provide additional insights into the source and radiation properties.

The beamforming equivalent source results are shown in Fig. 5.21(a) for the INTER engine condition with levels given relative to the respective maximum level of each frequency. At INTER, the maximum levels of the beamforming results are shifted about 2-3 m upstream of the MIL

results [in Fig. 5.10(b)] Additionally, the source width—as measured from the 3 dB down contour lines—is similar to those of MIL for frequencies up to about 80 Hz [e.g., 10.9 m (1.27λ) at INTER vs 10.4 m (1.2λ) for MIL at 40 Hz], but it thereafter is smaller for higher frequencies [e.g., 1.9 m (10.8λ) at INTER vs 2.5 m (14.3λ) for MIL at 2000 Hz]. The largest deviations, however, occur in the coherence calculations shown by the red dashed lines overlaid on the beamforming results. They indicate that while the width of the coherence results, referenced to the peak level locations, are marginally less at INTER for frequencies above 160 Hz, the differences grow for frequencies below 160 Hz when compared to the MIL results. For example, at 50 Hz, $L_{\gamma^2} = 3.0$ m at INTER and $L_{\gamma^2} = 7.0$ m at MIL even though the difference in source size is only about 1.0 m as measured from the 3 dB down lines of the beamforming results. Neilsen *et al.*[91] showed that, according to ground array data for the INTER engine condition, the relative contribution in level of the fine- and large-scale structure radiation to the calculated spectra are within a few decibels of each other for radiated angles of $80 - 120°$, whereas the relative differences in level of the two spectra are much greater at MIL and AB conditions. A similar effect was observed for similarity spectral differences between the lab-scale jets of differing Mach numbers by Tam *et al.*[9] The combination of the two sources within the source region that have relatively equal levels may explain the small coherence lengths at INTER for frequencies below 160 Hz. It should also be noted that the maximum radiation region at INTER extends slightly beyond the measurement array for frequencies below about 160 Hz, thus, a portion of the radiation information is not adequately represented and the INTER coherence widths below 160 Hz may be larger than shown in Fig. 5.21(a).

The levels and coherence properties of the beamforming results at AB condition only show minor differences from those at MIL. As expected from the increases in jet velocity, the peak levels

at AB are about 1-2 m farther downstream compared with those at MIL. The source widths between MIL and AB vary only 1-2 m across the frequency bandwidth as measured by the 3 dB down contour lines, although the effect is most pronounced for frequencies above 125 Hz because the source width at AB shows less contraction with increasing frequency above 100 Hz. The coherence lengths are mostly similar between MIL and AB, except that the widths of the coherence between 100-200 Hz are slightly larger at MIL condition than at AB.

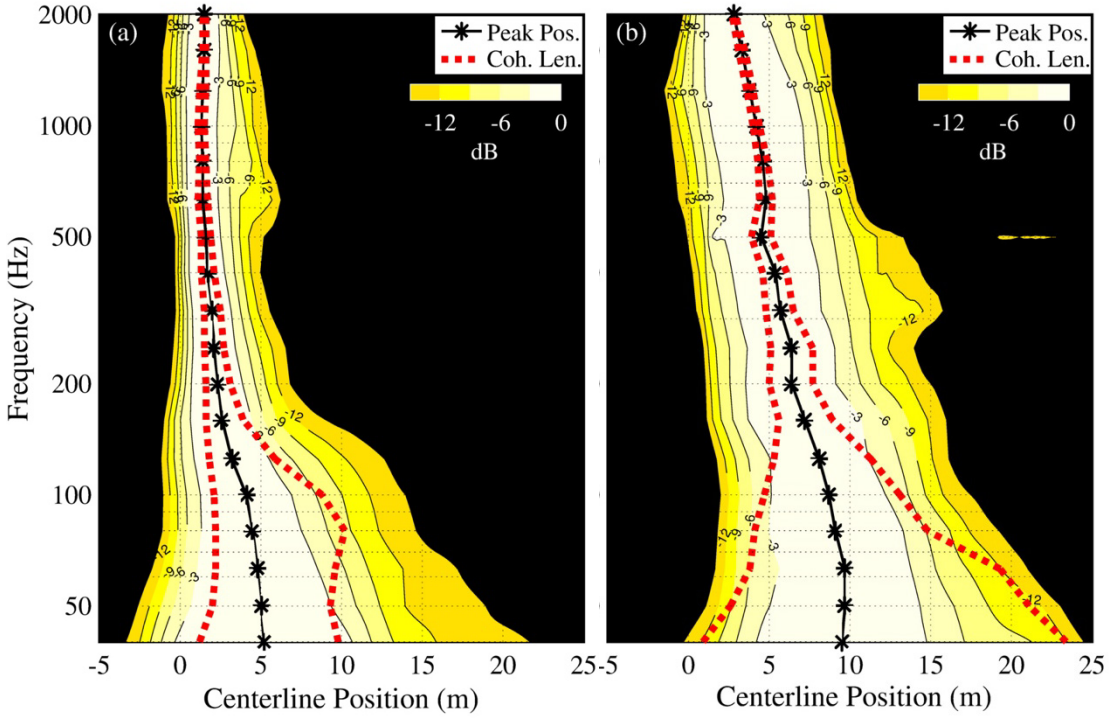

Fig. 5.21. One-third octave beamforming results at jet centerline shown relative to the maximum level of each frequency, for (a) INTER and (b) AB engine conditions [similar to Fig. 5.10(b) for MIL].

The MWP decompositions are performed on the beamforming results shown in Fig. 5.21, for example frequencies at 500 Hz, 200 Hz and 100 Hz in Fig. 5.22. For a given frequency, the amplitude contribution of each wavepacket does not vary significantly with engine condition, although the change in the beamforming source width and coherence lengths with frequency and engine condition produce significant differences in the MWP models. At 500 Hz, the difference in

source width is pronounced between INTER and AB conditions, with the INTER condition showing a very tightly packed set of overlapping wavepackets, and wavepackets in the AB condition more evenly distributed across the larger source distribution. Thus, while the L_{γ^2} values are only about 0.6 m larger at AB compared to INTER at 500 Hz, the source width is about 4 m larger. At 200 Hz, individual wavepacket contributions are more evenly spread compared to the examples at 500 Hz. The source width for AB is very similar between 200 Hz and 100 Hz, with the greatest difference being the smaller coherence lengths at 200 Hz necessitate a larger number of wavepackets dispersed throughout the source distribution, whereas one primary wavepacket constitutes most of the radiation at 100 Hz. In fact, the difference between the largest and second largest wavepacket amplitudes at 100 Hz, in dB, is 5.0 dB, 8.2 dB and 7.4 dB for the INTER, MIL and AB conditions, respectively. When normalized and scaled by wavelength the differences of the primary wavepackets in the engine conditions are not pronounced, although the trend is to grow slightly in width with increasing frequency as engine power is increased.

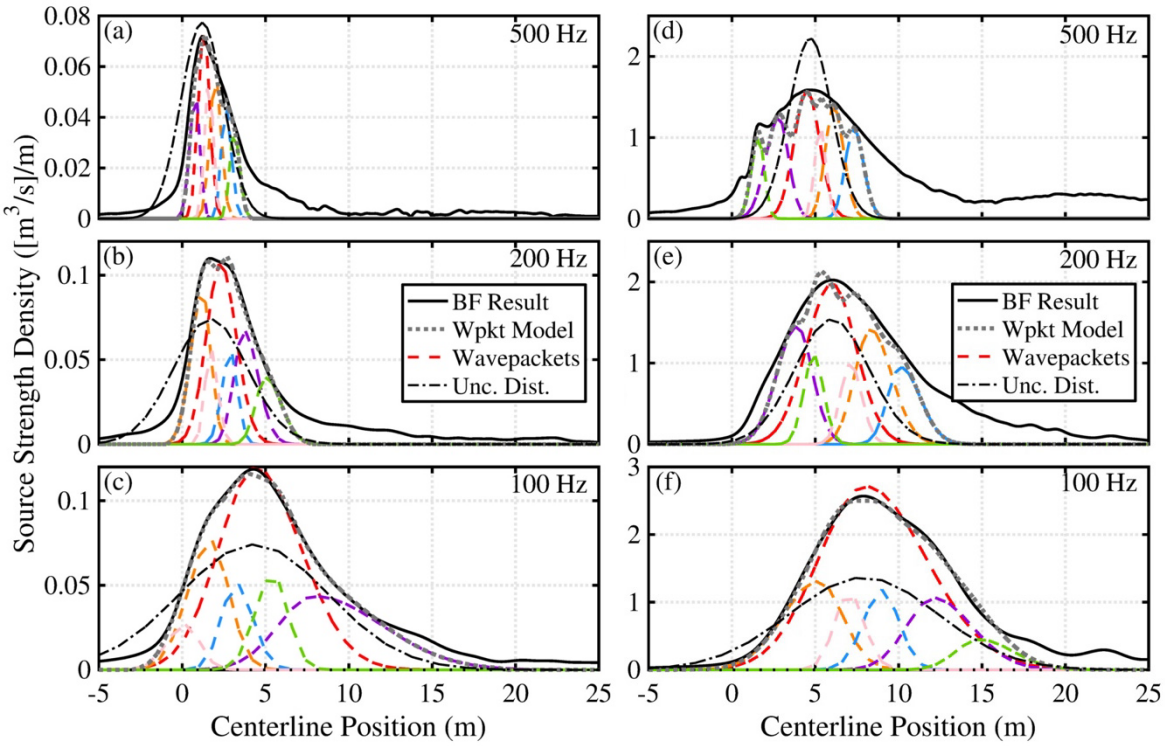

Fig. 5.22. Wavepacket examples at (a) 500 Hz, (b) 200 Hz, and (c) 100 Hz using six wavepackets are shown with the beamforming and resultant wavepacket model levels for (left) INTER and (right) AB engine conditions. The UD is shown with a dash-dot line.

In addition to the MWP models, the UD is also overlaid on each plot using dash-dot lines. Like the UD at the MIL condition, the full-width half maximum value of each is three wavelengths, with a minimum value of 3 m. The amplitude of each distribution varies with engine and frequency, and in some cases the distribution amplitude exceeds the amplitude of the beamforming results. This was also observed by Morgan *et al.*,[118] who noted that the UD amplitudes exceeded those of the correlated distribution amplitudes when both distributions were similarly shaped. In addition, they noted that the relative importance of the UD grew for higher frequencies and lower engine powers, which agrees with the findings here.

While the relative importance of additional wavepackets grows with frequency, the number of wavepackets required to generate an effective level-based MWP+UD model does not

significantly vary with a change in engine condition. While not shown here, similar errors in the predicted levels and coherence values, shown in Fig. 5.20 for the MIL model, are found for the predicted levels using the AB model. For example, 4-6 wavepackets adequately predicts levels at the measurement arc with average errors less than 3 dB for frequencies below 500 Hz, and fewer can be incorporated at lower frequencies. Similarly, the average predicted level errors at the INTER condition approach a limiting value using as few as 4 wavepackets.

While the average errors in the predicted levels can provide insight into the necessary number of wavepackets to describe the level radiation, the average L_{γ^2} errors provide a benchmark of a model's temporal capabilities. For example, a six-wavepacket MWP+UP model produces errors rangine from 0.8-3.8 m at INTER, 0.3-2.0 m at MIL, and 1.3-2.2 m at AB over the frequency range. These average L_{γ^2} errors are largest for the INTER condition and exceed 3 m for frequencies from 200 Hz to 600 Hz. Thus, the inclusion of a large number of wavepackets and the tight spacing of the wavepackets within the source distribution at 500 Hz shown in Fig. 5.22 shows the highly uncorrelated nature of the jet noise source at INTER, even in the maximum radiation region.

The MWP and MWP+UD models are validated by predicting the levels at the ground array, scan array and measurement arc for INTER and AB conditions in Fig. 5.23 and Fig. 5.24. In each case, predicted levels match to within 2 dB for most regions with few exceptions. Because of the INTER condition's high variability in the actual engine output from scan to scan along the measurement arc (See Ref. [24] for a similar effect at INTER), it is more difficult to accurately compare the predicted levels to the benchmark measurements. As a result, level predictions at the scan array and the measurement arc in Fig. 5.23 deviate by up to about 6 dB from the measurement levels. However, the radiation predicted at the ground array matches the input measurements to within 1 dB, and the predicted radiation does show good agreement with the measurements,

particularly at 100 Hz. In addition, the sideline radiation at INTER is more accurately predicted using the six MWP model compared to similar models at MIL and AB conditions, suggesting that because less directive radiation is present at this condition, the MWP model placed higher emphasis on the sideline radiation. Errors at the sideline, particularly for the ground array, are much greater at the AB condition in Fig. 5.24 with deviation exceeding 10 dB for the MWP model. However, the MWP+UD model boosts the sideline radiation and shows agreement to within 2 dB with most measurements at the scan and arc arrays. These predicted levels show that for multiple engine conditions and radiation angles, the MWP model predicts the INTER condition radiation as well as the large-scale structure radiation at AB condition using the reduced-order MWP model, and the UD addition allows for the accurate prediction of the sideline levels as well.

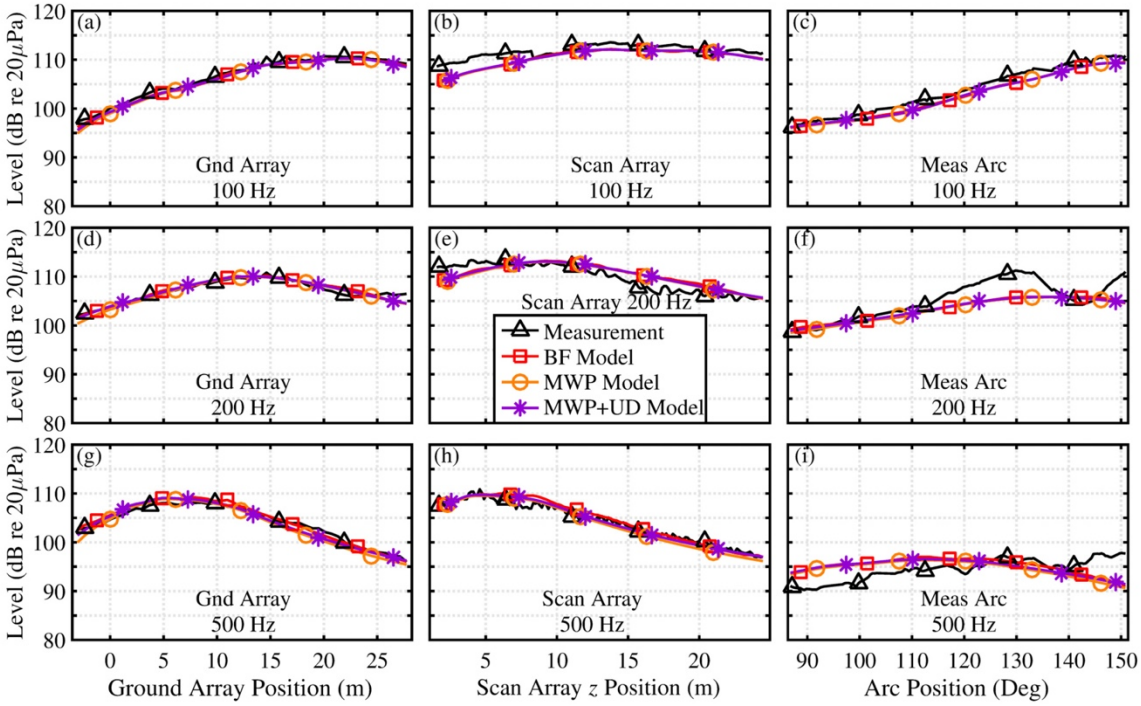

Fig. 5.23. Comparisons of measurements and predicted levels for (a-c) 100 Hz, (d-f) 200 Hz and (g-i) 500 Hz at (left) the ground array, (middle) the scan array, and (right) the measurement arc, at INTER engine condition (Compare with Fig. 5.13).

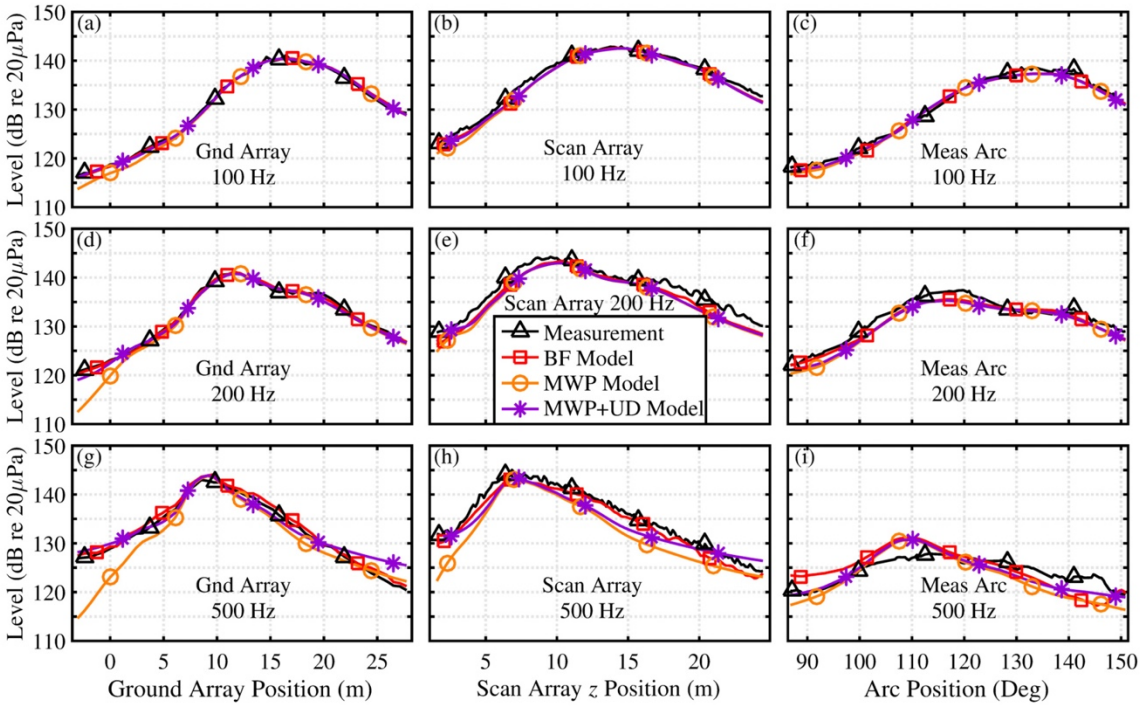

Fig. 5.24. Similar to Fig. 5.23 for AB engine condition.

The MWP+UD model, having been verified to accurately predict levels to within 2 dB at the three measured arrays (insofar as permitted by the beamforming model predictions), is now used to predict the radiation beyond measured locations. The predicted levels are shown in Fig. 5.25 for INTER, MIL and AB engine conditions using the MWP+UD model for frequencies of 100 Hz, 200 Hz and 500 Hz. With example frequencies at each of the engine conditions, a comparison of the radiation using the predicted levels using the MWP+UD model can be made. The general trends show that the maximum radiation angles are smaller with increasing engine condition, regardless of frequency. For example, at 100 Hz, the directivity angle of the primary wavepacket shifts from 141° at INTER to 122° at AB. In addition, the radiation becomes more directive with increasing condition, which may be a direct consequence of the greater relative contribution from large-scale structure radiation.[91] There are also frequency-specific differences in the radiation. While it may be present for all engine conditions, the distinct transition to

multilobe radiation occurs between the INTER and MIL cases at 200 Hz. Indications of a secondary radiating lobe are also present at the AB condition, although the differences in the directivities of the two lobes are less distinct. The distinct peaks are also found in the ground array results at 200 Hz in Fig. 5.24 for the AB case, and the presence of distinct lobes are confirmed in the spectral plots for similar ground array measurements in Ref. [90]. Interestingly, the differences in radiation angle of the lobes are greatest at MIL rather than at AB. Tam *et al.*[113] hypothesized that large-scale radiation and combustion noise are, respectively, the two contributing factors to the double-lobe phenomenon in the jet noise. However, while high engine powers exhibit strong effects due to combustion noise—which should radiate from the nozzle exit—the multilobe directivity pattern is also seen here at nonafterburner engine powers where combustion noise contributions would be smaller. Additionally, beamforming and MWP model decompositions reveal that both radiation lobes seem to originate many meters further downstream from the nozzle exit, where combustion noise is likely to originate.

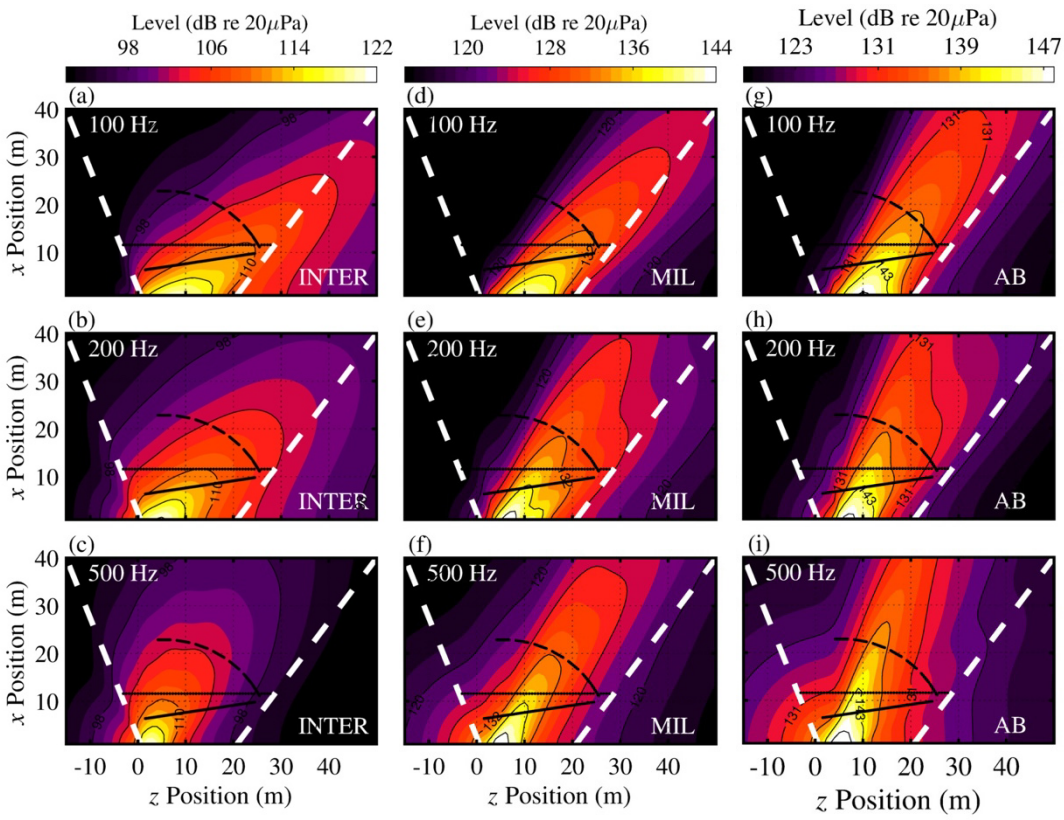

Fig. 5.25. Predicted levels across a horizontal plane with jet centerline on z axis. Cases for (top) 100 Hz, (middle) 200 Hz, and (bottom) 500 Hz are shown using MWP+UD model for (a-c) INTER, (d-f) MIL, and (g-i) AB engine conditions.

5.4 Conclusion

Multiple-wavepacket source models of the noise radiation from a high-performance tactical aircraft operating at MIL engine condition are developed using a decomposition of phased-array source reconstructions. The investigation builds on beamforming investigations that focus on source distributions as a function of frequency derived using the hybrid method (HM). The beamforming source is decomposed into a multiple-wavepacket (MWP) model consisting of six asymmetric-Gaussian-shaped wavepackets, with each having a distinct phase speed. This MWP model allows for the prediction of level-based radiation as well as coherence properties of the field where single wavepacket models fail. In addition, the MWP model can be augmented by an

uncorrelated distribution (MWP+UD) to accurately predict levels where fine-scale structure radiation dominates. These models are validated using benchmark level and coherence calculations at various distances and angles in the mid field. Average errors for the MWP model vary, although they are generally within 3 dB, and errors drop further when the MWP+UD model is used. The MWP+UD improvements are due to the inability of the reduced-order MWP model to capture the sideline radiation, which would otherwise require a significant number of wavepackets. The average errors of the predicted coherence lengths in the mid field are on average less than 2.9 m using the MWP model and coherence lengths to the sideline are improved further using the MWP+UD model so that average errors drop below 2 m for the frequency range.

The MWP models are used to predict level and coherence properties across a usable aperture, defined by the measurement array used in the beamforming analysis. The results are shown alongside the predicted beamforming results, and the predicted levels using the reduced-order models show consistency with the full-order beamforming predictions. The predicted levels capture the multilobe directivity patterns in the jet noise at 200 Hz for the MIL condition, and the fact that, with increasing frequency, the relative levels between the lobes shift such that the upstream lobes grow in level while the downstream lobes decrease. When the radiation of each contributing wavepacket is viewed separately, the multilobe radiation is reducible into two wavepackets, and the remaining wavepackets are necessary to reconstruct any residual energy. Reproduction of the multilobe directivity using the MWP model shows that overlapping sources with differing phase speeds can effectively generate multilobe radiation patterns.

An analysis of the primary wavepacket from the MWP model shows a high degree of similarity across the frequency range once normalized and scaled by the wavelength. This result, combined with the finding that the source size grows with increasing frequency, suggests that the

relative importance of the nonprimary wavepackets increases with frequency and that the combination of these wavepackets, when spatially distributed, comprise the source distribution. In addition, the primary wavepackets, which are connected to the primary radiation directivity, show a smooth transition in directivity to larger angles relative to the nozzle inlet from 40 Hz to 160 Hz. At 160 Hz the directivity of the primary wavepacket transitions to the more upstream lobe of the multilobe radiation, and thereafter the directivity slowly increases to larger angles with increasing frequency—albeit smaller than those of the more downstream radiation lobe.

An optimization study was also performed to determine the necessary number of wavepackets required to accurately predict the radiation and coherence properties of the field. While the addition of wavepackets reduces the error between the measured and predicted levels, these errors converge on limiting values of between 1-3 dB for frequencies below 500 Hz, although they increase with frequency due to the large sideline radiation errors. Using six wavepackets, the MWP shows level-based average predicted radiation level errors on the order of 2-3 dB for frequencies up to 500 Hz. The associated average coherence length errors fall to within about 2 m. However, when the uncorrelated distribution is included, as few as four wavepackets are sufficient to predict radiation levels to within 1-3 dB for frequencies below 500 Hz. The coherence length errors are also reduced using the MWP+UD model. For example, when four wavepackets are included in the model, the average errors fall to within less than 2 m for most frequencies below 800 Hz.

Additionally, intermediate (INTER) and afterburner (AB) engine conditions were analyzed and MWP models produced to predict the radiation properties. When decomposed into the MWP models using six wavepackets, the variation between the INTER and AB results led to more dispersed wavepackets across the source in the AB case and more densely-spaced overlapping

wavepackets at INTER. The MWP models were again successfully validated using benchmark measurements to show that, regardless of engine condition, a reduced order model of the jet noise was successfully obtained.

The ability of the MWP and MWP+UD models to efficiently and effectively predict the noise environment near high-performance tactical aircraft is a significant cost-reducing achievement by requiring fewer measurements and acquisition resources. Analytical functions that produce a reduced-order source model provide a modular and scalable framework that can be used to compare with other models. In addition, the model's analytical framework allows for future work to explicitly incorporate frequency into the MWP model parameters for a more complete picture of the radiated properties. The model is also important in its ability to reproduce the more intricate features of the radiation, including the multilobe directivity patterns found in tactical aircraft measurements. Building on the successes of previous wavepacket models, the ability of the MWP model to predict coherence properties brings analytical modeling efforts closer to physical properties of the radiation. Time-domain intermittency and impulses have not been considered in the present work, and it is hypothesized that future efforts to incorporate additional physical properties of the jet noise into a reduced-order analytical framework will provide better predictive capabilities for time-domain events.[3, 18, 139] This is particularly true for future efforts to improve upon the far-field capabilities of the MWP model, particularly for large propagation distances and high frequencies where nonlinear propagation effects increase, to provide a more complete model to globally predict the radiation properties.

Chapter 6

Conclusion

6.1 Dissertation Summary

Phased-array methods, i.e., beamforming, have been applied to pressure measurements in the vicinity of a tactical aircraft. The results have led to the acoustic characterization of the turbulent noise sources. The corresponding source models are useful to predict the radiation in the mid field of the jet, which may be used to improve existing noise propagation models and help to mitigate the noise exposure levels for personnel working in the vicinity of the aircraft.

An analysis of multiple beamforming-based methods has been performed to estimate the source characteristics of an extended, partially correlated source distribution. In a numerical case study, multiple methods have been compared, including cross beamforming (CBF), generalized inverse beamforming (GINV), hybrid method (HM), functional beamforming (FBF), and the mapping of acoustic correlated sources (MACS). Each method is successful in reconstructing the source distribution levels, and the source levels and coherence properties are predicted to the highest accuracy using beamforming algorithms that include regularization. The beamforming

results are also treated as an equivalent source model (ESM) to predict the levels and coherence properties of the radiation.

Prior to the application of the beamforming methods, a detailed time-waveform analysis of jet noise from a high-performance military aircraft has been completed. Correlation and coherence analyses have been presented from ground-array data collected near a tethered aircraft with a single engine operated at intermediate (INTER) and afterburner (AB) engine conditions. In addition, two complementary coherence studies have been presented: (1) the field coherence spectra and corresponding coherence lengths assessed and (2) a one-dimensional, equivalent source coherence estimate at the jet centerline. The cumulative results have provided a deeper understanding of jet-noise characteristics for a high-performance military aircraft and connections to phenomena shown in the literature.

The application of the hybrid method (HM) to acoustic measurements in the vicinity of a tactical aircraft represents one of the most extensive beamforming investigations to date on full-scale military aircraft noise. Beamforming results from a ground-based microphone array have been presented for the aircraft when one engine was operated at INTER, military (MIL) and AB engine conditions. The source levels and extent are examined, and the HM results provide insight into the coherence and phase speed of the apparent source distribution. In addition, beamforming from phased-array subsets has allowed for the independent characterization of the sources related to the fine- and large-scale turbulent mixing noise. These results have been presented in a full-order ESM at engine conditions ranging from INTER to AB.

The capstone of this work has been the decomposition of the beamforming results into analytical wavepacket functions that produce a reduced-order ESM of the jet noise. The investigation builds on beamforming investigations that focus on source distributions as a function

of frequency, derived using HM beamforming. The beamforming source is decomposed into a multiple wavepacket (MWP) model consisting of six asymmetric Gaussian-shaped wavepackets, with each having a distinct phase speed. This MWP model allows for the prediction of level-based radiation as well as coherence properties of the field where single wavepacket models fail. In addition, the MWP model can be augmented by an uncorrelated distribution (UD) to accurately predict levels where fine-scale structure radiation dominates. The ability of the MWP and MWP+UD models to efficiently and effectively predict the noise environment near high-performance tactical aircraft is a significant achievement to provide a more complete model to globally predict the radiation properties.

6.2 Contributions to Full-Scale Jet Noise Understanding

From this study, a number of additional findings have been reported that increase our understanding of tactical jet noise. The coherence analysis of ground-based linear array measurements has confirmed that many of the basic properties of laboratory jets are phenomenologically similar as those observed in a full-scale application. The spectral levels, correlation and coherence calculations indicate that the noise radiated at INTER engine condition seems to behave largely like a heated, convectively subsonic jet with uncorrelated, fine-scale turbulent mixing noise to the sideline and with a smooth transition to more correlated, large-scale mixing noise downstream. However, for the MIL and AB conditions, the analyses contain features that have not been observed for laboratory-scale jets.

The differences of high-power full-scale and convectively supersonic laboratory-scale jets appear primarily in the region of maximum overall sound pressure level. Autocorrelation functions reveal a secondary set of negative loops in this region, whereas laboratory-scale jets have shown

no loops to indicate fine-scale noise or a single set of loops to indicate noise associated with large-scale structures. In the cross-correlation analyses, the dominant features in the correlograms appear to split around and downstream of the dominant radiation direction, thus corresponding to multiple phase speeds across the array. Both analyses are additional indications of the multiple mutually incoherent radiating sources shown previously for a similar tactical dataset by Neilsen *et al.*[91] and Wall *et al.*[13] The current work relates the correlation and coherence properties to these dual-peaked spectral shapes and dual directivity lobes that have been observed for tactical jet measurements in the region of maximum overall level.

The unique spectral features also correspond to features in the beamforming and MWP source estimates. A beamforming study of the jet noise indicates that, while the source distribution contracts and moves towards the nozzle with increasing frequency, there is a major shift in the source region between 160-200 Hz (~0.2 Strouhol number, Sr). This is the frequency range at which two radiation lobes are evident in the spectral data. The source shift occurs at all three engine conditions, although it is most pronounced in the MIL data. For example, between 100 Hz and 200 Hz ($0.1 \leq Sr \leq 0.25$), the MIL source shifts upstream about 3 m (~5 jet nozzle diameters, D) and compresses about 3 m ($5D$) in width as measured by the 3 dB down points from the peak level. A source self-coherence analysis using the beamforming results shows that the coherence undergoes a large transition in this frequency range as well. The MWP model provides the peak directivity angle of the primary wavepacket and shows that discrete transitions in the directivity exist between the multi-lobed features. At 160 Hz (~0.2 Sr), the directivity angle of the primary wavepacket transitions to the more upstream lobe of the multilobe radiation. Above 160 Hz, the directivity slowly increases to larger angles with increasing frequency. Additional discrete transitions to upstream directivity angles also appear in the primary wavepacket analysis, at 400 Hz (0.5 Sr) and

630 Hz (0.75 Sr), that indicate additional multilobe features not visible in the one-third octave data that may also be present. This finding is supported by the additional multilobe features recently reported in the narrowband spectra of a similar tactical measurement.[130] Overall, the insights gained of the multilobe features support and build upon similar tactical jet noise studies that report multilobe radiation features of full-scale tactical engine noise.[13, 91] Because of these insights, a recent hypothesis,[113] that the radiation lobe centered at 100 Hz (0.1 Sr) is the result of combustion noise at afterburner powers, stands to question as the beamforming results presented here show radiation from both lobes directed far downstream from the nozzle, where combustion noise would likely emanate. In addition, the dual-lobed features have also been seen at non-afterburning powers, including MIL.

The detailed beamforming study of the tactical jet noise source reveals additional insights about the tactical source, particularly of the source coherence. While many studies have been focused solely on the source levels and distribution, the HM algorithm also estimates the source coherence properties. The source coherence estimates indicate that the maximum source coherence occurs downstream of the maximum source level. This result suggests that, as observed across the measurement array, the maximum source-level region is comprised of both uncorrelated and correlated sources and that the correlated source dominates farther downstream. In addition, a MWP study revealed that the primary wavepacket dimensions, when normalized and scaled by wavelength, were nearly identical across the frequency range, even though source coherence lengths decrease with increasing frequency. The two observations suggest that the relative importance of the nonprimary wavepackets (i.e., additional independent sources) increases with frequency and that the combination of these wavepackets, when spatially distributed, comprise the source distribution.

Additional insights on the individual sources comprising the distribution have been ascertained from a subarray beamforming analysis. The sideline radiation measurements, when used as an input to the HM, reveal a source distribution that is largely invariant in shape and peak location (2-3 m; ~3-5D) from the nozzle exit) as a function of frequency. Its source coherence statistics are also fairly straightforward and decrease uniformly with increasing frequency. Conversely, the source corresponding to the downstream subarray, reveals a source with large transitions in source dimensions and location with increasing frequency. In fact, the multilobe trends were found to correspond entirely with the downstream array radiation. In addition, the downstream-based source coherence values are approximately double those of the sideline-derived source for a given frequency. The level and coherence results point to a sideline radiation model that radiates omnidirectionally and which is derived of multiple independent sources, whereas the downstream radiation is much more directed and generated with higher amplitude sources that are more self-coherent, consistent with a two-source jet noise model.[9]

When the beamforming source is decomposed into an analytical representation, it was found that the jet noise source and field properties are reproducible using a low-order MWP model. For example, the multilobe radiation is reducible into two wavepackets plus a few additional wavepackets to reconstruct any residual energy. Reproduction of the multilobe directivity using the MWP model shows that overlapping sources with differing phase speeds can effectively generate multilobe radiation patterns.

An engine condition analysis of the beamforming results and corresponding MWP models highlighted differences across the engine conditions. When compared to the MIL beamforming results, the source width at INTER is much more contracted and the coherence length values are less. In addition, the corresponding INTER MWP model shows that multiple overlapping

wavepackets are required. In contrast, the AB source distribution is even larger than for MIL and much larger source coherence values, particularly in the downstream region of the source. Thus, the corresponding AB MWP model comprises wavepackets that are much more dispersed across the source. Finally, the MWP models have been successfully validated at each engine condition using benchmark measurements to show that, regardless of engine condition, a reduced-order model of the jet noise has been successfully obtained to effectively and efficiently predict the jet-noise radiation.

6.3 Contributions to Methods

To better understand the jet properties, several methods have been implemented and improved. First, a detailed numerical case study was performed to both validate beamforming methods for use with jet noise measurements and to select a most suitable method for application to the full-scale data. Because jet noise consists of sources that are noncompact and partially correlated, assumptions used in traditional beamforming methods are violated. A mathematical analysis has been provided to distinguish the traditional beamforming from the more generalized inverse methods that are successful in estimating jet source levels and coherence properties. It was found that all the advanced beamforming methods tested are successful in estimating the source levels, although FBF is not able to estimate the source coherence. In addition, the comparison showed that, when treated as ESMs, each method (except for FBF) can estimate the radiated levels and field coherence. Of the methods tested, HM and GINV produced the best estimates and have been validated for jet noise beamforming studies. A study on the optimum regularization values was also given to lend insight into the "art" of applying the appropriate regularization. The advanced beamforming methods were further used in source coherence estimates. A method for

measuring source coherence lengths has been developed, which builds upon a coherence length analysis for coherence calculations of field measurements.[94]

In addition, the unwrapped phase interpolation (UPAINT) method has been applied to the linear array measurements to increase the usable bandwidth of the array when used with beamforming methods.[50] This was the first such implementation to full-scale jet measurements, particularly for an array that spans the source. The UPAINT processing was validated in the numerical jet case study and produced improved beamforming results at frequencies up to seven times higher than the array spatial Nyquist frequency. The array measurements were processed as needed (i.e., above the spatial Nyquist frequency) and input into the HM algorithm to produce tactical jet noise source estimates.

Finally, the successful implementation of the UPAINT-HM methods provides an ESM to predict jet noise radiation. However, the ESM model is generally composed of more input parameters than is necessary, so a reduced-order analytical model has been to conveniently represent the full-order model. The MWP model was developed that incorporated the physical properties estimated by the beamforming-based ESM, including source coherence to determine the decay of each asymmetric-Gaussian wavepacket shape. In contrast to single wavepacket models, the MWP model was also designed to predict the radiated coherence properties. And where sideline radiation necessitated a large number of analytical wavepackets, a UD has been incorporated to imitate the sideline radiation levels and coherence properties of multiple independent sources.

6.4 Implications and Recommendations

This work represents a significant effort to characterize the radiation of a full-scale tactical aircraft using a linear array. While the axial coherence has been studied in detail, the source was assumed to have azimuthal symmetry. While this is not a poor assumption for sufficiently low frequencies,[23, 33] future efforts to incorporate azimuthal measurements will provide better source characterizations and improved radiation prediction capabilities. Azimuthal measurements could be taken using large cone-shaped cage arrays that span the jet both axially and azimuthally. For instance, cage array designs for azimuthal coverage have been reported in lab-scale implementations by Viswanathan *et al.*[23] and by Suzuki and Colonius[15]. These measurements could alternatively be taken using a scan-based approach using a cylindrical array that surrounds the engine and that slowly traverses downstream. The resultant measurements would then be stitched together using a separate fixed reference microphone array and a partial field decomposition.[131] The resultant calculated azimuthal radiation modes from the measurements can be incorporated to further extend the one-dimensional asymmetric-Gaussian wavepackets to characterize the azimuthal variation.

While the MWP models have been developed independently for each frequency, the model's analytical framework allows for future work to create a broadband analytical MWP model for a more complete picture of the radiated properties. In addition, efforts to incorporate additional physical properties of the jet noise into a reduced-order analytical framework will provide better predictive capabilities for time-domain events. This is particularly true for future efforts to extend the capabilities of the model to the far field, especially when cumulative nonlinear effects from propagation are significant.

Beamforming algorithms are ever evolving in their capabilities and, in many cases, can be fashioned to a particular need. The beamforming methods comparison study provided validation to multiple beamforming methods. However, some of these methods are complementary[70] and future efforts to merge these algorithms could extend their utility and robustness. In addition, time-domain intermittency and impulses have not been considered in the present work. While the focus here was on frequency-domain beamforming, event-based beamforming in the time domain should produce additional insights into the individual random impulses, their behavior how they differ from event to event. While the beamforming methods will necessarily change from the methods used here, it is expected that regularization-based methods using measurement inputs from linear arrays that span the source will most effectively estimate the source properties.

Finally, while this study has characterized the acoustic radiation, no attempts have been made to bridge the acoustic radiation to the generative effects of the turbulent structures and shear-layer interactions. These results provide a benchmark for similar large eddy simulations (LES) of tactical jets. A comparison with the LES and these results can also provide insight to the turbulence features that contribute to jet noise. In addition, these results will guide future LES efforts on such features as the dual-lobe phenomena that are present in the full-scale results.

References

[1]C. K. W. Tam, "Jet noise: Since 1952," *Theoretical and Computational Fluid Dynamics* **10**, 393-405 (1998).

[2]P. Jordan and T. Colonius, "Wave packets and turbulent jet noise," *Annual Review of Fluid Mechanics* **45**, 173-195 (2013).

[3]A. Towne, T. Colonius, P. Jordan, A. V. Cavalieri, and G. A. Brès, "Stochastic and nonlinear forcing of wavepackets in a Mach 0.9 jet," AIAA Paper 2015-2217, 2015.

[4]D. V. Affairs, "Annual Benefits Report Fiscal Year 2016," (2017).

[5]M. J. Lighthill, "On sound generated aerodynamically. II. Turbulence as a source of sound," *Proceedings of the Royal Society of London A: Mathematical, Physical and Engineering Sciences* **222**, 1-32 (1954).

[6]M. J. Lighthill, "On sound generated aerodynamically. I. General theory," *Proceedings of the Royal Society of London A: Mathematical, Physical and Engineering Sciences* **211**, 564-587 (1952).

[7]G. Lilley, "Jet noise classical theory and experiments," *Aeroacoustics of flight vehicles: theory and practice* **1**, 211-289 (1991).

[8]K. Viswanathan, "Mechanisms of jet noise generation: classical theories and recent developments," *International Journal of Aeroacoustics* **8**, 355-407 (2009).

[9]C. K. W. Tam, K. Viswanathan, K. K. Ahuja, and J. Panda, "The sources of jet noise: Experimental evidence," *Journal of Fluid Mechanics* **615**, 253-292 (2008).

[10]J. Liu, A. T. Corrigan, K. Kailasanath, and E. J. Gutmark, "Effects of Temperature on Noise Generation in Supersonic Jets," AIAA Paper 2016-2937, 2016.

[11]D. Long, "Evaluation of jet and shock cell noise via acoustic holography," AIAA Paper 2008-5, 2008.

[12]C. K. Tam, "Supersonic jet noise," *Annual Review of Fluid Mechanics* **27**, 17-43 (1995).

[13]A. T. Wall, K. L. Gee, T. B. Neilsen, B. M. Harker, S. A. McInerny, R. C. McKinley, and M. M. James, "Investigation of multi-lobed fighter jet noise sources using acoustical holography and partial field decomposition methods," AIAA Paper 2015-2379, 2015.

[14]K. L. Gee, T. B. Neilsen, A. T. Wall, J. M. Downing, and M. M. James, "The ‘ Sound Of Freedom’ : Characterizing Jet Noise From High- Performance Military Aircraft," *Acoustics Today* **9**, 8-21 (2013).

[15]T. Suzuki and T. Colonius, "Instability waves in a subsonic round jet detected using a near-field phased microphone array," *Journal of Fluid Mechanics* **565**, 197-226 (2006).

[16]D. Papamoschou, P. J. Morris, and D. K. McLaughlin, "Beamformed flow-acoustic correlations in high-speed jets," AIAA Paper 2009-3212, 2009.

[17]R. Reba, S. Narayanan, and T. Colonius, "Wave-packet models for large-scale mixing noise," *International Journal of Aeroacoustics* **9**, 533-558 (2010).

[18]M. Koenig, A. V. Cavalieri, P. Jordan, J. Delville, Y. Gervais, and D. Papamoschou, "Farfield filtering and source imaging of subsonic jet noise," *Journal of Sound and Vibration* **332**, 4067-4088 (2013).

[19]S. C. Crow and F. Champagne, "Orderly structure in jet turbulence," *Journal of Fluid Mechanics* **48**, 547-591 (1971).

[20]B. James and W. Mark, in *17th AIAA/CEAS Aeroacoustics Conference (32nd AIAA Aeroacoustics Conference)* (American Institute of Aeronautics and Astronautics, 2011).

[21]S. Karabasov, M. Afsar, T. Hynes, A. Dowling, W. McMullan, C. Pokora, G. Page, and J. McGuirk, "Jet noise: Acoustic analogy informed by large eddy simulation," *AIAA Journal* **48**, 1312-1325 (2010).

[22]A. Sinha, R. Schlinker, J. Simonich, R. A. Reba, and T. Colonius, "Toward active control of noise from hot supersonic jets," Proceedings of 19th AIAA/CEAS Aeroacoustics Conference, pp. 2234.

[23]K. Viswanathan, J. R. Underbrink, and L. Brusniak, "Space-time correlation measurements in near fields of jets," *AIAA Journal* **49**, 1577-1599 (2011).

[24]A. T. Wall, K. L. Gee, M. M. James, K. A. Bradley, S. A. McInerny, and T. B. Neilsen, "Near-field noise measurements of a high-performance military jet aircraft," *Noise Control Engineering Journal* **60**, 421-434 (2012).

[25]J. Panda, R. G. Seasholtz, and K. A. Elam, "Investigation of noise sources in high-speed jets via correlation measurements," *Journal of Fluid Mechanics* **537**, 349-385 (2005).

[26]J. Panda and R. G. Seasholtz, "Experimental investigation of density fluctuations in high-speed jets and correlation with generated noise," *Journal of Fluid Mechanics* **450**, 97-130 (2002).

[27]T. A. Stout, K. L. Gee, T. B. Neilsen, A. T. Wall, and M. M. James, "Source characterization of full-scale jet noise using acoustic intensity," *Noise Control Engineering Journal* **63**, 522-536 (2015).

[28]M. J. Fisher, M. Harper-Bourne, and S. A. L. Glegg, "Jet engine noise source location: The polar correlation technique," *Journal of Sound and Vibration* **51**, 23-54 (1977).

[29]A. T. Wall, K. L. Gee, T. B. Neilsen, R. L. McKinley, and M. M. James, "Military jet noise source imaging using multisource statistically optimized near-field acoustical holography," *The Journal of the Acoustical Society of America* **139**, 1938-1950 (2016).

[30]Z. Prime, A. Mimani, D. Moreau, and C. J. Doolan, in *20th AIAA/CEAS Aeroacoustics Conference* (American Institute of Aeronautics and Astronautics, 2014).

[31]A. T. Wall, K. L. Gee, M. D. Gardner, T. B. Neilsen, and M. M. James, "Near-field acoustical holography applied to high-performance jet aircraft noise," *Proceedings of Meetings on Acoustics* **9**, 040009 (2011).

[32]A. T. Wall, "The characterization of military aircraft jet noise using near-field acoustical holography methods," Dissertation, Brigham Young University, 2013.

[33]H. Vold, S. Parthiv, P. Morris, Y. Du, and D. Papamoschou, "Axisymmetry and azimuthal modes in jet noise," *AIAA Journal* **2012-2214**, (2012).

[34]R. P. Dougherty, "Beamforming in acoustic testing," *Experimental Fluid Mechanics Series, Berlin, Germany, Springer-Verlag GmbH, 2002*62-97 (2002).

[35]S. R. Venkatesh, D. R. Polak, and S. Narayanan, "Beamforming algorithm for distributed source localization and its application to jet noise," *AIAA Journal* **41**, 1238-1246 (2003).

[36]K. Viswanathan, "Distributions of noise sources in heated and cold jets: are they different?," *International Journal of Aeroacoustics* **9**, 589-625 (2010).

[37]T. F. Brooks, W. M. Humphreys, and G. E. Plassman, "DAMAS Processing for a Phased Array Study in the NASA Langley Jet Noise Laboratory," AIAA Paper 2010-3780, 2010.

[38]Barry D. Van Veen and K. M. Buckley, "Beamforming: A versatile approach to spatial filtering," *IEEE ASSP Magazine* **5**, 4-24 (1988).

[39]S. S. Lee and J. Bridges, "Phased-Array Study of Dual-Flow Jet Noise: Effect of Nozzles and Mixers," AIAA Paper 2006-2647, 2006.

[40]R. P. Dougherty, "Improved generalized inverse beamforming for jet noise," *International Journal of Aeroacoustics* **11**, 259-290 (2012).

[41]R. Schlinker, S. Liljenberg, D. Polak, K. Post, C. Chipman, and A. Stern, "Supersonic Jet Noise Source Characteristics & Propagation: Engine and Model Scale," AIAA Paper 2007-3623, 2007.

[42]T. F. Brooks and W. M. Humphreys, "A deconvolution approach for the mapping of acoustic sources (DAMAS) determined from phased microphone arrays," *Journal of Sound and Vibration* **294**, 856-879 (2006).

[43]T. F. Brooks and W. M. Humphreys Jr, "Extension of DAMAS phased array processing for spatial coherence determination (DAMAS-C)," AIAA Paper 2006-2654, 2006.

[44]U. Michel and S. Funke, "Noise source analysis of an aeroengine with a new inverse method SODIX," AIAA Paper 2008-2860, 2008.

[45]D. Papamoschou, "Wavepacket modeling of the jet noise source," AIAA Paper 2011-2835, 2011.

[46]T. Padois, A. Berry, P.-A. Gauthier, and N. Joshi, "Beamforming matrix regularization and inverse problem for sound source localization : application to aero-engine noise," AIAA Paper 2013-2212, 2013.

[47]T. Suzuki, "L1 generalized inverse beam-forming algorithm resolving coherent/incoherent, distributed and multipole sources," *Journal of Sound and Vibration* **330**, 5835-5851 (2011).

[48]R. P. Dougherty, "Functional Beamforming for Aeroacoustic Source Distributions," AIAA Paper 2014-3066, 2014.

[49]T. Yardibi, J. Li, P. Stoica, N. S. Z. L. N. Cattafesta, and III, "A covariance fitting approach for correlated acoustic source mapping," *The Journal of the Acoustical Society of America* **127**, 2920-2931 (2010).

[50]C. B. Goates, B. M. Harker, T. B. Neilsen, and K. L. Gee, "Extending the bandwidth of an acoustic beamforming array using phase unwrapping and array interpolation," *The Journal of the Acoustical Society of America* **141**, EL407-EL412 (2017).

[51]K. L. Gee, M. Akamine, K. Okamoto, T. B. Neilsen, M. R. Cook, S. Tsutsumi, S. Teramoto, and T. Okunuki, "Characterization of Supersonic Laboratory-Scale Jet Noise with Vector Acoustic Intensity," AIAA Paper 2017-3519, 2017.

[52]B. M. Harker, K. L. Gee, T. B. Neilsen, A. T. Wall, and M. M. James, "Wavepacket modeling and fullscale military jet noise beamforming analyses," AIAA Paper 2016-2129, 2016.

[53]J. Ffowcs Williams, J. Simson, and V. Virchis, "'Crackle': An annoying component of jet noise," *Journal of Fluid Mechanics* **71**, 251-271 (1975).

[54]C. Morfey and G. Howell, "Nonlinear propagation of aircraft noise in the atmosphere," *AIAA Journal* **19**, 986-992 (1981).

[55]K. L. Gee, V. W. Sparrow, M. M. James, J. M. Downing, C. M. Hobbs, T. B. Gabrielson, and A. A. Atchley, "The role of nonlinear effects in the propagation of noise from high-power jet aircraft," *Journal of the Acoustical Society of America* **123**, 4082-4093 (2008).

[56]R. Dougherty and J. Mendoza, "Phased Array Beamforming with 100-Foot Polar Arc Microphones in a Static Engine Noise Test," AIAA Paper 2008-51, 2008.

[57]B. J. Tester and K. Holland, "Estimating the sound power radiated by the nozzle-based source on a long cowl engine using phased arrays in a semi-reverberant test cell," AIAA Paper 2015-2979, 2015.

[58]P. Sijtsma, "CLEAN based on spatial source coherence," *International Journal of Aeroacoustics* **6**, 357-374 (2007).

[59]J. S. Bendat and A. G. Piersol, *Random Data: Analysis and Measurement Procedures*, 4th ed. (John Wiley & Sons, Hoboken, NJ, 2010), pp. 109-503

[60]T. Padois, P.-A. Gauthier, and A. Berry, "Inverse problem with beamforming regularization matrix applied to sound source localization in closed wind-tunnel using microphone array," *Journal of Sound and Vibration* **333**, 6858-6868 (2014).

[61]J. P. Erwin, P. Panickar, P. Vogel, and N. Sinha, "Acoustic Source Localization of Rectangular Jets using Large Eddy Simulation with Numerical Phased Arrays," AIAA Paper 2014-0179, 2014.

[62]R. P. Dougherty, "Extensions of DAMAS and Benefits and Limitations of Deconvolution in Beamforming," AIAA Paper 2005-2961, 2005.

[63]K. Ehrenfried and L. Koop, "Comparison of iterative deconvolution algorithms for the mapping of acoustic sources," *AIAA Journal* **45**, 1584-1595 (2007).

[64]T. Yardibi, J. Li, P. Stoica, L. N. Cattafesta, and III, "Sparsity constrained deconvolution approaches for acoustic source mapping," *The Journal of the Acoustical Society of America* **123**, 2631-2642 (2008).

[65]E. Sarradj, G. Herold, P. Sijtsma, R. Merino-Martinez, T. F. Geyer, C. J. Bahr, R. Porteous, D. Moreau, and C. J. Doolan, "A microphone array method benchmarking exercise using synthesized input data," AIAA Paper 2017-3719, 2017.

[66]C. J. Bahri, W. M. Humphreys Jr, D. Ernstiii, T. Ahlefeldtiv, C. Spehrv, A. Pereiravi, Q. Leclerevii, C. Picardviii, R. Porteousix, and D. J. Moreaux, "A Comparison of Microphone Phased Array Methods Applied to the Study of Airframe Noise in Wind Tunnel Testing," AIAA Paper 2017-3718, 2017.

[67]B. M. Harker, T. B. Neilsen, K. L. Gee, A. T. Wall, and M. M. James, "Spatiotemporal Correlation Analysis of Jet Noise from a High-Performance Military Aircraft," *AIAA Journal* (Accepted Dec. 2015).

[68]D. Papamoschou, "Imaging of Distributed Directional Noise Sources," *AIAA paper* **2008-2885**, (2008).

[69]P. A. Ravetta, R. A. Burdisso, and W. F. Ng, "Noise source localization and optimization of phased-array results," *AIAA Journal* **47**, 2520-2533 (2009).

[70]S. Li, Z. Xu, Z. Zhang, Y. He, and J. Mao, "Functional generalized inverse beamforming with regularization matrix applied to sound source localization," *Journal of Vibration and Control,*1-12 (2016).

[71]J. R. Underbrink, "Pletharrays for aeroacoustic phased array applications," *International Journal of Aeroacoustics* **16**, 202-229 (2017).

[72]D. Robert and P. Gary, in *15th AIAA/CEAS Aeroacoustics Conference (30th AIAA Aeroacoustics Conference)* (American Institute of Aeronautics and Astronautics, 2009).

[73]J. Panda, R. Mosher, and B. Porter, "Noise source identification during rocket engine test firings and a rocket launch," *Journal of Spacecraft and Rockets* **51**, 1761-1772 (2014).

[74]T. Suzuki, "Coherent noise sources of a subsonic round jet investigated using hydrodynamic and acoustic phased-microphone arrays," *Journal of Fluid Mechanics* **730**, 659-698 (2013).

[75]K. K. Ahuja, D. K. Nance, J. Carrigan, and A. Karon, "On Coherence of Jet Noise," AIAA Paper 2014-2339, 2014.

[76]M. M. James, A. R. Salton, J. M. Downing, K. L. Gee, T. B. Neilsen, B. O. Reichman, R. L. McKinley, A. T. Wall, and H. L. Gallagher, "Acoustic Emissions from F-35 Aircraft during Ground Run-Up," AIAA Paper 2015-2375, 2015.

[77]L. Brusniak, J. Underbrink, E. Nesbitt, D. Lynch, and M. Martinez, "Phased array measurements of full-scale engine exhaust noise," AIAA Paper 2007-3612, 2007.

[78]B. M. Harker, K. L. Gee, T. B. Neilsen, A. T. Wall, and M. M. James, "Wavepacket modeling and fullscale military jet noise beamforming analyses," AIAA Paper 2016-2129, 2016.

[79]L. E. Kinsler, A. R. Frey, A. B. Coppens, and J. V. Sanders, *Fundamentals of Acoustics, 4th Edition*. (John Wiley and Sons, Inc., 2000), pp. 171-176

[80]E. Sarradj, "Three-Dimensional Acoustic Source Mapping with Different Beamforming Steering Vector Formulations," *Advances in Acoustics and Vibration* **2012**, (2012).

[81]T. Suzuki, "A review of diagnostic studies on jet-noise sources and generation mechanisms of subsonically convecting jets," *Fluid Dynamics Research* **42**, 014001 (2010).

[82]T. K. Moon and W. C. Stirling, *Mathematical methods and algorithms for signal processing*. (Prentice hall, 2000), pp. 139

[83]E. G. Williams, "Regularization methods for near-field acoustical holography," *The Journal of the Acoustical Society of America* **110**, 1976-1988 (2001).

[84]G. H. Golub, M. Heath, and G. Wahba, "Generalized cross-validation as a method for choosing a good ridge parameter," *Technometrics* **21**, 215-223 (1979).

[85]L. Reichel and Q. Ye, "Simple square smoothing regularization operators," *Electron. Trans. Numer. Anal* **33**, 63-83 (2009).

[86]S. Noschese and L. Reichel, "Inverse problems for regularization matrices," *Numerical Algorithms* **60**, 531-544 (2012).

[87]J. F. Sturm, "Using SeDuMi 1.02, a MATLAB toolbox for optimization over symmetric cones," *Optimization methods and software* **11**, 625-653 (1999).

[88]M. R. Cook, K. L. Gee, S. D. Sommerfeldt, and T. B. Neilsen, "Coherence-based phase unwrapping for broadband signals," *Proceedings of Meetings on Acoustics* **30**, 055005 (2017).

[89]Y. Du and P. J. Morris, "Numerical simulation of the effect of a low bypass cooling stream on supersonic jet noise," AIAA Paper 2014-1402, 2014.

[90]B. M. Harker, T. B. Neilsen, K. L. Gee, A. T. Wall, and M. M. James, "Spatiotemporal Correlation Analysis of Jet Noise from a High-Performance Military Aircraft," *AIAA Journal* **54**, 1554-1566 (2016).

[91]T. B. Neilsen, K. L. Gee, A. T. Wall, and M. M. James, "Similarity spectra analysis of high-performance jet aircraft noise," *Journal of the Acoustical Society of America* **133**, 2116-2125 (2013).

[92]T. B. Neilsen, K. L. Gee, B. M. Harker, and M. M. James, "Level-educed Wavepacket Representation of Noise Radiation from a High-Performance Military Aircraft," Proceedings of 54th AIAA Aerospace Sciences Meeting, pp. 1880.

[93]B. M. Harker, K. L. Gee, T. B. Neilsen, A. T. Wall, and M. M. James, "Phased-array measurements of full-scale military jet noise," AIAA Paper 2014-3069, 2014.

[94]A. T. Wall, M. D. Gardner, K. L. Gee, and T. B. Neilsen, "Coherence length as a figure of merit in multireference near-field acoustical holography," *Journal of the Acoustical Society of America* **132**, El215-El221 (2012).

[95]A. T. Wall, K. L. Gee, T. B. Neilsen, and M. M. James, "On near-field acoustical inverse measurements of partially coherent sources," *Proceedings of Meetings on Acoustics* **11**, 040007 (2012).

[96]Z. Wang and S. F. Wu, "Helmholtz equation–least-squares method for reconstructing the acoustic pressure field," *The Journal of the Acoustical Society of America* **102**, 2020-2032 (1997).

[97]B. M. Harker, T. B. Neilsen, K. L. Gee, M. M. James, and A. T. Wall, "Spatiotemporal Correlation Analysis of Jet Noise from a High-Performance Military Aircraft," AIAA Paper 2015-2376, 2015.

[98]C. K. Tam, N. N. Pastouchenko, and K. Viswanathan, "Continuation of the Near Acoustic Field of a Jet to the Far Field. Part I: Theory," AIAA Paper 2010-3728, 2010.

[99]C. K. W. Tam, K. Viswanathan, N. N. Pastouchenko, and B. Tam, "Continuation of Near-Acoustic Fields of Jets to the Far Field: Part II Experimental Validation and Noise Source Characteristics," AIAA Paper 2010-3729, 2010.

[100]B. M. Harker, K. L. Gee, T. B. Neilsen, A. T. Wall, S. A. McInerny, and M. M. James, "On autocorrelation analysis of jet noise," *Journal of the Acoustical Society of America* **133**, EL458-EL464 (2013).

[101]U. Michel, "The role of source interference in jet noise," AIAA Paper 2009-3377, 2009.

[102]S. A. Miller, "Prediction of Near-Field Jet Cross Spectra," *AIAA Journal* **53**, 2130-2150 (2014).

[103]B. L. Clarkson, "Correlation of pressures around a jet engine," Proceedings of WADC University of Minnesota Conference on Acoustical Fatigue, WADC TR 59-676 (Mar. 1961), pp. 85-98.

[104]H. V. Fuchs, "Space correlations of the fluctuating pressure in subsonic turbulent jets," *Journal of Sound and Vibration* **23**, 77-99 (1972).

[105]H. V. Fuchs, "Application of acoustic mirror, telescope and polar correlation techniques to jet noise source location," *Journal of Sound and Vibration* **58**, 117-126 (1978).

[106]L. Maestrello, "Two-point correlations of sound pressure in the far field of a jet: Experiment," *NASA TM X-72835* (1976).

[107]H. Ribner, "Two point correlations of jet noise," *Journal of Sound and Vibration* **56**, 1-19 (1978).

[108]C. K. W. Tam, "Influence of nozzle geometry on the noise of high-speed jets," *AIAA Journal* **36**, 1396-1400 (1998).

[109]C. K. W. Tam, M. Golebiowski, and J. M. Seiner, "On the two components of turbulent mixing noise from supersonic jets," AIAA Paper 96-1716, 1996.

[110]S. A. Kumar, N. Karthikeyan, and L. Venkatakrishnan, "Correlation Studies in the Acoustic Far-Field of Non-ideally Expanded Supersonic Jets," AIAA Paper 2013-2082, 2013.

[111]J. Liu, A. T. Corrigan, K. Kailasanath, N. S. Heeb, and E. J. Gutmark, "Numerical Study of Noise Sources Characteristics in An Underexpanded Jet Flow," AIAA Paper 2014-2604, 2014.

[112]T. B. Neilsen, K. L. Gee, and M. M. James, "Spectral Characterization in the Near and Mid-field of Military Jet Aircraft Noise," AIAA Paper 2013-2191, 2013.

[113]C. K. Tam and S. Parrish, "Noise of high-performance aircrafts at afterburner," AIAA Paper 2014-2754, 2014.

[114]T. B. Neilsen, K. L. Gee, A. T. Wall, M. M. James, and A. A. Atchley, "Comparison of supersonic full-scale and laboratory-scale jet data and the similarity spectra for turbulent mixing noise," *Proceedings of Meetings on Acoustics* **19**, 040071 (2013).

[115]A. Wall, K. Gee, T. Neilson, D. Krueger, M. James, S. Sommerfeldt, and J. Blotter, "Full-Scale Jet Noise Characterization Using Scan-Based Acoustical Holography," AIAA Paper 2012-2081, 2012.

[116]A. T. Wall, K. L. Gee, T. B. Neilsen, R. L. McKinley, and M. M. James, "Military jet noise source imaging using multisource statistically optimized near-field acoustical holography," *Journal of the Acoustical Society of America* (submitted for publication).

[117]T. A. Stout, K. L. Gee, T. B. Neilsen, A. T. Wall, and M. M. James, "Acoustic intensity near a high-powered military jet aircraft," *The Journal of the Acoustical Society of America* **138**, EL1-EL7 (2015).

[118]J. Morgan, T. B. Neilsen, K. L. Gee, A. T. Wall, and M. M. James, "Simple-source model of military jet aircraft noise," *Noise Control Engineering Journal* **60**, 435-449 (2012).

[119]B. J. Greska, "Supersonic jet noise and its reduction using microjet injection," Dissertation, The Florida State University, 2005.

[120]W. J. Baars, C. E. Tinney, N. E. Murray, B. J. Jansen, and P. Panickar, "The effect of heat on turbulent mixing noise in supersonic jets," AIAA Paper 2011-1029, 2011.

[121]J. Seiner, B. Jansen, and L. Ukeiley, "Acoustic fly-over studies of F/AE/F Aircraft during FCLP mission," AIAA Paper 2003-3330, 2003.

[122]A. Krothapalli, L. Venkatakrishnan, and L. Lourenco, "Crackle: a dominant component of supersonic jet mixing noise," AIAA Paper 2000-2024, 2000.

[123]W. J. Baars and C. E. Tinney, "Shock-structures in the acoustic field of a Mach 3 jet with crackle," *Journal of Sound and Vibration* **333**, 2539-2553 (2014).

[124]J. M. Seiner, M. K. Ponton, B. J. Jansen, and N. T. Lagen, "The effects of temperature on supersonic jet noise emission," Proceedings of 14th DGLR/AIAA aeroacoustics conference, pp. 295-307.

[125]C. K. W. Tam and K. B. M. Q. Zaman, "Subsonic Jet Noise from Nonaxisymmetric and Tabbed Nozzles," *AIAA Journal* **38**, 592-599 (2000).

[126]A. T. Wall, K. L. Gee, and T. B. Neilsen, "Multisource statistically optimized near-field acoustical holography," *The Journal of the Acoustical Society of America* **137**, 963-975 (2015).

[127]Y. Khalighi, J. W. Nichols, S. Lele, F. Ham, and P. Moin, "Unstructured large eddy simulation for prediction of noise issued from turbulent jets in various configurations," AIAA Paper 2011-2886, 2011.

[128]S. S. Lee and J. Bridges, "Phased-Array Measurements of Single Flow Hot Jets," AIAA Paper 2005-2842, 2005.

[129]J. Hald, "Combined NAH and beamforming using the same microphone array," *Sound and Vibration* **38**, 18-27 (2004).

[130]A. T. Wall, K. M. Leete, K. L. Gee, T. B. Neilsen, M. M. James, and R. L. McKinley, "Preliminary Investigation of Multiple Fighter Jet Noise Sources Using Acoustical Holography," AIAA Paper 2017-3520, 2017.

[131]J. Hald, "STSF-a unique Technique for scan-based Near-field Acoustic Holography without restriction on coherence," *B & K Technical Review No. 1* (1989).

[132]A. Sinha, D. Rodríguez, G. A. Brès, and T. Colonius, "Wavepacket models for supersonic jet noise," *Journal of Fluid Mechanics* **742**, 71-95 (2014).

[133]A. Towne, A. V. Cavalieri, P. Jordan, T. Colonius, O. Schmidt, V. Jaunet, and G. A. Brès, "Acoustic resonance in the potential core of subsonic jets," *Journal of Fluid Mechanics* **825**, 1113-1152 (2017).

[134]A. V. Cavalieri, P. Jordan, T. Colonius, and Y. Gervais, "Axisymmetric superdirectivity in subsonic jets," *Journal of Fluid Mechanics* **704**, 388-420 (2012).

[135]I. A. Maia, P. Jordan, V. Jaunet, and A. V. Cavalieri, "Two-point wavepacket modelling of jet noise," AIAA Paper 2017-3380, 2017.

[136]R. Schmidt, "Multiple emitter location and signal parameter estimation," *IEEE transactions on antennas and propagation* **34**, 276-280 (1986).

[137]S. Hassani, *Mathematical physics: a modern introduction to its foundations*. (Springer Science & Business Media, 2013), pp. 33-35

[138]R. Reba, J. Simonich, and R. Schlinker, "Sound radiated by large-scale wave-packets in subsonic and supersonic jets," AIAA Paper 2009-3256, 2009.

[139]M. Kearney-Fischer, "A model function for jet noise events at aft angles and what it says about the statistical relationships of the events," *Journal of Sound and Vibration* **338**, 217-236 (2015).